Variations of depositional redox conditions across the Cambrian-Ordovician boundary (GSSP, Green Point Formation) in western Newfoundland: Implications from Mo-, U-, and S-isotope signatures and I/Ca ratios

by

©Jie Li

A thesis submitted to the School of Graduate Studies in partial fulfillment of the requirements for the degree of

Doctor of Philosophy

Department of Earth Sciences

Memorial University of Newfoundland

January 2024

St. John’s, Newfoundland and Labrador, Canada

Abstract

The Green Point Formation in western Newfoundland, Canada, includes the Global Boundary Stratotype Section and Point (GSSP) of the Cambrian-Ordovician (Є-O) boundary. This formation consists mainly of slope deposits of alternating lime mudstone and shale interbeds (rhythmites). In this study, we conducted an analysis of the isotopic and elemental signals of Mo and U in the shale and limestone. Additionally, we examined the textures and bulk $\delta^{34}S_{py}$ signals of biological pyrite in the shale and investigated the I/Ca ratios of the limestone. These analyses aim to provide a more comprehensive understanding of the depositional environments and marine redox conditions during the Є-O transition.

The analysis revealed broad ranges of the shale authigenic $\delta^{98}Mo_{auth}$ (−0.40 to +3.16‰) and the limestone $\delta^{98}Mo_{carb}$ (−0.30 to +2.34‰) values. These observations, combined with significantly low Mo concentrations and the lack of fossils and bioturbations, suggest that the shale and limestone were both deposited under weakly oxygenated (dysoxic to anoxic) bottom conditions. Furthermore, an inverse correlation between the shale $\delta^{98}Mo_{auth}$ and $\delta^{238}U_{auth}$ values, similar to those observed in modern semi-restricted basins, indicates that the local continental margin seawater was probably partially isolated from the open ocean. In accordance with this inference, significant inverse relationships are observed between the $\delta^{34}S_{py}$ values and the contents of terrigenous elements (Al, Th, and ∑REE), indicating that terrestrial inputs might have influenced the regional seawater sulfate level. Interestingly, parallel changes are noted between the bulk $\delta^{34}S_{py}$ values and abundances of pyrite precipitated in sedimentary porewaters,

suggesting that the $\delta^{34}S_{py}$ variability could also be influenced by varying amounts of pyrite formed at different diagenetic stages within the samples. As a result, the fluctuation of bulk $\delta^{34}S_{py}$ signals alone may not necessarily indicate perturbations of the global marine sulfur cycle.

Despite the evidence for partial basin isolation, the average shallow seawater $\delta^{238}U$ signals (−0.70 ± 0.24‰, 1σ), inferred from the limestone $\delta^{238}U_{carb}$ values, were probably close to coeval open oceans. With this estimated mean oceanic $\delta^{238}U$ value, our three-sink U-isotope mass balance model predicts that the Є-O transition was a time of expanded marine anoxia with anoxic to euxinic seawater covering 1.0 to 21.1% of the ocean floor. This prediction aligns with the observation of substantially low I/Ca ratios ranging from 0.02 to 0.33 μmol/mol in the limestone. These ratios fall well below the Proterozoic Eon background I/Ca values of ~0.5 to 1 μmol/mol, indicating the presence of a shallow marine oxycline along the regional continental margin. Similar observations have been reported in several other age-equivalent sections deposited along the shelf and slope of the ancient Iapetan and Laurentian continental margins. Consequently, it is plausible to suggest that seawater surrounding the Iapetan and Laurentian continental margins during the Є-O transition might have been poorly oxygenated, with shallow oxyclines or expanded oxygen minimum zones in the shelf and/or slope areas. These findings agree with earlier viewpoints that the middle-late Cambrian to the Early Ordovician marine biodiversity plateau was linked to widespread oceanic anoxia.

Co-Authorship Statement

The research topics of this thesis were initiated by my supervisor Dr. Karem Azmy. I was responsible for the three research projects (Chapters 2 to 4) from all aspects, including reviewing the literature, preparing samples, analyzing and interpreting the obtained data, and completing the manuscripts. The co-authors, Dr. Karem Azmy and Dr. Brian Kendall, provided research guidance and helped to review and edit the manuscripts.

Chapter 2 is a reformatted version of a paper published in the journal Chemical Geology (https://doi.org/10.1016/j.chemgeo.2022.120882). The co-authors, Dr. Karem Azmy and Dr. Brian Kendall, provided research supervision and assisted with the review and editing of the manuscript. This study was presented by Jie Li at the Geological Association of Canada Newfoundland and Labrador Section (GAC-NL) Annual Technical Meeting in St. John's in April 2023.

Chapter 3 is a reformatted version of a paper published in the journal Chemical Geology (https://doi.org/10.1016/j.chemgeo.2023.121891). Dr. Karem Azmy reviewed and edited the manuscript and assisted in shaping the research ideas. In addition, this work was presented by Jie Li at the GAC-MAC Joint Annual Meeting in Sudbury in May 2023.

Chapter 4 is a reformatted version of a paper published in the journal Marine and Petroleum Geology (https://doi.org/10.1016/j.marpetgeo.2023.106408). Dr. Karem Azmy supervised this research and helped to review and edit the manuscript. This study was presented by Jie Li at the Geological Association of Canada Newfoundland and Labrador Section (GAC-NL) Annual Technical Meeting in St. John’s in April 2023.

Acknowledgments

Firstly, I would like to express my sincere gratitude to my supervisor Dr. Karem Azmy for his invaluable guidance and support throughout my PhD study. Also, I am truly grateful to Memorial University of Newfoundland for providing me with the opportunity to pursue my research in Canada.

Secondly, the guidance and constructive suggestions from Dr. Brian Kendall, Dr. Nicole Bingham-Koslowski, Dr. Peir Pufahl, and Dr. Elliott Burden have been invaluable, and I am sincerely thankful for their support. I also want to express my sincere gratitude to my thesis examiners, Dr. Linda Kah, Dr. Achim Herrmann, and Dr. Geoffrey Gilleaudeau, for their insightful ideas and invaluable insights. Special thanks are extended to Dr. David Lowe and Mr. Dylan Goudie for their assistance with the petrographic and SEM analyses, as well as to Dr. Gwyneth W. Gordon, Dr. Jennifer Houghton, and Dr. Thibauld Conte for their invaluable support with the Mo-, U-, pyrite S-isotope, and I/Ca analyses.

Thirdly, I would like to acknowledge the financial support provided by MITACS, the Petroleum Exploration Enhancement program, the Canada Research Chair program, and the NSERC Discovery Grant program. Their funding has played a crucial role in enabling the successful execution of my research.

Last but not least, I am deeply thankful to my parents, Shanyou Li and Jumei Jiao, my sister Fang Li, and my cousin Yijun Jiao for their constant encouragement during my PhD journey. Their support and sacrifices have been invaluable in my pursuit of knowledge and personal growth.

Table of Contents

List of Tables

List of Figures

List of Appendices

Preamble

This thesis is written in a manuscript style, where the main body comprises three peer-reviewed journal papers (Chapters 2 to 4). Chapter 1 introduces the geological background, the early Paleozoic marine biodiversity and redox conditions, and objectives of this thesis. Chapter 5 summarizes conclusions reached in Chapters 2 to 4 and offers suggestions for future work.

Chapter 1

1. Introduction

1.1. Geological background

1.1.1. Lithostratigraphy and biostratigraphy

The Green Point Formation in western Newfoundland (Figure 1.1a), which has the Global Stratotype Section and Point (GSSP) for the base of the Ordovician system, is part of the Humber Arm Allochthon in the northeast Canadian Appalachians (James and Stevens, 1986; Waldron et al., 1998; Cooper et al., 2001). This formation accumulated at a slope toe area within the Taconic Seaway during the Cambrian-Ordovician transition and was later buried under low-energy carbonates of the St. George Group (James and Stevens, 1986; Knight et al., 2007, 2008; Lavoie et al., 2012; White and Waldron, 2022). The Taconic Seaway was likely a retroarc basin separating the eastern Laurentian continental margin from a series of off-margin microcontinents (White and Waldron, 2022). The lithology of the Green Point Formation has been studied and discussed in detail by James and Stevens (1986). This formation consists of three conformable members: the basal Martin Point Member, the middle Broom Point Member, and the upper St. Pauls Member. These members are dominated by shale, siltstone, and ribbon to parted limestone[1], with minor conglomerate or breccia beds.

---

[1] Ribbon limestone refers to alternating limestone and argillaceous beds with similar thicknesses, while the limestone beds of parted limestones are several times thicker than the alternating argillaceous layers.

The basal Martin Point Member, a 100−150 m thick late Cambrian sequence, is dominated by green, gray, and black shale with minor thin conglomerate beds and a few layers of thin siltstone, fine-grained calcareous sandstone, and ribbon to parted limestone. The Broom Point Member, early Tremadocian age, is a ~80 m sequence of ribbon to parted lime mudstone with thin green, gray, black shale, and sporadic conglomerate beds. The upper St. Pauls Member, a 130 to 150m mid-late Early Ordovician sequence overlain by the Lower Head sandstone, consists primarily of red, green, and black shale with minor parted to ribbon limestone, conglomerate beds, and buff-weathering siliceous dolomite layers of variable thicknesses. The shale, siltstone, and ribbon/parted limestone are hemipelagites that were probably deposited by gravity flows and/or pelagic fallout (James and Stevens, 1986; Coniglio and James, 1990). The conglomerates were likely deposited as a result of margin collapses linked to subaerial erosions or large storm waves (James and Stevens, 1986).

The studied interval of the Green Point Formation spans the upper part of the Martin Point Member and the lower part of the Broom Point Member (Beds 17 to 27, Figure 1.1b). This interval has been mildly affected by thermal alternation as suggested by low conodont alteration indices (≤ 1.5, Cooper et al., 2001). Petrographic and geochemical evidence supports the good preservation of the near-micritic limestone (Azmy et al., 2014, 2015). In addition, a reasonable Re-Os age of 484 ± 16 Ma obtained from the shale points to insignificant influence from postdepositional diagenesis and weathering (Tripathy et al., 2014). Earlier studies revealed that

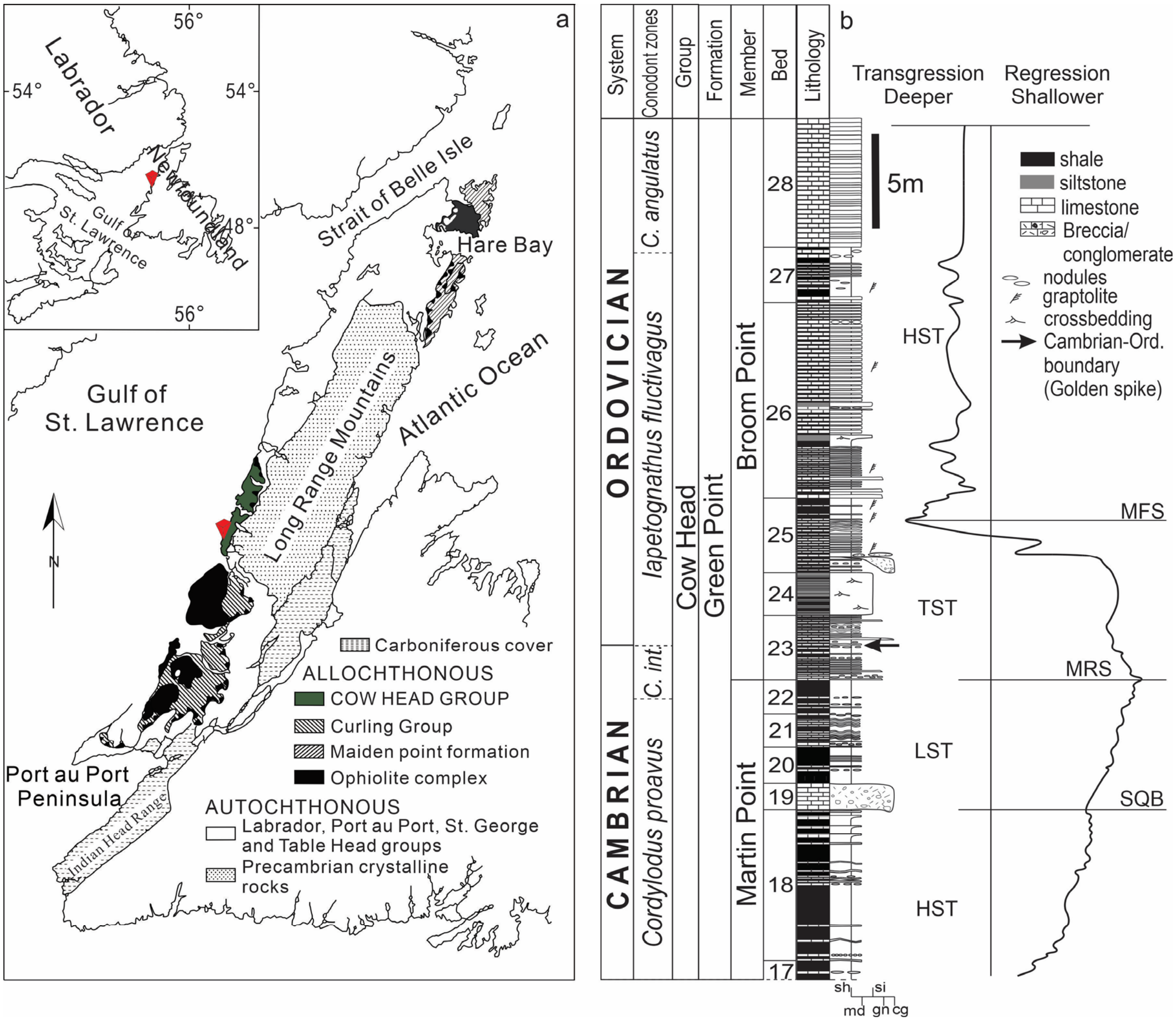

Figure 1.1: (a) Location (49° 40’ 51” N, 57° 57’ 36” W, marked by inverted pyramids) of the Cambrian-Ordovician GSSP boundary section at Green Point in western Newfoundland, Canada (following Cooper et al., 2001). (b) Stratigraphic framework of the investigated interval of the Green Point Formation showing bed numbers and the reconstructed sea-level variation across the boundary (modified from Azmy et al., 2015). Abbreviations: HST= high stand systems tract, LST = low stand systems tract, TST = transgressive systems tract, MRS = maximum regressive surface, MFS = maximum flooding surface, and SQB = sequence boundary.

this interval was deposited under oxygen-depleted but non-euxinic bottom conditions as indicated by the lack of fossils and bioturbations, relatively high carbonate Ce/Ce* values (~0.8 to 1.0), and depletions of shale Mo, U, and Re compared to Phanerozoic euxinic shale (James and Stevens, 1986; Azmy et al., 2014; Tripathy et al., 2014).

The conodont zone of this interval consists of, in ascending order, the *Cordylodus proavus* Zone, the *Cordylodus caboti* Zone, the *Cordylodus intermedius* Zone, the *Iapetognathus fluctivagus* Zone, and the *Cordylodus angulatus* Zone (Barnes, 1988; Cooper et al., 2001; Zhang and Barnes, 2004). The first appearance datum of the *Iapetognathus fluctivagus* Zone, the marker of the Cambrian–Ordovician boundary in the GSSP section at Green Point, was identified within Bed 23 at the bottom of the Broom Point Member (Cooper et al., 2001).

1.1.2. Tectonics

The Green Point Formation of the Cow Head Group in western Newfoundland was deposited along the eastern Laurentian margin developed by active rifting of the Rodinia during ~570 to 550 Ma (Cawood et al., 2001). The passive Laurentian margin began to transform into a convergent continental margin in the latest Cambrian due to Taconic Orogeny, which resulted in the transformation of the continental shelf to a foreland basin and the progressive destruction of the Taconic Seaway (Knight et al., 1991; Waldron et al., 1998; White and Waldron, 2022). This formation then experienced several episodes of uplift and subsidence and was deformed and transported westward to the present position attributed to the middle-late Ordovician Taconic, the Silurian Salinian, and the Early Devonian Acadian orogenic events (Jacobi, 1981; Knight et al., 1991; Waldron et al., 1998; van der Velden et al., 2004 and references therein).

1.2. The early Paleozoic marine biodiversity and redox conditions

During the early Paleozoic, the marine realm experienced remarkable radiations of organisms, prominently highlighted by two notable events, namely the Cambrian Explosion (CE) and the Great Ordovician Biodiversification Event (GOBE) (e.g., Harper et al., 2006; Payne and Finnegan, 2006; Schmitz et al., 2007; Alroy et al., 2008, 2010; Servais et al., 2008, 2010; Terfelt et al., 2014; Nowak et al., 2015; Algeo et al., 2016; Buatois et al., 2016; Stigall et al., 2019). The early-middle Cambrian (Terreneuvian–Epoch 2) witnessed a significant surge in marine diversity, commonly referred to as the CE, which was probably rooted in the late Ediacaran radiation (Zhu et al., 2017). Paleontological evidence shows that radiation of the early Cambrian marine life started in open shallow marine settings and then expanded to deeper marine environments (Mángano et al., 2014). After this rapid biodiversification, the marine biodiversity reached a plateau from the middle Cambrian (Epoch 3) to the earliest Ordovician (early Tremadocian) (e.g., Buatois et al., 2016; Stigall et al., 2019). The GOBE later took place during the mid-late Tremadocian to Katian, marking another phase of spectacular diversification of marine life at nearly all taxonomic levels and the development of more complex marine ecosystems than those of the Cambrian (Trotter et al., 2008; Servais et al., 2010; Kröger, 2017). Following the GOBE, the latest Ordovician witnessed dramatic mass extinctions that may have led to the loss of ~85% of marine species (Harper et al., 2014; Zou et al., 2018; Bond and Grasby, 2020).

The breakup of continents (Rasmussen et al., 2019) and increased interplay between faunas (Kröger and Landing, 2010; Fan et al., 2021) might have played roles in the CE and the GOBE. However, rises in oceanic and atmospheric oxygen levels have been widely accepted as the key triggers for rapid biodiversifications in the early Paleozoic (Trotter et al., 2008; Sperling et al., 2013; Marenco et al., 2016; Servais et al., 2016, 2019; Adiatma et al., 2019; Dahl et al., 2019; Kozik et al., 2019; Goldberg et al., 2021). Mass extinctions during this time period have been commonly attributed to expansions of ocean anoxia linked to enhanced primary productivities (Zhang et al., 2010; Dahl et al., 2014, 2019; Gerhardt and Gill, 2016; Marenco et al., 2016; D'Arcy et al., 2017; Li et al., 2017; Zou et al., 2018; Pruss et al., 2019; Wei et al., 2020; Young et al., 2020) or upwelling of deep anoxic waters onto shallow marine settings (Elrick et al., 2011; Pagès and Schmid, 2016; Li et al., 2019; LeRoy et al., 2021).

1.3. Motivation and objectives

The early Paleozoic witnessed two spectacular radiations of marine organisms, namely the CE and the GOBE, as mentioned above. However, the period between them was characterized by a marine biodiversity plateau, which has been attributed to recurrent biocrises linked to expanded marine anoxia and greenhouse climates (e.g., Saltzman et al., 2015; LeRoy et al., 2021). To substantiate this explanation, further studies on marine redox states during this time interval are necessary. Additionally, the lime mudstone of this interval exhibits a pronounced negative $\delta^{13}C_{carb}$ excursion of ~6.0‰ near the Є-O boundary likely linked to variations in primary productivity (Azmy et al., 2014, 2015). Nonetheless, the factors contributing to changes in primary productivity at the Є-O boundary and whether this prominent $\delta^{13}C_{carb}$ excursion was associated with oscillations of the marine carbon cycle have not been thoroughly understood. Furthermore, the depositional environments and the potential role of basin restriction effects during the deposition require further investigations. Geochemical proxies, including sedimentary pyrite $\delta^{34}S$ signals, U and Mo isotopic and elemental signatures of shale and carbonate, and carbonate I/Ca ratios, are essential tools for studying depositional environments and reconstructing paleo-oceanic redox conditions (e.g., Algeo et al., 2009; Lu et al., 2010, 2016; Gill et al., 2011; Kendall et al., 2011, 2013, 2015, 2020; Dahl et al., 2014, 2019; Hardisty et al., 2014, 2017; Song et al., 2014; Zhou et al., 2014, 2015; Gilleaudeau and Kah, 2015; Gerhardt and Gill, 2016; Edwards et al., 2018; Siedenberg et al., 2018; Lu et al., 2018; Luo et al., 2018; Wei et al., 2018, 2020, 2021; Gilleaudeau et al., 2019; Raven et al., 2019; Thomazo et al., 2019; Tostevin et al., 2019; Paiste et al., 2020; Goto et al., 2021). Therefore, various tools like the isotopic and elemental signals of Mo and U, I/Ca ratios, and pyrite textures and $\delta^{34}S$ signals in the shale/limestone from the Є-O boundary GSSP section at Green Point in western Newfoundland are employed to address the aforementioned questions.

1.4. Thesis outline

In Chapter 2, the isotopic and elemental data of Mo and U in shale and lime mudstone of the Green Point Formation were employed to understand the local depositional environments and coeval marine redox states. This chapter has been published as “Li, J., Azmy, K., Kendall, B., 2022. The Mo- and U-isotope signatures in alternating shale and carbonate beds of rhythmites: A comparison and implications for redox conditions across the Cambrian-Ordovician boundary. Chem. Geol. 602, p.120882”.

Chapter 3 investigates factors (e.g., positions of sedimentary pyrite formation and the basin restriction effect) influencing the bulk biological pyrite $\delta^{34}S$ variability as well as the depositional redox conditions. This chapter has been accepted by the journal Chemical Geology as “Li, J., Azmy, K., 2023. Variability of sedimentary pyrite $\delta^{34}S$ records: A case study of slope shale of the Green Point Formation in western Newfoundland, Canada”.

Chapter 4 explores the local continental margin seawater and global marine redox conditions using the lime mudstone I/Ca ratios and a three-sink U isotope mass balance model. This chapter is under review in the journal Marine and Petroleum Geology as “Li, J., Karem, A., 2023. Expanded marine anoxia at the Cambrian-Ordovician transition: Evidence from lime mudstone I/Ca and $\delta^{238}U$ signatures of the GSSP in western Newfoundland, Canada. Mar. Pet. Geol., JMPG-D-23-00344”.

Chapter 5 provides a summary of the key findings and general conclusions derived from this research. In addition, this chapter also provides suggestions for future work.

References

Adiatma, Y.D., Saltzman, M.R., Young, S.A., Griffith, E.M., Kozik, N.P., Edwards, C.T., Leslie, S.A., Bancroft, A.M., 2019. Did early land plants produce a stepwise change in atmospheric oxygen during the Late Ordovician (Sandbian ~458 Ma)? Palaeogeogr. Palaeoclimatol. Palaeoecol. 534.

Algeo, T.J., Marenco, P.J., Saltzman, M.R., 2016. Co-evolution of oceans, climate, and the biosphere during the 'Ordovician Revolution': A review. Palaeogeogr. Palaeoclimatol. Palaeoecol. 458, 1-11.

Algeo, T.J., Tribovillard, N., 2009. Environmental analysis of paleoceanographic systems based on molybdenum–uranium covariation. Chem. Geol. 268(3-4), 211-225.

Alroy, J., 2010. Geographical, environmental and intrinsic biotic controls on Phanerozoic marine diversification. Palaeontology 53(6), 1211-1235.

Alroy, J., al., e., 2008. Phanerozoic Trends in the Global Diversity of Marine Invertebrates. Science 321, 97-100.

Azmy, K., Kendall, B., Brand, U., Stouge, S., Gordon, G.W., 2015. Redox conditions across the Cambrian–Ordovician boundary: Elemental and isotopic signatures retained in the GSSP carbonates. Palaeogeogr. Palaeoclimatol. Palaeoecol. 440, 440-454.

Azmy, K., Stouge, S., Brand, U., Bagnoli, G., Ripperdan, R., 2014. High-resolution chemostratigraphy of the Cambrian–Ordovician GSSP: Enhanced global correlation tool. Palaeogeogr. Palaeoclimatol. Palaeoecol. 409, 135-144.

Barnes, C.R., 1988. The proposed Cambrian–Ordovician global Boundary stratotype and point (GSSP) in Western Newfoundland, Canada. Geol. Mag. 125(4), 381-414.

Bond, D.P.G., Grasby, S.E., 2020. Late Ordovician mass extinction caused by volcanism, warming, and anoxia, not cooling and glaciation. Geology 48(8), 777-781.

Buatois, L.A., Mangano, M.G., Olea, R.A., Wilson, M.A., 2016. Decoupled evolution of soft and hard substrate communities during the Cambrian Explosion and Great Ordovician Biodiversification Event. Proc. Natl. Acad. Sci. U. S. A. 113(25), 6945-6948.

Cawood, P.A., McCausland, P.J.A., Dunning, G.R., 2001. Opening Iapetus; constraints from the Laurentian margin in Newfoundland. Geol. Soc. Am. Bull. 113, 443-453.

Coniglio, M., James, N.P., 1990. Origin of fine-grained carbonate and siliciclastic sediments in an Early Palaeozoic slope sequence, Cow Head Group, western Newfoundland. Sedimentology 37, 215-230.

Cooper, R.A., Nowlan, G.S., Williams, S.H., 2001. Global Stratotype Section and Point for base of the Ordovician System. Episodes 24, 19-28.

Dahl, T.W., Boyle, R.A., Canfield, D.E., Connelly, J.N., Gill, B.C., Lenton, T.M., Bizzarro, M., 2014. Uranium isotopes distinguish two geochemically distinct stages during the later Cambrian SPICE event. Earth Planet. Sci. Lett. 401, 313-326.

Dahl, T.W., Connelly, J.N., Li, D., Kouchinsky, A., Gill, B.C., Porter, S., Maloof, A.C., Bizzarro, M., 2019. Atmosphere-ocean oxygen and productivity dynamics during early animal radiations. Proc. Natl. Acad. Sci. U. S. A. 116(39), 19352-19361.

D'Arcy, J., Gilleaudeau, G.J., Peralta, S., Gaucher, C., Frei, R., 2017. Redox fluctuations in the Early Ordovician oceans: An insight from chromium stable isotopes. Chem. Geol. 448, 1-12.

Edwards, C.T., Fike, D.A., Saltzman, M.R., Lu, W., Lu, Z., 2018. Evidence for local and global redox conditions at an Early Ordovician (Tremadocian) mass extinction. Earth Planet. Sci. Lett. 481, 125-135.

Elrick, M., Rieboldt, S., Saltzman, M., McKay, R.M., 2011. Oxygen-isotope trends and seawater temperature changes across the Late Cambrian Steptoean positive carbon-isotope excursion (SPICE event). Geology 39(10), 987-990.

Fan, R.-y., Zong, R.-w., Gong, Y.-m., 2021. Behavioural imprint of the Ordovician Radiation: Evidence from Middle–Upper Ordovician deep-sea trace fossils in western Inner Mongolia, North China. Palaeogeogr. Palaeoclimatol. Palaeoecol. 563.

Gerhardt, A.M., Gill, B.C., 2016. Elucidating the relationship between the later Cambrian end-Marjuman extinctions and SPICE Event. Palaeogeogr. Palaeoclimatol. Palaeoecol. 461, 362-373.

Gill, B.C., Lyons, T.W., Young, S.A., Kump, L.R., Knoll, A.H., Saltzman, M.R., 2011. Geochemical evidence for widespread euxinia in the later Cambrian ocean. Nature 469(7328), 80-83.

Gilleaudeau, G.J., Kah, L.C., 2015. Heterogeneous redox conditions and a shallow chemocline in the Mesoproterozoic ocean: Evidence from carbon–sulfur–iron relationships. Precambrian Res. 257, 94-108.

Gilleaudeau, G.J., Romaniello, S.J., Luo, G., Kaufman, A.J., Zhang, F., Klaebe, R.M., Kah, L.C., Azmy, K., Bartley, J.K., Zheng, W., Knoll, A.H., Anbar, A.D., 2019. Uranium isotope evidence for limited euxinia in mid-Proterozoic oceans. Earth Planet. Sci. Lett. 521, 150-157.

Goldberg, S.L., Present, T.M., Finnegan, S., Bergmann, K.D., 2021. A high-resolution record of early Paleozoic climate. Proc. Natl. Acad. Sci. U. S. A. 118(6).

Goto, K.T., Sekine, Y., Ito, T., Suzuki, K., Anbar, A.D., Gordon, G.W., Harigane, Y., Maruoka, T., Shimoda, G., Kashiwabara, T., Takaya, Y., Nozaki, T., Hein, J.R., Tetteh, G.M., Nyame, F.K., Kiyokawa, S., 2021. Progressive ocean oxygenation at ~ 2.2 Ga inferred from geochemistry and molybdenum isotopes of the Nsuta Mn deposit, Ghana. Chem. Geol.

Hardisty, D.S., Lu, Z., Bekker, A., Diamond, C.W., Gill, B.C., Jiang, G., Kah, L.C., Knoll, A.H., Loyd, S.J., Osburn, M.R., Planavsky, N.J., Wang, C., Zhou, X., Lyons, T.W., 2017.

Perspectives on Proterozoic surface ocean redox from iodine contents in ancient and recent carbonate. Earth Planet. Sci. Lett. 463, 159-170.

Hardisty, D.S., Lu, Z., Planavsky, N.J., Bekker, A., Philippot, P., Zhou, X., Lyons, T.W., 2014. An iodine record of Paleoproterozoic surface ocean oxygenation. Geology 42(7), 619-622.

Harper, D.A.T., 2006. The Ordovician biodiversification: Setting an agenda for marine life. Palaeogeogr. Palaeoclimatol. Palaeoecol. 232(2-4), 148-166.

Harper, D.A.T., Hammarlund, E.U., Rasmussen, C.M.Ø., 2014. End Ordovician extinctions: A coincidence of causes. Gondwana Res. 25(4), 1294-1307.

Jacobi, R.D., 1981. Peripheral bulge—a causal mechanism for the Lower/Middle Ordovician unconformity along the western margin of the Northern Appalachians. Earth Planet. Sci. Lett. 56, 245-251.

James, N.P., Stevens, R.K., 1986. Stratigraphy and correlation of the Cambro-Ordovician Cow Head group, western Newfoundland. Geological Survey of Canada, pp. 1, 26-49, 81-93.

Kendall, B., Brennecka, G.A., Weyer, S., Anbar, A.D., 2013. Uranium isotope fractionation suggests oxidative uranium mobilization at 2.50Ga. Chem. Geol. 362, 105-114.

Kendall, B., Gordon, G.W., Poulton, S.W., Anbar, A.D., 2011. Molybdenum isotope constraints on the extent of late Paleoproterozoic ocean euxinia. Earth Planet. Sci. Lett. 307(3-4), 450-460.

Kendall, B., Komiya, T., Lyons, T.W., Bates, S.M., Gordon, G.W., Romaniello, S.J., Jiang, G., Creaser, R.A., Xiao, S., McFadden, K., Sawaki, Y., Tahata, M., Shu, D., Han, J., Li, Y., Chu, X., Anbar, A.D., 2015. Uranium and molybdenum isotope evidence for an episode of widespread ocean oxygenation during the late Ediacaran Period. Geochim. Cosmochim. Acta 156, 173-193.

Kendall, B., Wang, J., Zheng, W., Romaniello, S.J., Over, D.J., Bennett, Y., Xing, L., Kunert, A., Boyes, C., Liu, J., 2020. Inverse correlation between the molybdenum and uranium isotope compositions of Upper Devonian black shales caused by changes in local depositional conditions rather than global ocean redox variations. Geochim. Cosmochim. Acta 287, 141-164.

Knight, I., Azmy, K., Boyce, W.D., Lavoie, D., 2008. Tremadocian carbonate rocks of the lower St. George group, Port au Port. Current Research (2008) Newfoundland and Labrador Department of Natural Resources Geological Survey Report 08-1, 115-149.

Knight, I., Azmy, K., Greene, M.G., Lavoie, D., 2007. Lithostratigraphic setting of diagenetic, isotopic, and geochemistry studies of Ibexian and Whiterockian carbonate rocks of the St. George and table head groups, Western Newfoundland. Current Research (2007) Newfoundland and Labrador Department of Natural Resources Geological Survey, Report 07-1, 55-84.

Knight, I., James, N.P., Lane, T.E., 1991. The Ordovician St. George unconformity, Northern Appalachians; the relationship of plate convergence at the St. Lawrence Promontory to the Sauk/Tippecanoe Sequence boundary. Geol. Soc. Am. Bull. 103, 1200-1225.

Kozik, N.P., Young, S.A., Bowman, C.N., Saltzman, M.R., Them, T.R., 2019. Middle–Upper Ordovician (Darriwilian–Sandbian) paired carbon and sulfur isotope stratigraphy from the Appalachian Basin, USA: Implications for dynamic redox conditions spanning the peak of the Great Ordovician Biodiversification Event. Palaeogeogr. Palaeoclimatol. Palaeoecol. 520, 188-202.

Kröger, B., 2017. Changes in the latitudinal diversity gradient during the Great Ordovician Biodiversification Event. Geology 46(2), 127-130.

Kröger, B., Landing, E., 2010. Early Ordovician community evolution with eustatic change through the middle Beekmantown Group, northeast Laurentia. Palaeogeogr. Palaeoclimatol. Palaeoecol. 294(3-4), 174-188.

Lavoie, D., Desrochers, A., Dix, G., Knight, I., Hersi, O.S., 2012. The Great American Carbonate Bank in eastern Canada: an overview. in J. R. Derby, R. D. Fritz, S. A. Longacre, W. A. Morgan, and C. A. Sternbach, eds., The great American carbonate bank: The geology and economic resources of the Cambrian – Ordovician Sauk megasequence of Laurentia: AAPG Mem. 98, 499-523.

LeRoy, M.A., Gill, B.C., Sperling, E.A., McKenzie, N.R., Park, T.-Y.S., 2021. Variable redox conditions as an evolutionary driver? A multi-basin comparison of redox in the middle and later Cambrian oceans (Drumian-Paibian). Palaeogeogr. Palaeoclimatol. Palaeoecol. 566.

Li, C., Jin, C., Planavsky, N.J., Algeo, T.J., Cheng, M., Yang, X., Zhao, Y., Xie, S., 2017. Coupled oceanic oxygenation and metazoan diversification during the early–middle Cambrian? Geology.

Li, D., Zhang, X., Zhang, X., Zhu, H., Peng, S., Sun, L., Shen, Y., 2019. A paired carbonate–organic δ13C approach to understanding the Cambrian Drumian carbon isotope excursion (DICE). Precambrian Res. 349.

Lu, W., al., e., 2018. Late inception of a resiliently oxygenated upper ocean. Science 361, 174-177.

Lu, Z., Hoogakker, B.A.A., Hillenbrand, C.-D., Zhou, X., Thomas, E., Gutchess, K.M., Lu, W., Jones, L., Rickaby, R.E.M., 2016. Oxygen depletion recorded in upper waters of the glacial Southern Ocean. Nature communications 7, 1-8.

Lu, Z., Jenkyns, H.C., Rickaby, R.E.M., 2010. Iodine to calcium ratios in marine carbonate as a paleo-redox proxy during oceanic anoxic events. Geology 38(12), 1107-1110.

Luo, G., Richoz, S., van de Schootbrugge, B., Algeo, T.J., Xie, S., Ono, S., Summons, R.E., 2018. Multiple sulfur-isotopic evidence for a shallowly stratified ocean following the Triassic-Jurassic boundary mass extinction. Geochim. Cosmochim. Acta 231, 73-87.

Mángano, M.G., Buatois, L.A., Astini, R., Rindsberg, A.K., 2014. Trilobites in early Cambrian tidal flats and the landward expansion of the Cambrian explosion. Geology 42(2), 143-146.

Marenco, P.J., Martin, K.R., Marenco, K.N., Barber, D.C., 2016. Increasing global ocean oxygenation and the Ordovician Radiation: Insights from Th/U of carbonates from the Ordovician of western Utah. Palaeogeogr. Palaeoclimatol. Palaeoecol. 458, 77-84.

Nowak, H., Servais, T., Monnet, C., Molyneux, S.G., Vandenbroucke, T.R.A., 2015. Phytoplankton dynamics from the Cambrian Explosion to the onset of the Great Ordovician Biodiversification Event: A review of Cambrian acritarch diversity. Earth-Science Reviews 151, 117-131.

Pagès, A., Schmid, S., 2016. Euxinia linked to the Cambrian Drumian carbon isotope excursion (DICE) in Australia: Geochemical and chemostratigraphic evidence. Palaeogeogr. Palaeoclimatol. Palaeoecol. 461, 65-76.

Paiste, K., Pellerin, A., Zerkle, A.L., Kirsimäe, K., Prave, A.R., Romashkin, A.E., Lepland, A., 2020. The pyrite multiple sulfur isotope record of the 1.98 Ga Zaonega Formation: Evidence for biogeochemical sulfur cycling in a semi-restricted basin. Earth Planet. Sci. Lett. 534.

Payne, J.L., Finnegan, S., 2006. Controls on marine animal biomass through geological time. Geobiology 4, 1-10.

Pruss, S.B., Jones, D.S., Fike, D.A., Tosca, N.J., Wignall, P.B., 2019. Marine anoxia and sedimentary mercury enrichments during the Late Cambrian SPICE event in northern Scotland. Geology 47(5), 475-478.

Rasmussen, C.M.O., Kroger, B., Nielsen, M.L., Colmenar, J., 2019. Cascading trend of Early Paleozoic marine radiations paused by Late Ordovician extinctions. Proc. Natl. Acad. Sci. U. S. A. 116(15), 7207-7213.

Raven, M.R., Fike, D.A., Bradley, A.S., Gomes, M.L., Owens, J.D., Webb, S.A., 2019. Paired organic matter and pyrite δ34S records reveal mechanisms of carbon, sulfur, and iron cycle disruption during Ocean Anoxic Event 2. Earth Planet. Sci. Lett. 512, 27-38.

Saltzman, M.R., Edwards, C.T., Adrain, J.M., Westrop, S.R., 2015. Persistent oceanic anoxia and elevated extinction rates separate the Cambrian and Ordovician radiations. Geology 43(9), 807-810.

Schmitz, B., Harper, D.A.T., Peucker-Ehrenbrink, B., Stouge, S., Alwmark, C., Cronholm, A., Bergström, S.M., Tassinari, M., Xiaofeng, W., 2007. Asteroid breakup linked to the Great Ordovician Biodiversification Event. Nat. Geosci. 1(1), 49-53.

Servais, T., Cascales-Miñana, B., Cleal, C.J., Gerrienne, P., Harper, D.A.T., Neumann, M., 2019. Revisiting the Great Ordovician Diversification of land plants: Recent data and perspectives. Palaeogeogr. Palaeoclimatol. Palaeoecol. 534.

Servais, T., Lehnert, O., Li, J.U.N., Mullins, G.L., Munnecke, A., NÜTzel, A., Vecoli, M., 2008. The Ordovician Biodiversification: revolution in the oceanic trophic chain. Lethaia 41(2), 99-109.

Servais, T., Owen, A.W., Harper, D.A.T., Kröger, B., Munnecke, A., 2010. The Great Ordovician Biodiversification Event (GOBE): The palaeoecological dimension. Palaeogeogr. Palaeoclimatol. Palaeoecol. 294(3-4), 99-119.

Servais, T., Perrier, V., Danelian, T., Klug, C., Martin, R., Munnecke, A., Nowak, H., Nützel, A., Vandenbroucke, T.R.A., Williams, M., Rasmussen, C.M.Ø., 2016. The onset of the 'Ordovician Plankton Revolution' in the late Cambrian. Palaeogeogr. Palaeoclimatol. Palaeoecol. 458, 12-28.

Siedenberg, K., Strauss, H., Podlaha, O., van den Boorn, S., 2018. Multiple sulfur isotopes (δ34S, Δ33S) of organic sulfur and pyrite from Late Cretaceous to Early Eocene oil shales in Jordan. Org. Geochem. 125, 29-40.

Song, H., Tong, J., Algeo, T.J., Song, H., Qiu, H., Zhu, Y., Tian, L., Bates, S., Lyons, T.W., Luo, G., Kump, L.R., 2014. Early Triassic seawater sulfate drawdown. Geochim. Cosmochim. Acta 128, 95-113.

Sperling, E.A., Frieder, C.A., Raman, A.V., Girguis, P.R., Levin, L.A., Knoll, A.H., 2013. Oxygen, ecology, and the Cambrian radiation of animals. Proc. Natl. Acad. Sci. U. S. A. 110(33), 13446-13451.

Stigall, A.L., Edwards, C.T., Freeman, R.L., Rasmussen, C.M.Ø., 2019. Coordinated biotic and abiotic change during the Great Ordovician Biodiversification Event: Darriwilian assembly of early Paleozoic building blocks. Palaeogeogr. Palaeoclimatol. Palaeoecol. 530, 249-270.

Terfelt, F., Eriksson, M.E., Schmitz, B., 2014. The Cambrian–Ordovician transition in dysoxic facies in Baltica — diverse faunas and carbon isotope anomalies. Palaeogeogr. Palaeoclimatol. Palaeoecol. 394, 59-73.

Thomazo, C., Brayard, A., Elmeknassi, S., Vennin, E., Olivier, N., Caravaca, G., Escarguel, G., Fara, E., Bylund, K.G., Jenks, J.F., Stephen, D.A., Killingsworth, B., Sansjofre, P., Cartigny, P., 2019. Multiple sulfur isotope signals associated with the late Smithian event and the Smithian/Spathian boundary. Earth-Science Reviews 195, 96-113.

Tostevin, R., Clarkson, M.O., Gangl, S., Shields, G.A., Wood, R.A., Bowyer, F., Penny, A.M., Stirling, C.H., 2019. Uranium isotope evidence for an expansion of anoxia in terminal Ediacaran oceans. Earth Planet. Sci. Lett. 506, 104-112.

Tripathy, G.R., Hannah, J.L., Stein, H.J., Yang, G., 2014. Re-Os age and depositional environment for black shales from the Cambrian-Ordovician boundary, Green Point, western Newfoundland. Geochem. Geophys. Geosyst. 15(4), 1021-1037.

Trotter, J.A., Williams, I.S., Barnes, C.R., Lécuyer, C., Nicoll, R.S., 2008. Did Cooling Oceans Trigger Ordovician Biodiversification? Evidence from Conodont Thermometry. Science 321, 550-554.

van der Velden, A.J., van Staal, C.R., Cook, F.A., 2004. Crustal structure, fossil subduction, and the tectonic evolution of the Newfoundland Appalachians: Evidence from a reprocessed seismic reflection survey. Geol. Soc. Am. Bull. 116(11-12), 1485-1498.

Waldron, J.W.F., Anderson, S.D., Cawood, P.A., Goodwin, L.B., Hall, J., Jamieson, R.A., Palmer, S.E., Stockmal, G.S., Williams, P.F., 1998. Evolution of the Appalachian Laurentian margin: Lithoprobe results in western Newfoundland. Can. J. Earth Sci. 35, 1271-1287.

Wei, G.-Y., Planavsky, N.J., He, T., Zhang, F., Stockey, R.G., Cole, D.B., Lin, Y.-B., Ling, H.-F., 2021. Global marine redox evolution from the late Neoproterozoic to the early Paleozoic constrained by the integration of Mo and U isotope records. Earth-Science Reviews 214.

Wei, G.-Y., Planavsky, N.J., Tarhan, L.G., Chen, X., Wei, W., Li, D., Ling, H.-F., 2018. Marine redox fluctuation as a potential trigger for the Cambrian explosion. Geology 46(7), 587-590.

Wei, G.-Y., Planavsky, N.J., Tarhan, L.G., He, T., Wang, D., Shields, G.A., Wei, W., Ling, H.-F., 2020. Highly dynamic marine redox state through the Cambrian explosion highlighted by authigenic δ238U records. Earth Planet. Sci. Lett. 544.

White, S.E., Waldron, J.W.F., 2022. Along-strike variations in the deformed Laurentian margin in the Northern Appalachians: Role of inherited margin geometry and colliding arcs. Earth-Science Reviews 226, 103931.

Young, S.A., Benayoun, E., Kozik, N.P., Hints, O., Martma, T., Bergström, S.M., Owens, J.D., 2020. Marine redox variability from Baltica during extinction events in the latest Ordovician–early Silurian. Palaeogeogr. Palaeoclimatol. Palaeoecol. 554.

Zhang, S., Barnes, C.R., 2004. Late Cambrian and Early Ordovician conodont communities from platform and slope facies, western Newfoundland: a statistical approach. Geological Society, London, Special Publications 230, 47-72.

Zhang, T., Shen, Y., Algeo, T.J., 2010. High-resolution carbon isotopic records from the Ordovician of South China: Links to climatic cooling and the Great Ordovician Biodiversification Event (GOBE). Palaeogeogr. Palaeoclimatol. Palaeoecol. 289(1-4), 102-112.

Zhou, X., Jenkyns, H.C., Owens, J.D., Junium, C.K., Zheng, X.-Y., Sageman, B.B., Hardisty, D.S., Lyons, T.W., Ridgwell, A., Lu, Z., 2015. Upper ocean oxygenation dynamics from I/Ca ratios during the Cenomanian-Turonian OAE 2. Paleoceanography 30(5), 510-526.

Zhou, X., Thomas, E., Rickaby, R.E.M., Winguth, A.M.E., Lu, Z., 2014. I/Ca evidence for upper ocean deoxygenation during the PETM. Paleoceanography 29(10), 964-975.

Zhu, M., Zhuravlev, A.Y., Wood, R.A., Zhao, F., Sukhov, S.S., 2017. A deep root for the Cambrian explosion: Implications of new bio- and chemostratigraphy from the Siberian Platform. Geology 45(5), 459-462.

Zou, C., Qiu, Z., Poulton, S.W., Dong, D., Wang, H., Chen, D., Lu, B., Shi, Z., Tao, H., 2018. Ocean euxinia and climate change "double whammy" drove the Late Ordovician mass extinction. Geology 46(6), 535-538.

Chapter 2

2. The Mo- and U-isotope signatures in alternating shales and carbonate beds of rhythmites: A comparison and implications for redox conditions across the Cambrian-Ordovician boundary

This chapter is a reformatted version of a paper published in the journal Chemical Geology in 2022. Dr. Karem Azmy provided research supervision, and Dr. Brain Kendall performed the analyses of Mo and U isotopic and elemental signals. Both of them helped to review and edit the manuscript.

Li, J., Azmy, K., Kendall, B., 2022. The Mo- and U-isotope signatures in alternating shales and carbonate beds of rhythmites: A comparison and implications for redox conditions across the Cambrian-Ordovician boundary. Chem. Geol. 602, 120882. https://doi.org/10.1016/j.chemgeo.2022.120882

Abstract

The Green Point Formation (GPF) of the Cow Head Group in western Newfoundland (Canada) includes the Global Boundary Stratotype Section and Point (GSSP) for the Cambrian-Ordovician (Є-O) boundary on Laurentia. This formation is composed primarily of thick, deep subtidal to slope deposits (rhythmites) of alternating lime mudstone and shale interbeds. Here, we employ isotopic and elemental data of Mo and U of the shale and carbonate to better understand their depositional environments and the open ocean redox conditions at the Є-O transition. The variability of $\delta^{98}Mo_{auth}$ (–0.40 to +3.16‰) indicates variable aqueous sulfide concentrations ($[H_2S]_{aq}$) in the bottom water or porewater during deposition of the shale. A significant positive correlation of shale $[Mo]_{auth}$ with $[U]_{auth}$, coupled with low Mo concentrations compared to Phanerozoic euxinic shales further, points to weakly reducing (~dysoxic/suboxic to anoxic) benthic conditions with H_2S_{aq} primarily confined to porewaters. For the lime mudstone, the $\delta^{98}Mo$ variability (–0.30 to +2.34‰) suggests variable $[H_2S]_{aq}$ in porewaters during early diagenesis. Low Mo concentrations ($[Mo]_{carb} = 0.25 \pm 0.80$ μg/g, 2σ) and a poor correlation of $[Mo]_{carb}$ with $\delta^{98}Mo_{carb}$ indicate weak sulfidic ($[H_2S]_{aq} < 11$ μM) porewater conditions and possibly dysoxic to suboxic bottom environments. Thus, the $\delta^{98}Mo_{carb}$ may not track the $\delta^{98}Mo$ of basin water because of low $[H_2S]_{aq}$ in porewaters and insignificant accumulation of authigenic Mo during early diagenesis. This explanation is consistent with a poor correlation between $\delta^{98}Mo_{carb}$ and the $\delta^{238}U$ of basin water (estimated from $\delta^{238}U_{carb}$). A cautious examination of

Mo_{EF}/U_{EF}, $\delta^{98}Mo_{auth}$, and $\delta^{238}U_{auth}$ of the shale suggests that the GPF was likely deposited in a basin with topographic barriers. During deposition of the lower and middle part of the studied interval, the barriers in combination with sea-level fluctuations may have caused partial isolation of the local basin from the open ocean.[2] Rapid sea-level rises in the earliest Ordovician greatly increased the connectivity between the basin and the open ocean, resulting in remarkable increases in Mo_{EF}/U_{EF}, $[Mo]_{auth}$, and $[U]_{auth}$ of the shale. The $\delta^{238}U$ of the earliest Ordovician open oceans, inferred from $\delta^{238}U_{carb}$, exhibited perturbations and an average value of –0.78 ± 0.33‰ (2σ), reflecting oceanic redox oscillations and expanded ocean euxinia compared to the modern oceans.

2.1. Introduction

The early Paleozoic was characterized by spectacular radiations of marine organisms (Harper et al., 2006; Servais et al., 2008, 2010; Van Roy et al., 2010, 2015; Terfelt et al., 2014; Candela, 2015; Nowak et al., 2015), whereas the late Cambrian and the Early Ordovician only witnessed a moderate increase in marine biodiversity (Buatois et al., 2016; Servais et al., 2016; Rasmussen et al., 2019; Stigall et al., 2019). This rate change could be attributed to greenhouse climates (Trotter et al., 2008; Goldberg et al., 2021) and repetitive ocean anoxic events (Saltzman et al., 2015; D'Arcy et al., 2017; Edwards et al., 2018; Pruss et al., 2019). Nonetheless, Saltzman

---

[2] New evidence suggests that the whole studied interval was likely deposited in a partially isolated basin. Please check Section 3.5.2.2.

et al. (2011) proposed a dramatic increase in atmospheric pO_2 to 28% in the earliest Ordovician compared to 21% today, favoring the expansion of ocean oxygenation. Thus, the Cambrian-Ordovician transition was likely a time of significant oscillations in oceanic redox conditions (e.g., Saltzman et al., 2015). This proposition, however, has not been well constrained by redox-sensitive elements and their isotopes (e.g., Mo and U).

2.1.1. Mo and U in non-carbonate sediments

Isotope compositions and concentrations of Mo and U in sediments have been widely applied to study local depositional environments and reconstruct paleo-ocean redox conditions due to their redox sensitive natures (e.g., Wille et al., 2007; Dahl et al., 2010b, 2014; Scheiderich et al., 2010; Duan et al., 2010; Brennecka et al., 2011; Wen et al., 2011; Kendall et al., 2011, 2013, 2015, 2020; Zhou et al., 2012; Baldwin et al., 2013; Proemse et al., 2013; Herrmann et al., 2018; Zhang et al., 2020; Wei et al., 2021). In oxygenated ocean waters, Mo and U exist primarily as soluble molybdate (MoO_4^{2-}) and uranyl complexes (e.g., $UO_2(CO_3)_3^{4-}$, Djogić et al., 1986; Morford and Emerson, 1999). Dissolved Mo and U in the modern oceans have much longer residence times (~ 440 kyr and ~ 320–560 kyr, respectively, Dunk et al., 2002; Miller et al., 2011) compared with the ocean mixing time (~1kyr, Sarmiento and Gruber, 2006). This resulted in homogeneous δ^{98}Mo and δ^{238}U signatures of the modern seawater ($\delta^{98}Mo_{SW} = +2.34 \pm 0.10‰$ (2σ), $\delta^{238}U_{SW} = -0.39 \pm 0.01‰$ (2σ), Nägler et al., 2013; Tissot and Dauphas, 2015).

Under oxic conditions ($[O_2]_{aq} > \sim 60\text{-}90\ \mu M$), the ^{95}Mo isotope is preferentially adsorbed by Mn-Fe (oxyhydr)oxides, which are isotopically lower than seawater by ~3.0‰ (Barling et al., 2001; Siebert et al., 2003). Dissolved MoO_4^{2-} ions are reduced to particle-reactive thiomolybdates ($MoO_xS_{4-x}^{2-}$, where x = 0 to 3) in sulfidic porewaters or bottom waters, and the reduced Mo species can be removed into sediments by fixing into reactive polysulfides, iron or iron-sulfur phases, or organic matter (Helz et al., 1996; Erickson and Helz, 2000; Siebert et al., 2006; Nägler et al., 2011; Dahl et al., 2010a; Noordmann et al., 2015; Wagner et al., 2017; King et al., 2017; Helz and Vorlicek, 2019).

Sediments deposited under dysoxic/anoxic ($[O_2]_{aq}$ = 0 to ~ 60-90 μM) to weak sulfidic ($H_2S]_{aq}$ <11μM) bottom conditions are commonly lower than seawater in δ^{98}Mo by ~ 0.7 to 2.8‰, probably attributed to non-quantitative removal of aqueous Mo because of incomplete conversion of MoO_4^{2-} to MoS_4^{2-}. In contrast, under strong sulfidic ($[H_2S]_{aq} \geq 11$μM) benthic conditions, sediments usually exhibit seawater-like δ^{98}Mo signatures due to complete conversion of MoO_4^{2-} to tetrathiomolybdate (MoS_4^{2-}) and the subsequent quantitative removal of Mo from bottom waters (Erickson and Helz, 2000; Poulson et al., 2006; Dahl et al., 2010a; Nägler et al., 2011; Scott and Lyons, 2012; Noordmann et al., 2015; Goldberg et al., 2016; Wagner et al., 2017; Helz and Vorlicek, 2019). However, the δ^{98}Mo of reducing sediments could become lower than expected as the result of the operation of particulate Fe-Mn shuttle processes (e.g., Ostrander et al., 2019; Kendall et al., 2020).

The δ^{238}U of modern oxic marine sediments (e.g., Mn-Fe (oxyhydr)oxides) are commonly lower than that of the seawater by ~ 0.1 to 0.2‰, whereas reducing sediments are generally more enriched in the heavier U isotope attributed to incorporation of reduced U^{4+} phases (Weyer et al., 2008; Stirling et al., 2015; Tissot and Dauphas, 2015 and references therein). Dissolved U^{6+} can be reduced to U^{4+} by bacteria at the Fe^{2+}–Fe^{3+} redox boundary, which primarily occurs in sedimentary porewaters (Zheng et al., 2002a,b; Algeo and Tribovillard, 2009; Bura-Nakić et al., 2018). Theoretically, this process can cause large U isotope fractionations ($\Delta^{238}U_{U^{4+}-U^{6+}}$) of ~ +1.2‰ (Andersen et al., 2014). However, the observed $\Delta^{238}U_{U^{4+}-U^{6+}}$ in reducing sediments are generally lower than this value because of U diffusive-reactive processes in porewaters (Andersen et al., 2014; Lau et al., 2020). The product U^{4+} ions are then removed into sediments as organic matter-associated U species or uraninite precipitates (Weyer et al., 2008; Stirling et al., 2015; Stylo et al., 2015). The δ^{238}U of sediments formed under weakly oxygenated and anoxic/euxinic waters are usually heavier than that of seawater by ~ 0 to 0.2‰ and ~ 0.3 to 0.8‰, respectively (Weyer et al., 2008; Andersen et al., 2014; Rolison et al. 2017; Bura-Nakić et al., 2018; Brüske et al. 2020). The average U isotope fractionation associated with U pore-water diffusion and reduction under anoxic/euxinic benthic conditions is ~ +0.6‰ (Andersen et al., 2014; Tissot and Dauphas, 2015). In addition to redox conditions, the isotope fractionation between U^{6+} and U^{4+} can also be affected by organic matter burial rates, sedimentation rates, and basin reservoir effects (Andersen et al., 2014; Lau et al., 2020).

2.1.2. Mo and U in carbonates

Molybdenum exists in carbonates primarily as authigenic Mo phases formed during early diagenesis (e.g., Romaniello et al., 2016) and Mo accommodated on calcite surfaces (Midgley et al., 2020). Natural non-skeletal carbonates (e.g., ooid sands) and synthesized carbonates have been reported to exhibit negligible Mo isotope fractionations from ambient solutions (Voegelin et al., 2009; Chen et al., 2021). Seemingly, ancient limestone may have the potential to capture the δ^{98}Mo of coeval ocean waters (Voegelin et al., 2010). However, the δ^{98}Mo of bulk carbonates would be lower than that of seawater if they are formed within weak sulfidic porewaters (Romaniello et al., 2016) or mixed with Mo adsorbed onto Fe-Mn (oxyhydr)oxides and organic matter (King et al., 2017; Bura-Nakić et al., 2020; Chen et al., 2021). In fact, only carbonate sediments deposited within strong sulfidic porewaters and with significant enrichments of syndepositional authigenic Mo are likely to capture the δ^{98}Mo of seawater (Romaniello et al., 2016).

Uranium can be incorporated into calcite by substituting calcium with U^{6+} or U^{4+} (Sturchio et al., 1998; Reeder et al., 2000; Kelly et al., 2003, 2006). Both biogenic and abiogenic primary carbonates are found to capture seawater-like δ^{238}U (Romaniello et al., 2013; Stirling et al., 2015). Nonetheless, δ^{238}U of modern bulk carbonates are commonly heavier than that of seawater by ~ 0.25‰, which have been attributed to the addition of reduced U phases during early diagenesis (Romaniello et al., 2013; Chen et al., 2018; Tissot et al., 2018; Bura-Nakić et al., 2020). Consequently, this δ^{238}U offset needs to be corrected when using δ^{238}U of ancient bulk carbonates to constrain ancient seawater redox conditions (Chen et al., 2018; Tissot et al., 2018; Bura-Nakić et al., 2020).

2.1.3 [Mn] and Mn/Al of non-carbonate sediments

[Mn] and Mn/Al of non-carbonate sediments can be applied as independent local redox proxies (e.g., Scheiderich et al., 2010; Scott and Lyons, 2012; Bond et al., 2020). The insoluble oxidized $Mn^{3+/4+}$ can be transformed to soluble Mn^{2+} under suboxidized conditions, and thus the rise in [Mn] and Mn/Al of sediments may indicate increased redox potentials (Algeo and Li, 2020 and references therein). A [Mn] higher than 850 μg/g (the average crust) is usually used as an indication of oxidized conditions (Young et al., 2020 and references therein).

In this study, we present new Mo and U isotope data of the Green Point shale, together with geochemical data of the Green Point carbonate and shale previously reported by Azmy et al. (2014, 2015) and Bisnaire (2018), to 1) improve the understanding of the depositional conditions of the investigated interval and 2) provide an estimate of global redox conditions for the earliest Ordovician oceans.

2.2. Geological background

2.2.1. Geologic Settings

The Green Point Formation in western Newfoundland (Figure 2.1) is a part of the Humber Arm Allochthon in the northern Appalachian Orogen. It was deposited along the low latitude (~ 30˚S, Scotese, 2014) Laurentian margin during the late Cambrian to early Ordovician (James and Stevens, 1986; Waldron et al., 1998; Cooper et al., 2001). The Laurentian plate developed by active rifting of Rodinia around 570 to 550 Ma, which also resulted in the opening of the Iapetus

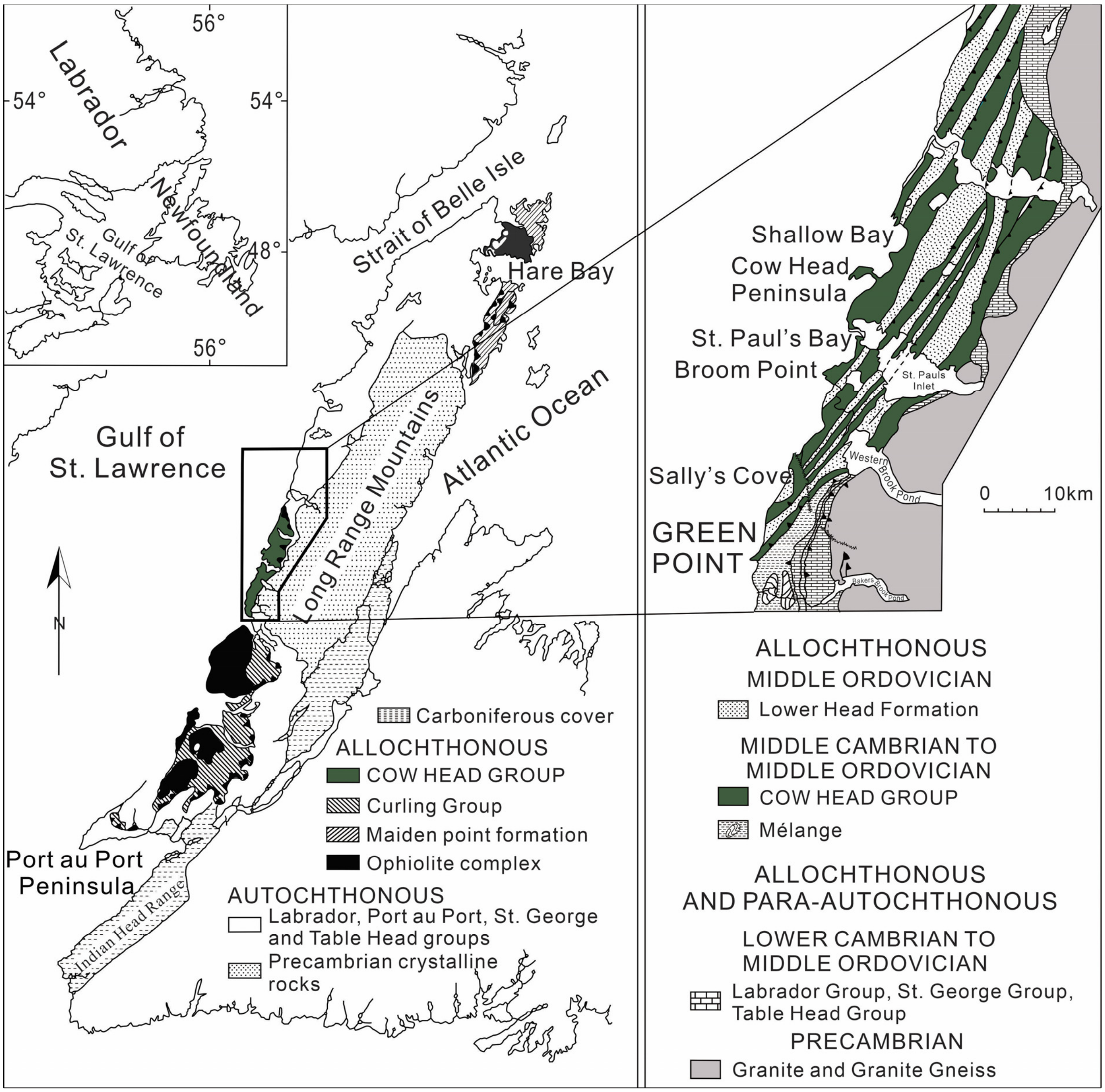

Figure 2.1: Location of the Cow Head Group and the Green Point Formation in western Newfoundland (modified from Cooper et al., 2001).

Ocean (Cawood et al., 2001). Then, a pre–platform shelf formed and was eventually covered by clastic sediments during the Neoproterozoic to early Cambrian (James et al., 1989). A major transgression flooded the Laurentian platform margin and resulted in the accumulation of thick carbonate deposits between the early Cambrian and early Ordovician (Wilson et al., 1992; Lavoie et al., 2013). The platform deposits, dominated by high-energy carbonates, were deposited during the middle to late Cambrian and similarly the coeval carbonate/shale slope deposits of the Cow Head Group. Those sediments were later buried under the low-energy carbonates of the St. George Group during the early to earliest middle Ordovician (cf. Knight et al., 2007, 2008; Lavoie et al., 2013). Then, they were deformed and transported westward by the mid-late Ordovician Taconic, the Silurian Salinian, and the Early Devonian Acadian orogenic events (Jacobi, 1981; Knight et al., 1991; Waldron et al., 1998; van der Velden et al., 2004 and references therein).

2.2.2. Lithostratigraphy

The lithostratigraphy of the Є-O boundary section, which is part of the Green Point Formation (GPF) of the Cow Head Group (Figure 2.2), has been studied and discussed in detail by James and Stevens (1986) and references therein. The GSSP boundary section spans the uppermost Cambrian Martin Point and lowermost Ordovician Broom Point members. The GPF comprises the fine-grained siliciclastic-carbonate hemipelagic slope deposits of the Cow Head Group, which are generally composed of dark gray to black fissile shale alternating with thin (~ 1cm-thick) interbeds of ribbon limestone rhythmites. Siltstone interbeds (up to 1 cm thick) may co-occur with shale, and the limestone interbeds vary from isolated and thin to up to 20 cm thick. Conglomerate beds may occur and contain debris of shallow-water carbonates and/or early lithified upper slope deposits that were transported into deep-water facies along the slope of the

Laurentian margin, possibly by turbidity currents (James and Stevens, 1986; Coniglio and James, 1990).

The current spike marking the Є-O boundary in the GSSP section at Green Point (Figure 2.2) is placed within Bed 23 (Cooper et al., 2001). A geochemical anomaly marked by a negative $\delta^{13}C_{carb}$ excursion (~6‰, Figure 2.3) has been documented starting at a stratigraphic level approximately in the middle of Bed 22 (Azmy et al., 2014, 2015).

2.3. Methodology

2.3.1. Samples and sample digestion

Shale samples were collected from the rhythmites of the Martin Point Member and Broom Point Member of the GPF (Figure 2.2, Table 2.1) at high resolution (sampling intervals as small as 10 cm) from the Є-O GSSP boundary section (49° 40′ 51″ N; 57° 57′ 36″ W) at Green Point, western Newfoundland (Figure 2.1). Around 9g of material from each sample was powdered using a mechanical mill. Powdered samples (75–100 mg each) were then ashed overnight at 550 ºC and dissolved completely by HF–HNO_3–HCl acid digestion.

2.3.2. Uranium Isotopes

Uranium isotope measurements for the carbonates were previously reported in Azmy et al. (2015). In this study, we report U isotope data for the shale following methods outlined in Weyer et al. (2008) and Kendall et al. (2013). Before ion-exchange chromatography, a portion of each sample solution was equilibrated with an appropriate amount of double spike solution

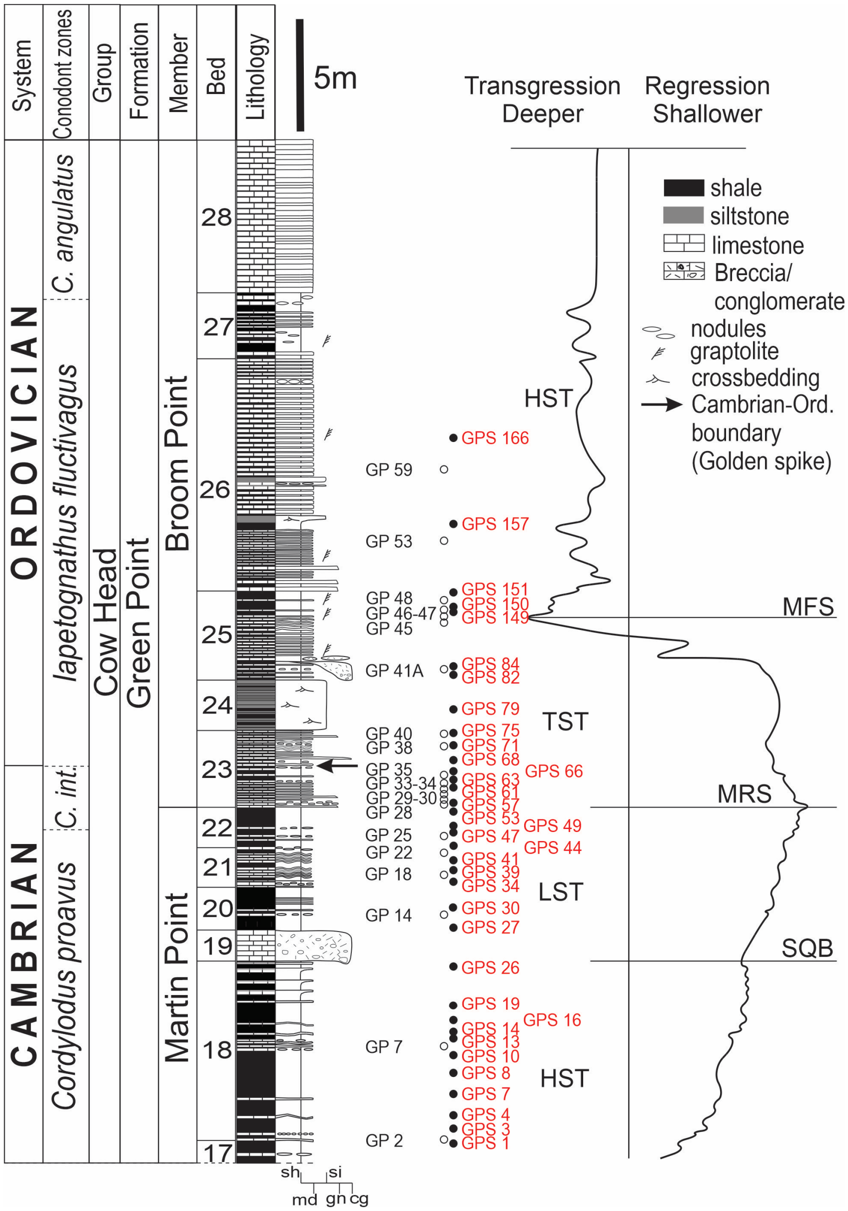

Figure 2.2: Stratigraphic framework of the Cambrian-Ordovician GSSP boundary section in western Newfoundland, Canada showing bed number and detailed measured section with the positions of investigated samples (GP and GPS refer to carbonate and shale samples, respectively) and the reconstructed sea-level variation across the boundary (modified from Azmy et al., 2015 and Bisnaire, 2018). Abbreviations as follows: HST- high stand systems tract, LST - low stand systems tract, TST - transgressive systems tract, MRS - maximum regressive surface, MFS - maximum flooding surface, and SQB - sequence boundary.

(^{233}U–^{236}U) to facilitate the correction for isotope fractionation during column chromatography and mass spectrometry. Uranium was isolated and purified from sample solutions using

Eichrom® UTEVA resin. The U isotope compositions of the samples were determined using a Thermo Scientific Neptune multiple collector (MC) ICP-MS instrument equipped with an ESI Apex desolvating inlet system at Arizona State University. Sample U isotope compositions ($\delta^{238}U$) were reported relative to the CRM145 standard as follows:

$$\delta^{238}U\ (‰) = ({}^{238/235}U_{\text{sample}} / {}^{238/235}U_{\text{CRM145}} - 1) \times 1000$$

Repeated measurements of the U isotope standards Ricca and CRM129a during the course of this study yielded average $\delta^{238}U$ values of –0.21 ± 0.06‰ (2σ; n = 12) and –1.69 ± 0.09‰ (2σ; n = 12), respectively. The values for Ricca and CRM129a agree well with those reported in previous studies (Yang et al., 2017; Zhang et al., 2018). During this study, the United States Geological Survey (USGS) standards SBC-1 and SGR-1b were processed and analyzed in an identical manner as samples and yielded average $\delta^{238}U$ values of –0.20 ± 0.05‰ (2σ, n = 2) and –0.22 ± 0.06‰ (2σ, n = 3), respectively. These values are statistically identical to those reported by Rolison et al. (2017) and Yang et al. (2017).

2.3.3. Molybdenum Isotopes

Molybdenum isotope measurements for the carbonates have been reported by Bisnaire (2018). The measurements for the molybdenum isotope compositions of the shale followed methods outlined in Duan et al. (2010) and Herrmann et al. (2012). After equilibration of a portion of the sample solution with an appropriate amount of double spike (${}^{97}Mo$–${}^{100}Mo$), Mo was isolated and purified using first anion exchange chromatography (isolates Mo + Fe) and then cation exchange chromatography (to separate Mo from Fe) (Barling et al., 2001; Arnold et al., 2004; Duan et al., 2010). The Mo isotope compositions of the samples were determined using the Neptune MC-ICP-MS at Arizona State University. Sample Mo isotope compositions (δ^{98}Mo) are calculated relative to in-house standard RochMo2 and then corrected to be reported relative to the NIST SRM 3134 standard by taking into consideration the measured isotopic composition of NIST SRM 3134 relative to RochMo2 during the course of the study. Following Nägler et al. (2013), the NIST SRM 3134 standard is set to 0.25‰. Sample Mo isotope data are thus reported as follows:

$$\delta^{98}\text{Mo (‰)} = 1000 \times [(^{98}\text{Mo}/^{95}\text{Mo})_{\text{sample}} / (^{98}\text{Mo}/^{95}\text{Mo})_{\text{NIST SRM 3134}}) - 1] + 0.25$$

The USGS standard SDO-1 was measured alongside samples and yielded an average δ^{98}Mo of 1.05 ± 0.04‰ (2σ, n=10), in agreement with previous studies (Kendall et al., 2015; Lu et al., 2017). We also report average δ^{98}Mo values of 0.66 ± 0.04‰ (2σ, n=4) and 0.63 ± 0.02‰ (2σ, n=3) for SBC-1 and SGR-1b, respectively, which are potential standards to replace the now-exhausted SDO-1 standard.

2.3.4. Calculation of authigenic δ^{238}U and δ^{98}Mo of the Green Point shale

Bulk sample δ^{98}Mo and δ^{238}U for shale with low Mo and U concentrations can be influenced significantly by the U- and Mo-bearing detrital minerals, which is particularly important for siliciclastic-dominated shale. In this study, we estimate the authigenic U and Mo isotope compositions for the shale using the following formulas:

$$c(M)_{\text{det}} = [c(M)/c(Al)]_{\text{local crust}} \times c(Al)_{\text{sam}}$$

$$c(M)_{\text{auth}} = c(M)_{\text{sam}} - c(M)_{\text{det}}$$

$$\delta^{238}U_{auth} = [\delta^{238}U_{sam} \times c(U)_{sam} - \delta^{238}U_{det} \times c(U)_{det}] / c(U)_{auth}$$

$$\delta^{98}Mo_{auth} = [\delta^{98}Mo_{sam} \times c(Mo)_{sam} - \delta^{98}Mo_{det} \times c(Mo)_{det}] / c(Mo)_{auth}$$

where c(M) refers to the concentration of Mo or U, auth = authigenic, sam = sample, and det = detrital (following Noordmann et al., 2015).

The average upper continental crust is often used to approximate the composition of detrital components (e.g., Bura-Nakić et al., 2018; Brüske et al., 2020). However, the detrital [Mo] and [U] in the Green Point Shale could be overestimated (indicated by numerous negative inferred $[Mo]_{auth}$ and $[U]_{auth}$ values, Supplementary data) if the detrital correction was based on the average upper crust ([Al] = 8.15 wt%, [Mo] = 1.1 µg/g, [U] = 2.7 µg/g, Rudnick and Gao, 2014). This scenario may be caused by the spatial heterogeneity in the composition of detrital material to marine basins (e.g., Cole et al., 2017).

Here, the average eastern Canadian Precambrian Shield (Northern Quebec) ([Al] = 9.05 wt%, [U] = 1.2 µg/g, Eade and Fahrig, 1973) is used to represent the detrital component. It is dominated by granitic rocks (Eade and Fahrig, 1971) and was the possible source of terrestrial materials to the investigated stratigraphic interval. However, the average [Mo] of the eastern Canadian Precambrian Shield has not been constrained, and thus it is represented by the average [Mo] of granitic rocks (~ 0.5µg/g, Hu and Gao, 2008; Greber et al., 2011; Neubert et al., 2011; Voegelin et al., 2012). The isotopic compositions of detrital Mo and U are assumed to be similar to average granitic rocks ($\delta^{98}Mo = +0.5‰$ and $\delta^{238}U = -0.3‰$, Greber et al., 2011; Neubert et al., 2011; Voegelin et al., 2012; Tissot and Dauphas, 2015).

Detrital Mo and U could be the primary components of the Mo and U budgets of shale if their bulk Mo and U EFs (enrichment factors, $X_{EF} = (X/Al)_{sample}/(X/Al)_{local\ detrital\ component}$, where X and Al denote concentrations of X and Al) are lower than 2 (e.g., Lu et al., 2020). Therefore, shale with bulk Mo and U EFs less than 2 are not used to calculate the abundances and isotope compositions of authigenic Mo and U in this study.

In addition to detrital Mo and U, the Green Point shale may also contain carbonate-associated Mo and U as they were deposited on a slope adjacent to a carbonate platform (James and Stevens, 1986). However, the carbonate-associated Mo and U of the shale may be negligible because of their low [Ca] (4.2 ± 5.7 wt%, 2σ, Table 2.1) and poor correlations of [Ca] with $[Mo]_{auth}$ and $[U]_{auth}$ ($R^2 = 0.003$ and 0.007, respectively, Figure 2.4a). Thus, the calculation results (Figure 2.3, Table 2.1) will be treated as the abundances and isotopic compositions of authigenic Mo and U phases of the shale.

2.3.5. Estimation of basin water $\delta^{238}U$ signatures

The $\delta^{238}U$ of ocean or basin waters can be estimated by carbonate $\delta^{238}U$ (e.g., Dahl et al., 2014, 2019; Wei et al., 2018, 2020; Tostevin et al., 2019; Zhang et al., 2020). A moderate positive correlation of $\delta^{238}U_{carb}$ with U/Ca ($R^2 = 0.51$, $p < 0.01$, Figure 2.4b, Table 2.2) implies that $\delta^{238}U$ of the primary carbonate precipitates were likely altered by ^{238}U-enriched syndepositional authigenic U (e.g., Romaniello et al., 2013). Therefore, $\delta^{238}U$ of the basin water ($\delta^{238}U_{BW}$) are estimated based on the finding that the addition of syndepositional authigenic U can increase the $\delta^{238}U$ of primary carbonates by ~ +0.25‰ ($\delta^{238}U_{BW} = \delta^{238}U_{carb} - 0.25‰$) (Chen et al., 2018; Tissot et al., 2018; Bura-Nakić et al., 2020). Noteworthily, the calculated $\delta^{238}U_{BW}$ (Figure 2.3, Table 2.2) should represent the surface basin water as the carbonates were primarily derived from the carbonate platform (James and Stevens, 1986).

2.4. Results

The TOC, [Al], [Ca], [Mn], $[Mo]_{bulk}$, and $[U]_{bulk}$ of the shale (Figure 2.3, Table 2.1) are collected from Bisnaire (2018). To investigate depositional redox conditions of the shale, only concentrations and isotope compositions of the authigenic Mo and U are considered in this study. The $[Mo]_{auth}$ and $[U]_{auth}$ of the shale vary between 0.16 and 24.30 µg/g (3.97 ± 10.26 µg/g, 2σ) and between 0.46 and 12.61 µg/g (2.94 ± 5.20 µg/g, 2σ), respectively. $\delta^{98}Mo_{auth}$ values exhibit a wide range from –0.40 to +3.16 ‰, and $\delta^{238}U_{auth}$ values span from –0.62 to +0.12 ‰ and are also highly variable. Poor correlations of [Mn] with $[Mo]_{auth}$ and $\delta^{98}Mo_{auth}$ values ($R^2 = 0.0004$ and 0.02, respectively, Figure 2.4c) and of $[Mo]_{auth}$ with $\delta^{98}Mo_{auth}$ values ($R^2 = 0.001$, Figure 2.4d). These observations suggest negligible influences of the operation of particulate Fe-Mn shuttle processes on the shale.

The $\delta^{13}C$, TOC, [Al], [Mn], [Mo], [U], $\delta^{98}Mo$, $\delta^{234}U$, and $\delta^{238}U$ of the Green Point carbonates (Figure 2.3, Table 2.2) have been reported by Azmy et al. (2014, 2015) and Bisnaire (2018). In this study, detrital corrections for Mo and U concentrations and isotopic compositions of carbonates are unnecessary as these samples are depleted in Al and were leached by weak acid to avoid dissolving detrital silicate materials (Azmy et al., 2015; Bisnaire, 2018). The [Mo] and

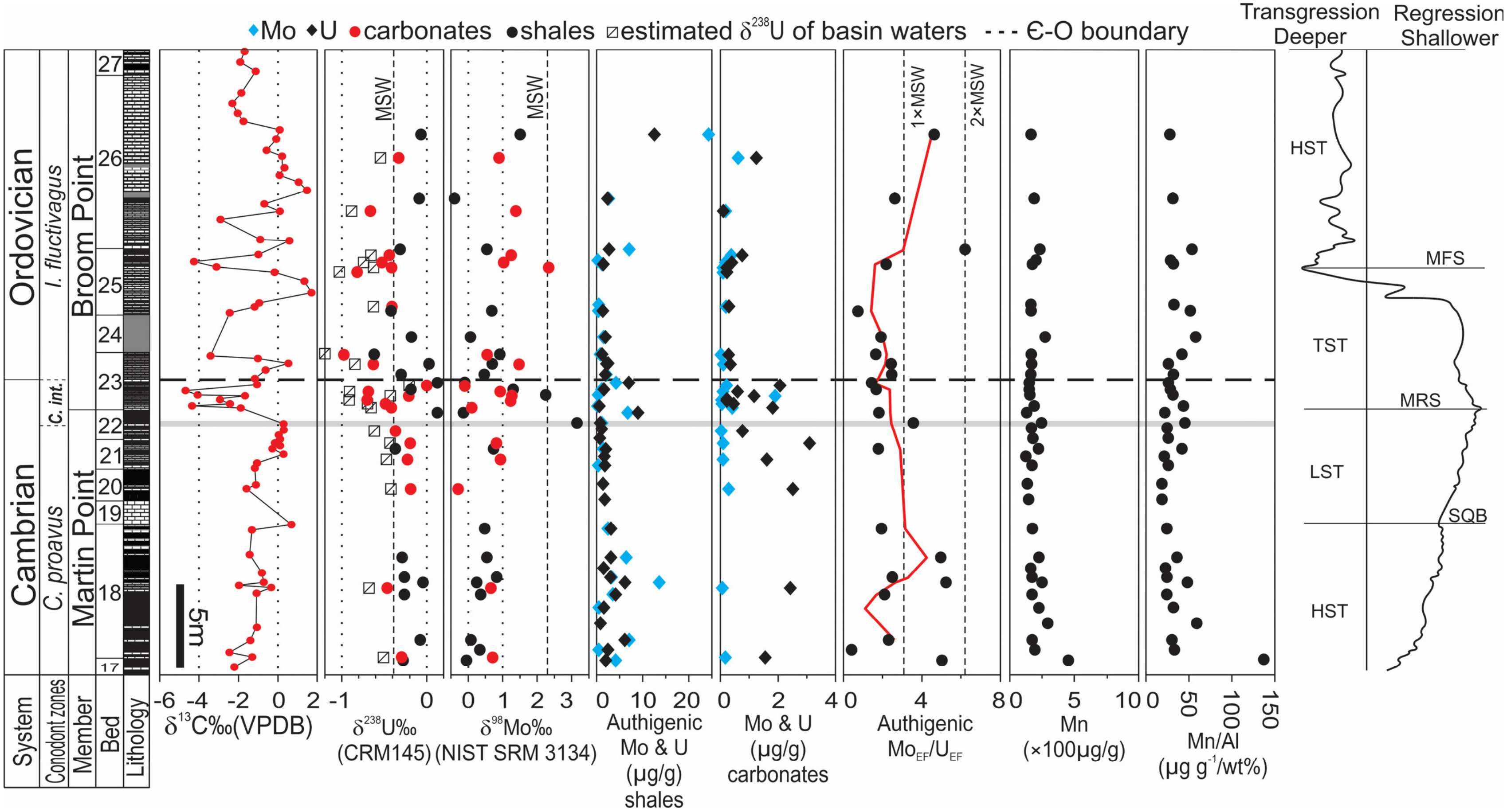

Figure 2.3: Stratigraphic and geochemical profiles across the Cambrian-Ordovician GSSP boundary in Green Point (western Newfoundland, Canada) (Modified from Cooper et al., 2001 and Azmy et al., 2014). The dashed horizontal black line marks the current level of the Cambrian-Ordovician biostratigraphic boundary (Cooper et al., 2001). The solid gray line refers to the level of the geochemical anomaly documented by Azmy et al. (2014, 2015). The modern seawater $\mathrm{Mo_{EF}/U_{EF}}$ value is calculated based on the concentrations of Mo and U in modern ocean waters (~10.05μg/g and ~3.238μg/g, respectively) reported by Sun et al. (2000) and Chen et al. (1986). MSW = modern seawater, the solid red line represents the three-point moving average of the $\mathrm{Mo/U_{EF}}$ values. This figure is a modified version of the original figure.

[U] of the carbonate interbeds range from 0.02 to 1.91 µg/g (0.25 ± 0.80 µg/g, 2σ) and 0.11 to 3.10 µg/g (1.06 ± 1.76 µg/g, 2σ), respectively. The $\delta^{98}Mo_{carb}$ values vary between –0.30 and +2.34 ‰, which are generally lower than that of modern seawater (~+2.34‰, Nägler et al., 2013) except for sample GP46 ($\delta^{98}Mo$ = +2.34‰). The $\delta^{238}U_{carb}$ and the estimated $\delta^{238}U_{BW}$ values span from –0.97 to 0 ‰ and from −1.22 to −0.25‰, respectively. Poor correlations of $[Mn]_{carb}$ with $[Mo]_{carb}$ and $\delta^{98}Mo_{carb}$ (R^2 = 0.04 and 0.002, respectively, Figure 2.5a) suggest that the $\delta^{98}Mo_{carb}$ variability was not caused by the operation of Mn-Fe (oxyhydr)oxide shuttle processes. Limited variation is observed in $\delta^{234}U$, with most samples falling within 15‰ of secular equilibrium.

2.5. Discussion

2.5.1. Evaluation of diagenetic influence

The evaluation of the diagenetic control on the geochemical signatures of the carbonates has been discussed in detail by Azmy et al. (2014, 2015) and will be summarized here. The petrographic examination indicated dominant fabric retentive lime mudstone (rhythmites of micritic to near-micritic grain size) with insignificant recrystallization and non- to dull-luminescence under cold cathodoluminoscope, thus supporting a high degree of petrographic preservation (Azmy et al., 2014). The geochemical preservation was supported by the insignificant correlations of the $\delta^{13}C_{org}$ with TOC wt. % (R^2 = 0.01) and the $\delta^{234}U$ with $\delta^{238}U$ (R^2 = 0.02) values and the limited deviation in $\delta^{234}U$ from secular equilibrium, thus suggesting the minimal modification of $\delta^{238}U$ signatures by recent fluid flow during the past ~2 Myr. Also, the insignificant correlations ($R^2 < 0.1$) between elements known to be sensitive to diagenesis and enriched in crustal clastic rocks, such as Sr, Al, and Ti with the [U], [Mo], $\delta^{238}U$, and $\delta^{98}Mo$ values argue for good preservation of depositional signatures and minimal overprint by silicate inclusions (Azmy et al., 2015; Bisnaire, 2018).

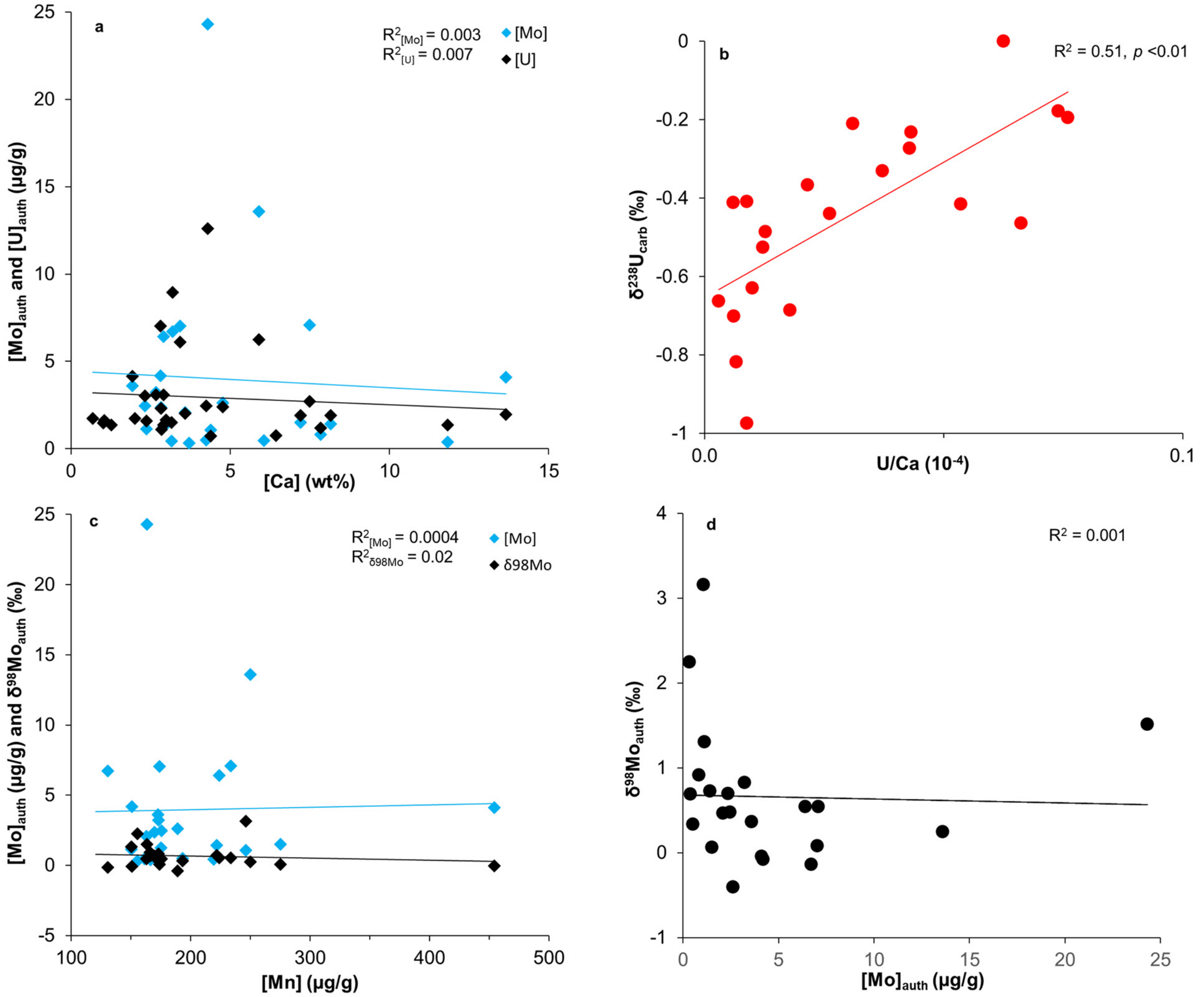

Figure 2.4: Crossplots of (a) [Mo]$_{auth}$ and [U]$_{auth}$ vs. [Ca], (b) $\delta^{238}U_{carb}$ vs. U/Ca, (c) [Mo]$_{auth}$ and $\delta^{98}Mo_{auth}$ vs. [Mn], (d) [Mo]$_{auth}$ vs. $\delta^{98}Mo_{auth}$. Poor correlations of [Ca] with [Mo]$_{auth}$ and [U]$_{auth}$ (R^2= 0.003 and 0.007, respectively) indicate minimal carbonate-associated Mo and U in the shale. A moderate correlation between $\delta^{238}U_{carb}$ and U/Ca ($R^2 = 0.51$, $p < 0.01$) implies that $\delta^{238}U$ of the primary carbonates were likely altered by ^{238}U-enriched syndepositional authigenic U. Negligible correlations of [Mn] with [Mo]$_{auth}$ and $\delta^{98}Mo_{auth}$ ($R^2 = 0.0004$ and 0.02, respectively) and of [Mo]$_{auth}$ with $\delta^{98}Mo_{auth}$ ($R^2 = 0.001$) imply insignificant influences of the operation of Mn-Fe (oxyhydr)oxide shuttle processes on the shale. The black, blue, and red solid lines are regression lines for data with corresponding colors. These figures are updated versions of the original figures.

The shale samples are free of obvious diagenetic features such as quartz/carbonate veins and secondary macroscopic pyrite nodules. Weathered materials with altered pyrite were avoided during field sampling. Significantly, a geologically reasonable Re-Os age of 484 ± 16 Ma has been obtained for the Green Point shale that supports insignificant postdepositional disturbance from both outcrop weathering and diagenesis (Tripathy et al., 2014). Although the relatively large uncertainty on the Re-Os age (3.3%) indicates some disturbances, the agreement between the Re-Os age and biostratigraphy suggests that mobilization of Re and/or Os was likely spatially limited. Diffusion between beds in the finely interbedded shale and carbonate could produce chemical variability only on a millimeter scale. Consequently, the petrographic and geochemical evidence of preservation of carbonate (more susceptible to diagenetic modification relative to shale) and similarly the alternating shale interbeds support a high degree of preservation of sediments in the investigated section.

2.5.2. Depositional redox conditions of the Green Point shale and carbonate

2.5.2.1. The Green Point shale

The $\delta^{98}Mo_{auth}$ of the shale shows a large range (–0.40 to +3.16‰) and stratigraphic variations. These observations can be explained by variable Mo isotope fractionations between authigenic Mo and basin water due to incomplete conversion of MoO_4^{2-} to MoS_4^{2-} under weak sulfidic $(H_2S]_{aq}$ <11μM) conditions (e.g., Poulson et al., 2006; Dahl et al., 2010a; Scott and Lyons, 2012; Wagner et al., 2017). A strong positive correlation of $[Mo]_{auth}$ with $[U]_{auth}$ ($R^2 = 0.73$, $p < 0.05$, Figure 2.5b) further indicates that Mo adsorption may take place along with U sequestration, with generally low Mo concentrations (compared to Phanerozoic euxinic shales, cf. Scheiderich et al., 2010; Proemse et al., 2013; Noordmann et al., 2015; Goldberg et al., 2016; Kendall et al., 2020) suggesting that dissolved sulfide was mainly confined to porewaters (e.g., Brüske et al., 2020). Therefore, the shale could be mainly deposited under variable and non-sulfidic (perhaps dysoxic/suboxic to anoxic) benthic redox conditions, consistent with the color variation (dominated by green, green-gray, and gray colors) exhibited by the shale (James and Stevens, 1986).

Table 2.1: Statistics of the geochemical results of the shale samples (data source: TOC, [Al], [Ca], [Mn], $[\text{Mo}]_{\text{bulk}}$, and $[\text{U}]_{\text{bulk}}$ from Bisnaire, 2018).

Sample ID	TOC[a] wt %	Al wt %	Ca wt %	Mn µg/g	Mo_{bulk} µg/g	Mo_{bulk} EF	U_{bulk} µg/g	U_{bulk} EF	Mo_{auth} µg/g	U_{auth} µg/g	Mo_{auth} EF	U_{auth} EF	$\text{Mo/U}_{\text{auth}}$[b] EF	$\delta^{98}\text{Mo}$[c] ‰	±2σ	*n*	$\delta^{238}\text{U}$[d] ‰	±2σ	*n*	$\delta^{98}\text{Mo}_{\text{auth}}$[e] ‰	$\delta^{238}\text{U}_{\text{auth}}$[f] ‰
Shale																					
GPS1	0.96	3.3	13.7	454.4	4.29	23.53	2.40	5.48	4.11	1.96	22.53	4.48	5.02	-0.02	0.01	3	-0.28		1	-0.04	-0.28
GPS3		5.8	4.2	193.4	0.83	2.60	3.22	4.19	0.51	2.45	1.33	3.19	0.42	0.40	0.01	3	-0.39	0.05	3	0.34	-0.42
GPS4	4.10	5.8	3.4	174.0	7.36	23.05	6.86	8.96	7.04	6.09	18.38	7.96	2.31	0.10	0.04	3	-0.10	0.05	3	0.08	-0.07
GPS7		5.0	6.4	291.7	0.51	1.88	1.42	2.16	*	0.76	*	1.16	*								
GPS8	0.25	6.7	3.2	219.1	0.81	2.18	2.39	2.69	0.44	1.50	0.98	1.69	0.58								
GPS10	1.80	7.2	1.9	172.8	4.00	10.10	5.09	5.36	3.60	4.14	9.10	4.36	2.09	0.38	0.04	3	-0.27		1	0.37	-0.26
GPS13		5.2	5.9	250.1	13.87	48.35	6.93	10.06	13.59	6.24	47.35	9.06	5.23	0.25	0.07	3	-0.07	0.05	3	0.24	-0.04
GPS13rpt														0.25	0.02	3					
GPS14	1.86	7.0	2.7	173.1	3.62	9.33	4.03	4.33	3.23	3.10	8.33	3.33	2.50	0.79	0.05	3	-0.27	0.10	3	0.82	-0.26
GPS14rpt																	-0.29	0.05	3		
GPS16	0.12	7.1	1.0	159.0	0.43	1.08	2.43	2.57		1.49		1.57									
GPS19		6.3	2.9	224.0	6.76	19.52	3.93	4.73	6.41	3.10	18.52	3.73	4.97	0.54	0.03	3	-0.29		1	0.54	-0.29
GPS26	1.45	7.1	2.3	175.6	2.85	7.23	3.98	4.20	2.46	3.03	6.23	3.20	1.95	0.48	0.01	3				0.48	
GPS27	0.74	7.9	0.7	142.2	0.58	1.32	2.79	2.67	*	1.75	*	1.67	*								
GPS30	0.11	7.2	1.3	134.4	0.30	0.74	2.33	2.43	*	1.37	*	1.43	*	0.67	0.01	2				*	
GPS34	0.17	6.6	2.0	168.2	0.56	1.54	2.61	2.99	*	1.74	*	1.99	*								
GPS39	0.58	5.8	3.0	120.4	0.49	1.53	2.41	3.12	*	1.64	*	2.12	*								
GPS41		5.3	8.1	221.9	1.71	5.86	2.60	3.72	1.42	1.91	4.86	2.72	1.78	0.69	0.01	2	-0.35	0.08	3	0.73	-0.37
GPS44	0.12	6.8	2.4	175.4	0.62	1.63	1.61	1.78	*	*	*	*	*								
GPS47		6.8	2.8	164.0	0.72	1.91	2.00	2.21	*	1.09	*	1.21	*								
GPS49	0.11	5.4	4.4	246.1	1.38	4.60	1.45	2.01	1.08	0.73	3.60	1.01	3.57	2.58	0.05	4				3.16	
GPS53	1.79	5.9	3.2	130.6	7.05	21.50	9.74	12.38	6.72	8.95	20.50	11.38	1.80	-0.11	0.02	3	0.09	0.10	3	-0.14	0.12
GPS57	0.24	4.4	4.0	189.5	0.40	1.68	1.04	1.79	*	*	*	*	*	0.73	0.05	2				*	
GPS61	0.20	5.0	3.7	155.5	0.61	2.22	1.19	1.79	0.33	*	1.22	*	*	1.46	0.03	3				2.25	
GPS63	0.58	5.3	2.4	150.3	1.42	4.85	2.31	3.28	1.13	1.60	3.85	2.28	1.69	1.14	0.02	2	-0.22	0.12	3	1.31	-0.18
GPS66		5.8	2.8	150.9	4.51	14.09	7.79	10.13	4.19	7.02	13.09	9.13	1.43	-0.04	0.01	3	0.08	0.04	3	-0.08	0.12
GPS68	1.04	5.1	3.6	163.0	2.37	8.41	2.71	3.99	2.09	2.03	7.41	2.99	2.47	0.47	0.03	3	-0.30	0.04	3	0.47	-0.30
GPS71		6.4	2.8	169.7	2.72	7.66	3.17	3.71	2.36	2.31	6.66	2.71	2.45	0.67	0.04	3	-0.06	0.07	3	0.70	0.03
GPS75	0.95	4.0	7.8	165.9	1.04	4.74	1.72	3.26	0.82	1.19	3.74	2.26	1.66	0.83	0.03	4	-0.52	0.06	2	0.92	-0.62
GPS79	1.10	4.7	7.2	275.3	1.78	6.82	2.54	4.05	1.52	1.91	5.82	3.05	1.91	0.13	0.05	4	-0.21	0.06	3	0.07	-0.18

Table 2.1 (*continued*)

Sample id #	TOC[a] wt %	Al wt %	Ca wt %	Mn µg/g	Mo$_{bulk}$ µg/g	Mo$_{bulk}$ EF	U$_{bulk}$ µg/g	U$_{bulk}$ EF	Mo$_{auth}$ µg/g	U$_{auth}$ µg/g	Mo$_{auth}$ EF	U$_{auth}$ EF	Mo/U$_{auth}$[b] EF	δ^{98}Mo[c] ‰	±2σ	*n*	δ^{238}U[d] ‰	±2σ	*n*	δ^{98}Mo$_{auth}$[e] ‰	δ^{238}U$_{auth}$[f] ‰
Shale																					
GPS82	0.45	3.2	11.8	166.5	0.57	3.21	1.80	4.22	0.39	1.37	2.21	3.22	0.69	0.63	0.01	2	-0.39	0.06	3	0.69	-0.42
GPS84		5.0	6.1	161.3	0.75	2.71	1.19	1.80	0.47	*	1.71	*	*								
GPS149		5.5	2.9	175.1	1.54	5.10	2.09	2.88	1.24	1.36	4.10	1.88	2.18								
GPS150		7.1	1.0	200.4	0.60	1.53	2.56	2.72	*	1.62	*	1.72	*								
GPS151	2.37	4.4	7.5	233.6	7.32	30.32	3.30	5.70	7.08	2.72	29.32	4.70	6.24	0.54	0.04	3	-0.31	0.08	3	0.54	-0.31
GPS157	1.24	6.1	4.8	188.9	2.96	8.85	3.19	3.98	2.62	2.39	7.85	2.98	2.63	-0.30	0.03	3	-0.14	0.02	3	-0.40	-0.09
GPS166	8.81	5.9	4.3	163.3	24.63	75.33	13.40	17.07	24.30	12.61	74.33	16.07	4.63	1.50	0.03	3	-0.08	0.06	2	1.51	-0.07
GPS166rpt														1.51	0.03	3	-0.04	0.05	3		

EF denotes the enrichment factor.

Rpt refers to a replicate analysis.

[a] TOC = total organic carbon.

[b] Ratios of MoEF to UEF (authigenic).

[c, d] The bulk $\delta^{238/235}$U and $\delta^{98/95}$Mo.

[e, f] The authigenic $\delta^{238/235}$U and $\delta^{98/95}$Mo.

* The detrital fraction of [Mo]$_{bulk}$ and [U]$_{bulk}$ too dominant to estimate authigenic [Mo], [U], MoEF, UEF, MoEF/UEF, and $\delta^{98/95}$Mo.

Table 2.2: Statistics of the geochemical results of the carbonate samples (data source: [Mo] and δ^{98}Mo from Bisnaire (2018), TOC, [Al], [Ca], [Mn], [Sr], [U], δ^{234}U, and δ^{238}U from Azmy et al. (2015)).

Sample ID	TOC[a] wt %	Al µg/g	Ca wt %	Mn µg/g	Sr µg/g	Mo µg/g	U µg/g	U/Ca 10^{-4}	δ^{234}U[b] ‰	±2σ	n	δ^{98}Mo[c] ‰	±2σ	*n*	δ^{238}U[d] ‰	±2σ	*n*	δ^{238}U$_{BW}$[e] ‰
Carbonates																		
GP 2	1.5	372	36.36	800	285	0.17	1.56	0.04	1.9	1.7	4	0.71	0.01		-0.27	0.04	4	-0.52
GP 2rpt									5.3	7.9	2				-0.30	0.09	2	
GP 7	4.1	520	36.84	346	261	0.07	2.44	0.07	0.8	5.5	3	0.66	0.01	2	-0.46	0.05	3	-0.71
GP 14	0.8	878	34.20	671	227	0.29	2.53	0.07	28.2	5.2	4	-0.30	0.12	3	-0.18	0.08	4	-0.43
GP 18	2.4	640	37.50	280	297	0.09	1.62	0.04	5.3		1	0.94	0.03	2	-0.23		1	-0.48
GP 22	1.6	371	40.78	369	250	0.10	3.10	0.08	-14.3	1.4	3	0.82	0.04		-0.19	0.01	3	-0.44
GP 25	0.7	1083	36.14	628	190	0.04	0.78	0.02	9.8		1				-0.37		1	-0.62
GP 28	0.8	1104	34.15	365	482	0.41	1.83	0.05	6.3	4.8	3	0.10	0.04	3	-0.41	0.09	3	-0.66
GP 28rpt									6.7	0.7	4				-0.39	0.15	4	
GP 29	0.4	766	36.14	405	179	0.05	0.46	0.01	14.6	5.7	4				-0.49	0.10	4	-0.74

Table 2.2 (*continued*)

Sample ID	**TOC[a] wt %**	**Al µg/g**	**Ca wt %**	**Mn µg/g**	**Sr µg/g**	**Mo µg/g**	**U µg/g**	**U/Ca 10^{-4}**	**δ^{234}U[b] ‰**	**±2σ**	**n**	**δ^{98}Mo[c] ‰**	**±2σ**	***n***	**δ^{238}U[d] ‰**	**±2σ**	***n***	**$\delta^{238}U_{BW}$[e] ‰**
GP 30	0.4	703	38.95	376	246	0.03	0.24	0.01	2.3	2.3	3	1.23	0.28	4	-0.70	0.04	3	-0.95
GP 33	0.3	1571	38.42	273	397	1.91	1.19	0.03			1	1.26	0.03	3	-0.21		1	-0.46
GP 34	0.3	920	33.77	325	222	0.09	0.60	0.02	11.2	2.1	4	0.93	0.04	3	-0.69	0.12	4	-0.94
GP 35	0.2	1188	33.32	474	180	0.20	2.08	0.06			3	-0.10	0.18	2	0.00	0.05	3	-0.25
GP 38	0.1	706	34.90	122	379	0.10	0.35	0.01	2.3	5.3	4	1.48	0.05	3	-0.63	0.09	4	-0.88
GP 40		745	33.76	254	215	0.02	0.30	0.01	7.9	6.3	4	0.55	0.02	3	-0.97	0.15	4	-1.22
GP 41A		579	34.03	210	243	0.21	0.30	0.01	-2.5	3.7	3				-0.41	0.02	3	-0.66
GP 45		427	35.92	824	189	0.08	0.24	0.01	-7.3	0.9	3				-0.82	0.02	3	-1.07
GP 46	0.3	286	33.35	834	213	0.09	0.20	0.01	-21.3		1	2.34	0.19	3	-0.41		1	-0.66
GP 47		644	33.51	385	211	0.17	0.41	0.01	-9.4	3.0	3	1.03	0.10	3	-0.53	0.06	3	-0.78
GP 48	0.7	1371	29.39	449	232	0.38	0.77	0.03	8.1	0.6	2	1.24	0.07	3	-0.44	0.09	2	-0.69
GP 53	0.2	406	36.47	128	325	0.19	0.11	0.00	-20.8	1.7	4	1.38	0.06	3	-0.66	0.11	4	-0.91
GP 59	1.4	487	33.55	129	295	0.62	1.25	0.04	6.1	5.7	4	0.89	0.04	3	-0.33	0.13	4	-0.58
GP 59rpt									4.9	1.2	3				-0.37	0.06	3	

Rpt refers to a replicate analysis.

[a] TOC = total organic carbon.

[b, c, d] The $\delta^{234/238}$U, and $\delta^{98/95}$Mo, and $\delta^{238/235}$U.

[e] The estimated $^{\delta 238/235}$U of surface basin water.

Noteworthily, two particularly high $\delta^{98}Mo_{auth}$ (+2.25‰ and +3.16‰, respectively) values recorded by GPS 49 and GPS 61 seem to indicate strong sulfidic bottom conditions. However, they do not show much greater enrichments of Mo and significant lower [Mn] and Mn/Al compared to adjacent samples with much lighter $\delta^{98}Mo_{auth}$ signals. High enrichments of the ^{98}Mo isotope in these samples might be explained by 1) the diffusion of ^{98}Mo-enriched shallower weak sulfidic porewaters into more intensely sulfidic deeper porewaters, and 2) the subsequent (near)quantitative removal of aqueous Mo during early diagenesis (e.g., Scheiderich et al., 2010).

2.5.2.2. The Green Point carbonates

The carbonates exhibit large variations in $\delta^{98}Mo$ and generally low $[Mo]_{carb}$ (0.13 ± 0.05 µg/g, 2σ, Table 2.2) that are significantly lower than shale $[Mo]_{auth}$ (3.97 ± 10.26 µg/g, 2σ). The $\delta^{98}Mo_{carb}$ variability may reflect variable $[H_2S]_{aq}$ in porewaters and the addition of authigenic Mo with different isotopic fractionations from basin water during early diagenesis (e.g., Romaniello et al., 2016).

Unlike a positive correlation of [Mo] with $\delta^{98}Mo$ shown by the modern Bahama carbonates (Romaniello et al., 2016), we observe an insignificant correlation of $[Mo]_{carb}$ with $\delta^{98}Mo_{carb}$ values ($R^2 = 0.003$, Figure 2.5c). This poor correlation, together with the depletion of Mo in the carbonates, suggests weak sulfidic ($[H_2S]_{aq} < 11$ µM) porewater conditions during early diagenesis, which could have reduced the effect of authigenic Mo on the $\delta^{98}Mo$ signatures of some carbonate samples. This interpretation is consistent with the previous view that these carbonates were deposited under dysoxic to suboxic environments (Azmy et al., 2015, Bisnaire, 2018). As a result, $\delta^{98}Mo$ of the carbonates may fail to track the $\delta^{98}Mo$ of the basin water due to weak sulfidic porewater conditions during early diagenesis (e.g., Romaniello et al., 2016) in concert with the poor correlation of $\delta^{98}Mo_{carb}$ with the $\delta^{238}U_{BW}$ values inferred from $\delta^{238}U_{carb}$ ($R^2 = 0.11$, $p > 0.05$, Figure 2.5d).

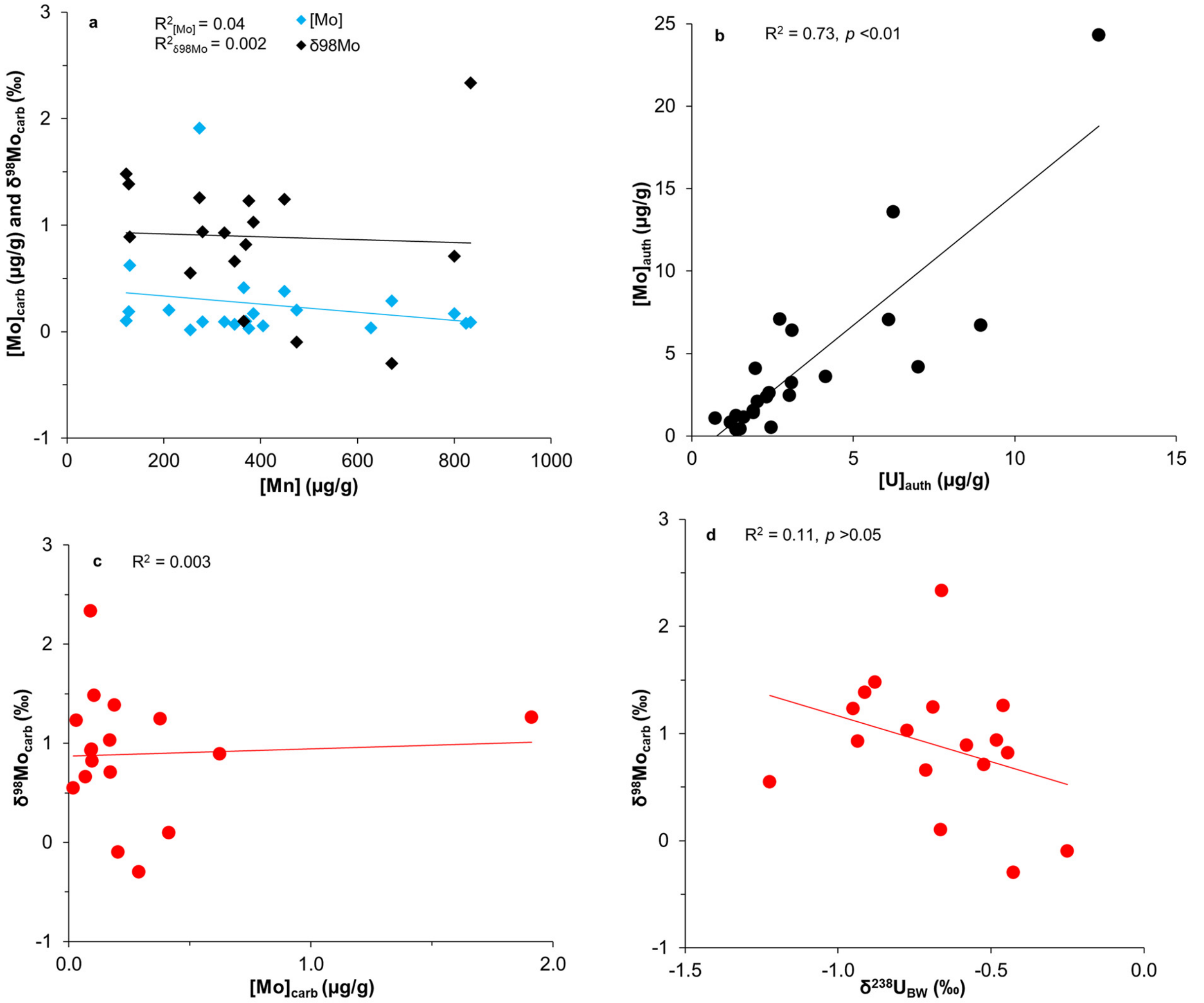

Figure 2.5: Scatter diagrams of (a) $[Mo]_{carb}$ and $δ^{98}Mo_{carb}$ vs. [Mn], (b) $δ^{98}Mo_{auth}$ vs. $δ^{238}U_{auth}$, (c) $[Mo]_{carb}$ vs. $δ^{98}Mo_{carb}$, (d) $δ^{98}Mo_{carb}$ vs. $δ^{238}U_{BW}$. Poor correlations of $[Mn]_{carb}$ with $[Mo]_{carb}$ and $δ^{98}Mo_{carb}$ ($R^2 = 0.04$ and 0.002, respectively) suggest negligible influences of the operation of a Mn-Fe (oxyhydr)oxide shuttle process on the carbonates. The strong positive correlation of shale $[Mo]_{auth}$ with $[U]_{auth}$ ($R^2 = 0.73$, $p < 0.01$) implies that Mo adsorption may take place along with U sequestration in sedimentary porewaters. The limestone $[Mo]_{carb}$ are poorly correlated with $δ^{98}Mo_{carb}$ ($R^2 = 0.003$), suggesting weak sulfidic ($[H_2S]_{aq} < 11$ µM) porewater conditions during early diagenesis. The negligible correlation of $δ^{98}Mo_{carb}$ with $δ^{238}U_{BW}$ ($R^2 = 0.11$) indicates that the $δ^{98}Mo_{carb}$ may fail to track the basin water. The black, blue, and red solid lines are regression lines for data with corresponding colors. These figures are updated versions of the original figures.

2.5.3. Evidence for basin restriction

The Mo_{EF}/U_{EF} values of the shale decrease gradually from ~ 1.7×MSW (the modern seawater value) at the middle of Bed 18 and reaches a minimum of ~ 0.3×MSW at the bottom of Bed 25, followed by a significant rebound at Bed 26 (Figure 2.3). Usually, the decrease/increase in authigenic Mo_{EF}/U_{EF} reflects decreased/increased Mo removal efficiency due to the decline/rises in $[H_2S]_{aq}$ in bottom waters or porewaters (Algeo and Tribovillard, 2009; Tribovillard et al., 2012). However, the moderately fluctuating [Mn] and Mn/Al suggest that redox variations may not be the sole cause of highly variable Mo_{EF}/U_{EF}.

Instead, the Mo_{EF}/U_{EF} variability was probably caused by changing connectivity between the local basin and the open ocean influenced by sea-level fluctuations. The gradual decline in Mo_{EF}/U_{EF} from the middle of Bed 18 to the bottom of Bed 25 was likely attributed to more intensified depletion of Mo_{aq} than U_{aq} as the result of slower bottom-water renewal, decreased depositional redox potentials, and more effective Mo removal to the sediments (e.g., Algeo and Tribovillard, 2009; Noordmann et al., 2015; Bura-Nakić et al., 2018). Probably, the local basin was partially isolated from the open ocean by topographic barriers driven by episodic regressions during deposition of this interval. Shale above this interval exhibit significant increases in Mo_{EF}/U_{EF}, $[Mo]_{auth}$, and $[U]_{auth}$, implying that the basin was probably highly connected to the open ocean due to rapid sea-level rises in the earliest Ordovician.

The forgoing explanation is further supported by an inverse correlation of $\delta^{98}Mo_{auth}$ with $\delta^{238}U_{auth}$ values ($R^2 = 0.36$, $p < 0.05$, Figure 2.6) recorded by shale from the middle of Bed 18 to the bottom of Bed 25. Similar inverse correlations of $\delta^{98}Mo_{auth}$ with $\delta^{238}U_{auth}$ have been observed in modern semi-restricted basin sediments (e.g., Black Sea, Cariaco Basin, and Mediterranean basin, Andersen et al., 2018; Brüske et al., 2020). These negative correlations have been attributed to changes in the $[H_2S]_{aq}$ and $\delta^{238}U$ of bottom waters and porewaters due to changing deep-water renewal rates (Andersen et al., 2018; Bura-Nakić et al., 2018; Brüske et al., 2020). Likely, the shale with higher $\delta^{98}Mo_{auth}$ was deposited under more reducing conditions caused by slower deep-water renewal, where the removal of aqueous Mo was more quantitative because of higher $[H_2S]_{aq}$ in porewaters. However, the shale was more depleted in the ^{238}U isotope as the result of decreased δ^{238}U of benthic waters driven by more efficient U reduction and ^{238}U removal to sediments. Conversely, the shale with higher $\delta^{238}U_{auth}$ and lower $\delta^{98}Mo_{auth}$ was possibly formed under less reducing conditions with higher δ^{238}U in bottom water and lower $[H_2S]_{aq}$ in porewater driven by faster bottom-water renewal.

2.5.4. Implications for global marine redox conditions

The $\delta^{238}U_{BW}$ variability during basin restriction should primarily reflect basinal scale redox oscillations. The decrease in $\delta^{238}U_{BW}$ could be caused by the expansion of reducing waters due to decreased bottom-water renewal rates. On the other hand, faster deep-water renewal as well as the subsequent contraction of reducing waters might have increased the $\delta^{238}U_{BW}$. Although redox oscillations of the open ocean may have impacts on the δ^{238}U of partially restricted basin water, this influence should be small because of slow bottom water renewal.[3] Above the middle of Bed 25, $\delta^{238}U_{BW}$ may represent open marine waters because of the high connectivity between the open ocean and the local basin. The $\delta^{238}U_{BW}$ variability points to global oceanic redox perturbations in the earliest Ordovician, probably triggered by changes in marine productivity (Saltzman et al., 2015). The $\delta^{238}U_{BW}$ exhibited an average value of −0.78 ± 0.33‰ (2σ), which is significantly lower than the modern seawater ($\delta^{238}U_{SW} \approx -0.39$‰, Tissot and Dauphas, 2015), suggesting largely expanded ocean euxinia (e.g., Lau et al., 2016; Bartlett et al., 2018) in concert with the earliest Ordovician greenhouse climates (Trotter et al., 2008; Goldberg et al., 2021).

---

[3] I have updated the interpretation of the estimated $\delta^{238}U_{BW}$ signals in Section 4.3.2. Studies suggest that the surface water δ^{238}U signatures of semi-restricted basins are comparable to open seawaters, while δ^{238}U signatures of the deeper bottom waters are influenced by deep-water renewal rates. All $\delta^{238}U_{BW}$ values in the current study are estimated from δ^{238}U values of lime mudstone originated from the shallow water carbonate platform. Thus, the inferred $\delta^{238}U_{BW}$ values should represent the shallow basin water and may be close to coeval open oceans. Please check Section 4.3.2 for details. The interpretation of the estimated $\delta^{238}U_{BW}$ variability is available in Section 4.5.4.

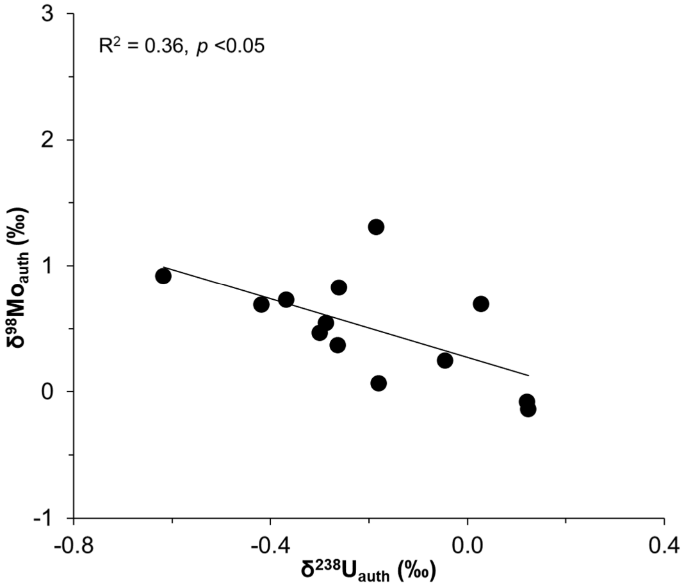

Figure 2.6: Crossplots of $\delta^{98}Mo_{auth}$ vs. $\delta^{238}U_{auth}$. An inverse correlation of $\delta^{98}Mo_{auth}$ with $\delta^{238}U_{auth}$ ($R^2 = 0.36$, $p < 0.05$) recorded by shale from the middle of Bed 18 to the bottom of Bed 25 provides further evidence for basin restriction. The black solid lines is the regression line. This figure is an updated version of the original figure.

Interestingly, a modern seawater-like $\delta^{98}Mo$ shown by sample GP46 ($\delta^{98}Mo$ = +2.34‰) appears to argue for the existence of transient highly oxygenated oceans during this time interval. However, the coeval $\delta^{238}U_{BW}$ (–0.66‰) points to expanded ocean euxinia compared to modern oceans (e.g., Gilleaudeau et al., 2019; Cole et al., 2020). One possible explanation is that this high $\delta^{98}Mo_{carb}$ might be caused by the diffusion of ^{98}Mo-enriched shallower weak sulfidic porewaters into more intensely sulfidic deeper porewaters during early diagenesis. It could be similar to the cause of excessive accumulation of the ^{98}Mo isotope in shale samples of Bed 22 and Bed 23 (e.g., Scheiderich et al., 2010, see Section 2.5.2.1). If so, the earliest Ordovician oceans were not episodically largely oxidized as suggested by this unexpected high $\delta^{98}Mo_{carb}$ value.

Alternatively, both aqueous Mo and U were perhaps removed from porewaters without significant isotope fractionations due to quantitative removal of these metals from bottom waters (e.g., Nägler et al., 2011; Lau et al., 2020) during deposition of this carbonate layer. Thus, the

δ^{98}Mo and δ^{238}U of seawater were likely directly captured by the carbonates. In this case, the δ^{238}U and δ^{98}Mo values (–0.41‰ and +2.34‰, respectively) recorded by GP46 were possibly close to those of coeval ocean waters, thus suggesting extensively oxygenated open oceans. However, neither of the above possibilities can be ruled out during this time, and therefore further study is still needed to verify if the earliest Ordovician oceans had been episodically extensively oxidized.

Conclusions

The highly variable shale $\delta^{98}Mo_{auth}$ (–0.40 to +3.16‰) suggests variable and less intensely reducing (~ dysoxic/suboxic to anoxic) bottom water conditions. A strong positive correlation of $[Mo]_{auth}$ with $[U]_{auth}$, coupled with low Mo concentrations (compared to Phanerozoic euxinic shale), further indicates that H_2S_{aq} was mainly confined to porewaters during deposition of the Green Point shale. Similarly, the variation in $\delta^{98}Mo_{carb}$ (–0.30 to +2.34‰) implies changing H_2S_{aq} levels in porewaters during the deposition of the lime mudstone. Low Mo concentrations in the carbonates ($[Mo]_{carb} = 0.25 \pm 0.80$ μg/g, 2σ) and a lack of correlation between $[Mo]_{carb}$ and $\delta^{98}Mo_{carb}$ point to weak sulfidic ($[H_2S]_{aq} < 11$ μM) porewater conditions during early diagenesis. Therefore, the carbonates may fail to capture the δ^{98}Mo of their coeval basin waters due to low H_2S_{aq} levels in porewaters, in line with an insignificant correlation of $\delta^{98}Mo_{carb}$ with $\delta^{238}U_{BW}$ estimated by the $\delta^{238}U_{carb}$ signals.

During deposition of the investigated interval, the local basin was probably partially isolated from the open ocean attributed to topographic barriers.[4] Changing bottom-water renewal rates during basin restriction resulted in a decline in shale Mo_{EF}/U_{EF} (~ 1.7 to 0.3×MSW) from

---

[4] A modification has been made to the original text by deleting "the lower and middle part of" and "and sea-level variations".

the middle of Bed 18 to the bottom of Bed 25, an inverse correlation between authigenic $\delta^{98}Mo_{shale}$ and $\delta^{238}U_{shale}$ values, and the variation in basin water $\delta^{238}U$ signatures [5]. Significant increases in shale Mo_{EF}/U_{EF}, $[Mo]_{auth}$, and $[U]_{auth}$ indicate that the basin was highly connected to the open marine after rapid sea-level rises in the earliest Ordovician. Open oceans during this time interval exhibited $\delta^{238}U$ perturbations and a low average $\delta^{238}U$ value of –0.78 ± 0.33‰ (2σ), which is significantly lower than the modern seawater $\delta^{238}U_{SW}$ of ~ –0.39‰. Therefore, the earliest Ordovician was possibly a time of oceanic redox variations and expanded marine euxinia compared to modern oceans. Although one of the carbonate samples exhibits a modern seawater-like $\delta^{98}Mo$ (+2.34‰) value, caution needs to be taken since all other supporting geochemical evidence does not support extensively oxidized earliest Ordovician oceans.

Acknowledgements

The authors wish to thank Dr. Christian France-Lanord (editor) and anonymous reviewers for their constructive reviews. Also, the efforts of Mr. Dhilip Kumar and Mr. T. Manavalan (Journal managers) are much appreciated. Special thanks to Dr. Gwyneth W. Gordon for her help with the isotope analyses. This project was supported by funding (to Karem Azmy) from Petroleum Exploration Enhancement Program (PEEP) and MITACS and (to Brian Kendall) from the Canada Research Chair program and the NSERC Discovery Grant program (RGPIN-04090-2019).

Supplementary data

Detrital Correction based on the average upper crust: [Al] = 8.15 wt%,[Mo] = 1.1µg/g, [U] = 2.7µg/g (Rudnick and Gao, 2014).

---

[5] The phrase “from the middle of Bed 18 to the bottom of Bed 25” was added to the original text to enhance the clarity of expression. The “$\delta^{238}U_{BW}$” in the original text was replaced with “basin water $\delta^{238}U$ signatures”.

Sample ID	Al wt %	Mo_{bulk} μg/g	U_{bulk} μg/g	Mo_{auth} μg/g	U_{auth} μg/g
Shale					
GPS1	3.3	4.29	2.40	3.84	1.31
GPS3	5.8	0.83	3.22	0.05	1.30
GPS4	5.8	7.36	6.86	6.58	4.95
GPS10	7.2	4.00	5.09	3.03	2.72
GPS13	5.2	13.87	6.93	13.17	5.21
GPS13rpt					
GPS14	7.0	3.62	4.03	2.67	1.70
GPS14rpt					
GPS19	6.3	6.76	3.93	5.91	1.85
GPS26	7.1	2.85	3.98	1.89	1.61
GPS30	7.2	0.30	2.33	-0.68	-0.06
GPS41	5.3	1.71	2.60	1.00	0.86
GPS49	5.4	1.38	1.45	0.65	-0.35
GPS53	5.9	7.05	9.74	6.25	7.77
GPS57	4.4	0.40	1.04	-0.19	-0.41
GPS61	5.0	0.61	1.19	-0.06	-0.47
GPS63	5.3	1.42	2.31	0.71	0.55
GPS66	5.8	4.51	7.79	3.73	5.87
GPS68	5.1	2.37	2.71	1.68	1.01
GPS71	6.4	2.72	3.17	1.85	1.04
GPS75	4.0	1.04	1.72	0.51	0.40
GPS79	4.7	1.78	2.54	1.14	0.97
GPS82	3.2	0.57	1.80	0.14	0.73
GPS149	5.5	1.54	2.09	0.80	0.28
GPS151	4.4	7.32	3.30	6.73	1.85
GPS157	6.1	2.96	3.19	2.14	1.19
GPS166	5.9	24.63	13.40	23.83	11.44
GPS166rpt					

References

Algeo, T.J., Li, C., 2020. Redox classification and calibration of redox thresholds in sedimentary systems. Geochim. Cosmochim. Acta 287, 8–26.

Algeo, T.J., Tribovillard, N., 2009. Environmental analysis of paleoceanographic systems based on molybdenum–uranium covariation. Chem. Geol. 268 (3–4), 211–225.

Andersen, M.B., et al., 2014. A modern framework for the interpretation of 238U/235U in studies of ancient ocean redox. Earth Planet. Sci. Lett. 400, 184–194.

Andersen, M.B., et al., 2018. A 10-fold decline in the deep Eastern Mediterranean thermohaline overturning circulation during the last interglacial period. Earth Planet. Sci. Lett. 503, 58–67.

Arnold, D.P., Blok, J., 2004. The coordination chemistry of tin porphyrin complexes. Coord. Chem. Rev. 248 (3–4), 299–319.

Azmy, K., Stouge, S., Brand, U., Bagnoli, G., Ripperdan, R., 2014. High-resolution chemostratigraphy of the Cambrian–Ordovician GSSP: Enhanced global correlation tool. Palaeogeogr. Palaeoclimatol. Palaeoecol. 409, 135–144.

Azmy, K., Kendall, B., Brand, U., Stouge, S., Gordon, G.W., 2015. Redox conditions across the Cambrian–Ordovician boundary: Elemental and isotopic signatures retained in the GSSP carbonates. Palaeogeogr. Palaeoclimatol. Palaeoecol. 440, 440–454.

Baldwin, G.J., N¨agler, T.F., Greber, N.D., Turner, E.C., Kamber, B.S., 2013. Mo isotopic composition of the mid-neoproterozoic Ocean: an iron formation perspective. Precambrian Res. 230, 168–178.

Barling, J., Arnold, G.L., Anbar, A.D., 2001. Natural mass-dependent variations in the isotopic composition of molybdenum. Earth Planet. Sci. Lett. 193, 447–457.

Bartlett, R., et al., 2018. Abrupt global-ocean anoxia during the late Ordovician-early Silurian detected using uranium isotopes of marine carbonates. Proc. Natl. Acad. Sci. U. S. A. 115 (23), 5896–5901.

Bisnaire, A.C., 2018. Oceanic Redox Conditions across the Cambrian-Ordovician Boundary. Thesis (Masters). Memorial University of Newfoundland.

Bond, D.P.G., Grasby, S.E., 2020. Late Ordovician mass extinction caused by volcanism, warming, and anoxia, not cooling and glaciation. Geology 48 (8), 777–781.

Brennecka, G.A., Herrmann, A.D., Algeo, T.J., Anbar, A.D., 2011. Rapid expansion of oceanic anoxia immediately before the end-Permian mass extinction. Proc. Natl. Acad. Sci. U. S. A. 108 (43), 17631–17634.

Brüske, A., et al., 2020. Correlated molybdenum and uranium isotope signatures in modern anoxic sediments: Implications for their use as paleo-redox proxy. Geochim. Cosmochim. Acta 270, 449–474.

Buatois, L.A., Mangano, M.G., Olea, R.A., Wilson, M.A., 2016. Decoupled evolution of soft and hard substrate communities during the Cambrian Explosion and Great Ordovician Biodiversification Event. Proc. Natl. Acad. Sci. U. S. A. 113 (25), 6945–6948.

Bura-Naki´c, E., et al., 2018. Coupled Mo-U abundances and isotopes in a small marine euxinic basin: Constraints on processes in euxinic basins. Geochim. Cosmochim. Acta 222, 212–229.

Bura-Naki´c, E., Sondi, I., Mikac, N., Andersen, M.B., 2020. Investigating the molybdenum and uranium redox proxies in a modern shallow anoxic carbonate rich marine sediment setting of the Malo Jezero (Mljet Lakes, Adriatic Sea). Chem. Geol. 533.

Candela, Y., 2015. Evolution of Laurentian brachiopod faunas during the Ordovician Phanerozoic Sea level maximum. Earth Sci. Rev. 141, 27–44.

Cawood, P.A., McCausland, P.J.A., Dunning, G.R., 2001. Opening Iapetus: Constraints from the Laurentian margin in Newfoundland. GSA Bull. 113, 443–453.

Chen, J.H., Edwards, R.L., Wasserburg, G.J., 1986. 238U, 234U and 232Th in seawater. Earth Planet. Sci. Lett. 80, 241–251.

Chen, X., et al., 2018. Diagenetic effects on uranium isotope fractionation in carbonate sediments from the Bahamas. Geochim. Cosmochim. Acta 237, 294–311.

Chen, X., Romaniello, S.J., Anbar, A.D., 2021. Preliminary exploration of molybdenum isotope fractionation during coprecipitation of molybdate with abiotic and microbial calcite. Chem. Geol. 566.

Cole, D.B., Zhang, S., Planavsky, N.J., 2017. A new estimate of detrital redox-sensitive metal concentrations and variability in fluxes to marine sediments. Geochim. Cosmochim. Acta 215, 337–353.

Cole, D.B., et al., 2020. Uranium isotope fractionation in non-sulfidic anoxic settings and the global uranium isotope mass balance. Glob. Biogeochem. Cycles 34 (8).

Coniglio, M., James, N.P., 1990. Origin of fine-grained carbonate and siliciclastic sediments in an early Palaeozoic slope sequence, Cow Head Group, western Newfoundland. Sedimentology 37, 215–230.

Cooper, R.A., Nowlan, G.S., Williams, S.H., 2001. Global stratotype section and point for base of the Ordovician System. Episodes 24, 19–28.

Dahl, T.W., et al., 2010a. The behavior of molybdenum and its isotopes across the chemocline and in the sediments of sulfidic Lake Cadagno, Switzerland. Geochim. Cosmochim. Acta 74 (1), 144–163.

Dahl, T.W., et al., 2010b. Devonian rise in atmospheric oxygen correlated to the radiations of terrestrial plants and large predatory fish. PNAS 107, 17911–17915.

Dahl, T.W., et al., 2014. Uranium isotopes distinguish two geochemically distinct stages during the later Cambrian SPICE event. Earth Planet. Sci. Lett. 401, 313–326.

Dahl, T.W., et al., 2019. Atmosphere-ocean oxygen and productivity dynamics during early animal radiations. Proc. Natl. Acad. Sci. U. S. A. 116 (39), 19352–19361.

D’Arcy, J., Gilleaudeau, G.J., Peralta, S., Gaucher, C., Frei, R., 2017. Redox fluctuations in the early Ordovician oceans: an insight from chromium stable isotopes. Chem. Geol. 448, 1–12.

Djogi´c, R., Sipos, L., Branica, M., 1986. Characterization of uranium (VI) in seawater. Limnol. Oceanogr. 31 (5), 1122–1131.

Duan, Y., et al., 2010. Molybdenum isotope evidence for mild environmental oxygenation before the Great Oxidation Event. Geochim. Cosmochim. Acta 74 (23), 6655–6668.

Dunk, R.M., Mills, R.A., Jenkins, W.J., 2002. A reevaluation of the oceanic uranium budget for the Holocene. Chem. Geol. 190, 45–67.

Eade, K.E., Fahrig, W.F., 1971. Geochemical Evolutionary Trends of Continental Plates a Preliminary Study of the Canadian Shield. Ottawa Dept. of Energy, Mines and Resources.

Eade, K.E., Fahrig, W.F., 1973. Regional, Lithological and Temporal Variation in the Abundances of some Trace Elements in the Canadian Shield. Geol. Sur. Canada Paper, Ontario, Ottawa (p. 72–46).

Edwards, C.T., Fike, D.A., Saltzman, M.R., Lu, W., Lu, Z., 2018. Evidence for local and global redox conditions at an early Ordovician (Tremadocian) mass extinction. Earth Planet. Sci. Lett. 481, 125–135.

Erickson, B.E., Helz, G.R., 2000. Molybdenum (VI) speciation in sulfidic waters: Stability and lability of thiomolybdates. Geochim. Cosmochim. Acta 64, 1149–1158.

Gilleaudeau, G.J., et al., 2019. Uranium isotope evidence for limited euxinia in midProterozoic oceans. Earth Planet. Sci. Lett. 521, 150–157.

Goldberg, T., Poulton, S.W., Wagner, T., Kolonic, S.F., Rehk¨amper, M., 2016. Molybdenum drawdown during cretaceous Oceanic Anoxic Event 2. Earth Planet. Sci. Lett. 440, 81–91.

Goldberg, S.L., Present, T.M., Finnegan, S., Bergmann, K.D., 2021. A high-resolution record of early Paleozoic climate. Proc. Natl. Acad. Sci. U. S. A. 118 (6).

Greber, N.D., Hofmann, B.A., Voegelin, A.R., Villa, I.M., N¨agler, T.F., 2011. Mo isotope composition in Mo-rich high- and low-T hydrothermal systems from the Swiss Alps. Geochim. Cosmochim. Acta 75 (21), 6600–6609.

Harper, D.A.T., 2006. The Ordovician biodiversification: setting an agenda for marine life. Palaeogeogr. Palaeoclimatol. Palaeoecol. 232 (2–4), 148–166.

Helz, G.R., Vorlicek, T.P., 2019. Precipitation of molybdenum from euxinic waters and the role of organic matter. Chem. Geol. 509, 178–193.

Helz, G.R., et al., 1996. Mechanism of molybdenum removal from the sea and its concentration in black shales: EXAFS evidence. Geochim. Cosmochim. Acta 60, 3631–3642.

Herrmann, A.D., et al., 2012. Anomalous molybdenum isotope trends in Upper Pennsylvanian euxinic facies: significance for use of δ98Mo as a global marine redox proxy. Chem. Geol. 324-325, 87–98.

Herrmann, A.D., Gordon, G.W., Anbar, A.D., 2018. Uranium isotope variations in a dolomitized Jurassic carbonate platform (Tithonian; Franconian Alb, Southern Germany). Chem. Geol. 497, 41–53.

Hu, Z., Gao, S., 2008. Upper crustal abundances of trace elements: a revision and update. Chem. Geol. 253 (3–4), 205–221.

Jacobi, R.D., 1981. Peripheral bulge—a causal mechanism for the lower/Middle Ordovician unconformity along the western margin of the Northern Appalachians. Earth Planet. Sci. Lett. 56, 245–251.

James, N.P., Stevens, R.K., 1986. Stratigraphy and correlation of the Cambro-Ordovician Cow head Group, western Newfoundland. Geological Survey of Canada, pp. 1–143.

James, N.P., Stevens, R.K., Barnes, C.R., Knight, I., 1989. Evolution of a lower paleozoic continental-margin carbonate platform, Northern Canadian Appalachians. In: Crevello, P.D. Wilson, Sarg, J.L., Read, J.F. (Eds.), Controls on Carbonate Platform and Basin Development, 44. Society of Economic Paleontologists and Mineralogists Special Publication, pp. 123–146.

Kelly, S.D., et al., 2003. Uranyl incorporation in natural calcite. Environ. Sci. Technol. 37, 1284–1287.

Kelly, S.D., Rasbury, E.T., Chattopadhyay, S., Kropf, A.J., Kemner, K.M., 2006. Evidence of a stable uranyl site in ancient organic-rich calcite. Environ. Sci. Technol. 40, 2262–2268.

Kendall, B., Gordon, G.W., Poulton, S.W., Anbar, A.D., 2011. Molybdenum isotope constraints on the extent of late Paleoproterozoic Ocean euxinia. Earth Planet. Sci. Lett. 307 (3–4), 450–460.

Kendall, B., Brennecka, G.A., Weyer, S., Anbar, A.D., 2013. Uranium isotope fractionation suggests oxidative uranium mobilization at 2.50Ga. Chem. Geol. 362, 105–114.

Kendall, B., et al., 2015. Uranium and molybdenum isotope evidence for an episode of widespread ocean oxygenation during the late Ediacaran Period. Geochim. Cosmochim. Acta 156, 173–193.

Kendall, B., Wang, J., Zheng, W., Romaniello, S.J., Jeffrey Over, D., Bennett, Y., Xing, L., Kunert, A., Boyes, C., Liu, J., 2020. Inverse correlation between the molybdenum and uranium isotope compositions of Upper Devonian black shales caused by changes in local depositional conditions rather than global ocean redox variations. Geochim. Cosmochim. Acta 287, 141–164.

King, E.K., Perakis, S.S., Pett-Ridge, J.C., 2017. Molybdenum isotope fractionation during adsorption to organic matter. Geochim. Cosmochim. Acta 222, 584–598.

Knight, I., James, N.P., Lane, T.E., 1991. The Ordovician St. George unconformity, Northern Appalachians; the relationship of plate convergence at the St. Lawrence Promontory to the Sauk/Tippecanoe sequence boundary. Geol. Soc. Am. Bull. 103, 1200–1225.

Knight, I., Azmy, K., Greene, M.G., Lavoie, D., 2007. Lithostratigraphic Setting of Diagenetic, Isotopic, and Geochemistry Studies of Ibexian and Whiterockian Carbonate Rocks. Current Research (2007) Newfoundland and Labrador Department of Natural Resources Geological Survey, Report 07-1, pp. 55–84.

Knight, I., Azmy, K., Boyce, W.D., Lavoie, D., 2008. Tremadocian carbonate rocks of the lower St. George group, Port au Port. In: Current Research (2008) Newfoundland and Labrador Department of Natural Resources Geological Survey Report 08–1, pp. 115–149.

Lau, K.V., et al., 2016. Marine anoxia and delayed Earth system recovery after the endPermian extinction. Proc. Natl. Acad. Sci. U. S. A. 113 (9), 2360–2365.

Lau, K.V., Lyons, T.W., Maher, K., 2020. Uranium reduction and isotopic fractionation in reducing sediments: Insights from reactive transport modeling. Geochim. Cosmochim. Acta 287, 65–92.

Lavoie, D., Andre, D., Dix, G., Knight, I., Hersi, O.S., 2013. The Great American Carbonate Bank in eastern Canada an overview. AAPG Mem. 98, 499–523.

Lu, X., et al., 2017. Marine redox conditions during deposition of late Ordovician and early Silurian organic-rich mudrocks in the Siljan ring district, Central Sweden. Chem. Geol. 457, 75–94.

Lu, X., Dahl, T.W., Zheng, W., Wang, S., Kendall, B., 2020. Estimating ancient seawater isotope compositions and global ocean redox conditions by coupling the molybdenum and uranium isotope systems of euxinic organic-rich mudrocks. Geochim. Cosmochim. Acta 290, 76–103.

Midgley, S.D., Taylor, J.O., Fleitmann, D., Grau-Crespo, R., 2020. Molybdenum and sulfur incorporation as oxyanion substitutional impurities in calcium carbonate minerals: a computational investigation. Chem. Geol. 553.

Miller, C.A., Peucker-Ehrenbrink, B., Walker, B.D., Marcantonio, F., 2011. Re-assessing the surface cycling of molybdenum and rhenium. Geochim. Cosmochim. Acta 75 (22), 7146–7179.

Morford, J.L., Emerson, S., 1999. The geochemistry of redox sensitive trace metals in sediments. Geochim. Cosmochim. Acta 63, 1735–1750.

N¨agler, T.F., Neubert, N., B¨ottcher, M.E., Dellwig, O., Schnetger, B., 2011. Molybdenum isotope fractionation in pelagic euxinia: evidence from the modern Black and Baltic Seas. Chem. Geol. 289 (1–2), 1–11.

N¨agler, T.F., et al., 2013. Proposal for an international molybdenum isotope measurement standard and data representation. Geostand. Geoanal. Res. 38, 149–151.

Neubert, N., et al., 2011. The molybdenum isotopic composition in river water: Constraints from small catchments. Earth Planet. Sci. Lett. 304 (1–2), 180–190.

Noordmann, J., et al., 2015. Uranium and molybdenum isotope systematics in modern euxinic basins: Case studies from the Central Baltic Sea and the Kyllaren fjord (Norway). Chem. Geol. 396, 182–195.

Nowak, H., Servais, T., Monnet, C., Molyneux, S.G., Vandenbroucke, T.R.A., 2015. Phytoplankton dynamics from the Cambrian Explosion to the onset of the Great Ordovician Biodiversification Event: a review of Cambrian acritarch diversity. Earth Sci. Rev. 151, 117–131.

Ostrander, C.M., et al., 2019. Multiple negative molybdenum isotope excursions in the Doushantuo Formation (South China) fingerprint complex redox-related processes in the Ediacaran Nanhua Basin. Geochim. Cosmochim. Acta 261, 191–209.

Poulson, R.L., Siebert, C., McManus, J., Berelson, W.M., 2006. Authigenic molybdenum isotope signatures in marine sediments. Geology 34 (8), 617–620.

Proemse, B.C., Grasby, S.E., Wieser, M.E., Mayer, B., Beauchamp, B., 2013. Molybdenum isotopic evidence for oxic marine conditions during the latest Permian extinction. Geology 41 (9), 967–970.

Pruss, S.B., Jones, D.S., Fike, D.A., Tosca, N.J., Wignall, P.B., 2019. Marine anoxia and sedimentary mercury enrichments during the late Cambrian SPICE event in northern Scotland. Geology 47 (5), 475–478.

Rasmussen, C.M.O., Kroger, B., Nielsen, M.L., Colmenar, J., 2019. Cascading trend of early Paleozoic marine radiations paused by late Ordovician extinctions. Proc. Natl. Acad. Sci. U. S. A. 116 (15), 7207–7213.

Reeder, R.J., Nugent, M., Lamble, G.M., Tait, C.D., Morris, D.E., 2000. Uranyl incorporation into calcite and aragonite: XAFS and luminescence studies. Environ. Sci. Technol. 34, 638–644.

Rolison, J.M., Stirling, C.H., Middag, R., Rijkenberg, M.J.A., 2017. Uranium stable isotope fractionation in the Black Sea: Modern calibration of the 238U/235U paleoredox proxy. Geochim. Cosmochim. Acta 203, 69–88.

Romaniello, S.J., Herrmann, A.D., Anbar, A.D., 2013. Uranium concentrations and 238U/235U isotope ratios in modern carbonates from the Bahamas: Assessing a novel paleoredox proxy. Chem. Geol. 362, 305–316.

Romaniello, S.J., Herrmann, A.D., Anbar, A.D., 2016. Syndepositional diagenetic control of molybdenum isotope variations in carbonate sediments from the Bahamas. Chem. Geol. 438, 84–90.

Rudnick, R.L., Gao, S., 2014. Composition of the continental crust. In: Treatise on Geochemistry, 4.1. Elsevier, pp. 1–45.

Saltzman, M.R., et al., 2011. Pulse of atmospheric oxygen during the late Cambrian. Proc. Natl. Acad. Sci. U. S. A. 108 (10), 3876–3881.

Saltzman, M.R., Edwards, C.T., Adrain, J.M., Westrop, S.R., 2015. Persistent oceanic anoxia and elevated extinction rates separate the Cambrian and Ordovician radiations. Geology 43 (9), 807–810.

Sarmiento, J.L., Gruber, N., 2006. Ocean Biogeochemical Dynamics. Princeton University Press.

Scheiderich, K., Zerkle, A.L., Helz, G.R., Farquhar, J., Walker, R.J., 2010. Molybdenum isotope, multiple sulfur isotope, and redox-sensitive element behavior in early Pleistocene Mediterranean sapropels. Chem. Geol. 279 (3–4), 134–144.

Scotese, C.R., 2014. Atlas of Cambrian and Early Ordovician Paleogeographic Maps (Mollweide Projection), Maps 81–88, Volumes 5, The Early Paleozoic, PALEOMAP Atlas for ArcGIS, PALEOMAP Project, Evanston, IL.

Scott, C., Lyons, T.W., 2012. Contrasting molybdenum cycling and isotopic properties in euxinic versus non-euxinic sediments and sedimentary rocks: refining the paleoproxies. Chem. Geol. 324-325, 19–27.

Servais, T., et al., 2008. The Ordovician Biodiversification: revolution in the oceanic trophic chain. Lethaia 41 (2), 99–109.

Servais, T., Owen, A.W., Harper, D.A.T., Kr¨oger, B., Munnecke, A., 2010. The Great Ordovician Biodiversification Event (GOBE): the palaeoecological dimension. Palaeogeogr. Palaeoclimatol. Palaeoecol. 294 (3–4), 99–119.

Servais, T., et al., 2016. The onset of the 'Ordovician Plankton Revolution' in the late Cambrian. Palaeogeogr. Palaeoclimatol. Palaeoecol. 458, 12–28.

Siebert, C., N¨agler, T.F., von Blanckenburg, F., Kramers, J.D., 2003. Molybdenum isotope records as a potential new proxy for paleoceanography. Earth Planet. Sci. Lett. 211 (1–2), 159–171.

Siebert, C., McManus, J., Bice, A., Poulson, R., Berelson, W.M., 2006. Molybdenum isotope signatures in continental margin marine sediments. Earth Planet. Sci. Lett. 241 (3–4), 723–733.

Stigall, A.L., Edwards, C.T., Freeman, R.L., Rasmussen, C.M.Ø., 2019. Coordinated biotic and abiotic change during the Great Ordovician Biodiversification Event: Darriwilian assembly of early Paleozoic building blocks. Palaeogeogr. Palaeoclimatol. Palaeoecol. 530, 249–270.

Stirling, C.H., Andersen, M.B., Warthmann, R., Halliday, A.N., 2015. Isotope fractionation of 238U and 235U during biologically-mediated uranium reduction. Geochim. Cosmochim. Acta 163, 200–218.

Sturchio, N.C., Antonio, M.R., Soderholm, L., Sutton, S.R., Brannon, J.C., 1998. Tetravalent uranium in calcite. Science 281, 971–973.

Stylo, M., et al., 2015. Uranium isotopes fingerprint biotic reduction. Proc. Natl. Acad. Sci. U. S. A. 112 (18), 5619–5624.

Sun, Y.C., Mierzwa, J., Lan, C.R., 2000. Direct determination of molybdenum in seawater by adsorption cathodic stripping square-wave voltammetry. Talanta 52, 417–424.

Terfelt, F., Eriksson, M.E., Schmitz, B., 2014. The Cambrian–Ordovician transition in dysoxic facies in Baltica — diverse faunas and carbon isotope anomalies. Palaeogeogr. Palaeoclimatol. Palaeoecol. 394, 59–73.

Tissot, F.L.H., Dauphas, N., 2015. Uranium isotopic compositions of the crust and ocean: Age corrections, U budget and global extent of modern anoxia. Geochim. Cosmochim. Acta 167, 113–143.

Tissot, F.L.H., et al., 2018. Controls of eustasy and diagenesis on the 238U/235U of carbonates and evolution of the seawater (234U/238U) during the last 1.4 Myr. Geochim. Cosmochim. Acta 242, 233–265.

Tostevin, R., et al., 2019. Uranium isotope evidence for an expansion of anoxia in terminal Ediacaran oceans. Earth Planet. Sci. Lett. 506, 104–112.

Tribovillard, N., Algeo, T.J., Baudin, F., Riboulleau, A., 2012. Analysis of marine environmental conditions based on molybdenum–uranium covariation—applications to Mesozoic paleoceanography. Chem. Geol. 324-325, 46–58.

Tripathy, G.R., Hannah, J.L., Stein, H.J., Yang, G., 2014. Re-Os age and depositional environment for black shales from the Cambrian-Ordovician boundary, Green Point, western Newfoundland. Geochem. Geophys. Geosyst. 15, 1021–1037.

Trotter, J.A., Williams, I.S., Barnes, C.R., L´ecuyer, C., Nicoll, R.S., 2008. Did cooling oceans trigger ordovician biodiversification? Evidence from conodont thermometry. Science 321, 550–554.

van der Velden, A.J., van Staal, C.R., Cook, F.A., 2004. Crustal structure, fossil subduction, and the tectonic evolution of the Newfoundland Appalachians: evidence from a reprocessed seismic reflection survey. Geol. Soc. Am. Bull. 116 (11−12), 1485–1498.

Van Roy, P., et al., 2010. Ordovician faunas of Burgess Shale type. Nature 465 (7295), 215–218.

Van Roy, P., Briggs, D.E.G., Gaines, R.R., 2015. The Fezouata fossils of Morocco; an extraordinary record of marine life in the early Ordovician. J. Geol. Soc. 172 (5), 541–549.

Voegelin, A.R., N¨agler, T.F., Samankassou, E., Villa, I.M., 2009. Molybdenum isotopic composition of modern and Carboniferous carbonates. Chem. Geol. 265 (3–4), 488–498.

Voegelin, A.R., N¨agler, T.F., Beukes, N.J., Lacassie, J.P., 2010. Molybdenum isotopes in late Archean carbonate rocks: Implications for early Earth oxygenation. Precambrian Res. 182 (1–2), 70–82.

Voegelin, A.R., et al., 2012. The impact of igneous bedrock weathering on the Mo isotopic composition of stream waters: Natural samples and laboratory experiments. Geochim. Cosmochim. Acta 86, 150–165.

Wagner, M., Chappaz, A., Lyons, T.W., 2017. Molybdenum speciation and burial pathway in weakly sulfidic environments: Insights from XAFS. Geochim. Cosmochim. Acta 206, 18–29.

Waldron, J.W.F., et al., 1998. Evolution of the Appalachian Laurentian margin: Lithoprobe results in western newfoundland. Can. J. Earth Sci. 35, 1271–1287.

Wei, G.-Y., et al., 2018. Marine redox fluctuation as a potential trigger for the Cambrian explosion. Geology 46 (7), 587–590.

Wei, G.-Y., et al., 2020. Highly dynamic marine redox state through the Cambrian explosion highlighted by authigenic δ238U records. Earth Planet. Sci. Lett. 544.

Wei, G.-Y., et al., 2021. Global marine redox evolution from the late Neoproterozoic to the early Paleozoic constrained by the integration of Mo and U isotope records. Earth Sci. Rev. 214.

Wen, H., et al., 2011. Molybdenum isotopic records across the Precambrian-Cambrian boundary. Geology 39 (8), 775–778.

Weyer, S., et al., 2008. Natural fractionation of 238U/235U. Geochim. Cosmochim. Acta 72 (2), 345–359.

Wille, M., et al., 2007. Evidence for a gradual rise of oxygen between 2.6 and 2.5Ga from Mo isotopes and Re-PGE signatures in shales. Geochim. Cosmochim. Acta 71 (10), 2417–2435.

Wilson, J.L., Medlock, P.L., Fritz, R.D., Canter, K.L., Geesaman, R.G., 1992. A review of Cambro–Ordovician Breccias in North America. In: Candelaria, M.P., Reed, C.L. (Eds.), Paleokarst, Karst–Related Diagenesis and Reservoir Development, SEPM– Permian Basin Section, Publication, vols. 92–33, pp. 19–29.

Yang, S., Kendall, B., Lu, X., Zhang, F., Zheng, W., 2017. Uranium isotope compositions of mid-Proterozoic black shales: evidence for an episode of increased ocean oxygenation at 1.36 Ga and evaluation of the effect of post-depositional hydrothermal fluid flow. Precambrian Res. 298, 187–201.

Young, S.A., et al., 2020. Marine redox variability from Baltica during extinction events in the latest Ordovician–early Silurian. Palaeogeogr. Palaeoclimatol. Palaeoecol. 554.

Zhang, F., et al., 2018. Extensive marine anoxia during the terminal Ediacaran Period. Sci. Adv. 4, 1–11.

Zhang, F., et al., 2020. Two distinct episodes of marine anoxia during the PermianTriassic crisis evidenced by uranium isotopes in marine dolostones. Geochim. Cosmochim. Acta 287, 165–179.

Zheng, Y., Anderson, R.F., Alexander, V.G., Martin, Q.F., 2002a. Preservation of particulate non-lithogenic uranium in marine sediments. Geochim. Cosmochim. Acta 60, 3085–3092.

Zheng, Y., Anderson, R.F., Alexander, V.G., Martin, Q.F., 2002b. Remobilization of authigenic uranium in marine sediments by bioturbation. Geochim. Cosmochim. Acta 66, 1759–1772.

Zhou, L., et al., 2012. U/Mo ratios and δ98/95Mo as local and global redox proxies during mass extinction events. Chem. Geol. 324-325, 99–107.

Chapter 3

3. Variability of sedimentary pyrite $\delta^{34}S$ records: A case study of slope shale of the Green Point Formation in western Newfoundland, Canada

This chapter is a reformatted version of a paper that has been published in the journal Chemical Geology in 2024. Dr. Karem Azmy provided research supervision and assisted with the review and editing of the manuscript.

Li, J., Karem, A., 2024. Variability of sedimentary pyrite $\delta^{34}S$ records: A case study of slope shale of the Green Point Formation in western Newfoundland, Canada. Chem. Geol. 646, 121891. https://doi.org/10.1016/j.chemgeo.2023.121891

Abstract

The Green Point Formation in western Newfoundland, GSSP of the Cambrian-Ordovician (Є-O) boundary, is dominated by slope rhythmites of alternating lime mudstone and shale interbeds. This formation was deposited in a semi-restricted basin with varying connectivity to the open ocean. In the current study, we investigate textures and bulk $\delta^{34}S$ signatures of pyrite ($\delta^{34}S_{py}$) in the shale to better understand factors influencing the sedimentary $\delta^{34}S_{py}$ fluctuation. Petrographic and SEM examinations reveal two major types of pyrite: (1) framboidal pyrite and (2) anhedral to euhedral pyrite. The latter is further categorized into two subtypes: type 2a anhedral to subhedral pyrite characterized by relict framboidal textures and larger sizes (~10 to 300 μm), and type 2b smaller (typically <10 μm) subhedral to euhedral pyrite. Type 1 pyrite was precipitated near the sediment-water interface (SWI), whereas type 2b pyrite was formed in sediments below the SWI with limited access to the overlying seawater sulfate. Type 2a pyrite was evolved from framboids during early and burial diagenesis. The bulk $\delta^{34}S_{py}$ values, marked by a significant scatter ($1\sigma = 10.62‰$), range broadly from −17.6 to +22.4‰ (VCDT) and exhibit a pronounced positive excursion of ~20‰ near the Є-O boundary. The abundance of type 2b pyrite generally mimics changes in the $\delta^{34}S_{py}$, suggesting that the substantial $\delta^{34}S_{py}$ dispersion could be partially attributed to differing proportions of type 2b pyrite within the samples. Moreover, notable negative correlations exist between the $\delta^{34}S_{py}$ values and the abundances of Al, Th, ∑REE, and Fe, indicating that riverine fluxes might have influenced the $\Delta^{34}S_{seawater-pyrite}$ by modulating the regional seawater sulfate and iron reservoir sizes. Therefore, rather than being indicative of oceanic redox oscillations, the positive $\delta^{34}S_{py}$ excursion of ~20‰ of this interval was probably driven by decreased sulfate and iron levels in the local waterbody. The decline in terrestrial input during this $\delta^{34}S_{py}$ shift might have also contributed to a negative $\delta^{13}C_{carb}$

excursion by reducing nutrient supply and inhibiting primary productivity. Collectively, the bulk sedimentary $\delta^{34}S_{py}$ variability recorded by the Green Point shale may be attributed to a combination of changes in regional terrigenous input and varying quantities of pyrite formed at different diagenetic stages. The general opposing trends between the $\delta^{34}S_{py}$ signals and the abundances of Al, Th, ∑REE, and Fe, however, imply that fluctuations in riverine influxes might have exerted a stronger influence on the overall $\delta^{34}S_{py}$ trend. These findings suggest that bulk sedimentary $\delta^{34}S_{py}$ variations alone may not be reliable evidence for perturbations of the global sulfur cycle.

3.1. Introduction

Sedimentary biological pyrite sulfur isotope ratios ($\delta^{34}S_{py}$) have been extensively employed to study ancient oceanic and basinal sulfur cycles (e.g., Paytan et al., 2004; Hurtgen et al., 2005, 2009; Thompson and Kah, 2012; Song et al., 2014; Algeo et al., 2015; Fike et al., 2015; Kah et al., 2016; Shi et al., 2018; Stebbins et al., 2019a; Thomazo et al., 2019). Variations in bulk sedimentary $\delta^{34}S_{py}$ signatures have been plausibly linked to oceanic sulfur cycle perturbations (e.g., Hurtgen et al., 2009; Gill et al., 2011; Halevy et al., 2012; Algeo et al., 2015; Sim et al., 2015; Schobben et al., 2017; Stebbins et al., 2019a,b; Young et al., 2020) or basin isolation effect (Gomes and Hurtgen, 2013; Kurzweil et al., 2015; Paiste et al., 2020). Sedimentary $\delta^{34}S_{py}$ signals, however, can also be influenced by the connectivity between porewater and the overlying water column affected by sedimentation rate (e.g., Hartmann and Nielsen, 1968; Goldhaber and Kaplan, 1980; Maynard, 1980; Wijsman et al., 2001; Pasquier et al., 2017, 2021; Liu et al., 2019; Richardson et al., 2019a), organic matter rain rate (e.g., Wijsman et al., 2001; Pasquier et al., 2021), and the position of pyrite formation relative to the sediment-water interface (SWI) (e.g., Gomes and Hurtgen, 2015; Wang et al., 2021).

Recent geological findings propose that the Green Point formation was deposited in a partially restricted basin situated in the Taconic Seaway along the eastern Laurentian margin (Li et al., 2022; White and Waldron, 2022). This study aims to unravel how the influences noted above, combined with the potential impact of changing sulfate levels in a semi-restricted basin (e.g., Algeo et al., 2015; Gomes and Hurtgen, 2013, 2015; Kurzweil et al., 2015; Paiste et al., 2020), shape the bulk $\delta^{34}S_{py}$ variability in the Green Point shale. Additionally, within the investigated interval, the lime mudstone records a pronounced negative $\delta^{13}C_{carb}$ excursion of ~6.0‰ near the Є-O boundary, which has been attributed to decreased primary productivity (Azmy et al., 2014). However, the specific factor contributing to this decline in primary productivity has not been well understood. Considering that paired changes in global/local sulfur and carbon cycles have been documented in numerous studies (e.g., Gill et al., 2011, 2021; Dahl et al., 2014; Edwards et al., 2018; Young et al., 2020; LeRoy et al., 2021), we also seek to provide a possible explanation for this negative $\delta^{13}C_{carb}$ shift.

3.1.1. Geochemistry of sulfur in oceans

Sulfur exists in modern oceans primarily as dissolved sulfate with an average concentration of ~28 mM (Millero, 2013). The modern seawater sulfate has a homogenous $\delta^{34}S$ value of ~+21‰ and a long residence time of ~20 Myr (Paytan and Kastner, 1998) relative to the ocean mixing time of ~1kyr (Sarmiento and Gruber, 2006). River runoff has been regarded as the major source of oceanic sulfate, which is influenced by oxidative weathering of continental sulfides closely linked to atmospheric oxygen levels (Cameron, 1982; Habicht et al., 2002; Canfield, 2004; Kah et al., 2004; Hurtgen et al., 2005; Canfield and Farquhar, 2009; Williford et al., 2009; Scott et al., 2014; Burke et al., 2018). Seawater sulfate can precipitate as sulfate minerals (e.g., gypsum, anhydrite, and barite) or be incorporated into the carbonate lattice as carbonate-associated sulfate (CAS) without significant S-isotope fractionations (Thode and Monster, 1965; Takano, 1985; Raab and Spiro, 1991; Staudt et al., 1994; Kampschulte and Strauss, 2004; Barkan et al., 2020; Toyama et al., 2020). Therefore, marine sulfate evaporite and carbonate phases have been extensively utilized to estimate ancient seawater $\delta^{34}S$ (Claypool et al., 1980; Paytan and Kastner, 1998; Kah et al., 2004; Kampschulte and Strauss, 2004; Paytan et al., 2004; Mazumdar and Strauss, 2006; Gill et al., 2008; Rennie et al., 2018; Toyama et al., 2020). However, the $\delta^{34}S$ of CAS in bulk carbonates, such as limestone, is susceptible to diagenesis (e.g., meteoric, early, and burial digenesis) and can be influenced by depositional environments (e.g., Rennie and Turchyn, 2014; Present et al., 2015, 2019; Richardson et al., 2019a, b, 2021; Toyama et al., 2020). Moreover, CAS is susceptible to contamination by sulfate derived from pyrite oxidation during laboratory extractions (e.g., Edwards et al., 2019). As a result, caution must be taken when using $\delta^{34}S_{CAS}$ as a proxy for the S-isotopic composition of ancient seawater.

3.1.2 Microbial sulfate reduction and the sulfur isotope fractionation between seawater sulfate and biological pyrite

At the other side of the redox spectrum, seawater sulfate can be reduced to hydrogen sulfide (H_2S) by dissimilatory microbial sulfate reduction (MSR) in the water column or within sedimentary porewater at low temperatures (~0 to 60°C, Hoefs, 2009; Misra, 2012). The ^{32}S-O bond during this process is preferentially split by microorganisms because of its lower bonding energy, resulting in the enrichment of ^{32}S in the resultant H_2S (Faure and Mensing, 2005; Mazumdar and Strauss, 2006; Misra, 2012; Marin-Carbonne et al., 2014). H_2S can then react with aqueous iron to form sulfide minerals (primarily pyrite) without significant S-isotope fractionations (Wilkin and Barnes, 1996; Gomes and Hurtgen, 2015). In modern oceans, however, a significant fraction (~90%) of the H_2S produced by MSR is reoxidized to sulfate or intermediate sulfur species prior to sequestration as pyrite (Canfield and Thamdrup, 1994; Diaz et al., 2012; Pellerin et al., 2015; Jørgensen et al., 2019). The sulfur isotope fractionation associated with this process can vary substantially and depends on somewhat whether the reaction is abiotically or biologically catalyzed (Fry et al., 1988; Zerkle et al., 2009).

MSR usually depletes the ^{34}S isotope in the resultant H_2S by ~2 to 70‰ relative to the starting SO_4^{2-} (Canfield, 2001b; Detmers et al., 2001; Habicht et al., 2005; Canfield et al., 2010; Sim et al., 2011a). This kinetic S-isotope fractionation by MSR (ε_{SR}) is influenced by several factors, including the type and abundance of electron donors (Canfield, 2001a,b; Detmers et al., 2001; Sim et al., 2011b), sulfate-reducing species (Canfield, 2001b; Detmers et al., 2001), cell-specific sulfate reduction rate (Canfield, 2001b; Wijsman et al., 2001; Leavitt et al., 2013), temperature (Canfield, 2001a,b; Canfield et al., 2006), concentration of aqueous sulfate (Canfield, 2001a,b; Habicht et al., 2002, 2005; Gomes and Hurtgen, 2013, 2015; Algeo et al., 2015; Sim et al., 2015; Young et al., 2019), and reversibility of the multi-step intracellular pathway (Wing and Halevy, 2014; Wenk et al., 2017). Among these factors, sulfate availability has been considered to be the first-order control on ε_{SR} (Kah et al., 2004; Canfield et al., 2010; Algeo et al., 2015). Studies on natural populations of sulfate reducers suggest that the ε_{SR} is significantly suppressed at $[SO_4^{2-}]_{aq} < \sim 2–5$ mM and becomes negligible at $[SO_4^{2-}]_{aq} < 200–300$ μM (Canfield, 2001a,b; Habicht et al., 2002, 2005; Gomes and Hurtgen, 2013, 2015). The subdued S-isotope fractionation at low sulfate concentrations is explained by limited exchanges of sulfate across the bacterial cell membrane (Canfield, 2001a,b; Habicht et al., 2002, 2005) or Rayleigh distillation (Wijsman et al., 2001; Jørgensen et al., 2004; Williford et al., 2009; Siedenberg et al., 2018).

The S-isotope fractionation by MSR in the geological record is not directly measurable, and it is therefore usually inferred from $\Delta^{34}S$ (e.g., Gomes and Hurtgen, 2015; Algeo et al., 2015):

$$\Delta^{34}S = \delta^{34}S_{SW} - \delta^{34}S_{py}$$

where the $\delta^{34}S_{SW}$ refers to seawater $\delta^{34}S$ which is commonly proxied by marine sulfate evaporite or carbonate phases. The $\delta^{34}S_{py}$ denotes sedimentary pyrite $\delta^{34}S$. The $\Delta^{34}S$ should be close to or equal to $\mathcal{E}_{SR}$ only if the pyrite is formed in an open system where the SO_4^{2-} consumed by MSR is rapidly replenished (Gilleaudeau and Kah, 2015; Gomes and Hurtgen, 2015). On the other hand, the $\Delta^{34}S$ becomes lower than $\mathcal{E}_{SR}$ when pyrite is formed in a system where the SO_4^{2-} consumption is faster than its replenishment (Kampschulte and Strauss, 2004; Ono et al., 2006; Johnston et al., 2008; Kurzweil et al., 2015; Gomes and Hurtgen, 2015; Gomes and Johnston, 2017). The $\Delta^{34}S$ could also technically be larger than $\mathcal{E}_{SR}$ if the $\delta^{34}S_{SW}$ is proxied by carbonates recrystallized in closed-system conditions with limited access to the overlying seawater sulfate (Rennie and Turchyn, 2014; Murray et al., 2020; Bryant et al., 2022). Moreover, under conditions where sulfate availability is extremely restricted, the $\delta^{34}S_{py}$ may evolve to values similar to or even higher than the original sulfate source as a result of Rayleigh distillation (Wijsman et al., 2001; Williford et al., 2009; Gomes and Hurtgen, 2013; Gilleaudeau and Kah, 2015; Fike et al., 2015; Siedenberg et al., 2018; Luo et al., 2018; Raven et al., 2019).

3.2. Geological background

The Green Point Formation in western Newfoundland (Figure 3.1), part of the Humber Arm Allochthon in the northeast Canadian Appalachians, contains the Global Stratotype Section and Point (GSSP) for the Є-O boundary (James and Stevens, 1986; Waldron et al., 1998; Cooper et al., 2001). This formation was deposited at the foot of a bypass slope in a low latitudinal area

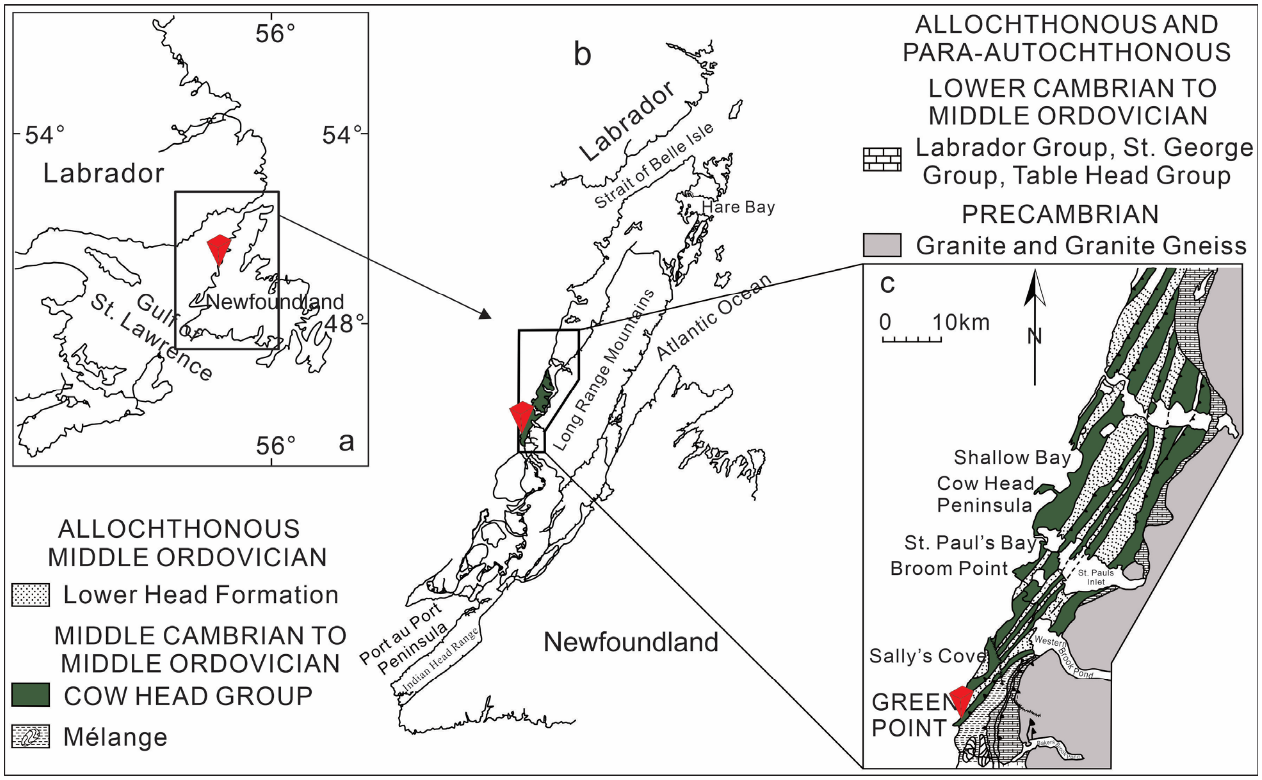

Figure 3.1: (a) and (b) Location of the Green Point Formation (marked by inverted pyramids) of the Cow Head Group in western Newfoundland, Canada. (c) Geology of western Newfoundland. Modified from Cooper et al. (2001).

(~30˚S, Figure 3.**2**) within the Taconic Seaway, which represents a retroarc basin separating the eastern Laurentian margin from a series of off-margin microcontinents (Jansa, 1974; James and Stevens, 1986; White and Waldron, 2022). From the Early Ordovician to the Early Devonian, the Laurentian margin was transformed into a convergent continental margin, and the Green Point Formation was deformed and transported westward to the present position by several tectonic events, including the Taconic, Salinian, and Acadian orogenies (Jacobi, 1981; Knight et al., 1991; Waldron et al., 1998; van der Velden et al., 2004). However, a recent study suggests that the transformation from a passive to a convergent continental margin may date back to the latest Cambrian (White and Waldron, 2022).

The lithostratigraphy of the Green Point Formation has been studied and discussed in detail by James and Stevens (1986). This formation consists of three conformably contacted

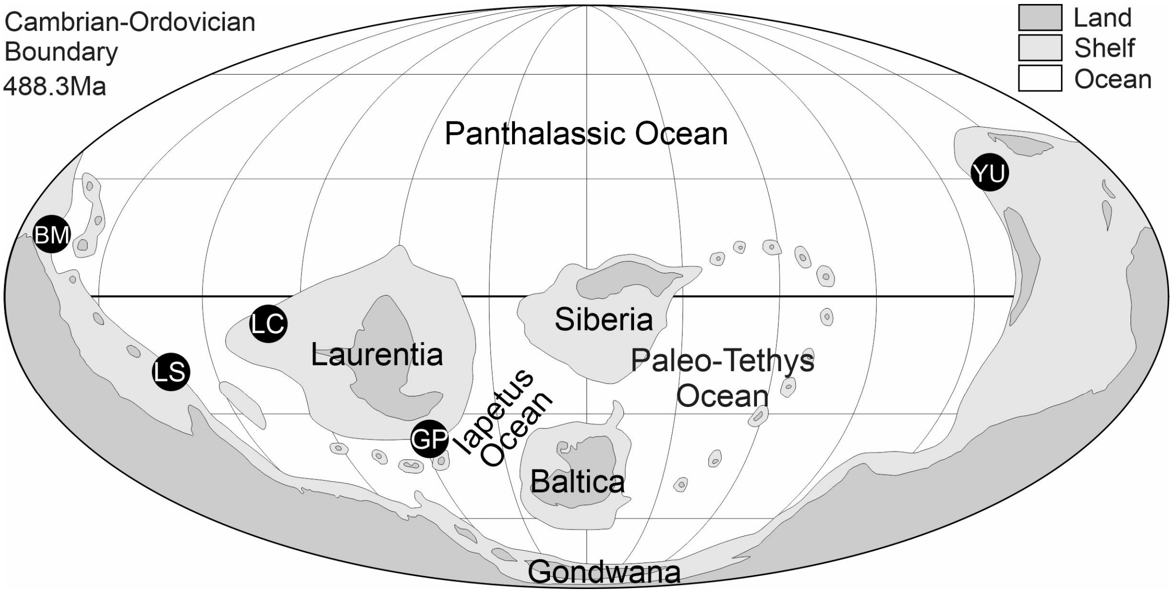

Figure 3.2: The paleogeographic reconstruction at the Cambrian-Ordovician boundary (~488.3Ma, modified from Scotese (2014)) showing locations of the Green Point Formation (GP) in western Newfoundland (Azmy et al., 2014), the Lawson Cove section (LC) in Utah, USA (Miller et al., 2011), the La Silla Formation (LS) in Argentina (Buggisch et al., 2003), the Black Mountain section (BM) in Australia (Ripperdan et al., 1992), and the Yeongweol Unit (YU) in South Korea (Hong et al., 2011).

members: the Martin Point Member (basal), the Broom Point Member (middle), and the St. Pauls Member (upper). These members are dominated by shale, siltstone, and ribbon to parted limestone, with minor conglomerate layers. The basal Martin Point Member, a 100−150 m-thick late Cambrian succession, is composed of green, gray, and black shale with minor thin conglomerate beds and a few layers of thin siltstone, fine-grained calcareous sandstone, and ribbon to parted limestone. The early Tremadocian Broom Point Member consists of ~80 m-thick deposits of ribbon to parted lime mudstone with thin green, gray, black shale, and sporadic conglomerate layers.

The sampled interval spans the upper part of the Martin Point Member and the lower part of the Broom Point Member (Figure 3.**3** and Figure 3.**4**). The shale and siltstone are hemipelagites deposited by gravity flows, while the ribbon to parted limestone was formed primarily by pelagic fallout (James and Stevens, 1986; Coniglio and James, 1990). The conglomerate formed as collapse deposits generated from rapid buildup, subaerial erosion, or large storm waves affecting the adjacent margin of the carbonate platform (James and Stevens, 1986). The sampled interval was deposited under dysoxic to anoxic conditions as supported by shale Re/Mo values between ~0.93 and 12.17 ($\times 10^{-3}$) and carbonate Ce/Ce* values between 0.8 and 1.0 (Azmy et al., 2014; Tripathy et al., 2014). These shale deposits are potential oil source rock composed mainly of type I/II organic matter. They have undergone mild thermal alteration with vitrinite reflectance (Ro) values, inferred from T_{max} values, ranging between ~0.7 and 0.8% (Schwangler et al., 2020 and references therein) and an average conodont color alteration index value of ~1.5 (Weaver and Macko 1988; Cooper et al., 2001). The conodont biozones of this interval consist of, in ascending order, the *Cordylodus proavus* Zone, the *Cordylodus caboti* Zone, the *Cordylodus intermedius* Zone, the *Iapetognathus fluctivagus* Zone, the *Cordylodus angulatus* Zone, and the *Rossodus manitouensis* Zone (Barnes, 1988; Cooper et al., 2001; Zhang and Barnes, 2004; Terfelt et al., 2014). The First Appearance Datum of the *Iapetognathus fluctivagus* Zone, the marker (Golden Spike) of the Є-O boundary in the GSSP section at Green Point, is identified within Bed 23 at the bottom of the Broom Point Member (Cooper et al., 2001).

3.3. Methodology

3.3.1. Pyrite texture

Eighteen samples (Table 3.1) were cut into polished thin sections, which were examined using a Zeiss Axioscope 5 microscope under reflected light and an FEI MLA 650FEG scanning electron microscope at Memorial University of Newfoundland to study pyrite textures. Images of pyrite taken by the SEM and optical microscope are available in Appendix 3.1.

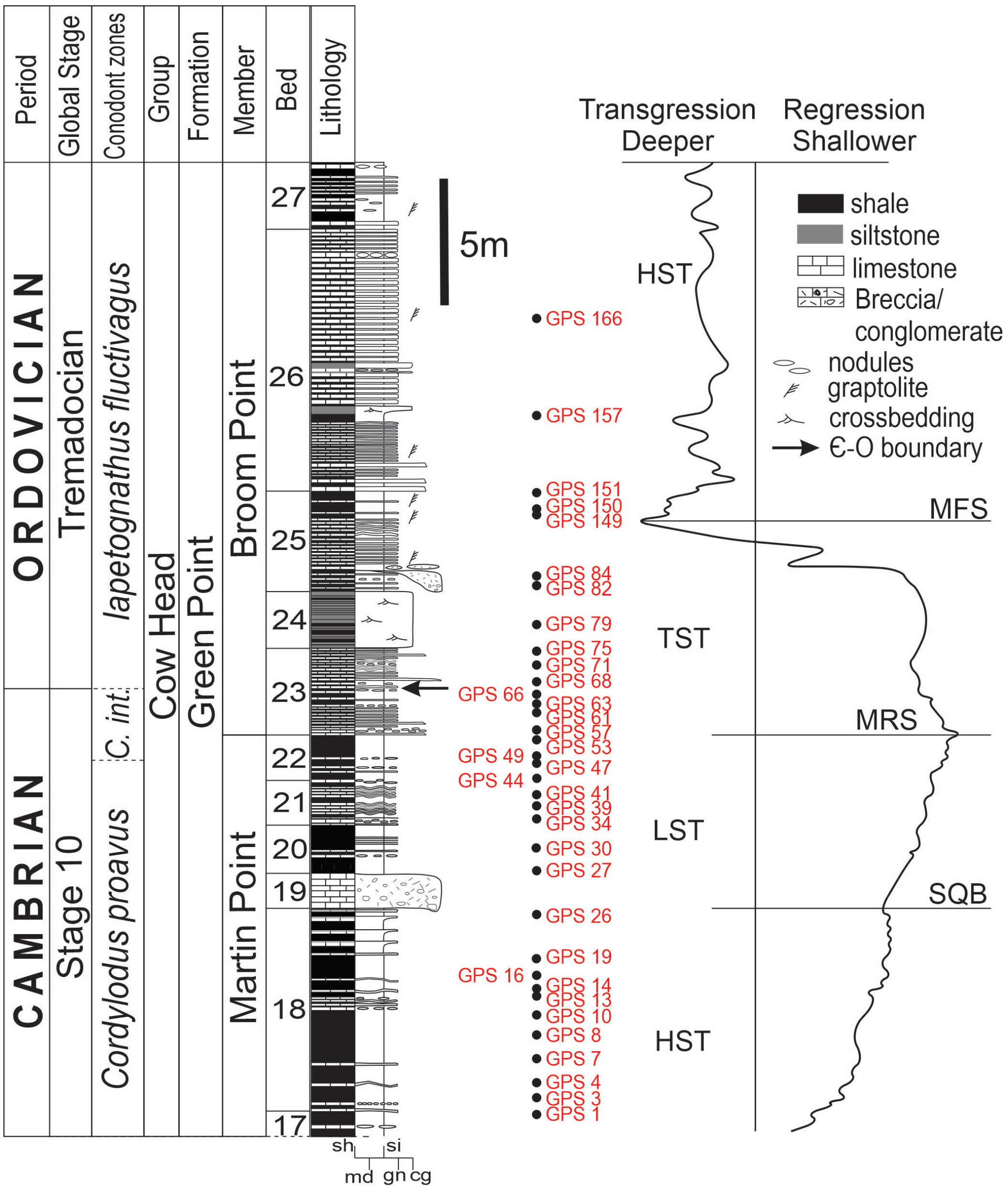

Figure 3.3: Sampling positions and the stratigraphic column of the Cambrian-Ordovician GSSP boundary section at Green Point in western Newfoundland. Abbreviations used in the reconstructed sea-level variation: HST: high stand systems tract, LST: low stand systems tract, TST: transgressive systems tract, MRS: maximum regressive surface, MFS: maximum flooding surface, and SQB: sequence boundary. Following Azmy et al. (2015) and Bisnaire (2018).

3.3.2. Pyrite sulfur isotopes

Thirty-five shale samples (Table 3.**2**, Figure 3.**3**) were collected from the Green Point Formation (Є-O GSSP boundary section, 49° 40′ 51″ N; 57° 57′ 36″ W) at Green Point, western Newfoundland, Canada (Figure 3.1). Shale of the GSSP interval at Green Point is absence of metamorphism and strong diagenesis (James and Stevens, 1986; Cooper et al., 2001). To obtain the best-preserved pyrite sulfur isotope signals, shale with weathered materials and visible diagenetic features was avoided during field sampling. Samples were washed with de-ionized water and dried overnight. Approximately 9g of each sample was powdered and homogenized using a mechanical mill.

Pyrite was extracted from the shale as chromium-reducible sulfur (CRS) using the chromium reduction method modified from Canfield et al. (1986). Measurements of pyrite sulfur abundance and isotopic compositions were performed at Washington University in St. Louis, USA. Each powdered sample (~0.2 to 0.5 g) was reacted with 6 M HCl, followed by a reaction with $CrCl_2$ at ~186 °C under constant stirring for 4 hours in a nitrogen atmosphere to liberate pyrite sulfur. The evolved gas was passed through a water trap before being trapped as Ag_2S in a test tube containing $AgNO_3$ solution in de-ionized water. The Ag_2S was then weighed after being rinsed and dried. The pyrite sulfur content (wt%) was calculated from the Ag_2S precipitate relative to the initial mass utilized for the extraction. For sulfur isotope analyses, ~350 μg Ag_2S of each sample was measured as SO_2 via combustion using a Costech ECS 4010 Elemental Analyzer coupled to a Delta V Plus mass-spectrometer. Sulfur isotope ratios are reported in per mil (‰) relative to the Vienna Canyon Diablo Troilite (VCDT), which is expressed as $\delta^{34}S = 1000 \cdot ({}^{34/32}S_{sample} / {}^{34/32}S_{VCDT} - 1)$.

The isotopic measurements were calibrated with international standards IAEA-S1 ($\delta^{34}S = -0.3‰$), IAEA-S3 ($\delta^{34}S = -32.55‰$), and NBS127 ($\delta^{34}S = +21.1‰$). The uncertainty of measurements based on international standards, check standards, and sample replicates (Appendix 3.2) is better than 0.7‰ (1σ).

Table 3.1: The $\delta^{34}S_{py}$ values, the relative abundances of the pyrite, and framboidal pyrite size distributions of eighteen samples in the studied interval.

Sample ID	**$\delta^{34}S_{py}$ ‰**	**Abundance of type 1 framboidal pyrite**	**Abundance of type 2 anhedral to euhedral pyrite**		**Framboid diameter/µm**
			Type 2a anhedral to subhedral	**Type 2b subhedral to euhedral**	
GPS3	-12.9	abundant	×	a few	1.0–11.4
GPS7	-15.1	abundant	a few	rare	1.2–7.9
GPS10	-3.3	abundant	×	quite a few	0.8–10.9
GPS27	-13.9	quite a few	abundant	rare	1.4–9.1
GPS39	-6.4	abundant	×	quite a few	1.2–30.2
GPS41	-2.4	abundant	×	abundant	1.1–6.9
GPS49	-17.6	abundant	rare	quite a few	1.5–7.0
GPS53	9.6	abundant	×	abundant	1.0–11.2
GPS57	11.4	abundant	×	quite a few	1.0–20.9
GPS61	1.1	abundant	a few	a few	1.2–12.9
GPS63	3.2	abundant	×	quite a few	1.1–10.4
GPS66	1.9	abundant	rare	quite a few	1.0–21.1
GPS71	7.0	abundant	rare	a few	1.2–11.8
GPS75	13.7	abundant	×	abundant	0.9–6.4
GPS79	6.1	abundant	×	abundant	1.2–12.0
GPS82	22.4	rare	×	abundant	*
GPS150	-1.3	abundant	a few	rare	0.7–9.7
GPS157	11.6	abundant	a few	abundant	0.9–10.9

Diameters of framboids and relative abundances of the pyrite are determined based on SEM and optical microscopic imaging (images are available in Appendix 3.1). Rare = very few of the pyrite type can be found (~<10%). A few = some of the pyrite type can be found but at a low percentage (~10 to 20%). Quite a few = plenty of the pyrite type can be found but its percentage (~20 to 40%) is still significantly lower than the other two types. Abundant = one of the pyrite types is significantly more abundant (>40%) than the other two types, or two of the pyrite types exhibit similar percentages (~50%). × = absent.

* The number of framboids is too small to allow an accurate determination of the range of framboid diameter.

Figure 3.4: Photo of outcrop at Green Point in western Newfoundland (49°40’58.4”N 57°57’52.6”W). The solid yellow line marks the Cambrian-Ordovician boundary defined by the first appearance of the conodont *Iapetognathus fluctivagus*, Є = Cambrian, O = Ordovician.

A portion of the homogenized powder of each shale sample had previously been analyzed to obtain the organic $\delta^{13}C_{org}$ values, K, Ca, TOC, Al, Th, ∑REE, and Fe contents (Bisnaire, 2018).

3.4. Results

Based on petrographic and SEM observations, two major morphological types of pyrite are identified: (1) framboidal pyrite, including both individual and grouped-multiple framboids, and (2) anhedral to euhedral pyrite. Framboidal pyrite grains, both as ungrouped individual framboids and those within grouped-multiple framboids, exhibit a wide size range, spanning approximately 1 to 30 μm in diameter (Table 3.1). The latter category, type 2 pyrite, is further divided into two subtypes: type 2a anhedral to subhedral pyrite with relict framboidal textures, and type 2b subhedral to euhedral pyrite lacking framboidal textures (Figure 3.**5**). Type 2a anhedral to subhedral pyrite grains are commonly large in size, ranging from 10 to 300 μm

Table 3.2: Geochemical data for the investigated interval of the Green Point Formation in western Newfoundland, Canada.

Sample ID	**Pyrite wt%**	**$\delta^{34}S_{py}$[a] ‰**	**Al wt %**	**Th μg/g**	**∑REE μg/g**	**Fe wt%**	**TOC[b] wt %**	**$\delta^{13}C_{org}$[c] ‰**	**K wt%**	**Ca wt %**
GPS1	1.3	-6.8	3.3	4.9	110.4	2.2	0.96	-29.84	2.1	13.7
GPS3	0.9	-12.9	5.8	9.3	181.6	2.6			3.8	4.2
GPS4	1.8	-10.7	5.8	8.7	134.1	2.7	4.10	-29.10	5.1	3.4
GPS7	0.4	-15.1	5.0	6.0	142.3	2.9			3.0	6.4
GPS8	0.9	-9.5	6.7	6.9	116.4	3.1	0.25	-28.46	4.2	3.2
GPS10	1.6	-3.3	7.2	7.5	90.2	2.8	1.80	-29.02	6.4	1.9
GPS13	2.1	-13.4	5.2	7.5	134.1	2.9			3.9	5.9
GPS14	1.0	-2.1	7.0	7.5	111.8	3.3	1.86	-28.79	6.2	2.7
GPS16	1.2	-1.8	7.1	5.7	135.7	3.4	0.12	-28.03	4.8	1.0
GPS19	1.6	-10.7	6.3	7.3	115.1	3.2			4.8	2.9
GPS26	1.1	-4.6	7.1	7.4	52.9	2.5	1.45	-29.10	6.8	2.3
GPS27	0.4	-13.9	7.9	10.0	90.4	4.0	0.74	-28.99	5.6	0.7
GPS30	0.1	-14.4	7.2	8.4	177.6	2.9	0.11	-27.52	4.9	1.3
GPS34	0.6	-10.7	6.6	7.4	97.8	3.3	0.17	-28.68	4.9	2.0
GPS39	0.7	-6.4	5.8	6.9	115.4	2.8	0.58	-29.05	5.3	3.0
GPS41	0.9	-2.4	5.3	6.7	135.5	2.2			5.1	8.1
GPS44	0.9	-12.0	6.8	7.3	156.8	4.0	0.12	-27.88	4.2	2.4
GPS47	1.1	-17.4	6.8	8.7	162.5	3.2			4.8	2.8
GPS49	0.9	-17.6	5.4	6.4	161.7	3.5	0.11	-27.52	3.8	4.4
GPS53	0.4	9.6	5.9	7.4	156.7	2.3	1.79	-29.86	5.6	3.2
GPS57	1.1	11.4	4.4	5.2	64.3	3.4	0.24	-29.13	2.5	4.0
GPS61	1.0	1.1	5.0	6.5	81.9	3.0	0.20	-28.82	2.7	3.7
GPS63	0.7	3.2	5.3	5.5	83.0	3.2	0.58	-29.71	3.1	2.4
GPS66	1.2	1.9	5.8	7.0	115.4	2.7			4.8	2.8
GPS68	1.1	13.9	5.1	4.8	82.2	2.6	1.04	-29.98	5.1	3.6
GPS71	1.2	7.0	6.4	6.4	79.5	2.9			6.3	2.8
GPS75	1.1	13.7	4.0	3.6	69.8	2.4	0.95	-29.80	3.3	7.8
GPS79	0.3	6.1	4.7	6.4	94.1	2.0	1.10	-29.89	3.6	7.2
GPS82	0.6	22.4	3.2	3.8	64.0	1.9	0.45	-29.40	1.8	11.8
GPS84	0.9	14.4	5.0	6.1	66.5	2.6			3.4	6.1
GPS149	0.8	12.4	5.5	5.1	78.3	2.1		-29.03	4.6	2.9
GPS150	2.5	-1.3	7.1	8.6	186.5	3.7			5.3	1.0
GPS151	1.4	3.9	4.4	4.9	129.7	2.3	2.37	-29.02	4.5	7.5
GPS157	1.7	11.6	6.1	7.3	104.8	2.7	1.24	-30.10	5.0	4.8
GPS166	1.3	2.0	5.9	8.7	122.0	2.4	8.81	-26.01	5.2	4.3

[a] The pyrite $\delta^{34/32}S$ value

[b] TOC = total organic carbon

[c] org = organic

(Figure 3.**5**c,d). In contrast, type 2b subhedral to euhedral pyrite grains are typically small, with sizes predominately falling below 10 µm. Qualitative estimates of abundances of these types of pyrite, determined by SEM and optical microscopic imaging (Appendix 3.1), are summarized in Table 3.1.

The $\delta^{34}S_{py}$ values of the Green Point shale range broadly from −17.6 to +22.4‰ and exhibit a significant scatter with a standard deviation (1σ) of 10.62‰ (Figure 3.6, Table 3.**2**). The $\delta^{34}S_{py}$ values of the Martin Point member fall between −17.6 and −1.8‰ with a mean value of −9.8 ± 10.4‰ (2σ). In contrast, the shale of the Broom Point member has more positive $\delta^{34}S_{py}$ values, which range between −1.3 and +22.4‰ and have a mean value of +8.3 ± 12.8‰ (2σ). Given the scattered nature of the $\delta^{34}S_{py}$ values, a LOWESS (Locally Weighted Scatterplot Smoothing) smoothed curve ($\alpha = 0.3$) is employed to reveal their overall trend. The curve displays a distinct positive shift of ~20‰ (from ~−10 to +10‰) from the bottom of Bed 22 to the bottom of Bed 25 before returning to less positive values at the upper part of the interval.

The pyrite abundances are generally lower than 2.0 wt%, with only two samples (GPS13 and GPS150) exceeding this threshold. Data from Bisnaire (2018) show that the abundances of Al, Th, rare earth elements (∑REE), and Fe span from 3.2 to 7.9 wt%, 3.6 to 10.0 µg/g, 52.9 to 186.5 µg/g, and 1.9 to 4.0 wt%, respectively. The TOC and organic $\delta^{13}C_{org}$ values vary between 0.1 and 8.1 wt% and −30.1 and −26.0‰, respectively. The K and Ca contents range from 1.8 to 6.8 wt% and 0.7 to 13.7 wt%, respectively. Interestingly, no significant changes in the pyrite abundance and TOC are observed during the positive $\delta^{34}S_{py}$ shift. Instead, this $\delta^{34}S_{py}$ excursion is accompanied by a decline in Fe and in terrigenous elements such as Al, Th, and ∑REE (Figure 3.6, Table 3.**2**). Moreover, there are significant negative correlations between the $\delta^{34}S_{py}$ records and the abundances of Al ($R^2 = 0.24$, $p < 0.01$, Figure 3.**7**a), Th ($R^2 = 0.40$, $p < 0.01$, Figure 3.**7**b),

∑REE ($R^2 = 0.38$, $p < 0.01$, Figure 3.7c), and Fe ($R^2 = 0.29$, $p < 0.01$, Figure 3.7d). A positive correlation is observed between the abundances of Al and Fe ($R^2 = 0.38$, $p < 0.01$, Figure 3.7e).

3.5. Discussion

3.5.1. Origin of the pyrite and evaluation of the $\delta^{34}S_{py}$ preservation

Pyrite found in sedimentary rocks can have various origins, including organic matter catagenesis (e.g., Amrani et al., 2005; Amrani, 2014; Rennie et al., 2018; Siedenberg et al., 2018), volcanic/hydrothermal activities (e.g., Williford et al., 2011; Diehl et al., 2012; Young et al., 2013; Paiste et al., 2018; Slack et al., 2019), and microbial sulfate reduction (e.g., Soliman and Goresy, 2012; Schobben et al., 2017; Blood et al., 2019; Stebbins et al., 2019a; Thomazo et al., 2019; Liao et al., 2020; Decraene et al., 2023).

In the case of pyrite formed through reaction of H_2S generated by organic matter thermal degradation with iron in porewaters, such pyrite is commonly isotopically heavier than the surrounding pyrite derived from MSR by ~10 to 20‰ (Canfield et al., 2001a; Amrani et al., 2005; Amrani, 2014; Rennie et al., 2018; Siedenberg et al., 2018). Typically, if pyrite was primarily formed through organic matter catagenesis, we would expect a positive relationship between $\delta^{34}S_{py}$ and $\delta^{13}C_{org}$ values, as organic matter catagenesis enriches the residue in ^{13}C by expelling ^{12}C-depleted hydrocarbons (Tissot and Welte, 1984; Faure and Mensing, 2005). However, when examining the Green Point shale, we find no correlations between TOC and pyrite content or $\delta^{34}S_{py}$ signals ($R^2 = 0.16$, $p > 0.05$, and 0.06, respectively, Figure 3.8a,b), and there is also no correlation between $\delta^{34}S_{py}$ values and pyrite content ($R^2 = 5\times10^{-5}$, Figure 3.8c). Notably, we observe a negative relationship between the $\delta^{34}S_{py}$ and $\delta^{13}C_{org}$ values ($R^2 = 0.47$, $p < 0.01$, Figure 3.8d). These observations suggest minimal accumulation of catagenic pyrite in the shale.

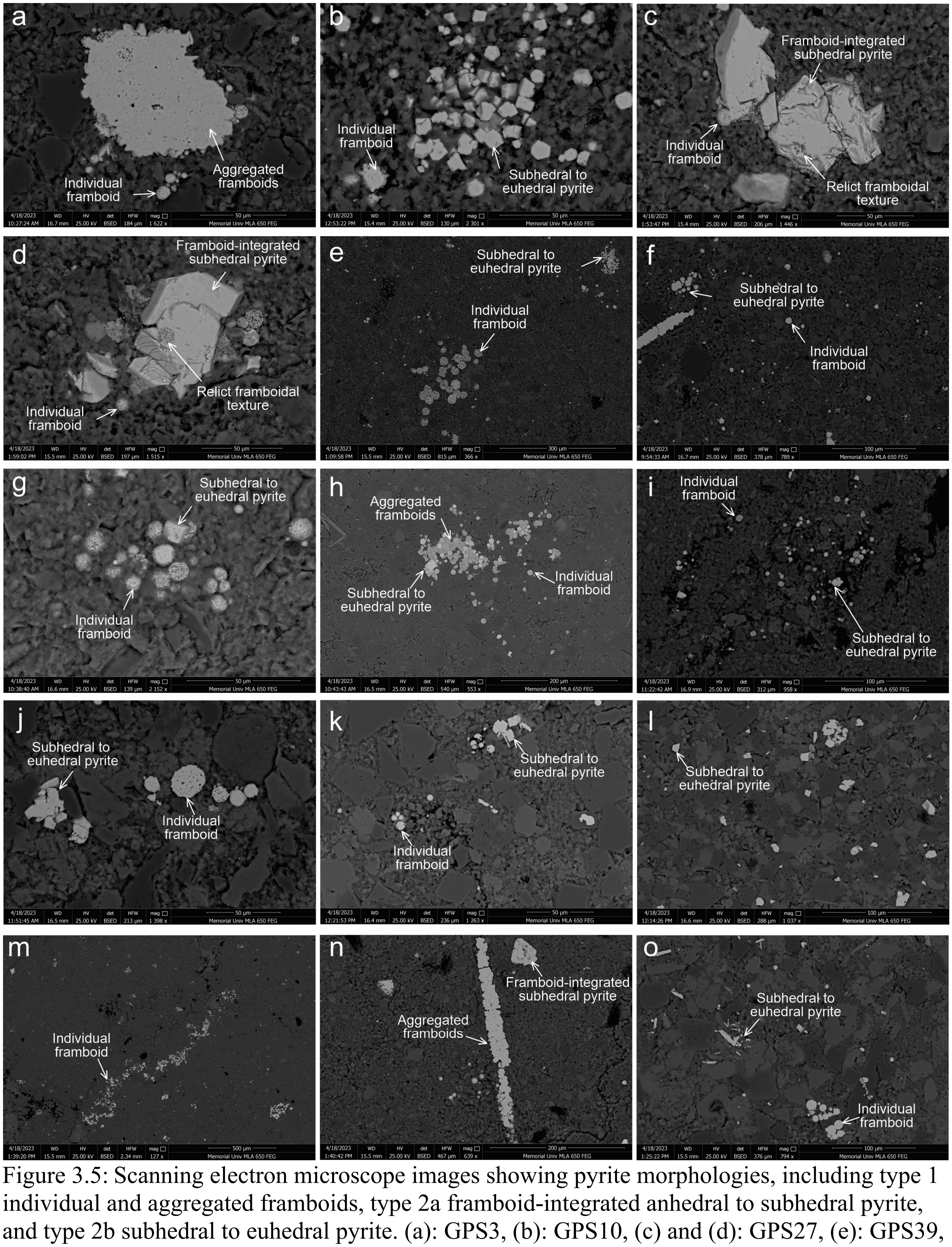

Figure 3.5: Scanning electron microscope images showing pyrite morphologies, including type 1 individual and aggregated framboids, type 2a framboid-integrated anhedral to subhedral pyrite, and type 2b subhedral to euhedral pyrite. (a): GPS3, (b): GPS10, (c) and (d): GPS27, (e): GPS39, (f): GPS41, (g) and (h): GPS49, (i): GPS57, (j): GPS61, (k): GPS79, (l): GPS82, (m) and (n): GPS150, and (o): GPS157.

Moreover, the Green Point Formation in western Newfoundland lacks hydrothermal fluid alteration products (e.g., pyrite veins, James and Stevens, 1986), and the shale exhibits low thermal maturity with R_o values below 0.8%, as inferred from T_{max} measurements (Schwangler et al., 2020). Therefore, the influence of hydrothermal alteration on the pyrite is unlikely. Taken together, these observations strongly suggest that organic matter catagenesis and hydrothermal processes have made limited contributions to pyrite in the Green Point shale, with microbial sulfate reduction likely serving as the primary source.

3.5.1.1. Origin of the pyrite

The precipitation of pyrite associated with MSR can occur in the water column under euxinic bottom-water conditions, near the sediment-water interface, and in sediments (Wijsman et al., 2001; Jørgensen et al., 2004, 2019; Gomes and Hurtgen, 2013, 2015; Fike et al., 2015). Pyrite formed in the water column is known as syngenetic pyrite, while pyrite precipitated near the SWI and in sediments is termed diagenetic pyrite. It is noteworthy that diagenetic and syngenetic pyrites differ in terms of size and morphology. Diagenetic pyrite formed in sediments is commonly subhedral to euhedral, whereas syngenetic pyrite precipitated in the water column and diagenetic pyrite formed close to the SWI are typically framboidal (Raiswell, 1982; Wilkin et al., 1996; Wilkin and Arthur, 2001; Stebbins et al., 2019a; Wang et al., 2021).

The precipitation of framboidal pyrite has been attributed to the presence of abundant reactive iron and supersaturation of both mackinawite and pyrite (Raiswell, 1982; Taylor and Macquaker, 2000). Although framboidal pyrite precipitated in both syngenetic and diagenetic settings shares the same morphology, notable differences exist in framboids' sizes. Studies on sedimentary pyrite revealed that syngenetic framboids are commonly small and exhibit limited size variation (~3–7 µm, e.g., Wilkin et al., 1996; Wignall and Newton, 1998). This size consistency has been attributed to the inherently limited duration that framboids of a certain size can remain entrained in euxinic water columns (Wilkin et al., 1996). In contrast, diagenetic framboids precipitated near the SWI tend to display a wider range of diameters, spanning from approximately one to several tens of microns due to variable growth rates and growth times (Wilkin et al., 1996; Wignall and Newton, 1998).

The formation of subhedral to euhedral pyrite has been interpreted to be the result of decreased iron availability and the supersaturation of pyrite alone in sediments (Raiswell, 1982; Taylor and Macquaker, 2000). Non-framboidal (anhedral to euhedral) pyrite grains, however, can also develop through the integration of individual framboids after their precipitation during early and burial diagenesis (Wilkin et al.,1996; Sawłowicz, 2000; Soliman and Goresy, 2012; Wei et al., 2015, 2016). According to Soliman and Goresy (2012), framboids in sediments are likely in a colloform state, allowing them to deform and adjust to compaction and the boundaries of adjacent materials. The evolution sequence, as described by Wilkin et al. (1996), Soliman and Goresy (2012), and Wei et al. (2015, 2016), typically involves the transformation of framboids into grouped multiple-framboids, infilled framboids, anhedral to subhedral pyrite mass, and ultimately euhedral pyrite. During this process, diagenetic pyrite precipitated in sediments is often incorporated into framboidal aggregates by filling interstitial spaces between framboids (Wilkin et al., 1996; Wilkin and Arthur, 2001; Soliman and Goresy, 2012). Usually, the integrated pyrite grains retain relict framboidal textures and often achieve larger sizes relative to individual framboids (Wilkin et al.,1996; Soliman and Goresy, 2012; Wei et al., 2016; Zou et al., 2018).

In the Green Point Shale, all thin-sectioned samples contain both framboidal (type 1) and non-framboidal (type 2a and 2b) pyrite. The framboids have broad size distributions from ~1 to 30 μm (Table 3.1). Although occasional underestimations of framboids' diameters may occur due to imperfect halving, research by Cashman and Ferry (1988), Wilkin et al. (1996), Tian et al. (2014), and Wei et al. (2016) consistently reports deviations from actual sizes to be generally ≤ 10%. The broad size distributions of framboids, together with non-euxinic bottom conditions indicated by wide ranges of the authigenic δ^{98}Mo values and depletions of Mo, U, and Re compared to Phanerozoic euxinic shales (Tripathy et al., 2014; Li et al., 2022), suggest that framboids in the Green Point shale were precipitated near the SWI with free diffusive connection to the overlying seawater.

The non-framboidal pyrite, as mentioned above, is categorized into two types: type 2a and 2b pyrite. The presence of relict framboidal textures and large sizes of type 2a pyrite (Figure 3.**5**c,d) suggest that it was probably formed through the integration of framboids during early and burial diagenesis (e.g., Soliman and Goresy, 2012; Wei et al., 2016; Zou et al., 2018; Wang et al., 2021). In contrast, because of the absence of framboidal textures, its smaller size, and subhedral to euhedral morphology, type 2b pyrite is interpreted to be precipitated in sediments with limited access to overlying seawater sulfate (e.g., Raiswell, 1982; Stebbins et al., 2019a; Wang et al., 2021).

3.5.1.2. Preservation of the $\delta^{34}S_{py}$ signals

Burial diagenesis of mudstone commonly leads to the enrichment of K and depletion of Ca due to illitization and calcite dissolution, respectively (Wintsch and Kvale, 1994). Three clay-mineral suites, including the illite-14A chlorite, the illite-expandable chlorite, and the corrensite-illite-smectite suites, have been recognized in the Green Point shale (Suchecki et al., 1977). However, the shale shows poor correlations of the K/Ca ratios with the pyrite abundance and δ^{34}S values ($R^2 = 6\times10^{-5}$ and 0.08, respectively, Figure 3.8e,f), arguing against substantial impact of burial diagenesis on the $\delta^{34}S_{py}$ records. Furthermore, a geologically reasonable Re-Os age of

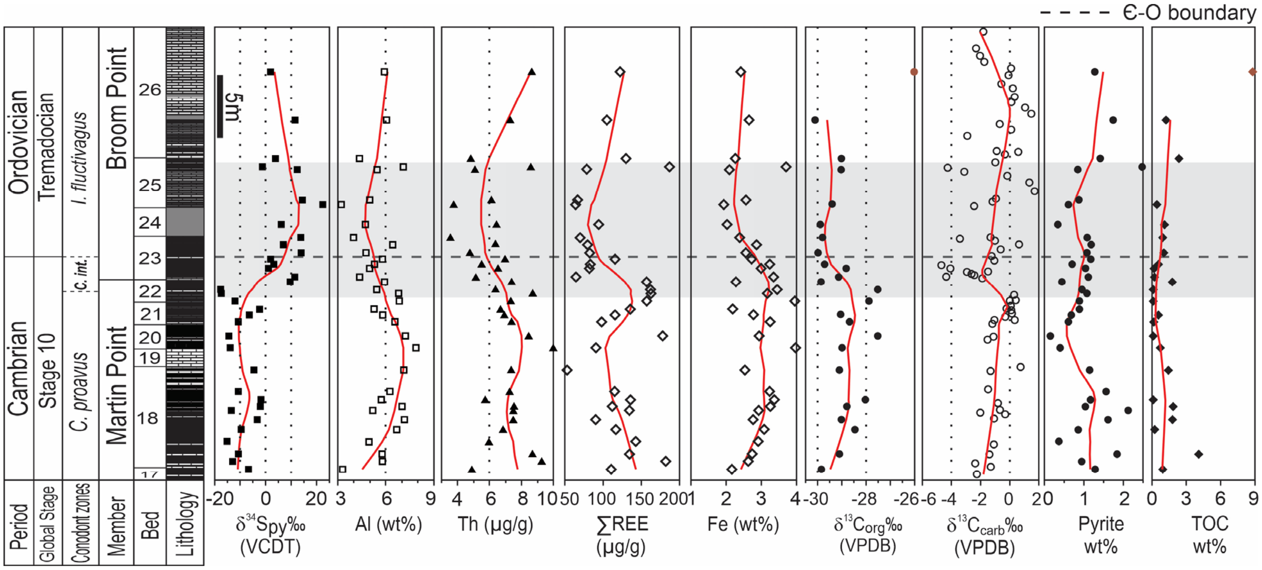

Figure 3.6: Geochemical and stratigraphic profiles across the Cambrian-Ordovician GSSP boundary of the Green Point Formation (modified from Cooper et al., 2001; Azmy et al., 2014). The dashed horizontal black line marks the level of the Cambrian-Ordovician biostratigraphic boundary (Cooper et al., 2001). The $\delta^{13}C_{org}$ and TOC outliers are plotted as brown symbols, Bisnaire (2018) suggests that the outliers might be linked to potential bituminization of the sample. The red lines represent LOWESS smoothed (α = 0.3) curves.

484 ± 16 Ma obtained from the Green Point shale supports minimum disturbance by weathering and postdepositional diagenesis (Tripathy et al., 2014). These observations, along with the absence of hydrothermal influence in the study area and the shale's low thermal maturity suggest that the $\delta^{34}S$ values represent at least near-primary signatures of pyrite originated from microbial sulfate reduction during early diagenesis.

3.5.2. Interpretation of the $\delta^{34}S_{py}$ records

The bulk $\delta^{34}S_{py}$ signals in the Green Point shale are characterized by a significant scatter ($1\sigma = 10.62‰$) and display a notable positive shift near the Є-O boundary (Figure 3.6). The observed positive $\delta^{34}S_{py}$ excursion may have several potential contributing factors. One possible explanation is the enhanced pyrite burial linked to expanded marine anoxia (e.g., Hurtgen et al., 2009; Gill et al., 2011; Stebbins et al., 2019b; Young et al., 2020). However, there is no significant perturbation in the global C cycle and marine redox conditions observed across the Є-

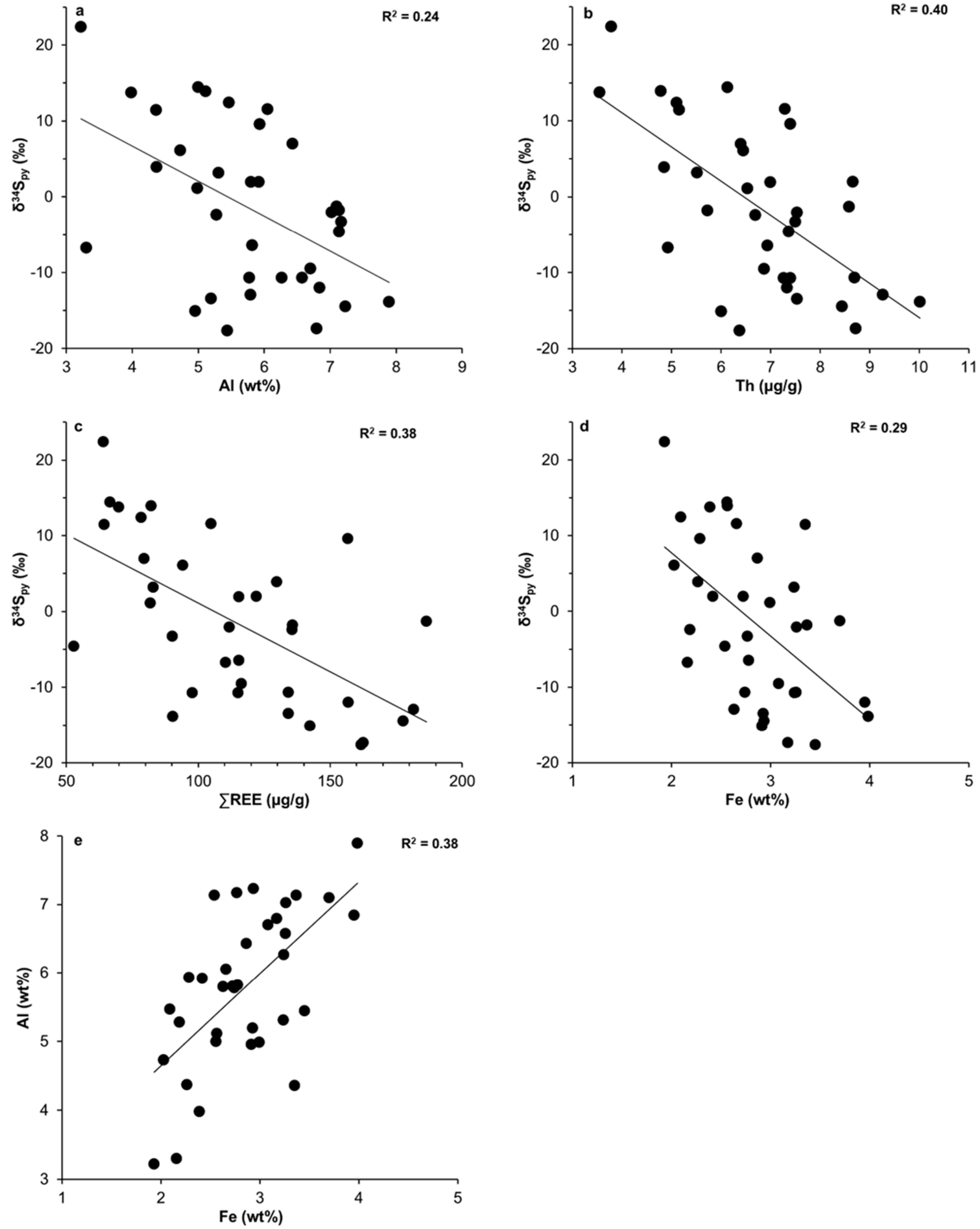

Figure 3.7: Crossplots of (a) $\delta^{34}S_{py}$ vs. [Al], $R^2 = 0.24$, $p < 0.01$; (b) $\delta^{34}S_{py}$ vs. [Th], $R^2 = 0.40$, $p < 0.01$; (c) $\delta^{34}S_{py}$ vs. ∑REE, $R^2 = 0.38$, $p < 0.01$; (d) $\delta^{34}S_{py}$ vs. [Fe], $R^2 = 0.29$, $p < 0.01$; and (e) [Al] vs [Fe], $R^2 = 0.38$, $p < 0.01$. Black solid lines are regression lines.

O transition (e.g., Saltzman et al., 2015; Rasmussen et al., 2019; Goldberg et al., 2021), suggesting that oceanic redox oscillations may not be the cause of the $\delta^{34}S_{py}$ variability.

Alternatively, this excursion could be driven by an increased sedimentation rate or elevated organic matter rain rate, both of which promote the development of more restricted sedimentary porewater conditions and the precipitation of ^{34}S-enriched pyrite (e.g., Pasquier et al., 2017; Liu et al., 2019). Nonetheless, the Green Point shale, interpreted as hemipelagites (James and Stevens, 1986), shows a decline in terrigenous elements (Al, Th, and ∑REE) during the $\delta^{34}S_{py}$ shift (Figure 3.6), challenging the scenario of an increased sedimentation rate. The absence of a noticeable increase in TOC as well as the pyrite abundance throughout the $\delta^{34}S_{py}$ excursion (Figure 3.6), coupled with the decrease in terrestrial input, also argues against the hypothesis of an elevated organic matter loading rate. Additionally, if the scatter of $\delta^{34}S_{py}$ was driven by fluctuations in sedimentation rate or organic matter rain rate, one would expect positive correlations with TOC or the abundances of terrigenous elements. However, the absence of the anticipated correlations (Figure 3.7a-c and Figure 3.8b) suggests that changes in sedimentation and organic matter rain rates may not explain the considerable scatter of $\delta^{34}S_{py}$.

The possibilities of fluctuations in marine redox conditions, sedimentation rate, organic matter loading rate appear less likely as the primary drivers of the $\delta^{34}S_{py}$ variability. Therefore, our investigation turns to discerning the impact of the pyrite formation stage and the water chemistry of this semi-restricted basin, including sulfate and Fe levels, on the observed variability.

3.5.2.1. Influence of biological pyrite formation stage on the $\delta^{34}S_{py}$ variation

The morphology of biological pyrite, as discussed above, is influenced by the diagenetic stage of pyrite formation (e.g., Raiswell, 1982; Taylor and Macquaker, 2000; Stebbins et al.,

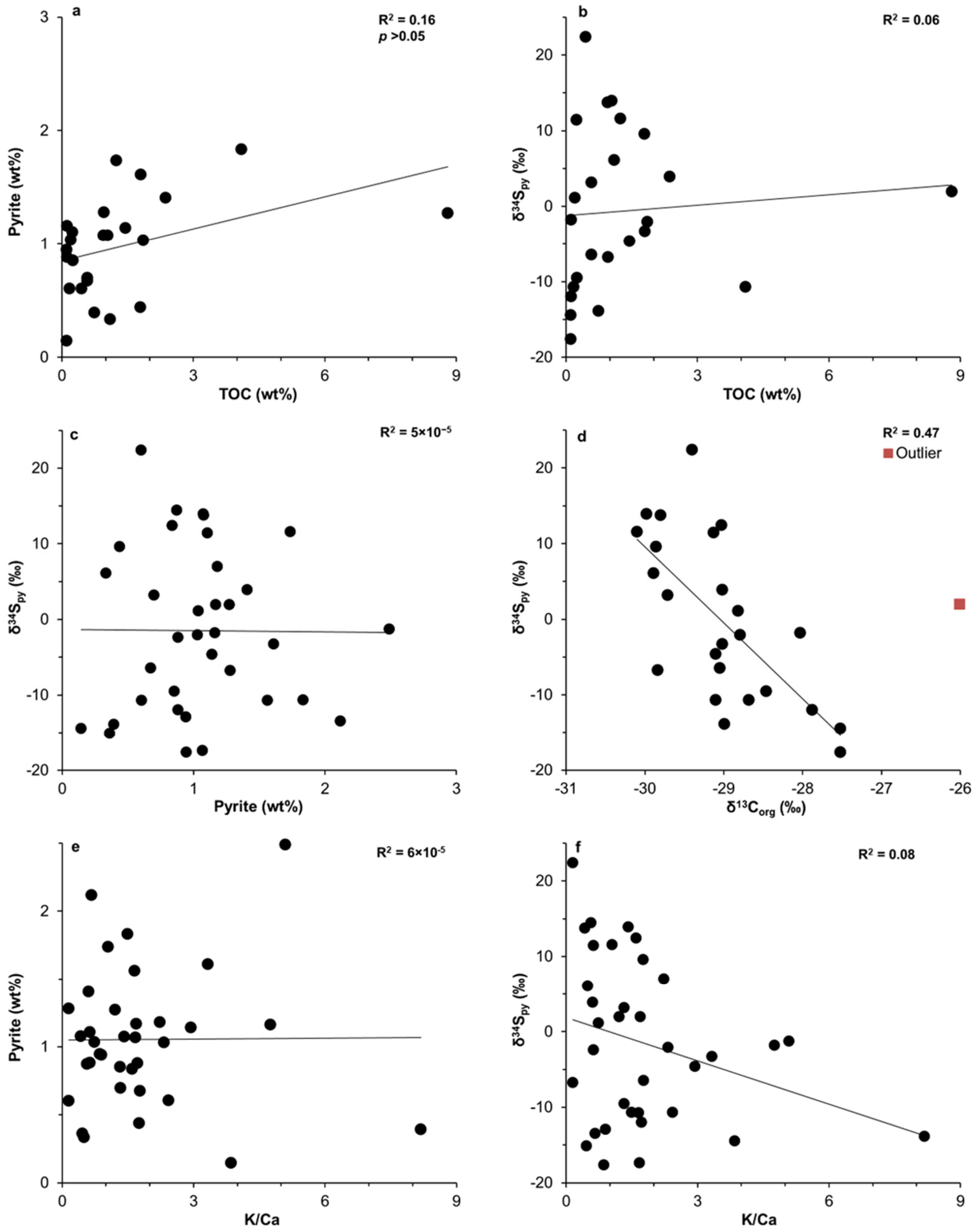

Figure 3.8: Scatter diagrams of (a) pyrite vs. TOC, $R^2 = 0.16$, $p > 0.05$; (b) $\delta^{34}S_{py}$ vs. TOC, $R^2 = 0.06$; (c) $\delta^{34}S_{py}$ vs. pyrite, $R^2 = 5\times10^{-5}$; (d): $\delta^{34}S_{py}$ vs. $\delta^{13}C_{org}$, $R^2 = 0.47$, $p < 0.01$ (excluding an outlier GPS166); (e) pyrite vs. K/Ca, $R^2 = 6\times10^{-5}$; and (f) $\delta^{34}S_{py}$ vs. K/Ca, $R^2 = 0.08$. Black solid lines are regression lines.

2019a; Wang et al., 2021), which, in turn, may affect the pyrite $\delta^{34}S$ signatures (e.g., Gomes and Hurtgen, 2015; Jørgensen et al., 2019; Raven et al., 2019). Precisely, in a particular sedimentary layer, framboidal syngenetic pyrite is expected to be less enriched in ^{34}S relative to diagenetic pyrite because the latter is formed under more confined conditions with slower sulfate renewal rates (e.g., Gomes and Hurtgen, 2015; Shawar et al., 2018; Raven et al., 2019; Wang et al., 2021). Moreover, subhedral to euhedral pyrite precipitated in sediments tends to be more enriched in ^{34}S than framboids formed near the SWI due to increased sulfate limitation (e.g., Stebbins et al., 2019a; Bryant et al., 2020; Wang et al., 2021). Although both type 1 framboidal pyrite and type 2a framboid-integrated pyrite in the shale may incorporate portions of interstitial pyrite precipitated in sediments with potentially higher $\delta^{34}S$ signatures (e.g., Wilkin et al., 1996; Wilkin and Arthur, 2001; Soliman and Goresy, 2012; Bryant et al., 2020), in each sample, type 2b subhedral to euhedral pyrite is expected to have a higher enrichment in ^{34}S as it was entirely precipitated in sediments with much slower sulfate renewal rates (e.g., Wang et al., 2021).

Since most of the samples contain abundant type 1 or 2a pyrite but with variable amounts of type 2b pyrite (Table 3.1), we would expect to see a potential correlation between the abundance of type 2b pyrite and the $\delta^{34}S$ values in our samples. In line with this hypothesis, the abundance of type 2b pyrite generally mimics the $\delta^{34}S_{py}$ variability, with only minor divergences (Figure 3.9). As a result, we propose that the significant $\delta^{34}S_{py}$ variability and the distinct $\delta^{34}S_{py}$ excursion may, at least in part, be attributed to the mixed signals of pyrite formed at different stages during early diagenesis.

3.5.2.2. Influence of terrestrial sulfate and iron inputs on the $\delta^{34}S_{py}$ variability

While a general parallel behavior is observed between the bulk $\delta^{34}S_{py}$ values and the abundance of type 2b pyrite, this relationship falls short in adequately explaining the pronounced

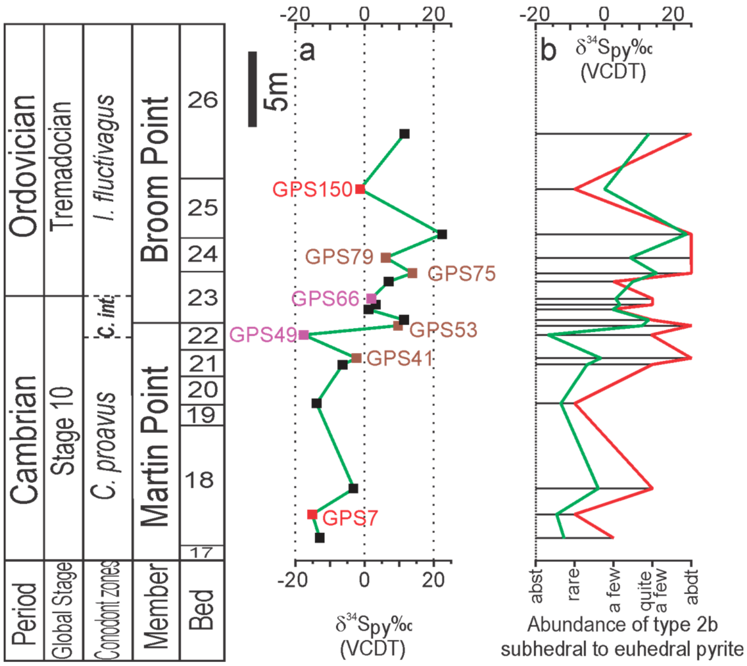

Figure 3.9: Profiles of the bulk $\delta^{34}S_{py}$ signals and the relative abundance of type 2b subhedral to euhedral pyrite. Solid green lines in (a) and (b) represent the bulk $\delta^{34}S_{py}$ variability. In figure (a), samples sharing the same colors (excluding those in black) have identical relative abundances of the pyrite types. The solid red line in (b) represents the variation of relative abundance of type 2b pyrite. Rare = very few of the pyrite type can be found (~<10%). A few = some of the pyrite type can be found but at a low percentage (~10 to 20%). Quite a few = plenty of the pyrite type can be found but its percentage (~20 to 40%) is still significantly lower than the other two types. Abundant = one of the pyrite types is significantly more abundant (>40%) than the other two, or two of the pyrite types have similar percentages (~50%). Abbreviation: abst = absent, abdt = abundant. Details in Table 3.1.

positive $\delta^{34}S_{py}$ excursion near the Є-O boundary and the apparent difference in the $\delta^{34}S_{py}$ mean values between the Martin Point and Broom Point members (Table 3.1, Figure 3.9). In addition, notable differences in $\delta^{34}S_{py}$ are evident among different sample groups (Table 3.1, Figure 3.9). These variations are observed in samples containing abundant type 1 and type 2b pyrite (GPS41, 53, 75, and 79), as well as in samples with abundant type 1, a few type 2a, and rare type 2b pyrite (GPS7 and 150). Differences can also be observed in samples with abundant type 1, rare type 2a, and quite a few type 2b pyrite (GPS 49 and 66). Consequently, these observations suggest the presence of other factor(s) contributing to the $\delta^{34}S_{py}$ variation.

It has been proposed that the investigated interval of the Green Point Formation was deposited in a semi-restricted basin with variable connectivity to open oceans (Li et al., 2022). Specifically, the shale records an inverse relationship between authigenic δ^{98}Mo and δ^{238}U values analogous to those observed from modern semi-restricted basins such as the Black Sea, the Cariaco Basin, and the Mediterranean (Andersen et al., 2018; Brüske et al., 2020, Figure 3.**10**). This pattern has been explained by variable anoxia resulting from sea-level fluctuations and varying connectivity between semi-restricted basins and open oceans (e.g., Andersen et al.,2018; Brüske et al., 2020). Supporting this presumption, a recent tectonic study by White and Waldron (2022) revealed that the Green Point Formation was deposited within a retroarc basin known as the Taconic Seaway. This basin was encircled by a series of off-margin microcontinents, which likely contributed to the isolation of seawater within the Taconic Seaway from open oceans.

We suggest that variations in the $\delta^{34}S_{py}$ of the Green Point shale were also, in part, driven by local changes in the sulfate input to the semi-restricted Taconic seaway. Our observations reveal statistically significant inverse correlations between the $\delta^{34}S_{py}$ values and the abundance of terrigenous elements (Al, Th, and ∑REE, Figure 3.**7**a-c). Given that terrestrial input has been recognized as the primary source for oceanic sulfate pool (e.g., Paytan et al., 2004; Canfield and Farquhar, 2009), and that the sulfate level plays an important factor affecting the $\Delta^{34}S$ ($\delta^{34}S_{SW}$ – $\delta^{34}S_{py}$) in semi-restricted systems (e.g., Algeo et al., 2015; Gomes and Hurtgen, 2015; Kurzweil et al., 2015; Paiste et al., 2020), these inverse correlations suggest that riverine fluxes may have played a role in regulating the local seawater sulfate levels, thereby influencing the pyrite $\delta^{34}S$ signatures. It is plausible that a decrease in terrestrial sulfate input facilitated porewater sulfate distillation, leading to the suppression of $\Delta^{34}S$ and precipitation of ^{34}S-enricehd pyrite. In contrast, high sulfate levels resulting from increased riverine input likely augmented the $\Delta^{34}S$,

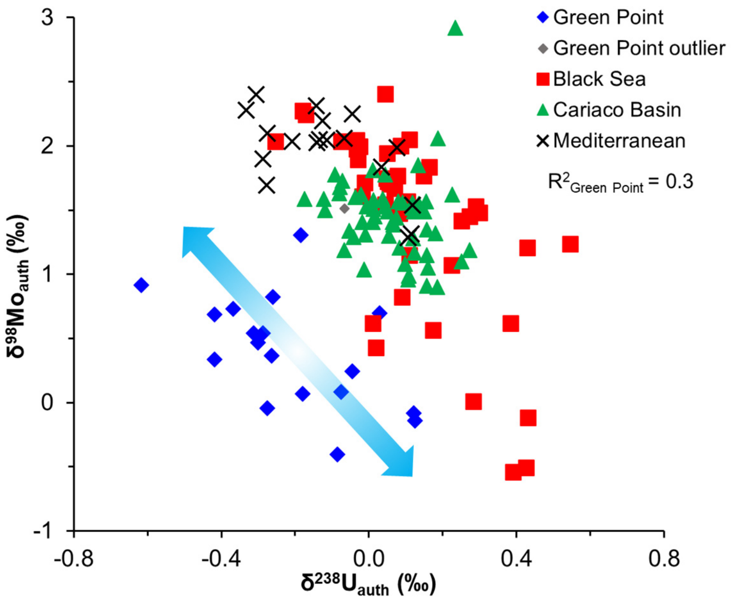

Figure 3.10: The Green Point shales record an inverse correlation between $\delta^{98}Mo_{auth}$ and $\delta^{238}U_{auth}$ ($R^2 = 0.3$, $p < 0.05$, data collected from Li et al., 2022), which is analogous to those observed in several modern semi-restricted basins. Data (available in Appendix 3.3) of sediments from the Black Sea, the Cariaco Basin, and the Mediterranean Sea are collected from Andersen et al. (2018) and Brüske et al. (2020).

resulting in the formation of pyrite less enriched in ^{34}S. This presumption is supported by a general positive relationship between the $\Delta^{34}S$ ($\delta^{34}S_{water} - \delta^{34}S_{sulfide}$) and $[SO_4^{2-}]_{aq}$ observed in various natural aqueous systems, including semi-restricted and restricted environments (e.g., Algeo et al., 2015; Gomes and Hurtgen, 2015).

Furthermore, we observe a considerable positive relationship between [Al] and [Fe] and an inverse correlation between the $\delta^{34}S_{py}$ and [Fe] (Figure 3.**7**d,e), suggesting that the availability of Fe in the regional seawater might have also contributed the $\delta^{34}S_{py}$ fluctuation. Presumably, a reduction in terrestrial input led to the drop of both sulfate and reactive Fe levels in the waterbody. This change facilitated porewater sulfate distillation, increased the accumulation of aqueous sulfide, and lowered the $\Delta^{34}S$ ($\delta^{34}S_{SW} - \delta^{34}S_{sulfide}$) offset, ultimately favoring the precipitation of ^{34}S enriched pyrite in sedimentary porewater. On the other hand, an increase in terrigenous input could have favored the precipitation of pyrite less enriched in ^{34}S. As a result, the prominent positive $\delta^{34}S_{py}$ excursion of ~20‰ near the Є-O boundary, accompanied by a significant decline in terrigenous input, can be reasonably explained, at least in part, by the shrinkage of the basinal sulfate and reactive Fe pools.

In summary, the significant $\delta^{34}S_{py}$ scatter might be associated with differing proportions of type 2b pyrite in the collected samples, while the change in basinal sulfate and iron levels may have greater influence on the comprehensive $\delta^{34}S_{py}$ pattern since we observe generally opposing trends, indicated by the LOWESS smoothed curves, between the $\delta^{34}S_{py}$ values and the abundances of Al, Th, ∑REE, and Fe (Figure 3.6).

3.5.3. Possible explanation for the negative $\delta^{13}C_{carb}$ excursion at the Є-O boundary

Limestone $\delta^{13}C_{carb}$ variations are often interpreted to be linked to oceanic redox oscillations driven by elevated/decreased marine primary productivity (e.g., Zhang et al., 2010; Gill et al., 2011; Algeo et al., 2016; Li et al., 2018; Adiatma et al., 2019; Dahl et al., 2019; Li et al., 2019). In the Green Point limestone, a significant negative $\delta^{13}C_{carb}$ shift of ~6.0‰ is observed near the Є-O boundary (Azmy et al., 2014). Notably, this $\delta^{13}C_{carb}$ shift contrasts with low amplitude positive $\delta^{13}C_{carb}$ excursions reported in age-equivalent stratigraphic sections on several other continents (Figure 3.11, Ripperdan et al., 1992; Buggisch et al., 2003; Hong et al., 2011; Miller et al., 2011). This discrepancy, coupled with the lack of significant oscillations of the oceanic carbon cycle observed during this time interval (Saltzman et al., 2015; Rasmussen et al., 2019; Goldberg et al., 2021), raises a reasonable inference that this negative $\delta^{13}C_{carb}$ excursion may not result from global-scale carbon cycle perturbations.

Negative $\delta^{13}C_{carb}$ shifts are also at times attributed to upwelling of nutrient-rich deep seawater and the subsequent oxidation of organic matter in shelf/slope environments (e.g., Howley and Jiang, 2010; Pagès and Schmid, 2016; Li et al., 2019). However, the absence of increased TOC, [Mo], and [U] observed in both shale and limestone from Beds 22 to 23 (Azmy et al., 2014, 2015; Li et al., 2022) argues against the notion of upwelling of organic-rich waters, as this would typically lead to temporary enhancements in organic matter burial and the preservation of redox-sensitive elements (e.g., Maloof et al., 2010; Pagès and Schmid, 2016; Li et al., 2019).

Considering that the sampled interval was deposited in a semi-restricted basin characterized by varying riverine fluxes and the fact that primary productivity in continental margin areas is significantly influenced by terrestrial nutrient input (e.g., Buggisch et al., 2003; Horacek et al., 2010; Zaffos et al., 2017; Adiatma et al., 2019; Pruss et al., 2019), it is plausible to infer that the primary productivity within the semi-restricted Taconic Seaway may have been impacted by terrestrial input. The current study reveals significant positive correlations between the $\delta^{13}C_{org}$ values and [Al] and ∑REE ($R^2 = 0.25$ and 0.32, respectively, $p < 0.05$, Figure 3.12a,b). This observation, together with an inverse relationship between the $\delta^{34}S_{py}$ and $\delta^{13}C_{org}$ values (Figure 3.8d), suggests that a decline in the influx of riverine nutrients might have potentially reduced the local primary productivity, resulting in decreased $\delta^{13}C_{org}$ and a decline in $\delta^{13}C$ of the local inorganic carbon budget (e.g., Ripperdan et al., 1992; Zhang et al., 2010). Conversely, an increase in riverine discharge could have triggered a rise in primary productivity, resulting in an increase in $\delta^{13}C_{org}$. Given the notable reduction in terrestrial input near the Є-O boundary suggested by declines in Al, Th, and REE abundances (Figure 3.6), the pronounced negative $\delta^{13}C_{carb}$ excursion, thus, could plausibly be explained by decreased local primary productivity.

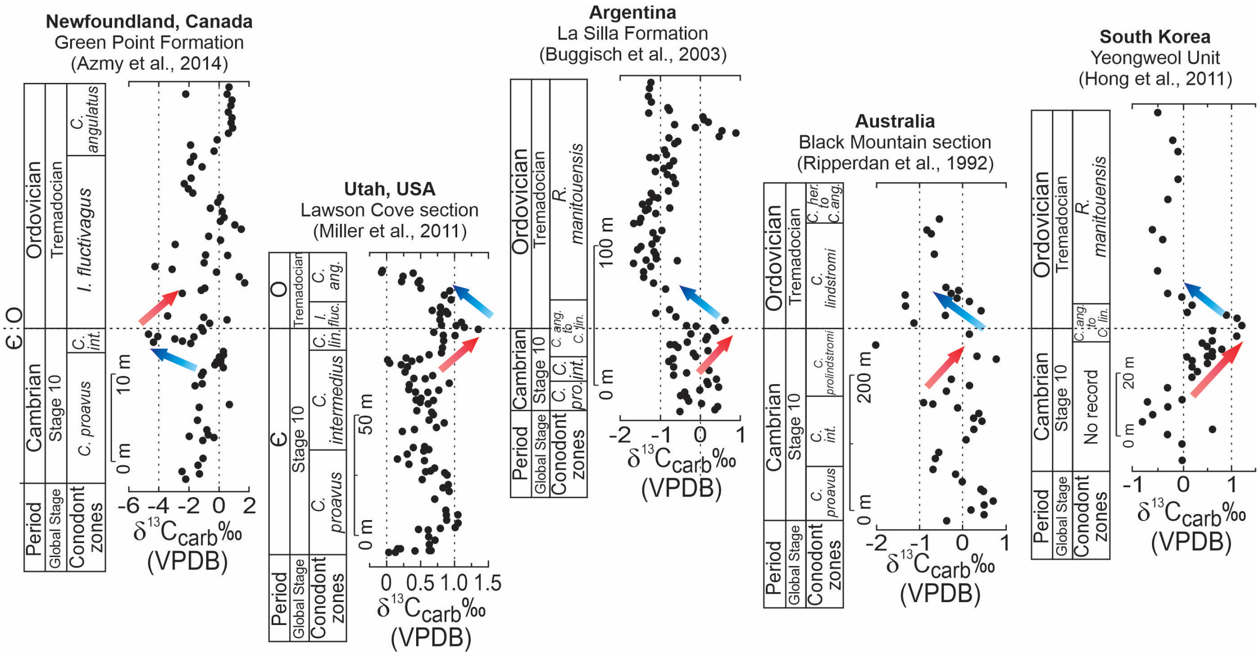

Figure 3.11: Global conodont zone and carbonate carbon isotope ($\delta^{13}C_{carb}$) correlations across the Cambrian–Ordovician boundary. The $\delta^{13}C_{carb}$ of the Green Point Formation displays a remarkable negative shift close to the Є-O boundary (Azmy et al., 2014), which is distinct from positive $\delta^{13}C_{carb}$ excursions reported from several other age-equivalent sections around the world, including the Lawson Cove section in the USA (Miller et al., 2011), the La Silla Formation in Argentina (Buggisch et al., 2003), the Black Mountain section in Australia (Ripperdan et al., 1992), and the Yeongweol Unit in South Korea (Hong et al., 2011). Locations of these stratigraphic sections at the Є-O transition are shown in Figure 3.**2**.

3.5.4. Implications for reconstructing paleo-oceanic redox states using bulk pyrite $\delta^{34}S$ signals

The variability in bulk biological $\delta^{34}S_{py}$ signals is often regarded as indicative of fluctuations in the global sulfur cycle and oceanic redox conditions (e.g., Hurtgen et al., 2005, 2009; Gill et al., 2011; Dahl et al., 2014). For instance, positive shifts in bulk $\delta^{34}S_{py}$ values have been attributed to enhanced burial of seawater ^{32}S associated with intensified MSR and expanded marine anoxia (e.g., Gill et al., 2011; Dahl et al., 2014). Additionally, bulk $\delta^{34}S_{py}$ signals have been employed to constrain paleo-oceanic sulfate levels through the MSR-trend method (e.g., Song et al., 2014; Shi et al., 2018; Stebbins et al., 2019a,b; Thomazo et al., 2019). This method is

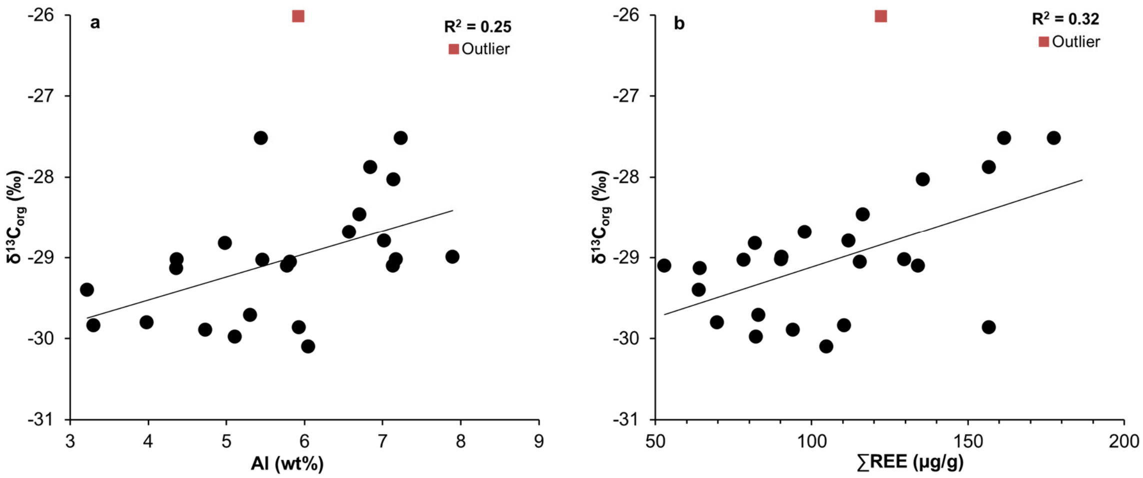

Figure 3.12: Crossplots of (a) $\delta^{13}C_{org}$ vs. [Al], $R^2 = 0.25$, $p < 0.05$ and (b) $\delta^{13}C_{org}$ vs. ∑REE, $R^2 = 0.32$, $p < 0.05$, excluding an outlier GPS166. Black solid lines are regression lines.

established on the basis of a general positive relationship between $\Delta^{34}S$ ($\delta^{34}S_{water} - \delta^{34}S_{sulfide}$[6]) and $[SO_4^{2-}]_{aq}$ observed in modern depositional systems, which depicts an increase in the $\Delta^{34}S$ from ~5‰ at 0.1 mM sulfate to ~30–60‰ at 29 mM sulfate (Algeo et al., 2015). However, a caveat with utilizing ancient bulk biological $\delta^{34}S_{py}$ signals is that they usually represent mixed signals from pyrite precipitated at different stages during early diagenesis, which significantly influences the pyrite $\delta^{34}S$ signatures (Section 3.5.2.1).

Variations in bulk sedimentary $\delta^{34}S_{py}$ can also be linked to changes in aqueous sulfate and iron levels in partially restricted basins. For example, positive $\delta^{34}S_{py}$ shifts could be explained by decreased terrestrial sulfate and iron inputs and reservoir effect in a semi-restricted basin (e.g., this study, Kurzweil et al., 2015; Paiste et al., 2020).

As a result, it is crucial to consider factors such as the stage of biological pyrite formation and the basin isolation effect before interpreting the variability of bulk $\delta^{34}S_{py}$ signals as evidence

---

[6] The $\delta^{34}S_{sulfide}$ denotes the $\delta^{34}S$ of aqueous H_2S in the bottom water or sedimentary sulfides located within a few centimeters of the SWI, which helps to minimize the influence of sulfate distillation in sediments on $\delta^{34}S$ of sulfides (Algeo et al., 2016).

of global sulfur cycle fluctuations and applying the MSR trend method to estimate ancient marine sulfate levels.

Conclusions

The Green Point Formation at Green Point in western Newfoundland consists primarily of slope rhythmites of alternating lime mudstone and shale interbeds. Several lines of evidence point out that this interval was deposited in a partially isolated basin situated within the Taconic Seaway. Two major types of pyrite are identified in the Green Point shale: (1) framboidal pyrite and (2) anhedral to euhedral pyrite. Type 2 pyrite is subdivided into type 2a anhedral to subhedral pyrite characterized by relict framboidal textures and larger sizes (~10 to 300 μm), and type 2b subhedral to euhedral pyrite with smaller sizes (typically <10 microns). Type 1 pyrite was formed in sedimentary porewaters close to the SWI with free diffusive connections to the overlying seawater. In contrast, type 2b subhedral to euhedral pyrite was precipitated in sediments with slower sulfate renewal rates. The type 2a anhedral to subhedral pyrite was probably evolved from framboids during early and burial diagenesis.

Bulk $\delta^{34}S_{py}$ values of the shale are characterized by a significant scatter ($\sigma = 10.62‰$) and display a remarkable positive shift of ~20‰ near the Ꞓ-O boundary. The lack of correlations between the $\delta^{34}S_{py}$ values and the K/Ca, TOC, and pyrite contents, along with the absence of hydrothermal fluid alteration products in the study area and low maturity of the shale, support negligible influence of postdepositional diagenesis on the $\delta^{34}S_{py}$ signals. Interestingly, we observe general parallel changes in the $\delta^{34}S_{py}$ values and the abundance of type 2b pyrite, suggesting that the $\delta^{34}S_{py}$ variation may be partially driven by the prevalence of pyrite formed within sediments. This is not surprising, as type 2b pyrite in a given sample is expected to be more enriched in ^{34}S than the other two types since it was precipitated below the SWI with limited access to the overlying seawater sulfate. Moreover, significant inverse relationships exist between the $\delta^{34}S_{py}$ values and the contents of Al, Th, ∑REE, and Fe, indicating that terrestrial sulfate and Fe influxes might have influenced the $\delta^{34}S$ offset between seawater and the pyrite. A decline in terrigenous input may have suppressed the $\Delta^{34}S_{seawater-pyrite}$ since the drop of sulfate and Fe levels would facilitate porewater sulfate distillation, favoring the precipitation of ^{34}S-enriched pyrite. Given that the positive $\delta^{34}S_{py}$ shift of ~20‰ near the Є-O boundary is accompanied by significant declines in the abundances of terrigenous elements and Fe, this shift may therefore be attributed to the contraction of basinal sulfate and Fe reservoir sizes. In addition, a negative $\delta^{13}C_{carb}$ shift is also observed during the positive $\delta^{34}S_{py}$ excursion and declines in Al, Th, and ∑REE, implying that the reduction of terrigenous input could have contributed to decreased primary productivity in the regional water column.

The bulk biological $\delta^{34}S_{py}$ variability recorded by the Green Point shale may be attributed to a combination of varying proportions of pyrite formed at different diagenetic stages and the changes in $\Delta^{34}S_{seawater-pyrite}$ impacted by terrestrial sulfate and Fe inputs. The general contrasting relationship between the $\delta^{34}S_{py}$ values and the abundances of Al, Th, ∑REE, and Fe revealed by the LOWESS smoothed curves, however, indicate that fluctuations in terrestrial inputs might have played a more substantial role in shaping the general $\delta^{34}S_{py}$ trend. These findings indicate that relying solely on the fluctuation in bulk sedimentary $\delta^{34}S_{py}$ may not offer dependable evidence for the global sulfur cycle perturbation.

Acknowledgements

The authors wish to thank Dr. Linda C. Kah and the other anonymous reviewer for their constructive reviews. We want to extend our appreciation to Dr. David Lowe and Mr. Dylan Goudie for their help with petrographic and SEM analyses. Special thanks to Dr. Jennifer

Houghton, Dr. David A. Fike, and Dr. Kärt Paiste for their help with the pyrite S-isotope analyses and Mr. Niraj Shukla (MITACS). Furthermore, we are grateful for the support rendered by Dr. Christian France-Lanord (the editor) and the journal managers. This project was supported by funding (to Karem Azmy) from Petroleum Exploration Enhancement Program (PEEP) and MITACS.

References

Adiatma, Y.D., Saltzman, M.R., Young, S.A., Griffith, E.M., Kozik, N.P., Edwards, C.T., Leslie, S.A., Bancroft, A.M., 2019. Did early land plants produce a stepwise change in atmospheric oxygen during the Late Ordovician (Sandbian ~458 Ma)? Palaeogeogr. Palaeoclimatol. Palaeoecol. 534.

Algeo, T.J., Luo, G.M., Song, H.Y., Lyons, T.W., Canfield, D.E., 2015. Reconstruction of secular variation in seawater sulfate concentrations. Biogeosciences 12(7), 2131-2151.

Algeo, T.J., Marenco, P.J., Saltzman, M.R., 2016. Co-evolution of oceans, climate, and the biosphere during the 'Ordovician Revolution': A review. Palaeogeogr. Palaeoclimatol. Palaeoecol. 458, 1-11.

Amrani, A., 2014. Organosulfur Compounds: Molecular and Isotopic Evolution from Biota to Oil and Gas. Annu. Rev. Earth Planet. Sci. 42(1), 733-768.

Amrani, A., Lewan, M.D., Aizenshtat, Z., 2005. Stable sulfur isotope partitioning during simulated petroleum formation as determined by hydrous pyrolysis of Ghareb Limestone, Israel. Geochim. Cosmochim. Acta 69(22), 5317-5331.

Andersen, M.B., Matthews, A., Vance, D., Bar-Matthews, M., Archer, C., de Souza, G.F., 2018. A 10-fold decline in the deep Eastern Mediterranean thermohaline overturning circulation during the last interglacial period. Earth Planet. Sci. Lett. 503, 58-67.

Azmy, K., Kendall, B., Brand, U., Stouge, S., Gordon, G.W., 2015. Redox conditions across the Cambrian–Ordovician boundary: Elemental and isotopic signatures retained in the GSSP carbonates. Palaeogeogr. Palaeoclimatol. Palaeoecol. 440, 440-454.

Azmy, K., Stouge, S., Brand, U., Bagnoli, G., Ripperdan, R., 2014. High-resolution chemostratigraphy of the Cambrian–Ordovician GSSP: Enhanced global correlation tool. Palaeogeogr. Palaeoclimatol. Palaeoecol. 409, 135-144.

Barkan, Y., Paris, G., Webb, S.M., Adkins, J.F., Halevy, I., 2020. Sulfur isotope fractionation between aqueous and carbonate-associated sulfate in abiotic calcite and aragonite. Geochim. Cosmochim. Acta 280, 317-339.

Barnes, C.R., 1988. The proposed Cambrian–Ordovician global Boundary stratotype and point (GSSP) in Western Newfoundland, Canada. Geol. Mag. 125(4), 381-414.

Bisnaire, A.C., 2018. Oceanic redox conditions across the Cambrian-Ordovician boundary. Master's thesis, Memorial University of Newfoundland, Canada, pp. 6, Appendix 2.1.

Blood, D.R., Schlaegle, S., Hefferan, C.M., Vazquez, A., McAllister, D., 2019. Diagenetic pyrite morphology in mudstones of the upper Ordovician point pleasant limestone, Appalachian Basin: evidence for dysoxic deposition, Memoir 120: mudstone diagenesis: research perspectives for shale hydrocarbon reservoirs. Seals Source Rocks 69–82.

Brand, U., Davis, A.M., Shaver, K.K., Blamey, N.J.F., Heizler, M., Lécuyer, C., 2021. Atmospheric oxygen of the Paleozoic. Earth Sci. Rev. 216.

Bryant, R.N., Jones, C., Raven, M.R., Owens, J.D., Fike, D.A., 2020. Shifting modes of iron sulfidization at the onset of OAE-2 drive regional shifts in pyrite δ34S records. Chem. Geol. 553.

Bryant, R.N., Present, T.M., Ahm, A.-S.C., McClelland, H.-L.O., Razionale, D., Blättler, C.L., 2022. Early diagenetic constraints on Permian seawater chemistry from the Capitan Reef. Geochim. Cosmochim. Acta 328, 1-18.

Brüske, A., Weyer, S., Zhao, M.Y., Planavsky, N.J., Wegwerth, A., Neubert, N., Dellwig, O., Lau, K.V., Lyons, T.W., 2020. Correlated molybdenum and uranium isotope signatures in modern anoxic sediments: Implications for their use as paleo-redox proxy. Geochim. Cosmochim. Acta 270, 449-474.

Buggisch, W., Keller, M., Lehnert, O., 2003. Carbon isotope record of Late Cambrian to Early Ordovician carbonates of the Argentine Precordillera. Palaeogeogr. Palaeoclimatol. Palaeoecol. 195(3-4), 357-373.

Burke, A., Present, T.M., Paris, G., Rae, E.C.M., Sandilands, B.H., Gaillardet, J., Peucker-Ehrenbrink, B., Fischer, W.W., McClelland, J.W., Spencer, R.G.M., Voss, B.M., Adkins, J.F., 2018. Sulfur isotopes in rivers: Insights into global weathering budgets, pyrite oxidation, and the modern sulfur cycle. Earth Planet. Sci. Lett. 496, 168-177.

Cameron, E.M., 1982. Sulphate and sulphate reduction in early Precambrian oceans. Nature 296, 145-148.

Canfield, D.E., 2001a. Biogeochemistry of Sulfur Isotopes. Rev. Mineral. Geochem. 43, 607-636.

Canfield, D.E., 2001b. Isotope fractionation by natural populations of sulfate-reducing bacteria. Geochim. Cosmochim. Acta 65, 1117-1124.

Canfield, D.E., 2004. The evolution of the Earth surface sulfur reservoir. Am. J. Sci. 304(10), 839-861.

Canfield, D.E., Farquhar, J., 2009. Animal evolution, bioturbation, and the sulfate concentration of the oceans. Proc. Natl. Acad. Sci. U. S. A. 106(20), 8123-8127.

Canfield, D.E., Farquhar, J., Zerkle, A.L., 2010. High isotope fractionations during sulfate reduction in a low-sulfate euxinic ocean analog. Geology 38(5), 415-418.

Canfield, D.E., Olesen, C.A., Cox, R.P., 2006. Temperature and its control of isotope fractionation by a sulfate-reducing bacterium. Geochim. Cosmochim. Acta 70(3), 548-561.

Canfield, D.E., Raiswell, R., Westrich, J.T., Reaves, C.M., Berner, R.A., 1986. The use of chromium reduction in the analysis of reduced inorganic sulfur in sediments and shales. Chem. Geol. 54, 149-155.

Canfield, D.E., Thamdrup, B., 1994. The production of 34S-depleted sulfide during bacterial disproportionation of elemental sulfur. Science 266, 1973-1975.

Cashman, K.V., Ferry, J.M., 1988. Crystal size distribution (CSD) in rocks and the kinetics and dynamics of crystallization: III. Metamorphic crystallization. Contrib. Mineral. Petrol. 99(4), 401-415.

Claypool, G.E., Holser, W.T., Kaplan, I.R., Sakai, H., Zak, I., 1980. The age curves of sulfur and oxygen isotopes in marine sulfate and their mutual interpretation. Chem. Geol. 28, 199-260.

Coniglio, M., James, N.P., 1990. Origin of fine-grained carbonate and siliciclastic sediments in an Early Palaeozoic slope sequence, Cow Head Group, western Newfoundland. Sedimentology 37, 215-230.

Cooper, R.A., Nowlan, G.S., Williams, S.H., 2001. Global Stratotype Section and Point for base of the Ordovician System. Episodes 24, 19-28.

Dahl, T.W., Boyle, R.A., Canfield, D.E., Connelly, J.N., Gill, B.C., Lenton, T.M., Bizzarro, M., 2014. Uranium isotopes distinguish two geochemically distinct stages during the later Cambrian SPICE event. Earth Planet. Sci. Lett. 401, 313-326.

Dahl, T.W., Connelly, J.N., Li, D., Kouchinsky, A., Gill, B.C., Porter, S., Maloof, A.C., Bizzarro, M., 2019. Atmosphere-ocean oxygen and productivity dynamics during early animal radiations. Proc. Nat. Acad. Sci. U.S.A. 116(39), 19352-19361.

Decraene, M.-N., Marin-Carbonne, J., Thomazo, C., Brayard, A., Bouvier, A.-S., Bomou, B., Adatte, T., Olivier, N., 2023. Pyrite iron isotope compositions track local sedimentation conditions through the Smithian-Spathian transition (Early Triassic, Utah, USA). Palaeogeogr. Palaeoclimatol. Palaeoecol. 617.

Detmers, J., Bruchert, V., Habicht, K.S., Kuever, J., 2001. Diversity of sulfur isotope fractionations by sulfate-reducing prokaryotes. Appl. Environ. Microbiol. 67(2), 888-894.

Diaz, R., Moreira, M., Mendoza, U., Machado, W., Böttcher, M.E., Santos, H., Belém, A., Capilla, R., Escher, P., Albuquerque, A.L., 2012. Early diagenesis of sulfur in a tropical upwelling system, Cabo Frio, southeastern Brazil. Geology 40(10), 879-882.

Diehl, S.F., Goldhaber, M.B., Koenig, A.E., Lowers, H.A., Ruppert, L.F., 2012. Distribution of arsenic, selenium, and other trace elements in high pyrite Appalachian coals: Evidence for multiple episodes of pyrite formation. Int. J. Coal Geol. 94, 238-249.

Edwards, C.T., Fike, D.A., Saltzman, M.R., Lu, W., Lu, Z., 2018. Evidence for local and global redox conditions at an Early Ordovician (Tremadocian) mass extinction. Earth Planet. Sci. Lett. 481, 125-135.

Edwards, C.T., Fike, D.A., Saltzman, M.R., 2019. Testing carbonate-associated sulfate (CAS) extraction methods for sulfur isotope stratigraphy: A case study of a Lower–Middle

Ordovician carbonate succession, Shingle Pass, Nevada, USA. Chem. Geol. 529, p.119297.

Faure, G., Mensing, T.M., 2005. Isotopes Principles and Applications. WILEY, pp. 761-763, 825-827.

Fike, D.A., Bradley, A.S., Rose, C.V., 2015. Rethinking the Ancient Sulfur Cycle. Annu. Rev. Earth Planet. Sci. 43(1), 593-622.

Fry, B., Ruf, W., Gest, H., Hayes, J.M., 1988. Sulfur isotope effects associated with oxidation of sulfide by O2 in aqueous solution. Chem. Geol. 73(3), 205-210.

Gill, B.C., Dahl, T.W., Hammarlund, E.U., LeRoy, M.A., Gordon, G.W., Canfield, D.E., Anbar, A.D., Lyons, T.W., 2021. Redox dynamics of later Cambrian oceans. Palaeogeogr. Palaeoclimatol. Palaeoecol. 581.

Gill, B.C., Lyons, T.W., Frank, T.D., 2008. Behavior of carbonate-associated sulfate during meteoric diagenesis and implications for the sulfur isotope paleoproxy. Geochim. Cosmochim. Acta 72(19), 4699-4711.

Gill, B.C., Lyons, T.W., Young, S.A., Kump, L.R., Knoll, A.H., Saltzman, M.R., 2011. Geochemical evidence for widespread euxinia in the later Cambrian ocean. Nature 469(7328), 80-83.

Gilleaudeau, G.J., Kah, L.C., 2015. Heterogeneous redox conditions and a shallow chemocline in the Mesoproterozoic ocean: Evidence from carbon–sulfur–iron relationships. Precambrian Res. 257, 94-108.

Goldberg, S.L., Present, T.M., Finnegan, S., Bergmann, K.D., 2021. A high-resolution record of early Paleozoic climate. Proc. Natl. Acad. Sci. U. S. A. 118(6).

Goldhaber, M.B., Kaplan, I.R., 1980. Mechanisms of sulfur incorporation and isotope fractionation during early diagenesis in sediments of the gulf of California. Mar. Chem. 9(2), 95-143.

Gomes, M.L., Hurtgen, M.T., 2013. Sulfur isotope systematics of a euxinic, low-sulfate lake: Evaluating the importance of the reservoir effect in modern and ancient oceans. Geology 41(6), 663-666.

Gomes, M.L., Hurtgen, M.T., 2015. Sulfur isotope fractionation in modern euxinic systems: Implications for paleoenvironmental reconstructions of paired sulfate–sulfide isotope records. Geochim. Cosmochim. Acta 157, 39-55.

Gomes, M.L., Johnston, D.T., 2017. Oxygen and sulfur isotopes in sulfate in modern euxinic systems with implications for evaluating the extent of euxinia in ancient oceans. Geochim. Cosmochim. Acta 205, 331-359.

Habicht, K.S., Gade, M., Thamdrup, B., Berg, P., Canfield, D.E., 2002. Calibration of Sulfate Levels in the Archean Ocean. Science 298(5602), 2372-2374.

Habicht, K.S., Salling, L., Thamdrup, B., Canfield, D.E., 2005. Effect of low sulfate concentrations on lactate oxidation and isotope fractionation during sulfate reduction by Archaeoglobus fulgidus strain Z. Appl. Environ. Microbiol. 71(7), 3770-3777.

Halevy, I., Peters, S.E., Fischer, W.W., 2012. Sulfate Burial Constraints on the Phanerozoic Sulfur Cycle. Science 337, 331-334.

Hartmann, M.N., Heimo, 1968. δ34S-Werte in rezenten Meeressedimenten und ihre Deutung am Beispiel einiger Sedimentprofile aus der westlichen Ostsee. Geol. Rundsch. 58(2), 621-655.

Hoefs, J., 2009. Stable Isotope Geochemistry. Springer, pp. 71-77.

Hong, S.K., Lee, Y.I., Jeong, S.Y., 2011. Carbon isotope composition of Upper Cambrian to Lower Ordovician carbonate in Korea, and its bearing on the Cambrian–Ordovician boundary and Lower Ordovician paleoceanography. J. Asian Earth Sci. 40(1), 252-260.

Horacek, M., Brandner, R., Richoz, S., Povoden-Karadeniz, E., 2010. Lower Triassic sulphur isotope curve of marine sulphates from the Dolomites, N-Italy. Palaeogeogr. Palaeoclimatol. Palaeoecol. 290(1-4), 65-70.

Howley, R.A., Jiang, G., 2010. The Cambrian Drumian carbon isotope excursion (DICE) in the Great Basin, western United States. Palaeogeogr. Palaeoclimatol. Palaeoecol. 296(1-2), 138-150.

Hurtgen, M.T., Arthur, M.A., Halverson, G.P., 2005. Neoproterozoic sulfur isotopes, the evolution of microbial sulfur species, and the burial efficiency of sulfide as sedimentary pyrite. Geology 33(1), 41-44.

Hurtgen, M.T., Pruss, S.B., Knoll, A.H., 2009. Evaluating the relationship between the carbon and sulfur cycles in the later Cambrian ocean: An example from the Port au Port Group, western Newfoundland, Canada. Earth Planet. Sci. Lett. 281(3-4), 288-297.

Jacobi, R.D., 1981. Peripheral bulge—a causal mechanism for the Lower/Middle Ordovician unconformity along the western margin of the Northern Appalachians. Earth Planet. Sci. Lett. 56, 245-251.

James, N.P., Stevens, R.K., 1986. Stratigraphy and correlation of the Cambro-Ordovician Cow Head group, western Newfoundland. Geol. Surv. Canada Bulletin 366, 1–143.

Jansa, L.F., 1974. Trace fossils from the Cambro-Ordovician cow head group, newfoundland, and their paleobathymetric implication. Palaeogeogr. Palaeoclimatol. Palaeoecol. 15, 233-244.

Johnston, D.T., Farquhar, J., Summons, R.E., Shen, Y., Kaufman, A.J., Masterson, A.L., Canfield, D.E., 2008. Sulfur isotope biogeochemistry of the Proterozoic McArthur Basin. Geochim. Cosmochim. Acta 72(17), 4278-4290.

Jørgensen, B.B., Böttcher, M.E., Lüschen, H., Neretin, L.N., Volkov, I.I., 2004. Anaerobic methane oxidation and a deep H2S sink generate isotopically heavy sulfides in Black Sea sediments. Geochim. Cosmochim. Acta 68(9), 2095-2118.

Jørgensen, B.B., Findlay, A.J., Pellerin, A., 2019. The Biogeochemical Sulfur Cycle of Marine Sediments. Front. Microbiol. 10, 849.

Kah, L.C., Lyons, T.W., Frank, T.D., 2004. Low marine sulphate and protracted oxygenation of the Proterozoic biosphere. Nature 431, 834-838.

Kah, L.C., Thompson, C.K., Henderson, M.A., Zhan, R., 2016. Behavior of marine sulfur in the Ordovician. Palaeogeogr. Palaeoclimatol. Palaeoecol. 458, 133-153.

Kampschulte, A., Strauss, H., 2004. The sulfur isotopic evolution of Phanerozoic seawater based on the analysis of structurally substituted sulfate in carbonates. Chem. Geol. 204(3-4), 255-286.

Knight, I., James, N.P., Lane, T.E., 1991. The Ordovician St. George unconformity, Northern Appalachians; the relationship of plate convergence at the St. Lawrence Promontory to the Sauk/Tippecanoe Sequence boundary. Geol. Soc. Am. Bull. 103, 1200-1225.

Krause, A.J., Mills, B.J.W., Zhang, S., Planavsky, N.J., Lenton, T.M., Poulton, S.W., 2018. Stepwise oxygenation of the Paleozoic atmosphere. Nat. Commun. 9(1), 4081.

Kurzweil, F., Drost, K., Pašava, J., Wille, M., Taubald, H., Schoeckle, D., Schoenberg, R., 2015. Coupled sulfur, iron and molybdenum isotope data from black shales of the Teplá-

Barrandian unit argue against deep ocean oxygenation during the Ediacaran. Geochim. Cosmochim. Acta 171, 121-142.

Leavitt, W.D., Halevy, I., Bradley, A.S., Johnston, D.T., 2013. Influence of sulfate reduction rates on the Phanerozoic sulfur isotope record. Proc. Natl. Acad. Sci. U. S. A. 110(28), 11244-11249.

LeRoy, M.A., Gill, B.C., Sperling, E.A., McKenzie, N.R., Park, T.-Y.S., 2021. Variable redox conditions as an evolutionary driver? A multi-basin comparison of redox in the middle and later Cambrian oceans (Drumian-Paibian). Palaeogeogr. Palaeoclimatol. Palaeoecol. 566, p.110209.

Li, D., Zhang, X., Hu, D., Chen, X., Huang, W., Zhang, X., Li, M., Qin, L., Peng, S., Shen, Y., 2018. Evidence of a large δ13Ccarb and δ13Corg depth gradient for deep-water anoxia during the late Cambrian SPICE event. Geology 46(7), 631-634.

Li, Y., Zhang, T., Shao, D., Shen, B., 2019. New U-Pb zircon age and carbon isotope records from the Lower Silurian Longmaxi Formation on the Yangtze Platform, South China: Implications for stratigraphic correlation and environmental change. Chem. Geol. 509, 249-260.

Li, D., Zhang, X., Zhang, X., Zhu, H., Peng, S., Sun, L., Shen, Y., 2019. A paired carbonate–organic δ13C approach to understanding the Cambrian Drumian carbon isotope excursion (DICE). Precambrian Res. 349, p.105503.

Li, J., Azmy, K., Kendall, B., 2022. The Mo- and U-isotope signatures in alternating shales and carbonate beds of rhythmites: A comparison and implications for redox conditions across the Cambrian-Ordovician boundary. Chem. Geol. 602, p.120882.

Liao, Z., Hu, W., Cao, J., Wang, X., Fu, X., 2020. Oceanic anoxia through the late Permian Changhsingian Stage in the Lower Yangtze region, South China: Evidence from sulfur isotopes and trace elements. Chem. Geol. 532.

Liu, X., Fike, D., Li, A., Dong, J., Xu, F., Zhuang, G., Rendle-Bühring, R., Wan, S., 2019. Pyrite sulfur isotopes constrained by sedimentation rates: Evidence from sediments on the East China Sea inner shelf since the late Pleistocene. Chem. Geol. 505, 66-75.

Luo, G., Richoz, S., van de Schootbrugge, B., Algeo, T.J., Xie, S., Ono, S., Summons, R.E., 2018. Multiple sulfur-isotopic evidence for a shallowly stratified ocean following the Triassic-Jurassic boundary mass extinction. Geochim. Cosmochim. Acta 231, 73-87.

Maloof, A.C., Porter, S.M., Moore, J.L., Dudas, F.O., Bowring, S.A., Higgins, J.A., Fike, D.A., Eddy, M.P., 2010. The earliest Cambrian record of animals and ocean geochemical change. Geol. Soc. Am. Bull. 122(11-12), 1731-1774.

Marin-Carbonne, J., Rollion-Bard, C., Bekker, A., Rouxel, O., Agangi, A., Cavalazzi, B., Wohlgemuth-Ueberwasser, C.C., Hofmann, A., McKeegan, K.D., 2014. Coupled Fe and S isotope variations in pyrite nodules from Archean shale. Earth Planet. Sci. Lett. 392, 67-79.

Maynard, J.B., 1980. Sulfur isotopes of iron sulfides in Devonian-Mississippian shales of the Appalachian Basin; control by rate of sedimentation. Am. J. Sci. 280(8), 772-786.

Mazumdar, A., Strauss, H., 2006. Sulfur and strontium isotopic compositions of carbonate and evaporite rocks from the late Neoproterozoic–early Cambrian Bilara Group (Nagaur-Ganganagar Basin, India): Constraints on intrabasinal correlation and global sulfur cycle. Precambrian Res. 149(3-4), 217-230.

Miller, J.F., Evans, K.R., Freeman, R.L., Ripperdan, R.L., Taylor, J.F., 2011. Proposed stratotype for the base of the Lawsonian Stage (Cambrian Stage 10) at the First Appearance Datum of Eoconodontus notchpeakensis (Miller) in the House Range, Utah, USA. Bull. Geosci., 595-620.

Millero, F.J., 2013. Chemical Oceanography, Fourth edition. CRC Press, pp. 93.

Misra, K.C., 2012. Introduction to Geochemistry: Principles and Applications. Wiley-Blackwell, pp. 268-272.

Murray, S.T., Higgins, J.A., Holmden, C., Lu, C., Swart, P.K., Hollis, C., 2020. Geochemical fingerprints of dolomitization in Bahamian carbonates: Evidence from sulphur, calcium, magnesium and clumped isotopes. Sedimentology 68(1), 1-29.

Ono, S., Wing, B., Johnston, D., Farquhar, J., Rumble, D., 2006. Mass-dependent fractionation of quadruple stable sulfur isotope system as a new tracer of sulfur biogeochemical cycles. Geochim. Cosmochim. Acta 70(9), 2238-2252.

Pagès, A., Schmid, S., 2016. Euxinia linked to the Cambrian Drumian carbon isotope excursion (DICE) in Australia: Geochemical and chemostratigraphic evidence. Palaeogeogr. Palaeoclimatol. Palaeoecol. 461, 65-76.

Paiste, K., Lepland, A., Zerkle, A.L., Kirsimäe, K., Izon, G., Patel, N.K., McLean, F., Kreitsmann, T., Mänd, K., Bui, T.H., Romashkin, A.E., Rychanchik, D.V., Prave, A.R., 2018. Multiple sulphur isotope records tracking basinal and global processes in the 1.98 Ga Zaonega Formation, NW Russia. Chem. Geol. 499, 151-164.

Paiste, K., Pellerin, A., Zerkle, A.L., Kirsimäe, K., Prave, A.R., Romashkin, A.E., Lepland, A., 2020. The pyrite multiple sulfur isotope record of the 1.98 Ga Zaonega Formation:

Evidence for biogeochemical sulfur cycling in a semi-restricted basin. Earth Planet. Sci. Lett. 534, p.116092.

Pasquier, V., Bryant, R.N., Fike, D.A., Halevy, I., 2021. Strong local, not global, controls on marine pyrite sulfur isotopes. Sci. Adv. 7(9), 1-10.

Pasquier, V., Sansjofre, P., Rabineau, M., Revillon, S., Houghton, J., Fike, D.A., 2017. Pyrite sulfur isotopes reveal glacial-interglacial environmental changes. Proc. Nat. Acad. Sci. U.S.A. 114(23), 5941-5945.

Paytan, A., Kastner, M., 1998. Sulfur isotopic composition of cenozoic seawater sulfate. Science 282, 1459-1462.

Paytan, A., Kastner, M., Campbell, D., Thiemens, M.H., 2004. Seawater sulfur isotope fluctuations in the cretaceous. Science 304, 1663-1665.

Pellerin, A., Bui, T.H., Rough, M., Mucci, A., Canfield, D.E., Wing, B.A., 2015. Mass-dependent sulfur isotope fractionation during reoxidative sulfur cycling: A case study from Mangrove Lake, Bermuda. Geochim. Cosmochim. Acta 149, 152-164.

Present, T.M., Gutierrez, M., Paris, G., Kerans, C., Grotzinger, J.P., Adkins, J.F., Tosca, N., 2019. Diagenetic controls on the isotopic composition of carbonate - associated sulphate in the Permian Capitan Reef Complex, West Texas. Sedimentology 66(7), 2605-2626.

Present, T.M., Paris, G., Burke, A., Fischer, W.W., Adkins, J.F., 2015. Large Carbonate Associated Sulfate isotopic variability between brachiopods, micrite, and other sedimentary components in Late Ordovician strata. Earth Planet. Sci. Lett. 432, 187-198.

Pruss, S.B., Jones, D.S., Fike, D.A., Tosca, N.J., Wignall, P.B., 2019. Marine anoxia and sedimentary mercury enrichments during the Late Cambrian SPICE event in northern Scotland. Geology 47(5), 475-478.

Raab, M., Spiro, B., 1991. Sulfur isotopic variations during seawater evaporation with fractional crystallization. Chem. Geol. (Isotope Geoscience Section) 86, 323-333.

Raiswell, R., 1982. Pyrite texture, isotopic composition and the availability of iron. Am. J. Sci. 282(8), 1244-1263.

Rasmussen, C.M.O., Kroger, B., Nielsen, M.L., Colmenar, J., 2019. Cascading trend of Early Paleozoic marine radiations paused by Late Ordovician extinctions. Proc. Natl. Acad. Sci. U. S. A. 116(15), 7207-7213.

Raven, M.R., Fike, D.A., Bradley, A.S., Gomes, M.L., Owens, J.D., Webb, S.A., 2019. Paired organic matter and pyrite δ34S records reveal mechanisms of carbon, sulfur, and iron cycle disruption during Ocean Anoxic Event 2. Earth Planet. Sci. Lett. 512, 27-38.

Rennie, V.C.F., Paris, G., Sessions, A.L., Abramovich, S., Turchyn, A.V., Adkins, J.F., 2018. Cenozoic record of δ34S in foraminiferal calcite implies an early Eocene shift to deep-ocean sulfide burial. Nat. Geosci. 11(10), 761-765.

Rennie, V.C.F., Turchyn, A.V., 2014. The preservation of δSSO434 and δOSO418 in carbonate-associated sulfate during marine diagenesis: A 25 Myr test case using marine sediments. Earth Planet. Sci. Lett. 395, 13-23.

Richardson, J.A., Keating, C., Lepland, A., Hints, O., Bradley, A.S., Fike, D.A., 2019a. Silurian records of carbon and sulfur cycling from Estonia: The importance of depositional environment on isotopic trends. Earth Planet. Sci. Lett. 512, 71-82.

Richardson, J.A., Lepland, A., Hints, O., Prave, A.R., Gilhooly, W.P., Bradley, A.S., Fike, D.A., 2021. Effects of early marine diagenesis and site-specific depositional controls on carbonate-associated sulfate: Insights from paired S and O isotopic analyses. Chem. Geol. 584.

Richardson, J.A., Newville, M., Lanzirotti, A., Webb, S.M., Rose, C.V., Catalano, J.G., Fike, D.A., 2019b. Depositional and diagenetic constraints on the abundance and spatial variability of carbonate-associated sulfate. Chem. Geol. 523, 59-72.

Ripperdan, R.L., Magaritz, M., Nicoll, R.S., Shergold, J.H., 1992. Simultaneous changes in carbon isotopes, sea level, and conodont biozones within the Cambrian-Ordovician boundary interval at Black Mountain, Australia. Geology 20(11), 1039-1042.

Saltzman, M.R., Edwards, C.T., Adrain, J.M., Westrop, S.R., 2015. Persistent oceanic anoxia and elevated extinction rates separate the Cambrian and Ordovician radiations. Geology 43(9), 807-810.

Sarmiento, J.L., Gruber, N., 2006. Ocean Biogeochemical Dynamics. Princeton University Press, pp. 7.

Sawłowicz, Z., 2000. Framboids: From their Origin to Application. Warsaw: Wydawnictwo Oddziału Polskiej Akademii Nauk 88, 1-58.

Schobben, M., Stebbins, A., Algeo, T.J., Strauss, H., Leda, L., Haas, J., Struck, U., Korn, D., Korte, C., 2017. Volatile earliest Triassic sulfur cycle: A consequence of persistent low seawater sulfate concentrations and a high sulfur cycle turnover rate? Palaeogeogr. Palaeoclimatol. Palaeoecol. 486, 74-85.

Schwangler, M., Harris, N.B., Waldron, J.W.F., 2020. Source rock characterization and oil-to-source rock correlation of a Cambrian -Ordovician fold-and-thrust belt petroleum system, western Newfoundland. Mar. Pet. Geol. 115, p.104283.

Scotese, C.R., 2014. Atlas of Cambrian and Early Ordovician Paleogeographic Maps (Mollweide Projection), Maps 81-88. Early Paleozoic, PALEOMAP Atlas for ArcGIS, PALEOMAP Project, Evanston, IL 5.

Scott, C., Wing, B.A., Bekker, A., Planavsky, N.J., Medvedev, P., Bates, S.M., Yun, M., Lyons, T.W., 2014. Pyrite multiple-sulfur isotope evidence for rapid expansion and contraction of the early Paleoproterozoic seawater sulfate reservoir. Earth Planet. Sci. Lett. 389, 95-104.

Shawar, L., Halevy, I., Said-Ahmad, W., Feinstein, S., Boyko, V., Kamyshny, A., Amrani, A., 2018. Dynamics of pyrite formation and organic matter sulfurization in organic-rich carbonate sediments. Geochim. Cosmochim. Acta 241, 219-239.

Shi, W., Li, C., Luo, G., Huang, J., Algeo, T.J., Jin, C., Zhang, Z., Cheng, M., 2018. Sulfur isotope evidence for transient marine-shelf oxidation during the Ediacaran Shuram Excursion. Geology 46(3), 267-270.

Siedenberg, K., Strauss, H., Podlaha, O., van den Boorn, S., 2018. Multiple sulfur isotopes (δ34S, Δ33S) of organic sulfur and pyrite from Late Cretaceous to Early Eocene oil shales in Jordan. Org. Geochem. 125, 29-40.

Sim, M.S., Bosak, T., Ono, S., 2011a. Large sulfur isotope fractionation does not require disproportionation. Science 333(6038), 74-77.

Sim, M.S., Ono, S., Donovan, K., Templer, S.P., Bosak, T., 2011b. Effect of electron donors on the fractionation of sulfur isotopes by a marine Desulfovibrio sp. Geochim. Cosmochim. Acta 75(15), 4244-4259.

Sim, M.S., Ono, S., Hurtgen, M.T., 2015. Sulfur isotope evidence for low and fluctuating sulfate levels in the Late Devonian ocean and the potential link with the mass extinction event. Earth Planet. Sci. Lett. 419, 52-62.

Slack, J.F., Shanks, W.C., Ridley, W.I., Dusel-Bacon, C., DesOrmeau, J.W., Ramezani, J., Fayek, M., 2019. Extreme sulfur isotope fractionation in the Late Devonian Dry Creek volcanogenic massive sulfide deposit, central Alaska. Chem. Geol. 513, 226-238.

Soliman, M.F., El Goresy, A., 2012. Framboidal and idiomorphic pyrite in the upper Maastrichtian sedimentary rocks at Gabal Oweina, Nile Valley, Egypt: Formation processes, oxidation products and genetic implications to the origin of framboidal pyrite. Geochim. Cosmochim. Acta 90, 195-220.

Song, H., Tong, J., Algeo, T.J., Song, H., Qiu, H., Zhu, Y., Tian, L., Bates, S., Lyons, T.W., Luo, G., Kump, L.R., 2014. Early Triassic seawater sulfate drawdown. Geochim. Cosmochim. Acta 128, 95-113.

Staudt, W.J., Reeder, R.J., Schoonen, M.A.A., 1994. Surface structural controls on compositional zoning of SO42- and SeO42- in synthetic calcite single crystals. Geochim. Cosmochim. Acta 58, 2087-2098.

Stebbins, A., Algeo, T.J., Krystyn, L., Rowe, H., Brookfield, M., Williams, J., Nye Jr, S.W., Hannigan, R., 2019a. Marine sulfur cycle evidence for upwelling and eutrophic stresses during Early Triassic cooling events. Earth Sci. Rev. 195, 68-82.

Stebbins, A., Algeo, T.J., Olsen, C., Sano, H., Rowe, H., Hannigan, R., 2019b. Sulfur-isotope evidence for recovery of seawater sulfate concentrations from a PTB minimum by the Smithian-Spathian transition. Earth Sci. Rev. 195, 83-95.

Suchecki, R.K., Perry Jr, E.A., Hubert, J.F., 1977. Clay petrology of Cambro-Ordovician continental margin, Cow Head klippe, western Newfoundland. Clays Clay Minerals 25, 163-170.

Takano, B., 1985. Geochemical implications of sulfate in sedimentary carbonates. Chem. Geol. 49, 393-403.

Taylor, K.G., Macquaker, J.H.S., 2000. Early diagenetic pyrite morphology in a mudstone-dominated succession: the Lower Jurassic Cleveland Ironstone Formation, eastern England. Sediment. Geol. 131(1-2), 77-86.

Terfelt, F., Eriksson, M.E., Schmitz, B., 2014. The Cambrian–Ordovician transition in dysoxic facies in Baltica — diverse faunas and carbon isotope anomalies. Palaeogeogr. Palaeoclimatol. Palaeoecol. 394, 59-73.

Thode, H.G., Monster, J., 1965. Sulphur isotope geochemistry of petroleum, evaporites, and ancient seas. AAPG Bull., 367-377.

Thomazo, C., Brayard, A., Elmeknassi, S., Vennin, E., Olivier, N., Caravaca, G., Escarguel, G., Fara, E., Bylund, K.G., Jenks, J.F., Stephen, D.A., Killingsworth, B., Sansjofre, P., Cartigny, P., 2019. Multiple sulfur isotope signals associated with the late Smithian event and the Smithian/Spathian boundary. Earth Sci. Rev. 195, 96-113.

Thompson, C.K., Kah, L.C., 2012. Sulfur isotope evidence for widespread euxinia and a fluctuating oxycline in Early to Middle Ordovician greenhouse oceans. Palaeogeogr. Palaeoclimatol. Palaeoecol. 313-314, 189-214.

Tian, L., Tong, J., Algeo, T.J., Song, H., Song, H., Chu, D., Shi, L., Bottjer, D.J., 2014. Reconstruction of Early Triassic ocean redox conditions based on framboidal pyrite from the Nanpanjiang Basin, South China. Palaeogeogr. Palaeoclimatol. Palaeoecol. 412, 68-79.

Tissot, B.P., Welte, D.H., 1984. Petroleum Formation and Occurrence. Springer, pp. 199-206.

Toyama, K., Paytan, A., Sawada, K., Hasegawa, T., 2020. Sulfur isotope ratios in co-occurring barite and carbonate from Eocene sediments: A comparison study. Chem. Geol. 535, p.119454.

Tripathy, G.R., Hannah, J.L., Stein, H.J., Yang, G., 2014. Re-Os age and depositional environment for black shales from the Cambrian-Ordovician boundary, Green Point, western Newfoundland. Geochem. Geophys. Geosyst. 15(4), 1021-1037.

van der Velden, A.J., van Staal, C.R., Cook, F.A., 2004. Crustal structure, fossil subduction, and the tectonic evolution of the Newfoundland Appalachians: Evidence from a reprocessed seismic reflection survey. Geol. Soc. Am. Bull. 116(11-12), 1485-1498.

Waldron, J.W.F., Anderson, S.D., Cawood, P.A., Goodwin, L.B., Hall, J., Jamieson, R.A., Palmer, S.E., Stockmal, G.S., Williams, P.F., 1998. Evolution of the Appalachian Laurentian margin: Lithoprobe results in western Newfoundland. Can. J. Earth Sci. 35, 1271-1287.

Wang, W., Hu, Y., Muscente, A.D., Cui, H., Guan, C., Hao, J., Zhou, C., 2021. Revisiting Ediacaran sulfur isotope chemostratigraphy with in situ nanoSIMS analysis of sedimentary pyrite. Geology 49(6), 611-616.

Weaver, F.J., Macko, S.A., 1988. Source rocks of western Newfoundland. Org. Geochem. 13(1), 411-421.

Wei, H., Algeo, T.J., Yu, H., Wang, J., Guo, C., Shi, G., 2015. Episodic euxinia in the Changhsingian (late Permian) of South China: Evidence from framboidal pyrite and geochemical data. Sediment. Geol. 319, 78-97.

Wei, H., Wei, X., Qiu, Z., Song, H., Shi, G., 2016. Redox conditions across the G–L boundary in South China: Evidence from pyrite morphology and sulfur isotopic compositions. Chem. Geol. 440, 1-14.

Wenk, C.B., Wing, B.A., Halevy, I., 2017. Electron carriers in microbial sulfate reduction inferred from experimental and environmental sulfur isotope fractionations. ISME J. 12(2), 495-507.

White, S.E., Waldron, J.W.F., 2022. Along-strike variations in the deformed Laurentian margin in the Northern Appalachians: Role of inherited margin geometry and colliding arcs. Earth Sci. Rev. 226, 103931.

Wignall, P.B., Newton, R., 1998. Pyrite framboid diameter as a measure of oxygen deficiency in ancient mudrocks.

Wijsman, J.W.M., Middelburg, J.J., Herman, P.M.J., Böttcher, M.E., Heip, C.H.R., 2001. Sulfur and iron speciation in surface sediments along the northwestern margin of the Black Sea. Mar. Chem. 74, 261-278.

Wilkin, R.T., Arthur, M.A., 2001. Variations in pyrite texture, sulfur isotope composition, and iron systematics in the Black Sea: evidence for Late Pleistocene to Holocene excursions of the o2-h2s redox transition. Geochim. Cosmochim. Acta 65(9), 1399-1416.

Wilkin, R.T., Barnes, H.L., 1996. Pyrite formation by reactions of iron monosulfides with dissolved inorganic and organic sulfur species. Geochim. Cosmochim. Acta 60(21), 4167-4179.

Wilkin, R.T., Barnes, H.L., Brantley, S.L., 1996. The size distribution of framboidal pyrite in modern sediments: An indicator of redox conditions. Geochim. Cosmochim. Acta 60(20), 3897-3912.

Williford, K.H., Foriel, J., Ward, P.D., Steig, E.J., 2009. Major perturbation in sulfur cycling at the Triassic-Jurassic boundary. Geology 37(9), 835-838.

Williford, K.H., Van Kranendonk, M.J., Ushikubo, T., Kozdon, R., Valley, J.W., 2011. Constraining atmospheric oxygen and seawater sulfate concentrations during Paleoproterozoic glaciation: In situ sulfur three-isotope microanalysis of pyrite from the Turee Creek Group, Western Australia. Geochim. Cosmochim. Acta 75(19), 5686-5705.

Wing, B.A., Halevy, I., 2014. Intracellular metabolite levels shape sulfur isotope fractionation during microbial sulfate respiration. Proc. Nat. Acad. Sci. U.S.A. 111(51), 18116-18125.

Wintsch, R.P., Kvale, C.M., 1994. Differential mobility of elements in burial diagenesis of siliciclastic rocks. J. Sediment. Res. 64(2), 349-361.

Young, S.A., Benayoun, E., Kozik, N.P., Hints, O., Martma, T., Bergström, S.M., Owens, J.D., 2020. Marine redox variability from Baltica during extinction events in the latest Ordovician–early Silurian. Palaeogeogr. Palaeoclimatol. Palaeoecol. 554.

Young, S.A., Kleinberg, A., Owens, J.D., 2019. Geochemical evidence for expansion of marine euxinia during an early Silurian (Llandovery–Wenlock boundary) mass extinction. Earth Planet. Sci. Lett. 513, 187-196.

Young, S.A., Loukola-Ruskeeniemi, K., Pratt, L.M., 2013. Reactions of hydrothermal solutions with organic matter in Paleoproterozoic black shales at Talvivaara, Finland: Evidence from multiple sulfur isotopes. Earth Planet. Sci. Lett. 367, 1-14.

Zaffos, A., Finnegan, S., Peters, S.E., 2017. Plate tectonic regulation of global marine animal diversity. Proc. Natl. Acad. Sci. U. S. A. 114(22), 5653-5658.

Zerkle, A.L., Farquhar, J., Johnston, D.T., Cox, R.P., Canfield, D.E., 2009. Fractionation of multiple sulfur isotopes during phototrophic oxidation of sulfide and elemental sulfur by a green sulfur bacterium. Geochim. Cosmochim. Acta 73(2), 291-306.

Zhang, S., Barnes, C.R., 2004. Late Cambrian and Early Ordovician conodont communities from platform and slope facies, western Newfoundland: a statistical approach. Geol. Soc. Lond. Spec. Publ. 230, 47-72.

Zhang, T., Shen, Y., Algeo, T.J., 2010. High-resolution carbon isotopic records from the Ordovician of South China: Links to climatic cooling and the Great Ordovician Biodiversification Event (GOBE). Palaeogeogr. Palaeoclimatol. Palaeoecol. 289(1-4), 102-112.

Zou, C., Qiu, Z., Wei, H., Dong, D., Lu, B., 2018. Euxinia caused the Late Ordovician extinction: Evidence from pyrite morphology and pyritic sulfur isotopic composition in the Yangtze area, South China. Palaeogeogr. Palaeoclimatol. Palaeoecol. 511, 1-11.

Chapter 4

4. Expanded marine anoxia at the Cambrian-Ordovician transition: Evidence from lime mudstone I/Ca and δ^{238}U signatures of the GSSP in western Newfoundland, Canada

This chapter is a reformed version of a paper published in the journal Marine and Petroleum Geology in 2023. Dr. Karem Azmy supervised this research and assisted with the review and editing of this manuscript.

Li, J., Azmy, K., 2023. Expanded marine anoxia at the Cambrian-Ordovician transition: Evidence from lime mudstone I/Ca and δ^{238}U signatures of the GSSP in western Newfoundland, Canada. Mar. Pet. Geol. 155, 106408. https://doi.org/10.1016/j.marpetgeo.2023.106408

Abstract

The early Paleozoic holds two spectacular radiations of marine organisms—the Cambrian (Є) Explosion and the Great Ordovician (O) Biodiversification Event. However, the period between them was characterized by a marine biodiversity plateau attributed to recurring biocrises. In the current study, we present the I/Ca records from slope lime mudstone of the Green Point Formation in western Newfoundland, along with a three-sink U-isotope mass balance model and previously reported limestone $\delta^{238}U_{carb}$ signals of the same interval, to further explore oceanic redox conditions at the Є-O boundary. The I/Ca ratios of the lime mudstone, deposited along the eastern Laurentian (western Iapetan) continental slope, exhibit a narrow range between 0.02 and 0.33 μmol/mol. Poor correlations between the I/Ca values and their [Sr], $\delta^{18}O$, Mn/Sr, Fe/Sr, Mg/Ca, and $\delta^{13}C_{org}$ counterparts, together with near-micritic textures of the limestone, argue against any significant influences of postdepositional alteration on the I/Ca signatures. The iodine-depleted lime mudstones, with I/Ca values well below the Proterozoic Eon baseline I/Ca ratios (~0.5 to 1 μmol/mol), suggest the presence of shallow marine oxic-anoxic interface along the regional continental margin. Substantially low carbonate I/Ca ratios (<0.5 μmol/mol) and dysoxic to anoxic depositional conditions have also been reported from several other age-equivalent sections deposited along the shelf and slope of ancient Iapetan and Laurentian continental margins. As a result, seawater surrounding the Iapetan and Laurentian continental margins at the Є-O transition might have been poorly oxygenated with shallow oxyclines or expanded oxygen minimum zones in the shelf and/or slope areas. This interpretation is further supported by our three-sink U mass balance modeling, which predicts widespread marine anoxia at the Є-O boundary with anoxic to euxinic water covering 1.0 to 21.1% of the ocean floor. Furthermore, the wide range of the estimated oceanic $\delta^{238}U_{OC}$ (−1.22 to −0.25‰) might reflect

marine redox oscillations during this period. However, the $\delta^{238}U_{OC}$ fluctuation could also be attributed to variable accumulations of the ^{238}U-enriched authigenic U phases. The overall evidence in this study aligns with earlier viewpoints that the slowness of marine biodiversity accumulation during the late Cambrian and the Early Ordovician was linked to widespread oceanic anoxia.

4.1. Introduction

During the early Paleozoic, there were notable surges in the diversity of marine life, with the Cambrian Explosion (CE) and the Great Ordovician Biodiversification Event (GOBE) being the most well-known (Servais et al., 2010; Nowak et al., 2015; Buatois et al., 2016; Stigall et al., 2019). Rises in oceanic and atmospheric oxygen levels have been regarded as major drivers of these two radiations (Sperling et al., 2013; Algeo et al., 2016; Lenton et al., 2016; Marenco et al., 2016; Servais et al., 2019; Dahl et al., 2019), although a recent study by del Rey et al. (2022) argues that the GOBE was likely linked to a general stable marine redox condition rather than increased ocean oxygenation. In addition, other factors like elevated nutrient supply from continental weathering, increased interplay between faunas, and the great continental dispersal could have also played roles in the early Paleozoic marine biodiversifications (Servais et al., 2008, 2010; Zaffos et al., 2017; Rasmussen et al., 2019; Fan et al., 2021).

Between the CE and the GOBE (~Epoch 3 to early Tremadocian, e.g., Buatois et al., 2016; Stigall et al., 2019) was a time of intense volcanism (McKenzie et al., 2016) and greenhouse climates (Trotter et al., 2008; Goldberg et al., 2021; Zhao et al., 2022). Evidence from sediment iron-speciation data and marine Mo and U isotope signatures indicates that oceans at that time were less oxygenated than the present day (Dahl et al., 2010, 2014; LeRoy et al., 2021). The marine biodiversity during this time interval reached a plateau (Buatois et al., 2016;

Rasmussen et al., 2019; Stigall et al., 2019; Deng et al., 2021, 2023), which has been attributed to expanded marine anoxia linked to greenhouse climates (e.g., Saltzman et al., 2015; LeRoy et al., 2021). However, further geochemical studies are necessary to substantiate this explanation. In this study, we aim to shed light on this issue by investigating the I/Ca and $\delta^{238}U$ signatures of the continental slope lime mudstone of the Green Point Formation, as well as using a three-sink U-isotope mass balance model to better understand the local continental margin seawater and global marine redox conditions at the Cambrian–Ordovician (Є-O) transition.

4.1.1. Geochemistry of iodine and carbonate I/Ca ratios

Iodine (I) in modern oceans has a residence time of ~300 kyr and a uniform concentration of ~0.45M (Lu et al., 2010, 2016; Hardisty et al., 2014). The marine iodine inputs primarily include riverine discharge, hydrothermal influx, and atmospheric precipitation, while the outputs are mainly associated with carbonate precipitation and organic matter burial (Lu et al., 2010; Fehn, 2012; Zhou et al., 2014; Álvarez et al., 2016). Iodine exists in oxygenated ocean waters as soluble iodate (IO_3^-), which is readily reduced to iodide (I^-) under anoxic conditions predominantly by bacteria (Wong and Brewer, 1977; Rue et al., 1997; Councell et al., 1997; Farrenkopf et al., 1997; Truesdale and Bailey, 2000; Amachi et al., 2007; Babbin et al., 2017). The reduced I^- is oxidized back to IO_3^- under well-oxygenated conditions, but this process is much slower than the IO_3^- reduction (Hardisty et al., 2021 and references therein). It has been reported that IO_3^- is the sole iodine species that can incorporate into calcite by replacing the carbonate ion (CO_3^{2-}), making the carbonate I/Ca ratio a potential redox proxy for ocean waters (Lu et al., 2010; Feng and Redfern, 2018).

Studies on the modern and Holocene planktonic foraminifera suggest that the I/Ca values lower than ~2.6 μmol/mol are signals for the presence of subsurface seawater (depth >50m) with

$[IO_3^-]_{aq}$ <0.25 μmol/L and $[O_2]_{aq}$ <~70–100 μmol/kg near sites where the foraminifera precipitated (Lu et al., 2016; Lu et al., 2019, 2021). Consistent with this finding, the I/Ca records of the Bahamas bank top primary bulk carbonates (>6.0 μmol/mol, Hardisty et al., 2017), formed in well-oxygenated shelf areas, are well above the maximum value of ~2.6 μmol/mol recorded by foraminifera precipitated near oxygen deficient zones (Lu et al., 2016; Lu et al., 2019, 2020, 2021). It is noteworthy that the I/Ca < ~2.6 μmol/mol does not necessarily indicate the depletion of oxygen within the foraminifera habitats or where the carbonates formed. This is because the $[IO_3^-]_{aq}$ of seawater in a specific area is determined by two processes: 1) the *in-situ* processes of iodine oxidation-reduction and 2) the mixing of regional water masses with $[IO_3^-]_{aq}$ gradients (Lu et al., 2016; Lu et al., 2018, 2019; Hardisty et al., 2021). Although it is still debatable whether the threshold I/Ca value of ~2.6 μmol/mol can be applied to ancient bulk carbonates in reconstructing paleo-marine redox conditions, multiple studies suggest that ancient limestones (or dolomicrites) with near-primary I/Ca (or I/(Mg+Ca) signatures below 0.5–1 μmol/mol (the Proterozoic baseline values) could serve as evidence for the presence of shallow marine oxic-anoxic interfaces and reducing subsurface seawater (e.g., Hardisty et al., 2017; Shang et al., 2019; Wei et al., 2019; He et al., 2020a,b).

Oceanic anoxic events were generally accompanied by declines in carbonate I/Ca ratios to low values due to decreased IO_3^- reservoir sizes of seawater, whereas the marine oxygenation episodes coincided with rises in the carbonate I/Ca ratios owing to increased oceanic IO_3^- budgets (Lu et al., 2010, 2016; Hardisty et al., 2014, 2017; Zhou et al., 2014, 2015; Edwards et al., 2018; Wei et al., 2019; He et al., 2020b). The effectiveness of the carbonate I/Ca ratio as a paleo-redox proxy is also supported by the covariation of curves of the maximum carbonate I/Ca ratio, the marine biodiversity, and the atmospheric oxygen level over geological time (Hardisty et al., 2017; Lu et al., 2018; Shang et al., 2019). However, caution must be taken when using this redox proxy as postdepositional diagenesis (e.g., meteoric diagenesis, recrystallization, and dolomitization) can only lower the primary carbonate I/Ca ratios by excluding IO_3^- ions bound in calcite (Zhou et al., 2015; Hardisty et al., 2017). In other words, the maximum carbonate I/Ca ratio for a given section should be the minimum estimate of the oxygen availability of local water masses (Hardisty et al., 2017).

4.1.2. Geochemistry of uranium and uranium isotopes

Uranium (U) exists in oxygenated seawater primarily as soluble uranyl complexes (Djogić et al., 1986; Morford and Emerson, 1999). It has a homogenous concentration of ~14 μmol/m^3 (Sarmiento and Gruber, 2006) and a uniform $\delta^{238}U$ value of ~−0.39‰ (Tissot and Dauphas, 2015) in the present-day oceans. The modern oceanic U input is dominated by riverine discharge (>90%), with a small contribution (<10%) from hydrothermal systems and aeolian crustal dust (Barnes and Cochran, 1993; Morford and Emerson, 1999; Henderson and Anderson, 2003). The modern marine U sinks consist primarily of oxic, oxygen-poor (dysoxic to suboxic) continental margin, and anoxic/euxinic sediments, with a minor sink associated with hydrothermal circulation and seafloor alteration (Dunk et al., 2002; Henderson and Anderson, 2003; Tissot and Dauphas, 2015).

Under oxidizing ocean waters, dissolved uranium (U^{6+}) is removed from seawater through adsorption onto Mn-Fe (oxyhydr)oxides or fixation into carbonates and pelagic clays, which are isotopically offset from seawater by average values of ~−0.24‰, +0.25‰, and +0.04‰, respectively (Tissot and Dauphas, 2015; Chen et al., 2018; Tissot et al., 2018; Bura-Nakić et al., 2020). Aqueous U^{6+} is reduced to U^{4+} by bacteria at the Fe^{2+}–Fe^{3+} redox boundary primarily within sedimentary porewaters, and a portion of the reduced U^{4+} is buried into sediments as organic matter-associated U species or uraninite precipitates (Zheng et al., 2002a,b; Algeo and Tribovillard, 2009; Stirling et al., 2015; Bura-Nakić et al., 2018). Theoretically, the bacterial uranium reduction can cause an intrinsic isotopic fractionation ($\Delta^{238}U_{U^{4+}-U^{6+}}$) of ~1.2‰; however, the observed fractionations in natural aqueous systems are much lower than this value because of U diffusive-reactive processes in porewaters (Andersen et al., 2014; Lau et al., 2020). Sediments formed under oxygen-poor (dysoxic to suboxic) and anoxic to euxinic environments have been reported to be heavier than seawater in $\delta^{238}U$ by average values of ~0.1‰ and 0.6‰, respectively (Weyer et al., 2008; Tissot and Dauphas, 2015).

4.2. Geological background

The Green Point Formation in western Newfoundland (Figure 4.1), part of the Humber Arm Allochthon in the northern Appalachian Orogen, includes the Global Stratotype Section and Point (GSSP) for the Cambrian–Ordovician boundary on Laurentia (James and Stevens, 1986; Cooper et al., 2001). The ancient Laurentian Plate was separated from west Gondwana cratons by rifting during ~570 to 550 Ma, which led to the opening of the Iapetus Ocean (Cawood et al., 2001) and the development of a pre–platform shelf along the eastern Laurentian margin. The shelf was then covered by clastic sediments during the Neoproterozoic and the early Cambrian (James et al., 1989). A major transgression between the early Cambrian and Early Ordovician flooded the Laurentian platform margin and resulted in the accumulation of thick carbonate deposits (Lavoie et al., 2012). The platform high-energy carbonates were deposited during the middle-late Cambrian and similarly the coeval carbonate/shale slope deposits of the Cow Head Group. They were later buried under the low-energy carbonates of the St. George Group from the Early Ordovician to the earliest Middle Ordovician (Knight et al., 2007, 2008; Lavoie et al., 2012). The platform and slope sediments were subsequently deformed and transported westward

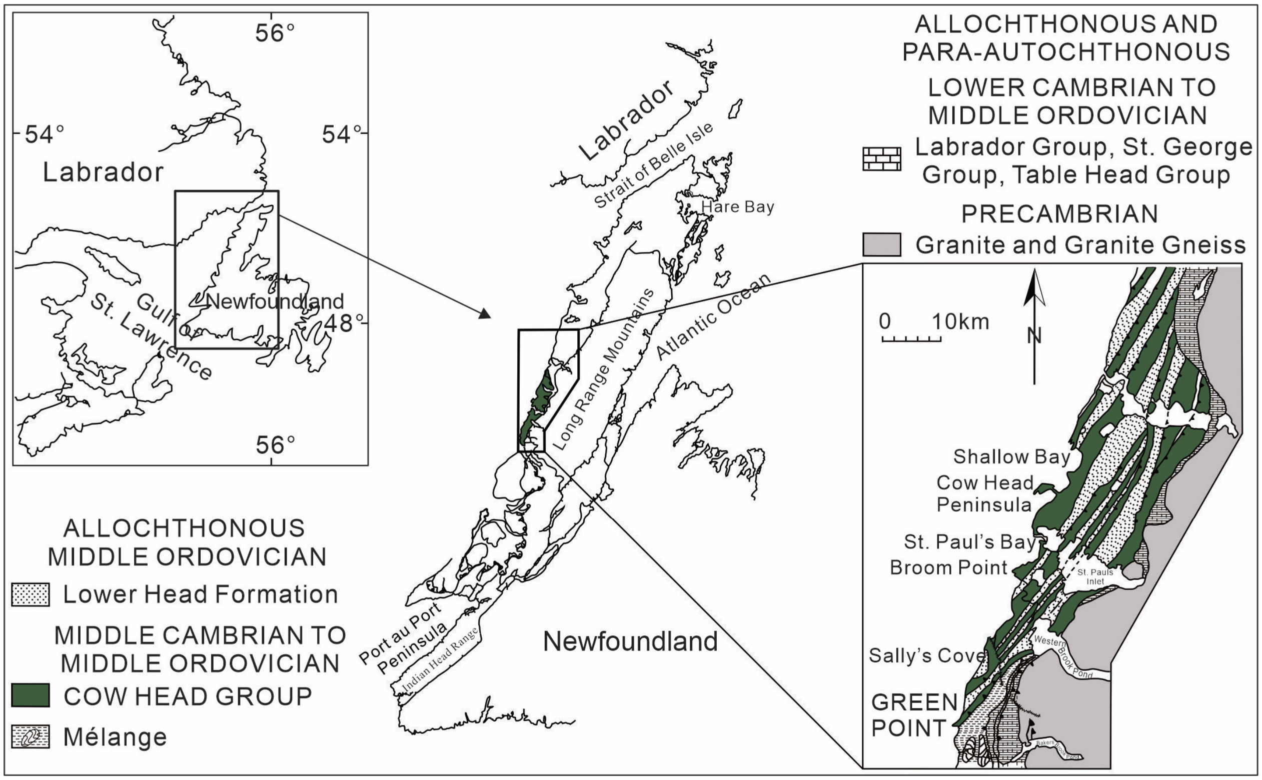

Figure 4.1: Geological map showing the location of Green Point Formation and the Cow Head Group in western Newfoundland, Canada (following Cooper et al., 2001).

by the Late Ordovician Taconic, Silurian Salinian, and Early Devonian Acadian orogenic events (Jacobi, 1981; Knight et al., 1991; Waldron et al., 1998; van der Velden et al., 2004).

The Green Point Formation was deposited along the low paleolatitude (~30˚S, Figure 4.2, Scotese, 2014) southeastern Laurentian continental margin at a water depth of ~200m during the late Cambrian and the Early Ordovician (Jansa, 1974; James and Stevens, 1986; Waldron et al., 1998). The lithostratigraphy of the currently investigated Є-O boundary section (Figure 4.3) has been studied and discussed in detail by James and Stevens (1986), and it is therefore only summarized here. The GSSP boundary section at Green Point, part of the Green Point Formation

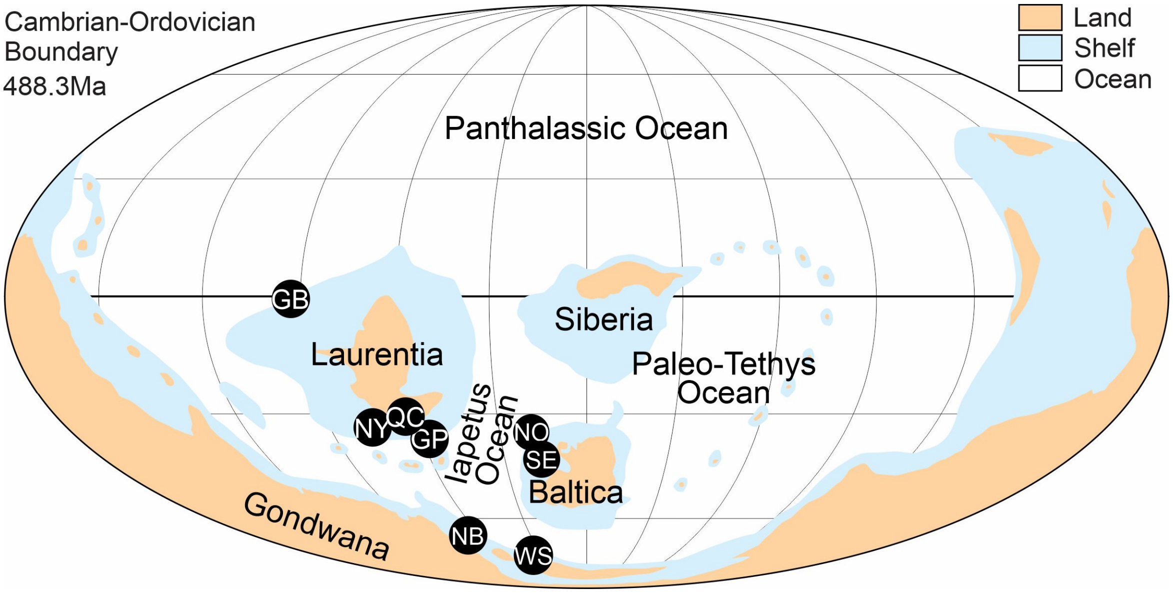

Figure 4.2: The paleogeographic reconstruction of the Cambrian-Ordovician boundary (~488.3Ma) showing locations of the Green Point Formation in western Newfoundland (GP) and the age-equivalent slope/shelf sediments in New York (NY), Quebec (QC), and the Great Basin of western USA (GB) deposited along the Laurentian continental margin (Landing, 2012; Edwards et al., 2018). The slope deposits in NY and QC are primarily dark mudstones (Landing, 2012). Coeval black shales formed along the eastern and southern Iapetan continental margin currently exposed in New Brunswick (NB) in eastern Canada, Wales (WS) in southwest Great Britain, Norway (NO), and Sweden (SE) (Berry et al., 1986; Wilde et al., 1989; Nielsen and Schovsbo, 2006; Zhao et al., 2022; Kozik et al., 2023). Modified from Scotese (2014).

of the Cow Head Group, spans the upper Cambrian Martin Point Member and the lower Ordovician Broom Point Member. This interval is dominated by hemipelagic shale, ribbon and parted lime mudstone with minor conglomerate beds and a few layers of siltstone. The shale, siltstone, and ribbon/parted limestone were deposited by gravity flows and/or pelagic fallout, with the carbonate materials primarily derived from the shallow water carbonate platform. The conglomerate beds may occur and contain debris of shallow-water carbonates or early lithified upper slope deposits that were transported into deep-water facies along the slope by turbidity currents (James and Stevens, 1986; Coniglio and James, 1990). A study by Tripathy et al. (2014) suggests that shale of this interval have an average *Re-Os* age of 484 ± 16 Myr. An inverse correlation between the shale $\delta^{98}Mo_{authigenic}$ and $\delta^{238}U_{authigenic}$ values (Appendix 4.1), analogous to those observed from the Black Sea and Cariaco Basin, indicates that the local basin was probably partially isolated from the open ocean during this interval (Li et al., 2022).

The conodont zonation scheme (Figure 4.3) of the studied interval includes, from bottom to top, the *Cordylodus proavus*, *Cordylodus caboti*, *Cordylodus intermedius*, *Iapetognathus fluctivagus*, and *Cordylodus angulatus* zones (Barnes, 1988; Cooper et al., 2001; Zhang and Barnes, 2004). The golden spike marking the Є-O boundary in the GSSP section at Green Point is placed within Bed 23, which is defined by the first appearance of the conodont *Iapetognathus fluctivagus* (Cooper et al., 2001).

4.3. Methodology

4.3.1. Petrographic evaluation and the iodine content analysis

Thirty-three lime mudstone samples were collected from the Green Point Formation (Є-O GSSP boundary section, 49° 40′ 51″ N; 57° 57′ 36″ W, Figure 4.1 and Figure 4.3) at Green Point, western Newfoundland, Canada. Samples were thin-sectioned, and the mirror-image slabs were polished. The thin sections were examined using a Zeiss Axioscope 5 at Memorial University of Newfoundland. For each thin section, over one hundred grains of a representative small aera are measured using ImageJ to estimate the average grain size (Appendix 4.2). The slabs were cleaned with deionized water and dried overnight at 50 °C before extracting the finest-grained material. Guided by the petrographic examination of thin sections under a polarized microscope, ~5 mg powder of each sample was extracted from the most micritic spots of the slab using a low-speed hand-held microdrill under a binocular microscope.

Measurements of the iodine content were performed at the Bureau de Recherches Géologiques et Minières (BRGM), France, using an Agilent 8900 triple quadrupole ICP-MS based on the methodology outlined in Lu et al. (2010) and Hardisty et al. (2017). For each

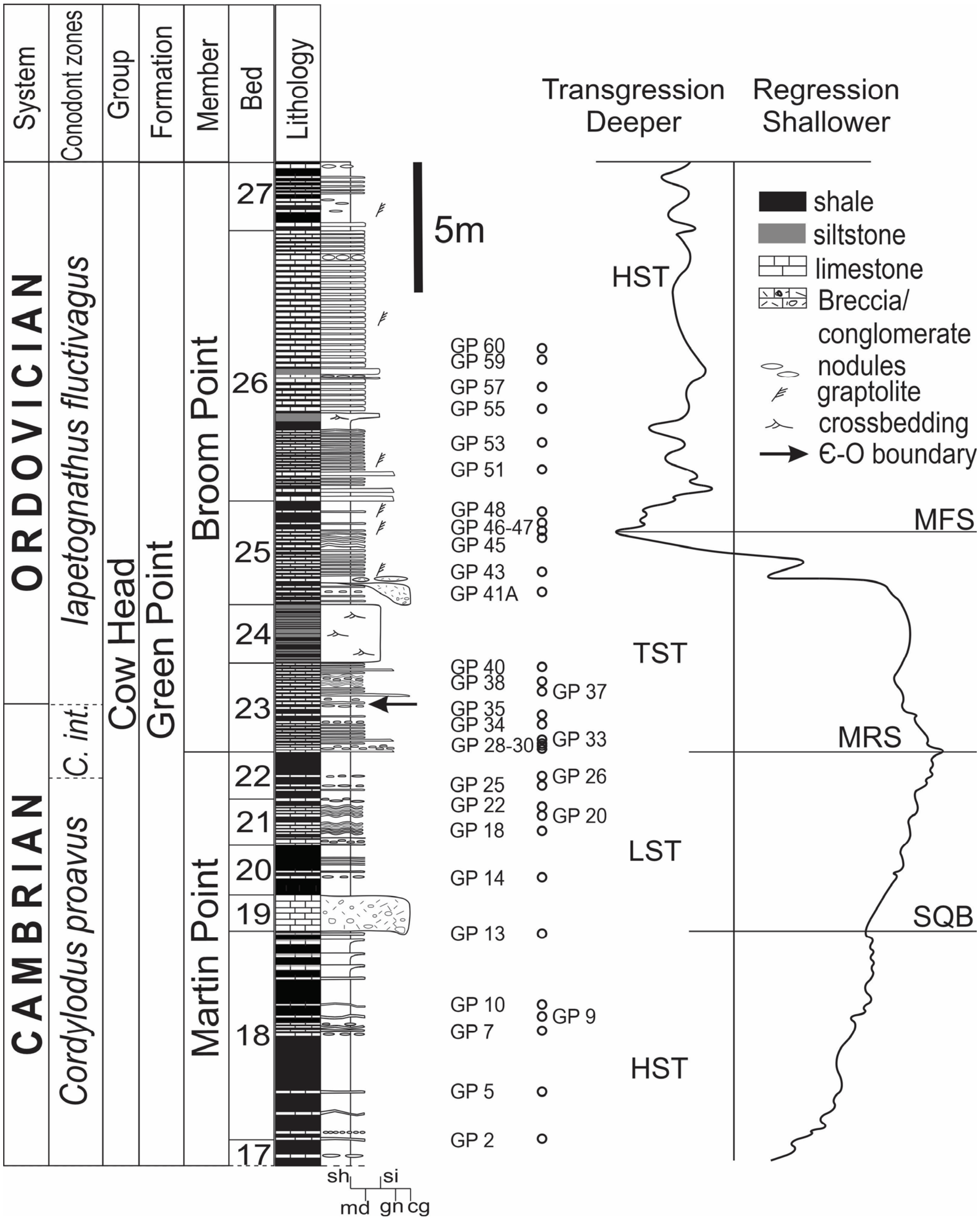

Figure 4.3: Stratigraphic framework of the Cambrian-Ordovician GSSP boundary section at Green Point (western Newfoundland, Canada) showing bed numbers, a detailed measured section with positions of the near-micritic limestone samples, and the reconstructed sea-level variation (modified from Cooper et al., 2001; Azmy et al., 2014). Abbreviations: HST = high stand systems tract, LST = low stand systems tract, TST = transgressive systems tract, MRS = maximum regressive surface, MFS = maximum flooding surface, and SQB = sequence boundary.

sample, ~5 mg powder was rinsed and centrifuged three times with deionized water to remove any potential soluble iodine salt and clay minerals (Zhou et al., 2015; Liu et al., 2020). The powder was dried overnight at 50 °C, weighed using a microgram balance, and then reacted with 3% nitric acid to completely dissolve all carbonate. The solution was centrifuged to obtain supernatant after the samples stopped bubbling. A 3% tertiary amine solution was added to the supernatant to stabilize iodine and then diluted to 0.5% with MQ water. The iodine concentration was measured within 48 hours to avoid any iodine loss (Lu et al., 2010). The accuracy of the calibration was validated by the Inorganic Venture single element iodine and the pure iodate potassium solution, and the standard reference GSD-11 was used to assess the long-term instrumental accuracy. Uncertainties of the measurements are better than 3% (1σ).

The [Ca], [Mg], [Sr], [Mn], [Fe], [Al], TOC, $\delta^{13}C_{org}$ (VPDB), and $\delta^{18}O_{carb}$ (VPDB) values of the lime mudstone have been reported by Azmy et al. (2014, 2015). The data examined here were obtained by testing powders microdrilled from the adjacent most micritic spots of the same slabs.

4.3.2. Approximation of seawater $\delta^{238}U$ at the Є-O boundary

The $\delta^{238}U$ ($\delta^{238}U_{carb}$) values and U contents of the lime mudstone have been evaluated and reported by Azmy et al. (2015) and Li et al. (2022). The $\delta^{238}U$ values of bulk carbonates, deposited in shallow-water platform, shelf, and slope environments, are reported to be higher than seawater by an average value of ~0.25‰ ($\Delta^{238}U_{\text{bulk carbonates-seawater}}$) owing to the addition of early diagenetic reduced U phases (Chen et al., 2018; Tissot et al., 2018). A study by Bura-Nakić et al. (2020) shows a similar average $\Delta^{238}U$ offset between seawater and bulk carbonates formed under dysoxic to anoxic conditions. The $\delta^{238}U$ values of the regional shallow basin water ($\delta^{238}U_{BW}$) were thus calculated by subtracting 0.25‰ from the $\delta^{238}U_{carb}$ values (Li et al., 2022, Table 4.1). However, in the present study the average value of $\delta^{238}U_{BW}$ (−0.70 ± 0.24‰, 1σ) is employed to represent the shallow basin water. This is because the observed $\Delta^{238}U_{\text{bulk carbonates-}}$

Table 4.1: Geochemical attributes of the lime mudstone.

Sample ID	I μg/g	Ca wt%	Mg wt%	Mg/Ca	I/Ca (μmol/mol)	$\delta^{18}O$ ‰	Sr μg/g	Mn μg/g	Mn/Sr	Fe μg/g	Fe/Sr	TOC wt %	$\delta^{13}C_{org}$ ‰	Al μg/g	U_{carb} μg/g	$\delta^{238}U_{carb}$ ‰	±2σ	*n*	$\delta^{238}U_{BW/OC}$ ‰	Average grain size μm
GP2	0.02	36.4	0.3	0.009	0.02	-7.21	285	800	2.80	1049	3.68	1.50	-26.97	372	1.56	-0.27	0.04	4	-0.52	6.1
GP5	0.16	35.9	0.5	0.015	0.14	-7.25	296	489	1.65	3102	10.49	2.21	-26.09	1328	0.93					5.2
GP7	0.03	36.8	0.3	0.009	0.03	-6.89	261	346	1.32	1006	3.85	4.14	-26.44	520	2.44	-0.46	0.05	3	-0.71	7.7
GP9	0.12	43.0	0.4	0.009	0.08	-7.08	266	389	1.47	1114	4.19	2.37	-26.37	568	0.84					7.1
GP10	0.03	37.7	0.3	0.009	0.03	-7.56	239	579	2.42	1548	6.47	0.97	-29.03	633	0.62					8.3
GP13	0.37	38.2	0.3	0.007	0.31	-6.87	211	267	1.27	661	3.13			302	0.54					9.5
GP14	0.03	34.2	0.3	0.009	0.02	-7.45	227	671	2.95	2871	12.64	0.80	-28.92	878	2.53	-0.18	0.08	4	-0.43	20.0
GP18	0.30	37.5	0.3	0.009	0.25	-6.98	297	280	0.94	1289	4.34	2.39	-26.55	640	1.62	-0.23		1	-0.48	7.3
GP20	0.36	38.0	0.3	0.008	0.30	-7.12	272	371	1.36	981	3.61	1.15	-28.17	483	0.70					4.8
GP22	0.26	40.8	0.4	0.009	0.20	-7.09	250	369	1.48	748	2.99	1.62	-28.54	371	3.10	-0.19	0.01	3	-0.44	12.2
GP25	0.02	36.1	0.4	0.011	0.02	-7.37	190	628	3.31	2105	11.10	0.74	-25.95	1083	0.78	-0.37		1	-0.62	7.3
GP26	0.04	25.5	0.5	0.018	0.05	-7.19	175	558	3.18	3194	18.21	1.52	-25.89	1558	0.78					14.7
GP28	0.06	34.1	0.5	0.014	0.06	-8.37	482	365	0.76	3620	7.52	0.83	-27.78	1104	1.83	-0.41	0.09	3	-0.66	*
GP29	0.04	36.1	0.4	0.010	0.03	-7.38	179	405	2.26	1482	8.28	0.43	-28.38	766	0.46	-0.49	0.10	4	-0.74	7.0
GP30	0.03	39.0	0.4	0.010	0.02	-7.37	246	376	1.53	1560	6.34	0.44	-28.59	703	0.24	-0.70	0.04	3	-0.95	4.7
GP33	0.04	33.2	0.5	0.015	0.04	-8.04	397	273	0.69	9370	23.59	0.34	-26.37	1571	1.19	-0.21		1	-0.46	5.2
GP34	0.18	33.8	0.4	0.011	0.17	-6.98	222	325	1.46	1472	6.63	0.27	-26.21	920	0.60	-0.69	0.12	4	-0.94	4.8
GP35	0.05	33.3	0.4	0.012	0.04	-6.92	180	474	2.63	1786	9.91	0.23	-29.36	1188	2.08	0.00	0.05	3	-0.25	6.7
GP37	0.10	37.2	0.5	0.013	0.09	-6.84	189	193	1.02	1573	8.30		-26.37	1142	1.19					4.0
GP38	0.05	34.9	0.4	0.011	0.05	-7.2	379	122	0.32	1098	2.90	0.13	-28.75	706	0.35	-0.63	0.09	4	-0.88	3.9
GP40	0.08	33.8	0.4	0.011	0.08	-7.44	286	273	0.95	1624	5.67			1010	0.30	-0.97	0.15	4	-1.22	5.5
GP41A	0.04	38.7	0.8	0.020	0.03	-7.11	243	210	0.86	1032	4.24			579	0.30	-0.41	0.02	3	-0.66	4.4
GP43	0.22	38.9	0.6	0.015	0.18	-6.98	367	94	0.26	489	1.33	0.11	-26.98	671	0.15					6.5
GP45	0.05	39.1	0.4	0.011	0.04	-6.86	189	824	4.37	422	2.24			427	0.24	-0.82	0.02	3	-1.07	8.3
GP46	0.02	39.1	0.4	0.009	0.02	-6.83	213	834	3.92	287	1.35	0.33	-26.31	286	0.20	-0.41		1	-0.66	7.0
GP47	0.12	39.1	0.4	0.009	0.09	-6.91	211	385	1.82	380	1.80			644	0.41	-0.53	0.06	3	-0.78	7.2
GP48	0.17	39.0	0.5	0.014	0.14	-7.49	232	449	1.94	349	1.51	0.72	-28.02	1371	0.77	-0.44	0.09	2	-0.69	4.9
GP51	0.32	39.1	0.4	0.009	0.25	-7.29	272	149	0.55	683	2.51			1036	0.43					7.5
GP53	0.06	39.0	0.5	0.012	0.05	-6.91	325	128	0.39	1407	4.32	0.22	-28.12	406	0.11	-0.66	0.11	4	-0.91	10.1
GP55	0.21	39.1	0.4	0.009	0.17	-7.12	309	148	0.48	723	2.34	0.26	-26.24	783	0.72					4.3
GP57	0.41	39.2	0.3	0.009	0.33	-7.92	269	179	0.67	697	2.59	0.36	-28.27	677	1.21					14.5
GP59	0.37	38.7	0.8	0.021	0.30	-7.38	295	129	0.44	1861	6.30	1.43	-28.97	487	1.25	-0.33	0.13	4	-0.58	23.1
GP60	0.22	39.0	0.5	0.013	0.18	-7.6	279	138	0.50	1433	5.14	0.85	-28.81	690	2.14					5.2

TOC = total organic carbon, org = organic, carb = carbonate, BW = basin water, OC = ocean, $\delta^{238}U_{BW/OC} = \delta^{238}U_{carb} - 0.25‰$, *: thin section missing.

$_{\text{seawater}}$ has a wide range from ~0.1 to 0.5‰ (Romaniello et al., 2013; Tissot et al., 2018; Bura-Nakić et al., 2020, Appendix 4.3), and thus for a specific bulk carbonate sample, an average value of 0.25‰ may not be a very accurate estimate for the δ^{238}U shift caused by the accumulation of authigenic U phases.

Although the local basin was likely partially isolated from open seawater during the sampled interval deposition (Li et al., 2022), the δ^{238}U of the shallow water may be close to open ocean. This inference is based on findings that the δ^{238}U of modern semi-restricted basin waters (except for waters deep below the chemocline in strongly restricted basins) have been reported to be comparable to open oceans (Noordmann et al., 2015; Tissot and Dauphas, 2015; Rolison et al., 2017; Li and Tissot, 2023, Appendix 4.4) and the limestone was not deposited under euxinic conditions (Azmy et al., 2014, 2015). Therefore, the mean value of $\delta^{238}U_{BW}$ (−0.70 ± 0.24‰, 1σ) is utilized to represent the value of open oceans ($\delta^{238}U_{OC}$) at the Є-O boundary. Given the fact that no $\delta^{238}U_{carb}$ values have been reported from other age-equivalent stratigraphic sections, we consider −0.70 ± 0.24‰ (1σ) to be the best estimate that is currently available for the marine δ^{238}U signature during the Є-O transition, albeit with a relatively large standard deviation.

4.3.3. The three-sink U-isotope mass balance model

The U-isotope mass balance models have been widely applied to study ancient oceanic redox conditions (e.g., Brennecka et al., 2011; Lau et al., 2016; Lu et al., 2017; Zhang et al., 2018a,b, 2020; Dahl et al., 2019; Gilleaudeau et al., 2019; Tostevin et al., 2019; Wei et al., 2021). In this study, we employ a three-sink U-isotope mass balance model (following Lau et al., 2016; Zhang et al., 2018a,b; Gilleaudeau et al., 2019; Tostevin et al., 2019) to investigate the oceanic redox conditions during the Є-O transition. This model is established based on the following assumptions:

- constant δ^{238}U signature of the riverine input over geologic time, and riverine discharge is the sole source of the oceanic U;
- the oceanic U sinks consist of only oxic, oxygen-poor (dysoxic to suboxic), and anoxic/euxinic sediments;
- fixed δ^{238}U fractionations between ocean waters and the three U sinks over geologic time;
- constant U removal rate constants (see discussion below) under oxic, dysoxic to suboxic, and anoxic/euxinic conditions over geologic time;
- oceans during the studied time interval were in a steady state, i.e., the oceanic U input was equal to the U output.

The relationship among the oceanic redox condition, the oceanic U reservoir size, and the δ^{238}U values can be described by the following differential mass balance equations:

$$\frac{dQ_{oc}}{dt} = Q_{riv} - Q_{ox} - Q_{oxp} - Q_{anox} \tag{1}$$

$$\frac{dQ_{oc}\cdot\delta^{238}U_{oc}}{dt} = Q_{riv}\cdot\delta^{238}U_{riv} - Q_{ox}\cdot\delta^{238}U_{ox} - Q_{oxp}\cdot\delta^{238}U_{oxp} - Q_{anox}\cdot\delta^{238}U_{anox} \tag{2}$$

where the Q_{oc}, Q_{riv}, $\delta^{238}U_{oc}$, and $\delta^{238}U_{riv}$ refer to the oceanic U reservoir size (mol), the riverine U input (mol), the oceanic δ^{238}U signature, and the δ^{238}U of discharged river waters, respectively. The Q_{ox}, Q_{oxp}, and Q_{anox} are the marine oxic, oxygen-poor (dysoxic to suboxic), and anoxic/euxinic U sinks (mol), respectively, and their δ^{238}U signatures are denoted by $\delta^{238}U_{ox}$, $\delta^{238}U_{oxp}$, and $\delta^{238}U_{anox}$, respectively.

In equations (1) and (2):

$$Q_{oc} = V_{oc}\cdot C_{oc,\,U} \tag{3}$$

$$Q_{riv} = V_{riv}\cdot C_{riv,\,U} \tag{4}$$

$$Q_{ox} = k_{ox} \cdot Q_{oc} \cdot f_{ox} \cdot A_{oc} \quad (5)$$

$$Q_{oxp} = k_{oxp} \cdot Q_{oc} \cdot f_{oxp} \cdot A_{oc} \quad (6)$$

$$Q_{anox} = k_{anox} \cdot Q_{oc} \cdot f_{anox} \cdot A_{oc} \quad (7)$$

$$\delta^{238}U_{ox} = \delta^{238}U_{oc} + \Delta_{ox} \quad (8)$$

$$\delta^{238}U_{oxp} = \delta^{238}U_{oc} + \Delta_{oxp} \quad (9)$$

$$\delta^{238}U_{anox} = \delta^{238}U_{oc} + \Delta_{anox} \quad (10)$$

$$f_{ox} + f_{oxp} + f_{anox} = 1, \text{ and } f_{ox}, f_{oxp}, \text{ and } f_{anox} \in [0,1] \quad (11)$$

where the V_{oc}, $C_{oc, U}$, V_{riv}, and $C_{riv, U}$ refer to the volume of ocean waters, the seawater U concentration, the volume of river waters discharged into oceans, and the U concentration of river waters, respectively. The k_{ox}, k_{oxp}, and k_{anox} are the rate constants for U removal under oxic, oxygen-poor, and anoxic/euxinic conditions, respectively, which are calculated from the modern U system. The f_{ox}, f_{oxp}, and f_{anox} represent the fractions of the ocean floor covered by oxic, oxygen-poor, and anoxic/euxinic waters, respectively. The A_{oc} denotes the area of the ocean floor. The Δ_{ox}, Δ_{oxp}, and Δ_{anox} refer to the U isotopic fractionations between seawater and the oxic, oxygen-poor, and anoxic/euxinic sinks, respectively. The values of parameters used in this modeling are summarized in **Error! Reference source not found.**.

Assuming that the ocean was in a steady state, then we have:

$$\frac{dQ_{oc}}{dt} = \frac{dQ_{oc} \cdot \delta^{238}U_{oc}}{dt} = 0 \quad (12)$$

Therefore, equations (1) and (2) can be simplified to:

$$Q_{riv} = Q_{ox} + Q_{oxp} + Q_{anox} \quad (13)$$

$$Q_{riv} \cdot \delta^{238}U_{riv} = Q_{ox} \cdot \delta^{238}U_{ox} + Q_{oxp} \cdot \delta^{238}U_{oxp} + Q_{anox} \cdot \delta^{238}U_{anox} \quad (14)$$

By solving equations (13) and (14) using equations (3) to (10), we obtain:

$$\delta^{238}\mathrm{U}_{\mathrm{oc}} = \delta^{238}\mathrm{U}_{\mathrm{riv}} - \frac{\mathrm{k}_{\mathrm{ox}}\cdot\mathrm{f}_{\mathrm{ox}}\cdot\Delta_{\mathrm{ox}} + \mathrm{k}_{\mathrm{oxp}}\cdot\mathrm{f}_{\mathrm{oxp}}\cdot\Delta_{\mathrm{oxp}} + \mathrm{k}_{\mathrm{anox}}\cdot\mathrm{f}_{\mathrm{anox}}\cdot\Delta_{\mathrm{anox}}}{\mathrm{k}_{\mathrm{ox}}\cdot\mathrm{f}_{\mathrm{ox}} + \mathrm{k}_{\mathrm{oxp}}\cdot\mathrm{f}_{\mathrm{oxp}} + \mathrm{k}_{\mathrm{anox}}\cdot\mathrm{f}_{\mathrm{anox}}} \quad (15)$$

Considering that $\mathrm{f}_{\mathrm{ox}} + \mathrm{f}_{\mathrm{oxp}} + \mathrm{f}_{\mathrm{anox}} = 1$, the following relations can be expressed as:

f_{ox} and $\mathrm{f}_{\mathrm{oxp}}$ vs. $\mathrm{f}_{\mathrm{anox}}$:

$$\mathrm{f}_{\mathrm{ox}} = \frac{\mathrm{f}_{\mathrm{anox}}\left[(\mathrm{k}_{\mathrm{anox}}-\mathrm{k}_{\mathrm{oxp}})(\delta^{238}\mathrm{U}_{\mathrm{riv}}-\delta^{238}\mathrm{U}_{\mathrm{oc}})+\mathrm{k}_{\mathrm{oxp}}\cdot\Delta_{\mathrm{oxp}}-\mathrm{k}_{\mathrm{anox}}\cdot\Delta_{\mathrm{anox}}\right]+\mathrm{k}_{\mathrm{oxp}}(\delta^{238}\mathrm{U}_{\mathrm{riv}}-\delta^{238}\mathrm{U}_{\mathrm{oc}}-\Delta_{\mathrm{oxp}})}{\mathrm{k}_{\mathrm{ox}}\cdot\Delta_{\mathrm{ox}}-\mathrm{k}_{\mathrm{oxp}}\cdot\Delta_{\mathrm{oxp}}-(\delta^{238}\mathrm{U}_{\mathrm{riv}}-\delta^{238}\mathrm{U}_{\mathrm{oc}})(\mathrm{k}_{\mathrm{ox}}-\mathrm{k}_{\mathrm{oxp}})} \quad (16)$$

$$\mathrm{f}_{\mathrm{oxp}} = \frac{\mathrm{f}_{\mathrm{anox}}\left[(\mathrm{k}_{\mathrm{anox}}-\mathrm{k}_{\mathrm{ox}})(\delta^{238}\mathrm{U}_{\mathrm{riv}}-\delta^{238}\mathrm{U}_{\mathrm{oc}})+\mathrm{k}_{\mathrm{ox}}\cdot\Delta_{\mathrm{ox}}-\mathrm{k}_{\mathrm{anox}}\cdot\Delta_{\mathrm{anox}}\right]+\mathrm{k}_{\mathrm{ox}}(\delta^{238}\mathrm{U}_{\mathrm{riv}}-\delta^{238}\mathrm{U}_{\mathrm{oc}}-\Delta_{\mathrm{ox}})}{\mathrm{k}_{\mathrm{oxp}}\cdot\Delta_{\mathrm{oxp}}-\mathrm{k}_{\mathrm{ox}}\cdot\Delta_{\mathrm{ox}}-(\delta^{238}\mathrm{U}_{\mathrm{riv}}-\delta^{238}\mathrm{U}_{\mathrm{oc}})(\mathrm{k}_{\mathrm{oxp}}-\mathrm{k}_{\mathrm{ox}})} \quad (17)$$

f_{ox} and $\mathrm{f}_{\mathrm{anox}}$ vs. $\mathrm{f}_{\mathrm{oxp}}$:

$$\mathrm{f}_{\mathrm{ox}} = \frac{\mathrm{f}_{\mathrm{oxp}}\left[(\mathrm{k}_{\mathrm{oxp}}-\mathrm{k}_{\mathrm{anox}})(\delta^{238}\mathrm{U}_{\mathrm{riv}}-\delta^{238}\mathrm{U}_{\mathrm{oc}})+\mathrm{k}_{\mathrm{anox}}\cdot\Delta_{\mathrm{anox}}-\mathrm{k}_{\mathrm{oxp}}\cdot\Delta_{\mathrm{oxp}}\right]+\mathrm{k}_{\mathrm{anox}}(\delta^{238}\mathrm{U}_{\mathrm{riv}}-\delta^{238}\mathrm{U}_{\mathrm{oc}}-\Delta_{\mathrm{anox}})}{\mathrm{k}_{\mathrm{ox}}\cdot\Delta_{\mathrm{ox}}-\mathrm{k}_{\mathrm{anox}}\cdot\Delta_{\mathrm{anox}}-(\delta^{238}\mathrm{U}_{\mathrm{riv}}-\delta^{238}\mathrm{U}_{\mathrm{oc}})(\mathrm{k}_{\mathrm{ox}}-\mathrm{k}_{\mathrm{anox}})} \quad (18)$$

$$\mathrm{f}_{\mathrm{anox}} = \frac{\mathrm{f}_{\mathrm{oxp}}\left[(\mathrm{k}_{\mathrm{oxp}}-\mathrm{k}_{\mathrm{ox}})(\delta^{238}\mathrm{U}_{\mathrm{riv}}-\delta^{238}\mathrm{U}_{\mathrm{oc}})+\mathrm{k}_{\mathrm{ox}}\cdot\Delta_{\mathrm{ox}}-\mathrm{k}_{\mathrm{oxp}}\cdot\Delta_{\mathrm{oxp}}\right]+\mathrm{k}_{\mathrm{ox}}(\delta^{238}\mathrm{U}_{\mathrm{riv}}-\delta^{238}\mathrm{U}_{\mathrm{oc}}-\Delta_{\mathrm{ox}})}{\mathrm{k}_{\mathrm{anox}}\cdot\Delta_{\mathrm{anox}}-\mathrm{k}_{\mathrm{ox}}\cdot\Delta_{\mathrm{ox}}-(\delta^{238}\mathrm{U}_{\mathrm{riv}}-\delta^{238}\mathrm{U}_{\mathrm{oc}})(\mathrm{k}_{\mathrm{anox}}-\mathrm{k}_{\mathrm{ox}})} \quad (19)$$

This model predicts a δ^{238}U value of ~−0.40‰ for the modern ocean, which is in good agreement with the reported modern oceanic δ^{238}U signature of ~−0.39‰ (Tissot and Dauphas, 2015). The minimum and maximum values of the $\mathrm{f}_{\mathrm{anox}}$ and $\mathrm{f}_{\mathrm{oxp}}$ for a given $\delta^{238}\mathrm{U}_{\mathrm{oc}}$ value are determined using equations (16) to (19) based on restrictions that $\mathrm{f}_{\mathrm{anox}}$ and $\mathrm{f}_{\mathrm{oxp}} \in [0,1]$, $\mathrm{f}_{\mathrm{ox}} + \mathrm{f}_{\mathrm{oxp}} \leq 1$, and $\mathrm{f}_{\mathrm{ox}} + \mathrm{f}_{\mathrm{anox}} \leq 1$.

4.4. Results

The geochemical attributes of the lime mudstone are listed in Table 4.1 and shown in Figure 4.4. The iodine concentrations range from 0.02 to 0.41 μg/g, and the corresponding I/Ca ratios fall within a narrow range between 0.02 and 0.33 μmol/mol. The limestone with Mn/Sr <2 exhibits the same range in I/Ca ratios (Section 4.5.1). The [Sr] and the carbonate δ^{18}O ($\delta^{18}\mathrm{O}_{\mathrm{carb}}$) values span from 175 to 482 μg/g and −8.37 to −6.83‰, respectively. The Mn, Fe, Mg, and Al concentrations vary between 94 and 834 μg/g, 287 and 9370 μg/g, 0.3 and 0.8 wt%, and 286 and

Table 4.2: The list of parameters and values for the three-sink U-isotope mass balance model.

Parameter	Meaning	Present value	Fixed value	References
$\delta^{238}U_{oc}$	The oceanic δ^{238}U signature	−0.39‰		1
A_{oc}	The area of the ocean floor	3.6184×10^{14} m^2		2
V_{oc}	The volume of the ocean water	1.3324×10^{18} m^3		2
$C_{oc,U}$	The seawater U concentration	14 μmol m^{-3}		3
Q_{riv}	The riverine U input	40 Mmol/yr		4
f_{ox}	The fraction of ocean floor covered by oxic water	~91.8%*		
f_{oxp}	The fraction of ocean floor covered by dysoxic to suboxic water	~8.0%		4, 5
f_{anox}	The fraction of ocean floor covered by anoxic/euxinic water	~0.2%		1, 6
$Q_{ox,U}$	The marine oxic U sink	~9 Mmol U/yr		4
$Q_{oxp,U}$	The marine oxygen-poor (continental margin) U sink	~25 Mmol U/yr**		
$Q_{anox,U}$	The marine anoxic/euxinic sink	~6 Mmol U/yr		4
$\delta^{238}U_{riv}$	The riverine δ^{238}U signature		−0.24‰	1
k_{ox}	The rate constant for oceanic U removal under oxic condition		1.45×10^{-21}***	
k_{oxp}	The rate constant for oceanic U removal under oxygen-poor condition		4.63×10^{-20} ****	
k_{anox}	The rate constant for oceanic U removal under anoxic/euxinic condition		4.44×10^{-19}*****	
Δ_{ox}	The isotopic fractionation between seawater and the oxic sink		+0.02‰******	1, 7, 8, 9
Δ_{oxp}	The isotopic fractionation between seawater and the oxygen-poor sink		+0.1‰	1
Δ_{anox}	The isotopic fractionation between seawater and the anoxic/euxinic sink		+0.6‰	1

* Calculated using equation 11
** Calculated at the steady state condition
*** Calculated using equation 5
**** Calculated using equation 6
***** Calculated using equation 7
****** The average value of $\Delta^{238}U_{\text{carb seds-SW}}$ (0.25‰), $\Delta^{238}U_{\text{pelagic red clay-SW}}$ (0.04‰), and $\Delta^{238}U_{\text{metalic seds-SW}}$ (−0.24‰); carb = carbonate, seds = sediments, SW = seawater.
References: 1 Tissot and Dauphas, 2015; 2 Charette and Walter, 2010; 3 Sarmiento and Gruber, 2006; 4 Morford and Emerson, 1999; 5 Klinkhammer and Palmer, 1991; 6 Lau et al., 2016; 7 Chen et al., 2018; 8 Tissot et al., 2018; 9 Bura-Nakić et al., 2020.

1571 μg/g, respectively. The TOC and the δ^{13}C of organic carbon ($\delta^{13}C_{org}$) values range from 0.11 to 4.14 wt% and −29.36 to −25.89‰, respectively. The carbonate δ^{238}U ($\delta^{238}U_{carb}$) and the inferred oceanic $\delta^{238}U_{OC}$ ($^{238}U_{OC} = \delta^{238}U_{carb} - 0.25$‰) values span widely from −0.97 to 0.00‰ and −1.22 to −0.25‰, respectively. The inferred $\delta^{238}U_{OC}$ values display moderate variations below Bed 22, followed by a serious of oscillations from Beds 23 to 25 before returning to less negative values in Bed 26. The estimated average $\delta^{238}U_{OC}$ for the Cambrian-Ordovician transition is −0.70 ± 0.24‰ (1σ).

Petrographic examination shows that the carbonates are fabric retentive lime mudstone with near micritic textures and average grain sizes between ~4 and 23 μm (Figure 4.5a-r, Table

4.1). All samples have undergone complete recrystallization, as indicated by the presence of relatively large grains (up to ~40 μm, Figure 4.5). The original fine crystals (probably <5 μm) may have been coarsened through aggrading neomorphism. However, it is important to note that the extracted materials were microdrilled from the most micritic spots, and there is no significant correlation between the average grain sizes and the I/Ca ratios (R^2 =0.06, **Error! Reference source not found.**).

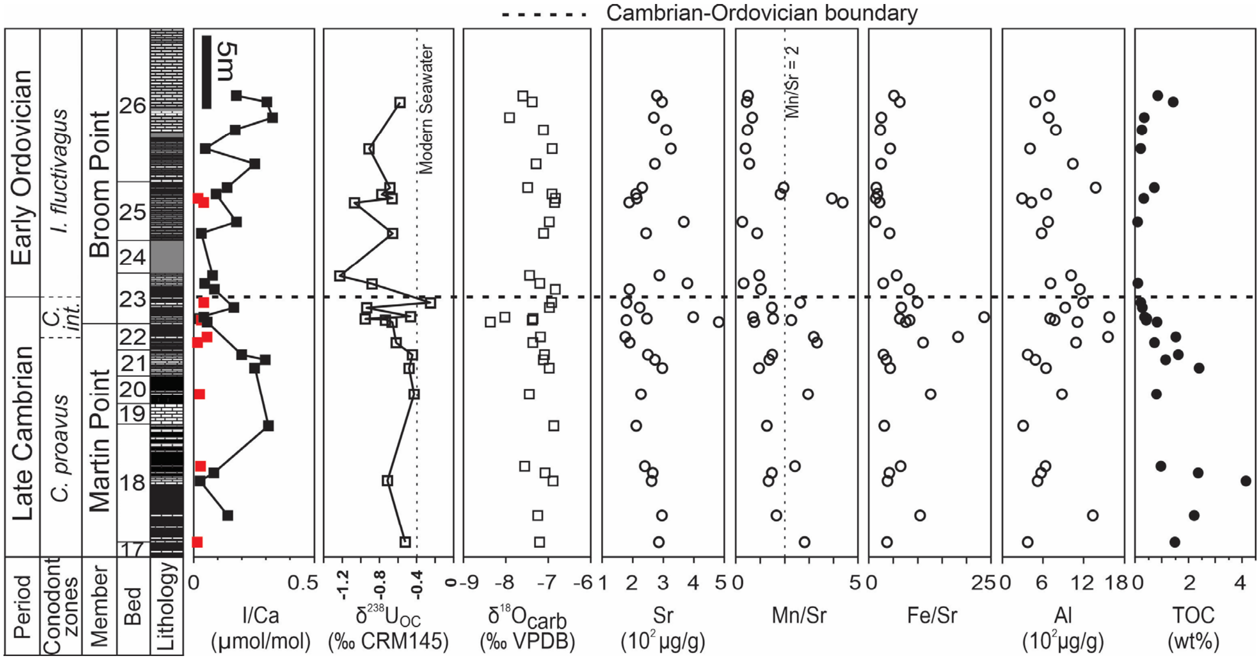

Figure 4.4: Stratigraphic profile and geochemical trends across the Cambrian-Ordovician GSSP boundary of the Green Point Formation in western Newfoundland, Canada. The dashed horizontal black line marks the level of the golden spike of the Cambrian-Ordovician biostratigraphic boundary (Cooper et al., 2001). The filled red squares are I/Ca ratios of samples with Mn/Sr >2.

4.5. Discussion

4.5.1. Evaluation of the I/Ca signature preservation

The iodine bound in calcite has been reported to be susceptible to diagenetic alteration (Zhou et al., 2015; Hardisty et al., 2017). Carbonates commonly lose the ^{18}O isotope and Sr but become enriched in Mn, Fe, and Mg due to postdepositional diagenesis such as recrystallization, meteoric alteration, and dolomitization (Brand and Veizer, 1980; Al-Aasm and Veizer, 1986;

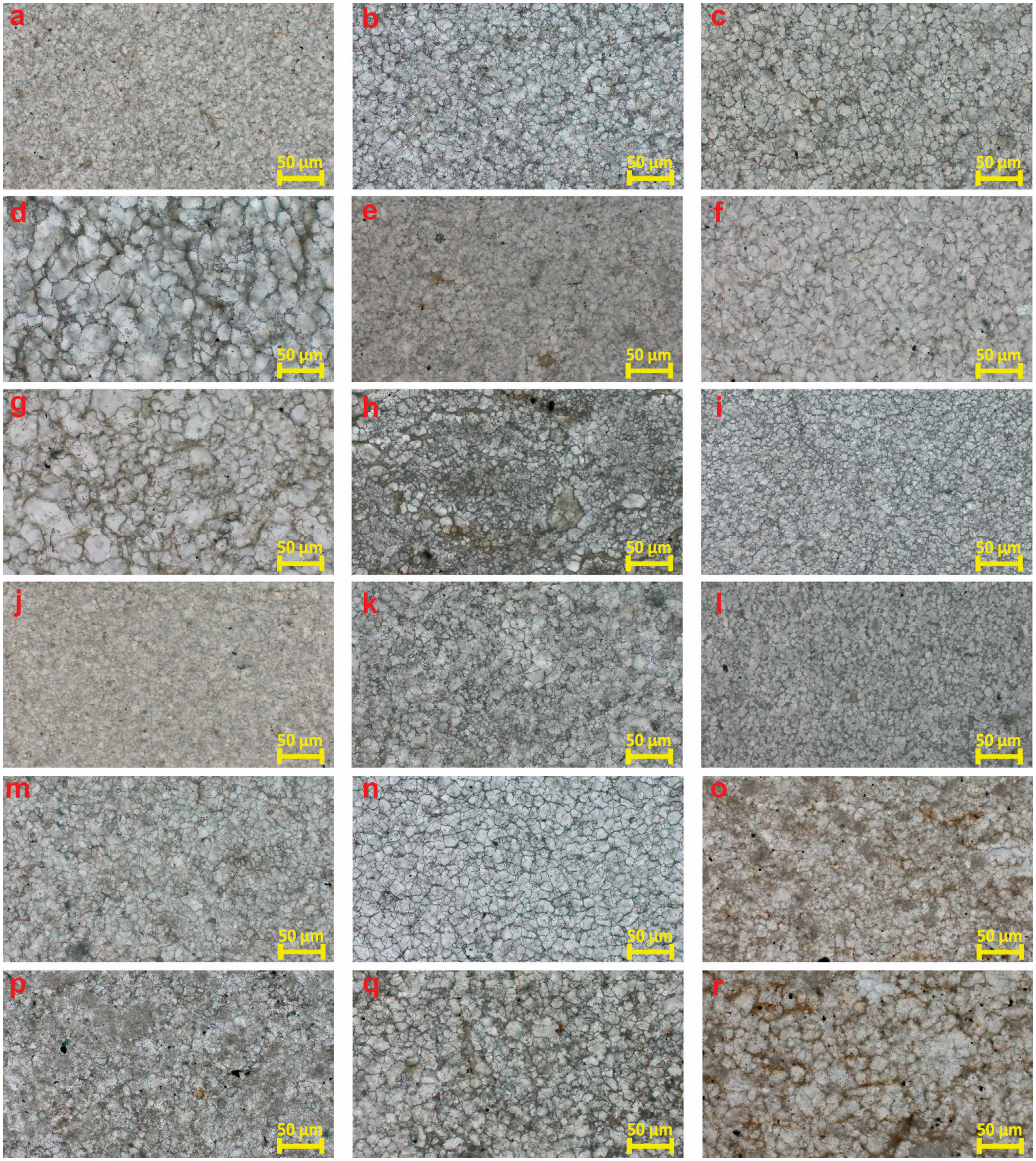

Figure 4.5: Photomicrographs (plane polarized light, 200× magnification, scale bar = 50 µm) of the lime mudstone samples, (a): GP2, (b): GP7, (c): GP10, (d): GP14, I: GP18, (f): GP 22, (g): GP26, (h): GP29, (i): GP30, (j): GP34, (k): GP37, (l): GP41A, (m): GP45, (n): GP46, (o): GP48, (p): GP51, (q): GP55, (I): GP59.

Banner and Hanson, 1990; Gao and Land, 1991; Azmy et al., 2011). Significant δ^{18}O isotopic exchange between carbonates and meteoric fluids can happen at very low porewater/rock ratios

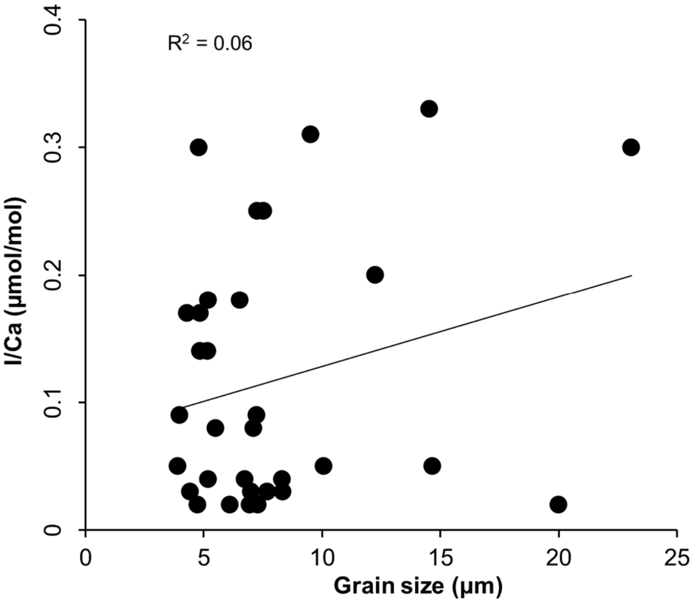

Figure 4.6: Crossplots of the average carbonate grain sizes and the I/Ca ratios (R^2 = 0.06). The solid black line is the regression line.

(Banner and Hanson, 1990; Algeo et al., 1992). Therefore, the lack of correlations between the I/Ca ratios and their [Sr], δ^{18}O, Fe/Sr, and Mg/Ca counterparts (R^2 = 0.01, 2×10^{-5}, 0.11, and 0.004, respectively, Figure 4.7a-d), along with the invariable δ^{18}O values and strong depletions of Mg (<0.9 wt%, Figure 4.4 and Table 4.1), argue against significant influences of diagenetic alteration on the I/Ca signals. The absence of correlation between the I/Ca ratios and the δ^{13}C$_{org}$ values (R^2 = 0.01, Figure 4.8a) also suggests negligible influence from organic matter catagenesis. These observations are consistent with the overall good preservation of the limestone as indicated by micritic to near-micritic textures and non- to dull-luminescence under a cold cathodoluminoscope (Azmy et al., 2014, 2015).

It is noteworthy that there is a weak negative correlation between the I/Ca ratios and Mn/Sr values (R^2 = 0.23, Figure 4.8b), implying that a few of the I/Ca signals might have been slightly altered by postdepositional diagenesis like recrystallization. Considering that the limestone with Mn/Sr >2 might have experienced a degree of diagenetic alteration (e.g., Song et al., 2014; Bartlett et al., 2018; Decraene et al., 2023), the I/Ca ratios of these samples are thus excluded from this study. The I/Ca ratios of samples with Mn/Sr <2, which also range from 0.02 to 0.33 µmol/mol, exhibit poor correlations with their [Sr], $\delta^{18}O$, Fe/Sr, Mg/Ca, $\delta^{13}C_{org}$, and Mn/Sr counterparts (R^2 = 0.05, 0.003, 0.10, 0.03, 0.05, and 0.01 respectively, Figure 4.7a-d and

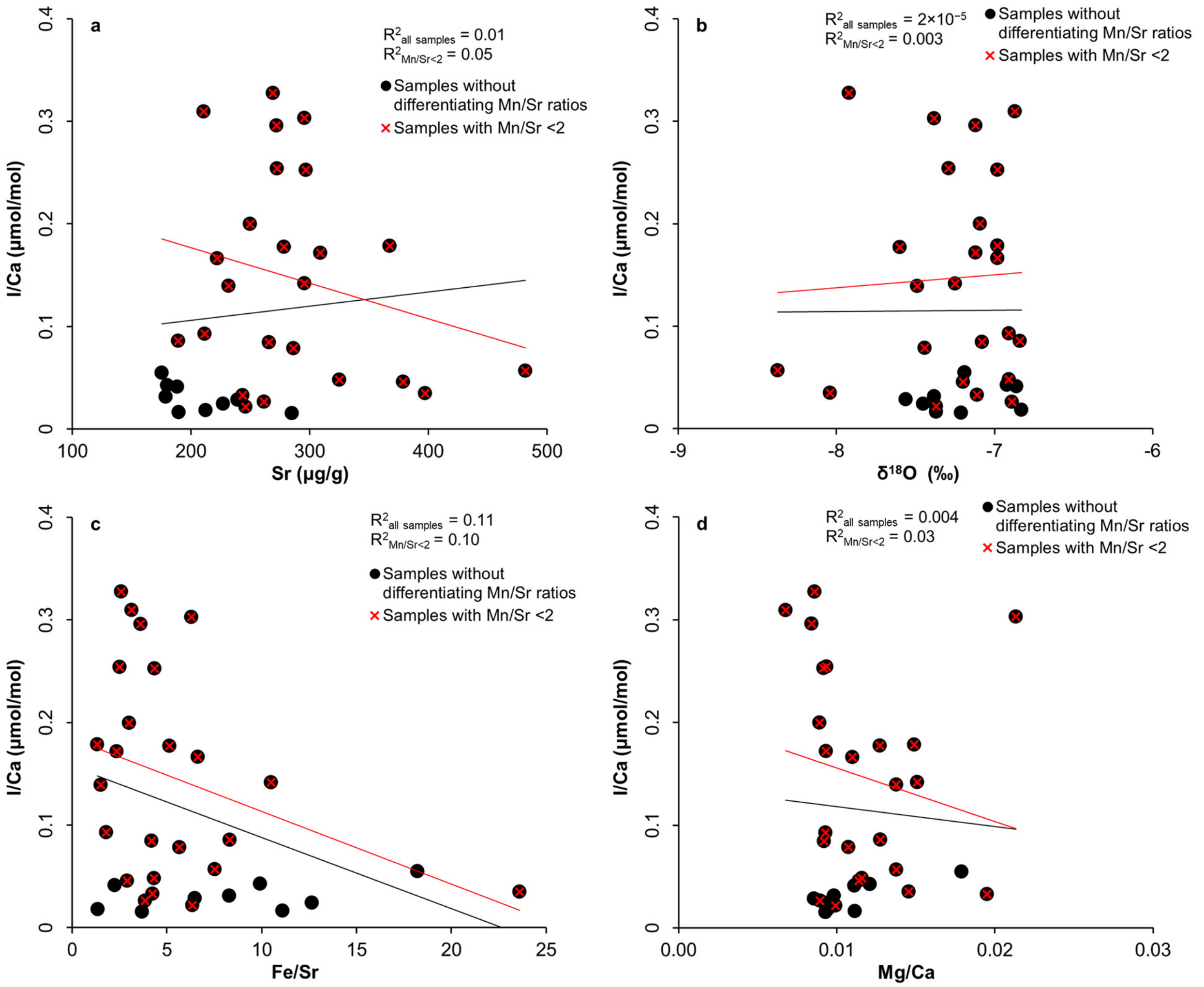

Figure 4.7: Scatter diagrams of (a) [Sr] vs. I/Ca ($R^2_{\text{all samples}}$= 0.01, $R^2_{\text{Mn/Sr<2}}$ = 0.05), (b) $\delta^{18}O_{carb}$ vs. I/Ca ($R^2_{\text{all samples}}$= 2×10^{-5}, $R^2_{\text{Mn/Sr<2}}$ = 0.003), (c) Fe/Sr vs. I/Ca ($R^2_{\text{all samples}}$= 0.11, p >0.05; $R^2_{\text{Mn/Sr<2}}$ = 0.10, p >0.05), and (d) Mg/Ca vs. I/Ca ($R^2_{\text{all samples}}$= 0.004, $R^2_{\text{Mn/Sr<2}}$ = 0.03). The filled black circles are samples without differentiating Mn/Sr ratios, and the red crosses are samples with Mn/Sr <2. Black and red solid lines represent the regression lines of all samples and the samples with Mn/Sr <2, respectively.

Figure 4.8a,b). Although minor iodine loss due to postdepositional diagenesis cannot be entirely ruled out for the lime mudstone, the overall evidence suggests that samples with Mn/Sr <2 are likely to have been insignificantly affected by diagenetic alteration. Therefore, these samples may retain at least near-primary I/Ca signals.

Iodine also exists in rocks as organic iodine and iodide (Togo et al., 2016), which might contaminate carbonate associated I/Ca signatures (e.g., He et al., 2020b). However, the poor correlation between the I/Ca values and TOC concentrations (R^2 of all samples and the samples with Mn/Sr <2 = 0.003 and 0.001, respectively, Figure 4.8c) demonstrates that negligible organically-bound iodine was released to solutions during sample dissolutions. Limestones of this interval are hemipelagic sediments with minor clay minerals coming from the continent (James and Stevens, 1986). In this study, the powders were rinsed three times with deionized water to minimize the contamination from clay minerals, which is supported by the absence of correlation between the I/Ca ratios and their [Al] counterparts (R^2 of all samples and the samples with Mn/Sr <2 = 0.04 and 0.09, respectively, Figure 4.8d).

4.5.2. Interpretation of the limestone I/Ca ratios

Near-primary carbonate I/Ca ratios below ~0.5 to 1 μmol/mol have been regarded as indicators for the presence of reducing subsurface waters (depth >50m) and shallow oxic-anoxic interfaces in ancient oceans (Hardisty et al., 2017; Shang et al., 2019; Wei et al., 2019; He et al., 2020a,b). Edwards et al. (2018) further suggested that near-zero lime mudstone I/Ca values could be evidence for regional seawater anoxia. The lime mudstone of the Green Point Formation is strongly depleted in iodine, with I/Ca ratios (0.02 to 0.33 μmol/mol) lower than the background I/Ca ratios of ~0.5 to 1 μmol/mol during the Proterozoic Eon which was a time of expanded marine anoxia (Hardisty et al., 2017; Lu et al., 2018). Therefore, the significantly low I/Ca ratios in the lime mudstone, with a narrow range, may indicate relatively invariable redox conditions and shallow marine oxycline along the regional continental slope throughout the studied interval.

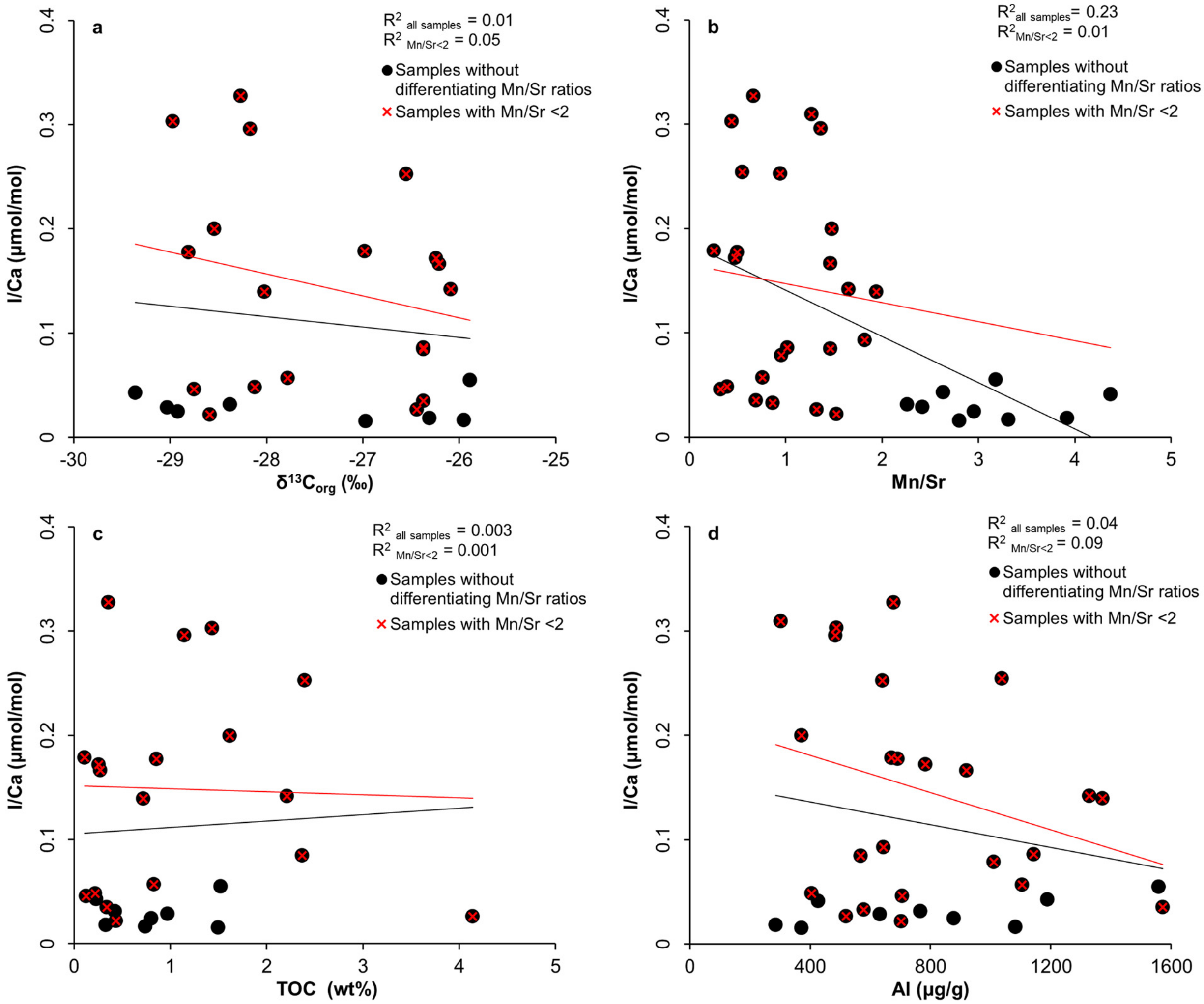

Figure 4.8: Crossplots of (a) $\delta^{13}C_{org}$ vs. I/Ca ($R^2_{\text{all samples}} = 0.01$, $R^2_{\text{Mn/Sr<2}} = 0.05$), (b) Mn/Sr vs. I/Ca ($R^2_{\text{all samples}} = 0.23$, $R^2_{\text{Mn/Sr<2}} = 0.01$), (c) TOC vs. I/Ca ($R^2_{\text{all samples}} = 0.003$, $R^2_{\text{Mn/Sr<2}} = 0.001$), and (d) [Al] vs. I/Ca ($R^2_{\text{all samples}} = 0.04$, $R^2_{\text{Mn/Sr<2}} = 0.09$). The filled black circles are samples without differentiating Mn/Sr ratios, and the red crosses are samples with Mn/Sr <2. Black and red solid lines represent the regression lines of all samples and the samples with Mn/Sr <2, respectively.

This interpretation agrees with earlier findings that the limestone was deposited under dysoxic to suboxic bottom conditions as suggested by their dark colors and relatively low Ce/Ce* values (<1) (Jansa, 1974; James and Stevens, 1986; Azmy et al., 2015). Some near-zero I/Ca ratios might indicate episodes of localized expanded seawater anoxia (e.g., Edwards et al., 2018). The positive/negative I/Ca shifts could be evidence of slight fluctuations in oxygen levels of local seawater. However, the caveat with this interpretation is that carbonate I/Ca ratios become less sensitive to oxygen availability of seawater when I/Ca ratios are lower than ~2.6 µmol/mol (Lu et al., 2016; Lu et al., 2019, Appendix 4.5).

Similar to the Green Point Formation in western Newfoundland, the coeval eastern Laurentian (western Iapetan) continental slope sediments, currently exposed in New York and Quebec (Figure 4.2), are dominated by black mudstone, suggesting dysoxic to anoxic depositional conditions (Landing, 2012). In addition, the earliest Tremadocian shelf limestone in the Great Basin region of western USA, deposited along the western Laurentian continental margin (Figure 4.2), were reported to be strongly depleted in iodine with I/Ca ratios commonly <0.5 µmol/mol, implying widespread anoxia along the regional continental margin (Edwards et al., 2018). Furthermore, black shales also dominate the latest Cambrian to the earliest Ordovician outer shelf to slope sediments deposited along the southern and eastern Iapetan margin currently exposed in New Brunswick (eastern Canada), Wales (southwest Great Britain), Norway, and Sweden (Berry et al., 1986; Wilde et al., 1989; Nielsen and Schovsbo, 2006; Zhao et al., 2022; Kozik et al., 2023, Figure 4.2).

As a result, it is likely that seawater surrounding the Iapetan and Laurentian continental margins at the Є-O transition was generally poorly oxygenated with a shallow oxic-anoxic interface or expanded oxygen minimum zones in shelf and/or slope areas (e.g, Kozik et al., 2023). This is not surprising since greenhouse climates during this time interval (Trotter et al., 2008; Goldberg et al., 2021) could have reduced latitudinal thermal gradients and inhibited ocean circulations, favoring the buildup and expansion of oxygen minimum zones (e.g., Elrick et al., 2011; Landing, 2012; Algeo et al., 2016). However, oceanic redox conditions in the early Paleozoic were likely variable due to differences in ocean circulation patterns (e.g., LeRoy et al., 2021; Pohl et al., 2021; Kozik et al., 2022). Therefore, the above inference needs to be proved by further investigations on redox conditions of seawater covering other parts of the Laurentian and Iapetan continental margins.

4.5.3. The oceanic redox condition at the Є-O transition

The average oceanic $\delta^{238}U$ signature during the Є-O transition, inferred from the $\delta^{238}U_{carb}$ values, was approximately −0.70 ± 0.24‰ (1σ, see Section 4.3.2). If we take the $\delta^{238}U_{oc}$ at the Є-O boundary as −0.70‰, our three-sink U-isotope mass balance model produces a maximum value of 21.1% and a minimum value of 1.0% for the f_{anox} (Figure 4.9), suggesting that the Є-O transition was a time of expanded marine anoxia relative to the modern day (f_{anox} = ~0.2%, Tissot and Dauphas, 2015; Lau et al., 2016). The modeling result agrees with the relatively low marine $\delta^{98}Mo$ signature (<+1.4‰, the modern $\delta^{98}Mo_{seawater} \approx +2.34‰$, Dahl et al., 2010; Nägler et al., 2013), intense greenhouse conditions, persistent oceanic anoxia (Trotter et al., 2008; Saltzman et al., 2015; Goldberg et al., 2021), and the conclusion of Section 4.5.2 that seawater with a shallow oxycline or expanded oxygen minimum zones likely surrounded the Laurentian and Iapetan continental margins at the Є-O transition. Our model also predicts a maximum value of 78.9% and a minimum value of 0% for the f_{oxp} in this time period (Figure 4.9). However, the broad range of the predicted f_{oxp} does not allow a solid evaluation of the fraction of ocean floor overlain by dysoxic to suboxic seawater.

The model output is highly sensitive to the $\delta^{238}U_{riv}$ and Δ_{anox} values. The predicted extent of ocean anoxia becomes smaller when more negative $\delta^{238}U_{riv}$ and more positive Δ_{anox} values are employed. Given the wide range of reported average $\delta^{238}U_{riv}$ values (from −0.24 to −0.34‰, Tissot and Dauphas, 2015; Andersen et al., 2016, 2017), we test possibilities when the $\delta^{238}U_{riv}$ equals −0.30‰ and −0.34‰. For a given $\delta^{238}U_{oc}$ value of −0.70‰, the solutions for f_{anox} range

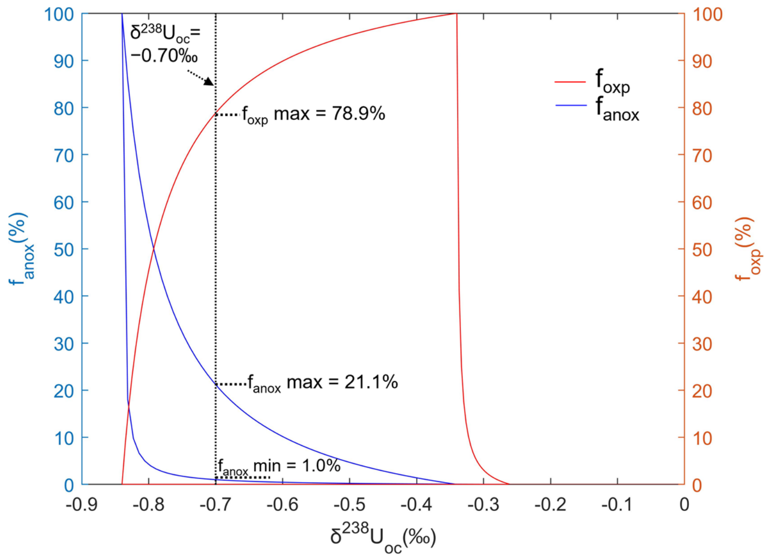

Figure 4.9: Solutions for the three-sink U-isotope mass balance model. The solid blue and red lines are solutions for f_{anox} and f_{oxp}, respectively. This model predicts that f_{anox} equals 0% and 100 % when $\delta^{238}U_{oc}$ = −0.34‰ and −0.84‰ (respectively). The predicted minimum f_{oxp} equals 0% when the $\delta^{238}U_{oc}$ is in the range of −0.84 to −0.26‰. For a given $\delta^{238}U$ value of −0.70‰, the solutions for the f_{anox} and f_{oxp} range from 1.0 to 21.1% and 0 to 78.9%, respectively. The MATLAB codes are available in Appendix 4.6.

from 0.6 to 13.5% and 0.5 to 10.1% when the $\delta^{238}U_{riv}$ equals −0.30‰ and −0.34‰, respectively (Figure 4.10a), which still points to large scale ocean anoxia relative to the present day.

We also explore the model's sensitivity to the Δ_{anox} value in the range of 0.4 to 0.8‰, where the Δ_{anox} value of 0.8‰ (close to the reported maximum Δ_{anox}) is only observed in sediments formed under strongly euxinic bottom conditions (Lau et al., 2020). The Δ_{anox} value of 0.4‰ is not reconciled with our model because a 100% of seafloor covered by anoxia/euxinic waters cannot produce a $\delta^{238}U_{oc}$ value of −0.70‰ (Figure 4.10b). For Δ_{anox} = 0.8‰, this model produces the minimum and maximum f_{anox} values of 0.4% and 9.9%, respectively (Figure 4.10b). In an extreme scenario that $\delta^{238}U_{riv}$ = −0.34‰ and Δ_{anox} = 0.8‰, the modeled minimum and maximum f_{anox} values are 0.3% and 5.8% (respectively) when $\delta^{238}U_{oc}$ equals −0.70‰ (Figure

4.10c). It should be noted that the Δ_{anox} values higher than 0.6‰ have been only observed in euxinic sediments (Weyer et al., 2008; Lau et al., 2020), which means that the result of this model should be a solution for the extent of ocean euxinia if the Δ_{anox} >0.6‰. As a result, the smallest estimate f_{anox} of 0.3% in the extreme scenario ($\delta^{238}U_{riv} = -0.34$‰, $\Delta_{anox} = 0.8$‰) should still indicate large-scale ocean anoxia. In summary, despite the high sensitivity of our model to parameters like $\delta^{238}U_{riv}$ and Δ_{anox}, the predicted expanded ocean anoxia during the Є-O transition cannot be simply explained by the variability of $\delta^{238}U_{riv}$ and Δ_{anox}.

4.5.4. Interpretation of the estimated $\delta^{238}U_{OC}$ variation

Below Bed 22, the estimated marine $\delta^{238}U_{OC}$ values display moderate fluctuations, with several values resembling the modern seawater $\delta^{238}U$ signature. However, from Beds 23 to 25, the $\delta^{238}U_{OC}$ exhibits strong oscillations and reaches a minimum value of −1.22% before returning to less negative values in Bed 26 (Figure 4.4). The $\delta^{238}U_{OC}$ fluctuation of the sampled interval may be explained by either of the following possible scenarios.

First, the recommended average $\delta^{238}U$ offset ($\Delta^{238}U_{bulk\ carbonate\text{-}seawater}$) of 0.25‰ (Chen et al., 2018; Tissot et al., 2018) could not be a universally applicable estimate for the $\delta^{238}U$ shift caused by the addition of authigenic U precipitates (see Section 4.3.2). In other words, for a particular bulk carbonate sample, the average value of 0.25‰ could be either an underestimation or an overestimation of the true $\Delta^{238}U_{bulk\ carbonate\text{-}seawater}$. Consistent with this inference, there is a positive correlation between the $\delta^{238}U_{carb}$ values and U contents ($R^2 = 0.49$, $p < 0.01$, Figure 4.11) analogous to modern primary aragonite precipitates in the Bahamas (Romaniello et al., 2013, Appendix 4.7). This pattern indicates that the true $\Delta^{238}U_{bulk\ carbonate\text{-}seawater}$ values for the limestone may be variable owing to differential accumulations of ^{238}U-enriched authigenic U phases during early diagenesis, which probably contributes to strong fluctuations of the inferred $\delta^{238}U_{OC}$ values.

In addition, this positive relationship implies that samples with least enrichments of ^{238}U ($\delta^{238}U_{carb}$ = −0.82 and −0.97) are most likely representative of seawater as they could have seen the least addition of diagenetic U phases. If this is the case, marine anoxia might have been more prevalent than the modelling result in Section 4.5.3. However, further investigations on seawater δ^{238}U during this time interval are required to verify this assumption.

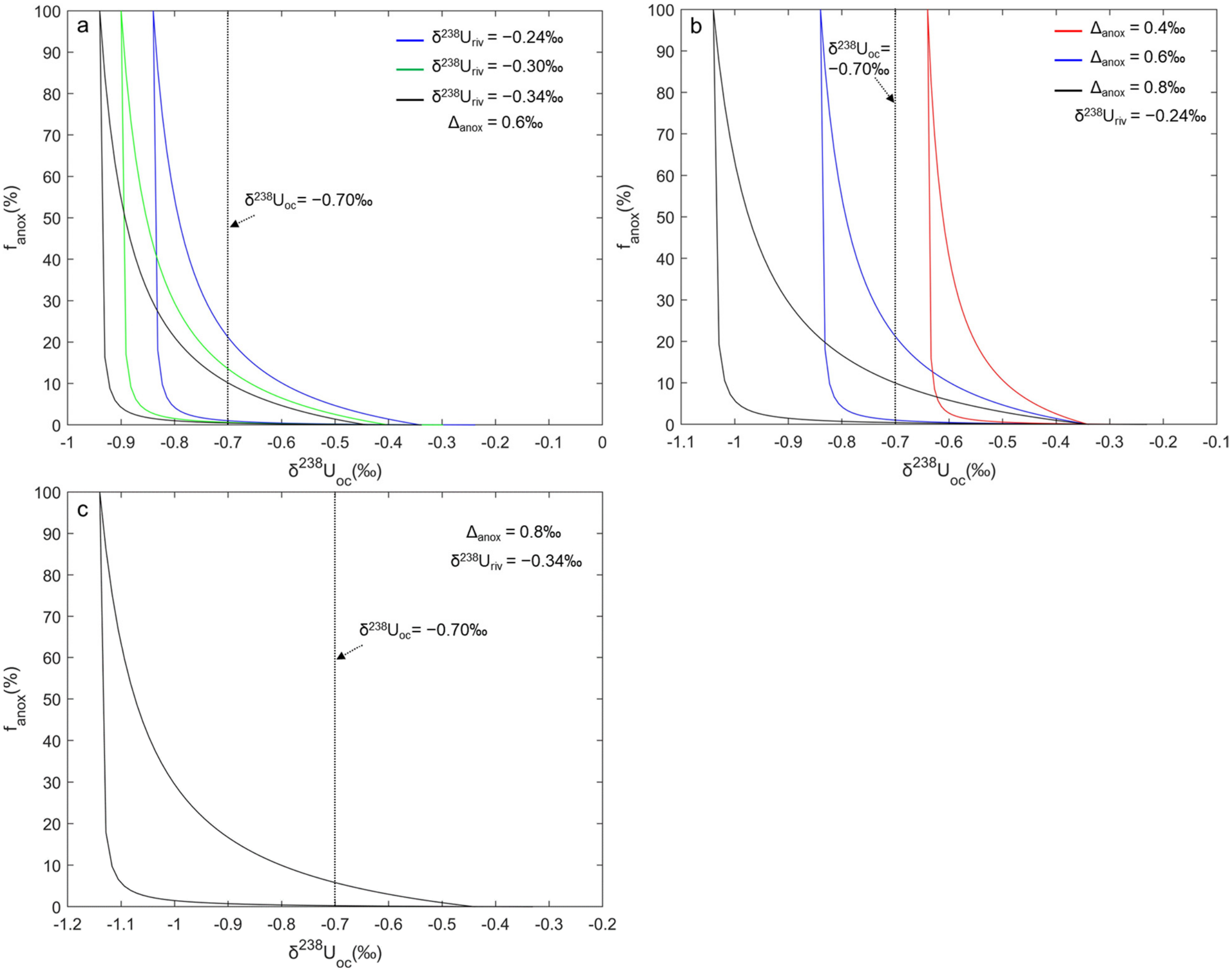

Figure 4.10: Model sensitivity analysis. (a) Solutions for the f_{anox} when $\delta^{238}U_{riv}$ equals −0.24‰ (blue), −0.30‰ (green), and −0.34‰ (black), respectively. (b) Solutions for the f_{anox} when Δ_{anox} equals 0.4‰ (red), 0.6‰ (blue), and 0.8‰ (black), respectively. (c) Solution for the f_{anox} in an extreme scenario when $\delta^{238}U_{riv}$ = −0.34‰ and Δ_{anox} = 0.8‰, and the modeled minimum and maximum f_{anox} values are 0.3% and 5.8% (respectively) for a given $\delta^{238}U_{oc}$ value of −0.70‰. Details in Section 4.5.3. The MATLAB codes are available in Appendix 4.6.

Second, the $\delta^{238}U_{OC}$ variations of this interval might be linked to marine redox fluctuations (e.g., Dahl et al., 2014; Kendall et al., 2015; Wei et al., 2018). The high amplitude $\delta^{238}U$ fluctuation near the Є-O boundary (from ~0.2 to 1.0‰, Figure 4.4), similar to or even greater than those associated with other globally recognized oceanic anoxic events, should have coincided with drastic oscillations of the global carbon cycle and severe oceanic mass extinctions (e.g., Brennecka et al., 2011; Dahl et al., 2014, 2019; Bartlett et al., 2018; Cheng et al., 2020). However, neither globally recognized pronounced carbonate $\delta^{13}C_{carb}$ excursions nor dramatic mass extinctions have been reported at the Є-O transition (Rasmussen et al., 2019; Stigall et al., 2019; Goldberg et al., 2021). Instead, only several globally recognized low amplitude $\delta^{13}C_{carb}$ excursions and low-level marine biocrises have been observed during this time period (Saltzman et al., 2015). Therefore, marine redox oscillations at the Є-O boundary may not be as strong as shown by the estimated $\delta^{238}U_{OC}$ values. Perhaps, the $\delta^{238}U_{OC}$ variation is amplified because the

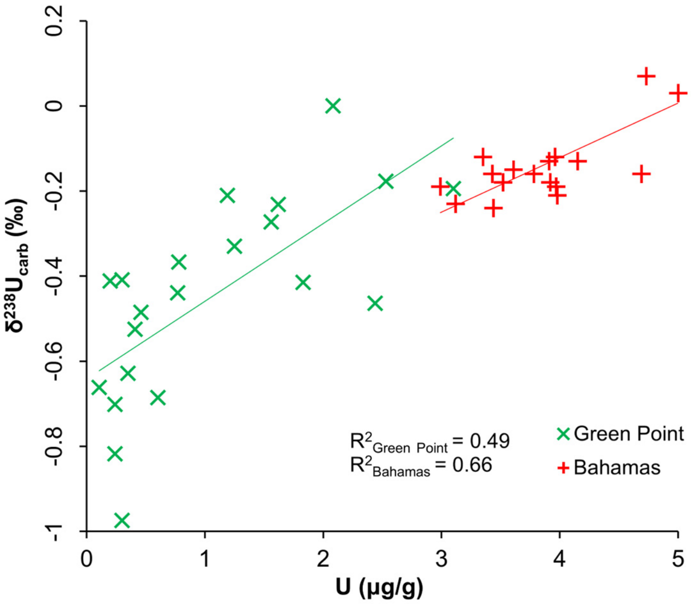

Figure 4.11: Lime mudstone of the Green Point Formation displaying a positive correlation between the $\delta^{238}U_{carb}$ values and U contents ($R^2 = 0.49$, $p < 0.01$), which is analogous to modern primary aragonite precipitates in the Bahamas (Romaniello et al., 2013, Appendix 4.7). Green and red solid lines represent the regression lines of samples from the Green Point Formation and the Bahamas, respectively.

$\delta^{238}U_{OC}$ values are estimated using the average $\Delta^{238}U_{\text{bulk carbonate-seawater}}$ value. Several modern seawater-like $\delta^{238}U_{OC}$ values of this interval could be either evidence of episodic marine oxygenation events or the result of using an inexact $\Delta^{238}U_{\text{bulk carbonate-seawater}}$ estimate.

However, neither of the above possibilities for fluctuations in the estimated $\delta^{238}U_{OC}$ values could be ruled out in the present study. Further studies on the $\delta^{238}U$ of carbonates from other correlated equivalent stratigraphic sections will contribute to the reconstruction of oceanic redox states at the Є-O transition and the refinement of the method for estimating marine $\delta^{238}U$ signatures using bulk carbonate $\delta^{238}U$ records.

Conclusions

The slope lime mudstone of the Green Point Formation (GSSP of the Є-O boundary) in western Newfoundland are strongly depleted in iodine, with I/Ca ratios spanning narrowly from 0.02 to 0.33 μmol/mol. Lack of correlations between the I/Ca ratios and the [Sr], $\delta^{18}O$, Mn/Sr, Fe/Sr, Mg/Ca, and $\delta^{13}C_{org}$ values, along with near-micritic textures and dull to non-luminescence of the limestone, demonstrate that the I/Ca signatures are insignificantly affected by diagenetic alteration.

The substantially low lime mudstone I/Ca ratios, which fall well below the background ratios of ~0.5 to 1 μmol/mol during the Proterozoic Eon, indicate the presence of a shallow marine oxic-anoxic interface along the regional continental margin during the studied time interval. Similarly, significantly low limestone I/Ca ratios and dysoxic to anoxic depositional conditions have been reported from several other age-equivalent shelf and slope sediments deposited along the Iapetan and Laurentian continental margins. This observation implies that seawater covering the shelf and/or slope areas along the Iapetan and Laurentian continental margins was probably commonly weakly oxygenated with a shallow oxycline or expanded oxygen minimum zones at the Є-O transition. Consistent with this interpretation, our three-sink U-isotope mass balance model predicts that the Є-O boundary was a time of expanded marine anoxia with anoxic to euxinic water covering 1.0 to 21.1% of the ocean floor, which is substantially higher than the modern ocean ($f_{anox} \approx 0.2\%$). Furthermore, the large variation of oceanic $\delta^{238}U_{OC}$ (−1.22 to −0.25‰) values, inferred from the limestone $\delta^{238}U_{carb}$ signals, might reflect oceanic redox oscillations during this time interval. However, these variations could also be attributed to the utilization of an inexact average $\Delta^{238}U_{bulk\ carbonate-seawater}$ estimate.

The current study provides further evidence for previous viewpoints that the slowness of marine biodiversity accumulation from the late Cambrian to the Early Ordovician was associated with expanded marine anoxia. The near-primary lime mudstone I/Ca signals of the GSSP Є-O boundary in western Newfoundland provide a more comprehensive picture of oceanic redox states in the early Paleozoic and a valuable complement to the existing carbonate I/Ca records.

Acknowledgments

The authors wish to thank Dr. Thomas J Algeo and the other two anonymous reviewers for their constructive reviews. Also, the efforts of Dr. Daniel S Alessi (editor) and journal managers are much appreciated. Special thanks to lab technicians from the BRGM for their help with the iodine concentration analyses. This project was supported by funding (to Karem Azmy) from Petroleum Exploration Enhancement Program (PEEP), Nalcor Energy (NL, Canada), and MITACS.

References

Al-Aasm, I.S., Veizer, J., 1986. Diagenetic stabilization of aragonite and low-Mg calcite; II, Stable isotopes in rudists. J. Sediment. Res. 56(6), 763-770.

Algeo, T.J., Marenco, P.J., Saltzman, M.R., 2016. Co-evolution of oceans, climate, and the biosphere during the 'Ordovician Revolution': A review. Palaeogeogr. Palaeoclimatol. Palaeoecol. 458, 1-11.

Algeo, T.J., Tribovillard, N., 2009. Environmental analysis of paleoceanographic systems based on molybdenum–uranium covariation. Chem. Geol. 268(3-4), 211-225.

Algeo, T.J., Wilkinson, B.H., Lohmann, K.C., 1992. Meteoric-burial diagenesis of Middle Pennsylvanian limestones in the Orogrande Basin, New Mexico; water/rock interactions and basin geothermics. J. Sediment. Res. 62(4), 652–670.

Álvarez, F., Reich, M., Snyder, G., Pérez-Fodich, A., Muramatsu, Y., Daniele, L., Fehn, U., 2016. Iodine budget in surface waters from Atacama: Natural and anthropogenic iodine sources revealed by halogen geochemistry and iodine-129 isotopes. Appl. Geochem. 68, 53-63.

Amachi, S., Kawaguchi, N., Muramatsu, Y., Tsuchiya, S., Watanabe, Y., Shinoyama, H., Fujii, T., 2007. Dissimilatory iodate reduction by marine Pseudomonas sp. strain SCT. Appl Environ Microbiol 73(18), 5725-5730.

Andersen, M.B., Romaniello, S., Vance, D., Little, S.H., Herdman, R., Lyons, T.W., 2014. A modern framework for the interpretation of 238U/235U in studies of ancient ocean redox. Earth Planet. Sci. Lett. 400, 184-194.

Andersen, M.B., Stirling, C.H., Weyer, S., 2017. Uranium Isotope Fractionation. Rev. Mineral. Geochem. 82(1), 799-850.

Andersen, M.B., Vance, D., Morford, J.L., Bura-Nakić, E., Breitenbach, S.F.M., Och, L., 2016. Closing in on the marine 238 U/ 235 U budget. Chem. Geol. 420, 11-22.

Azmy, K., Brand, U., Sylvester, P., Gleeson, S.A., Logan, A., Bitner, M.A., 2011. Biogenic and abiogenic low-Mg calcite (bLMC and aLMC): Evaluation of seawater-REE composition, water masses and carbonate diagenesis. Chem. Geol. 280(1-2), 180-190.

Azmy, K., Kendall, B., Brand, U., Stouge, S., Gordon, G.W., 2015. Redox conditions across the Cambrian–Ordovician boundary: Elemental and isotopic signatures retained in the GSSP carbonates. Palaeogeogr. Palaeoclimatol. Palaeoecol. 440, 440-454.

Azmy, K., Stouge, S., Brand, U., Bagnoli, G., Ripperdan, R., 2014. High-resolution chemostratigraphy of the Cambrian–Ordovician GSSP: Enhanced global correlation tool. Palaeogeogr. Palaeoclimatol. Palaeoecol. 409, 135-144.

Babbin, A.R., Peters, B.D., Mordy, C.W., Widner, B., Casciotti, K.L., Ward, B.B., 2017. Multiple metabolisms constrain the anaerobic nitrite budget in the Eastern Tropical South Pacific. Global Biogeochem. Cycles 31(2), 258-271.

Banner, J.L., Hanson, G.N., 1990. Calculation of simultaneous isotopic and trace element variations during water-rock interaction with applications to carbonate diagenesis. Geochim. Cosmochim. Acta 54(11), 3123-3137.

Barnes, C.E., Cochran, J.K., 1993. Uranium geochemistry in estuarine sediments: Controls on removal and release processes. Geochim. Cosmochim. Acta 57, 555-569.

Barnes, C.R., 1988. The proposed Cambrian–Ordovician global Boundary stratotype and point (GSSP) in Western Newfoundland, Canada. Geol. Mag. 125(4), 381-414.

Bartlett, R., Elrick, M., Wheeley, J.R., Polyak, V., Desrochers, A., Asmerom, Y., 2018. Abrupt global-ocean anoxia during the Late Ordovician-early Silurian detected using uranium isotopes of marine carbonates. Proc. Natl. Acad. Sci. U. S. A. 115(23), 5896-5901.

Berry, W.B.N., Wilde, P., Quinby-Hunt, M.S., Orth, C.J., 1986. Trace element signatures in Dictyonema Shales and their geochemical and stratigraphic significance. Norsk Geol. Tidsskr. 66(1), 45-51.

Brand, U., Veizer, J., 1980. Chemical diagenesis of a multicomponent carbonate system; 1, Trace elements. J. Sediment. Petrol. 50(4), 1219-1236.

Brennecka, G.A., Herrmann, A.D., Algeo, T.J., Anbar, A.D., 2011. Rapid expansion of oceanic anoxia immediately before the end-Permian mass extinction. Proc. Natl. Acad. Sci. U. S. A. 108(43), 17631-17634.

Buatois, L.A., Mangano, M.G., Olea, R.A., Wilson, M.A., 2016. Decoupled evolution of soft and hard substrate communities during the Cambrian Explosion and Great Ordovician Biodiversification Event. Proc. Natl. Acad. Sci. U. S. A. 113(25), 6945-6948.

Bura-Nakić, E., Andersen, M.B., Archer, C., de Souza, G.F., Marguš, M., Vance, D., 2018. Coupled Mo-U abundances and isotopes in a small marine euxinic basin: Constraints on processes in euxinic basins. Geochim. Cosmochim. Acta 222, 212-229.

Bura-Nakić, E., Sondi, I., Mikac, N., Andersen, M.B., 2020. Investigating the molybdenum and uranium redox proxies in a modern shallow anoxic carbonate rich marine sediment setting of the Malo Jezero (Mljet Lakes, Adriatic Sea). Chem. Geol. 533.

Cawood, P.A., McCausland, P.J.A., Dunning, G.R., 2001. Opening Iapetus; constraints from the Laurentian margin in Newfoundland. Geol. Soc. Am. Bull. 113, 443-453.

Charette, M.A., Smith, W.H.F., 2010. The Volume of earth's Ocean. Oceanography 23, 112-114.

Chen, X., Romaniello, S.J., Herrmann, A.D., Hardisty, D., Gill, B.C., Anbar, A.D., 2018. Diagenetic effects on uranium isotope fractionation in carbonate sediments from the Bahamas. Geochim. Cosmochim. Acta 237, 294-311.

Cheng, K., Elrick, M., Romaniello, S.J., 2020. Early Mississippian ocean anoxia triggered organic carbon burial and late Paleozoic cooling: Evidence from uranium isotopes recorded in marine limestone. Geology 48(4), 363-367.

Coniglio, M., James, N.P., 1990. Origin of fine-grained carbonate and siliciclastic sediments in an Early Palaeozoic slope sequence, Cow Head Group, western Newfoundland. Sedimentology 37, 215-230.

Cooper, R.A., Nowlan, G.S., Williams, S.H., 2001. Global Stratotype Section and Point for base of the Ordovician System. Episodes 24, 19-28.

Councell, T.B., Landa, E.R., Lovley, D.R., 1997. Microbial Reduction of Iodate. Water Air Soil Pollut. 100, 99-106.

Dahl, T.W., Boyle, R.A., Canfield, D.E., Connelly, J.N., Gill, B.C., Lenton, T.M., Bizzarro, M., 2014. Uranium isotopes distinguish two geochemically distinct stages during the later Cambrian SPICE event. Earth Planet. Sci. Lett. 401, 313-326.

Dahl, T.W., Connelly, J.N., Li, D., Kouchinsky, A., Gill, B.C., Porter, S., Maloof, A.C., Bizzarro, M., 2019. Atmosphere-ocean oxygen and productivity dynamics during early animal radiations. Proc. Natl. Acad. Sci. U. S. A. 116(39), 19352-19361.

Dahl, T.W., Hammarlund, E.U., Anbar, A.D., Bond, D.P., Gill, B.C., Gordon, G.W., Knoll, A.H., Nielsen, A.T., Schovsbo, N.H., Canfield, D.E., 2010. Devonian rise in atmospheric oxygen correlated to the radiations of terrestrial plants and large predatory fish. Proc. Natl. Acad. Sci. U. S. A. 107(42), 17911-17915.

Decraene, M.-N., Marin-Carbonne, J., Thomazo, C., Brayard, A., Bouvier, A.-S., Bomou, B., Adatte, T., Olivier, N., 2023. Pyrite iron isotope compositions track local sedimentation conditions through the Smithian-Spathian transition (Early Triassic, Utah, USA). Palaeogeogr. Palaeoclimatol. Palaeoecol. 617.

del Rey, A., Rasmussen, C.M.O., Calner, M., Wu, R., Asael, D., Dahl, T.W., 2022. Stable ocean redox during the main phase of the Great Ordovician Biodiversification Event. Commun Earth Environ 3(1), 220.

Deng, Y., Fan, J., Yang, S., Shi, Y., Lu, Z., Xu, H., Sun, Z., Zhao, F., Hou, Z., 2023. No Furongian Biodiversity Gap: Evidence from South China. Palaeogeogr. Palaeoclimatol. Palaeoecol. 618.

Deng, Y., Fan, J., Zhang, S., Fang, X., Chen, Z., Shi, Y., Wang, H., Wang, X., Yang, J., Hou, X., Wang, Y., Zhang, Y., Chen, Q., Yang, A., Fan, R., Dong, S., Xu, H., Shen, S., 2021. Timing and patterns of the Great Ordovician Biodiversification Event and Late Ordovician mass extinction: Perspectives from South China. Earth-Science Reviews 220.

Djogić, R., Sipos, L., Branica, M., 1986. Characterization of Uranium (VI) in Seawater. Limnol. Oceanogr. 31(5), 1122-1131.

Dunk, R.M., Mills, R.A., Jenkins, W.J., 2002. A reevaluation of the oceanic uranium budget for the Holocene. Chem. Geol. 190, 45-67.

Edwards, C.T., Fike, D.A., Saltzman, M.R., Lu, W., Lu, Z., 2018. Evidence for local and global redox conditions at an Early Ordovician (Tremadocian) mass extinction. Earth Planet. Sci. Lett. 481, 125-135.

Elrick, M., Rieboldt, S., Saltzman, M., McKay, R.M., 2011. Oxygen-isotope trends and seawater temperature changes across the Late Cambrian Steptoean positive carbon-isotope excursion (SPICE event). Geology 39(10), 987-990.

Fan, R.-y., Zong, R.-w., Gong, Y.-m., 2021. Behavioural imprint of the Ordovician Radiation: Evidence from Middle–Upper Ordovician deep-sea trace fossils in western Inner Mongolia, North China. Palaeogeogr. Palaeoclimatol. Palaeoecol. 563.

Farrenkopf, A.M., Dollhopf, M.E.C., Ní, S., Luther, G.W., Nealson, K.H., 1997. Reduction of iodate in seawater during Arabian Sea incubations and in laboratory cultures of the marine Shewanella putrefaciens strain MR-4. Mar. Chem. 57, 347-354.

Fehn, U., 2012. Tracing Crustal Fluids: Applications of Natural129I and36Cl. Annual Review of Earth and Planetary Sciences 40(1), 45-67.

Feng, X., Redfern, S.A.T., 2018. Iodate in calcite, aragonite and vaterite CaCO3: Insights from first-principles calculations and implications for the I/Ca geochemical proxy. Geochim. Cosmochim. Acta 236, 351-360.

Gao, G., Land, L.S., 1991. Geochemistry of Cambro-Ordovician Arbuckle limestone, Oklahoma: Implications for diagenetic d18O alteration and secular d13C and 87Sr/86Sr variation. Geochim. Cosmochim. Acta 55, 2911-2920.

Gilleaudeau, G.J., Romaniello, S.J., Luo, G., Kaufman, A.J., Zhang, F., Klaebe, R.M., Kah, L.C., Azmy, K., Bartley, J.K., Zheng, W., Knoll, A.H., Anbar, A.D., 2019. Uranium isotope evidence for limited euxinia in mid-Proterozoic oceans. Earth Planet. Sci. Lett. 521, 150-157.

Goldberg, S.L., Present, T.M., Finnegan, S., Bergmann, K.D., 2021. A high-resolution record of early Paleozoic climate. Proc. Natl. Acad. Sci. U. S. A. 118(6).

Hardisty, D.S., Horner, T.J., Evans, N., Moriyasu, R., Babbin, A.R., Wankel, S.D., Moffett, J.W., Nielsen, S.G., 2021. Limited iodate reduction in shipboard seawater incubations from the Eastern Tropical North Pacific oxygen deficient zone. Earth Planet. Sci. Lett. 554.

Hardisty, D.S., Lu, Z., Bekker, A., Diamond, C.W., Gill, B.C., Jiang, G., Kah, L.C., Knoll, A.H., Loyd, S.J., Osburn, M.R., Planavsky, N.J., Wang, C., Zhou, X., Lyons, T.W., 2017. Perspectives on Proterozoic surface ocean redox from iodine contents in ancient and recent carbonate. Earth Planet. Sci. Lett. 463, 159-170.

Hardisty, D.S., Lu, Z., Planavsky, N.J., Bekker, A., Philippot, P., Zhou, X., Lyons, T.W., 2014. An iodine record of Paleoproterozoic surface ocean oxygenation. Geology 42(7), 619-622.

He, R., Jiang, G., Lu, W., Lu, Z., 2020a. Iodine records from the Ediacaran Doushantuo cap carbonates of the Yangtze Block, South China. Precambrian Res. 347.

He, R., Lu, W., Junium, C.K., Ver Straeten, C.A., Lu, Z., 2020b. Paleo-redox context of the Mid-Devonian Appalachian Basin and its relevance to biocrises. Geochim. Cosmochim. Acta 287, 328-340.

Henderson, G.M., Anderson, R.F., 2003. The U-series toolbox for paleoceanography. Rev. Mineral. Geochem. 52, 493-531.

Jacobi, R.D., 1981. Peripheral bulge—a causal mechanism for the Lower/Middle Ordovician unconformity along the western margin of the Northern Appalachians. Earth Planet. Sci. Lett. 56, 245-251.

James, N.P., Stevens, R.K., 1986. Stratigraphy and correlation of the Cambro-Ordovician Cow Head group, western Newfoundland. Geological Survey of Canada, pp. 1-152.

James, N.P., Stevens, R.K., Barnes, C.R., Knight, I., 1989. Evolution of a Lower Paleozoic continental-margin carbonate platform, northern Canadian Appalachians. AAPG Bull. 44, 123-146.

Jansa, L.F., 1974. Trace fossils from the Cambro-Ordovician cow head group, newfoundland, and their paleobathymetric implication. Palaeogeogr. Palaeoclimatol. Palaeoecol. 15, 233-244.

Kendall, B., Komiya, T., Lyons, T.W., Bates, S.M., Gordon, G.W., Romaniello, S.J., Jiang, G., Creaser, R.A., Xiao, S., McFadden, K., Sawaki, Y., Tahata, M., Shu, D., Han, J., Li, Y., Chu, X., Anbar, A.D., 2015. Uranium and molybdenum isotope evidence for an episode of widespread ocean oxygenation during the late Ediacaran Period. Geochim. Cosmochim. Acta 156, 173-193.

Klinkhammer, G.P., Palmer, M.R., 1991. Uranium in the oceans: Where it goes and why. Geochim. Cosmochim. Acta 55, 1799-1806.

Knight, I., Azmy, K., Boyce, W.D., Lavoie, D., 2008. Tremadocian carbonate rocks of the lower St. George group, Port au Port. Current Research (2008) Newfoundland and Labrador Department of Natural Resources Geological Survey Report 08-1, 115-149.

Knight, I., Azmy, K., Greene, M.G., Lavoie, D., 2007. Lithostratigraphic setting of diagenetic, isotopic, and geochemistry studies of Ibexian and Whiterockian carbonate rocks of the St. George and table head groups, Western Newfoundland. Current Research (2007) Newfoundland and Labrador Department of Natural Resources Geological Survey, Report 07-1, 55-84.

Knight, I., James, N.P., Lane, T.E., 1991. The Ordovician St. George unconformity, Northern Appalachians; the relationship of plate convergence at the St. Lawrence Promontory to the Sauk/Tippecanoe Sequence boundary. Geol. Soc. Am. Bull. 103, 1200-1225.

Kozik, N.P., Young, S.A., Lindskog, A., Ahlberg, P., Owens, J.D., 2023. Protracted oxygenation across the Cambrian-Ordovician transition: A key initiator of the Great Ordovician Biodiversification Event? Geobiology 21(3), 323-340.

Kozik, N.P., Young, S.A., Newby, S.M., Liu, M., Chen, D., Hammarlund, E.U., Bond, D.P.G., Them, T.R., Owens, J.D., 2022. Rapid marine oxygen variability: Driver of the Late Ordovician mass extinction. Science advances 8(46), eabn8345.

Landing, E., 2012. Time-specific black mudstones and global hyperwarming on the Cambrian–Ordovician slope and shelf of the Laurentia palaeocontinent. Palaeogeogr. Palaeoclimatol. Palaeoecol. 367-368, 256-272.

Lau, K.V., Lyons, T.W., Maher, K., 2020. Uranium reduction and isotopic fractionation in reducing sediments: Insights from reactive transport modeling. Geochim. Cosmochim. Acta 287, 65-92.

Lau, K.V., Maher, K., Altiner, D., Kelley, B.M., Kump, L.R., Lehrmann, D.J., Silva-Tamayo, J.C., Weaver, K.L., Yu, M., Payne, J.L., 2016. Marine anoxia and delayed Earth system recovery after the end-Permian extinction. Proc. Natl. Acad. Sci. U. S. A. 113(9), 2360-2365.

Lavoie, D., Desrochers, A., Dix, G., Knight, I., Hersi, O.S., 2012. The Great American Carbonate Bank in eastern Canada: an overview. in J. R. Derby, R. D. Fritz, S. A. Longacre, W. A. Morgan, and C. A. Sternbach, eds., The great American carbonate bank: The geology and economic resources of the Cambrian – Ordovician Sauk megasequence of Laurentia: AAPG Mem. 98, 499-523.

Lenton, T.M., Dahl, T.W., Daines, S.J., Mills, B.J., Ozaki, K., Saltzman, M.R., Porada, P., 2016. Earliest land plants created modern levels of atmospheric oxygen. Proc. Nat. Acad. Sci. U.S.A. 113(35), 9704-9709.

LeRoy, M.A., Gill, B.C., Sperling, E.A., McKenzie, N.R., Park, T.-Y.S., 2021. Variable redox conditions as an evolutionary driver? A multi-basin comparison of redox in the middle and later Cambrian oceans (Drumian-Paibian). Palaeogeogr. Palaeoclimatol. Palaeoecol. 566.

Li, H., Tissot, F.L.H., 2023. UID: The uranium isotope database. Chem. Geol. 618.

Li, J., Azmy, K., Kendall, B., 2022. The Mo- and U-isotope signatures in alternating shales and carbonate beds of rhythmites: A comparison and implications for redox conditions across the Cambrian-Ordovician boundary. Chem. Geol. 602.

Liu, A., Tang, D., Shi, X., Zhou, X., Zhou, L., Shang, M., Li, Y., Fang, H., 2020. Mesoproterozoic oxygenated deep seawater recorded by early diagenetic carbonate concretions from the Member IV of the Xiamaling Formation, North China. Precambrian Res. 341.

Lu, W., Ridgwell, A., Thomas, E., Hardisty, D.S., Luo, G., Algeo, T.J., Saltzman, M.R., Gill, B.C., Shen, Y., Ling, H.-F., Edwards, C.T., Whalen, M.T., Zhou, X., Gutchess, K.M., Jin, L., Rickaby, R.E.M., Jenkyns, H.C., Lyons, T.W., Lenton, T.M., Kump, L.R., Lu, Z., 2018. Late inception of a resiliently oxygenated upper ocean. Science 361, 174-177.

Lu, W., Barbosa, C.F., Rathburn, A.E., Xavier, P.d.M., Cruz, A.P.S., Thomas, E., Rickaby, R.E.M., Zhang, Y.G., Lu, Z., 2021. Proxies for paleo-oxygenation: A downcore comparison between benthic foraminiferal surface porosity and I/Ca. Palaeogeogr. Palaeoclimatol. Palaeoecol. 579.

Lu, W., Dickson, A.J., Thomas, E., Rickaby, R.E.M., Chapman, P., Lu, Z., 2019. Refining the planktic foraminiferal I/Ca proxy: Results from the Southeast Atlantic Ocean. Geochim. Cosmochim. Acta 287, 318-327.

Lu, W., Rickaby, R.E.M., Hoogakker, B.A.A., Rathburn, A.E., Burkett, A.M., Dickson, A.J., Martínez-Méndez, G., Hillenbrand, C.-D., Zhou, X., Thomas, E., Lu, Z., 2020. I/Ca in epifaunal benthic foraminifera: A semi-quantitative proxy for bottom water oxygen in a multi-proxy compilation for glacial ocean deoxygenation. Earth Planet. Sci. Lett. 533.

Lu, X., Kendall, B., Stein, H.J., Li, C., Hannah, J.L., Gordon, G.W., Ebbestad, J.O.R., 2017. Marine redox conditions during deposition of Late Ordovician and Early Silurian organic-rich mudrocks in the Siljan ring district, central Sweden. Chem. Geol. 457, 75-94.

Lu, Z., Hoogakker, B.A.A., Hillenbrand, C.-D., Zhou, X., Thomas, E., Gutchess, K.M., Lu, W., Jones, L., Rickaby, R.E.M., 2016. Oxygen depletion recorded in upper waters of the glacial Southern Ocean. Nature communications 7, 1-8.

Lu, Z., Jenkyns, H.C., Rickaby, R.E.M., 2010. Iodine to calcium ratios in marine carbonate as a paleo-redox proxy during oceanic anoxic events. Geology 38(12), 1107-1110.

Marenco, P.J., Martin, K.R., Marenco, K.N., Barber, D.C., 2016. Increasing global ocean oxygenation and the Ordovician Radiation: Insights from Th/U of carbonates from the Ordovician of western Utah. Palaeogeogr. Palaeoclimatol. Palaeoecol. 458, 77-84.

McKenzie, N.R., Horton, B.K., E. Loomis, S., Stockli, D.F., Planavsky, N.J., Lee, C.-T.A., 2016. Continental arc volcanism as the principal driver of icehouse-greenhouse variability. Science 352, 444-447.

Morford, J.L., Emerson, S., 1999. The geochemistry of redox sensitive trace metals in sediments. Geochim. Cosmochim. Acta 63, 1735-1750.

Nielsen, A.T., Schovsbo, N.H., 2006. Cambrian to basal Ordovician lithostratigraphy in southern Scandinavia. Bulletin of the Geological Society of Denmark 53, 47-92.

Nägler, T.F., Anbar, A.D., Archer, C., Goldberg, T., Gordon, G.W., Greber, N.D., Siebert, C., Sohrin, Y., Vance, D., 2013. Proposal for an International Molybdenum Isotope Measurement Standard and Data Representation. Geostand. Geoanal. Res., 149-151.

Noordmann, J., Weyer, S., Montoya-Pino, C., Dellwig, O., Neubert, N., Eckert, S., Paetzel, M., Böttcher, M.E., 2015. Uranium and molybdenum isotope systematics in modern euxinic basins: Case studies from the central Baltic Sea and the Kyllaren fjord (Norway). Chem. Geol. 396, 182-195.

Nowak, H., Servais, T., Monnet, C., Molyneux, S.G., Vandenbroucke, T.R.A., 2015. Phytoplankton dynamics from the Cambrian Explosion to the onset of the Great Ordovician Biodiversification Event: A review of Cambrian acritarch diversity. Earth-Science Reviews 151, 117-131.

Pohl, A., Lu, Z., Lu, W., Stockey, R.G., Elrick, M., Li, M., Desrochers, A., Shen, Y., He, R., Finnegan, S., Ridgwell, A., 2021. Vertical decoupling in Late Ordovician anoxia due to reorganization of ocean circulation. Nat. Geosci. 14(11), 868-873.

Rasmussen, C.M.O., Kroger, B., Nielsen, M.L., Colmenar, J., 2019. Cascading trend of Early Paleozoic marine radiations paused by Late Ordovician extinctions. Proc. Natl. Acad. Sci. U. S. A. 116(15), 7207-7213.

Rolison, J.M., Stirling, C.H., Middag, R., Rijkenberg, M.J.A., 2017. Uranium stable isotope fractionation in the Black Sea: Modern calibration of the 238U/235U paleo-redox proxy. Geochim. Cosmochim. Acta 203, 69-88.

Romaniello, S.J., Herrmann, A.D., Anbar, A.D., 2013. Uranium concentrations and 238U/235U isotope ratios in modern carbonates from the Bahamas: Assessing a novel paleoredox proxy. Chem. Geol. 362, 305-316.

Rue, E.L., Smith, G.J., Cutter, G.A., Bruland, K.W., 1997. The response of trace element redox couples to suboxic conditions in the water column. Deep Sea Res. 44, 113-134.

Saltzman, M.R., Edwards, C.T., Adrain, J.M., Westrop, S.R., 2015. Persistent oceanic anoxia and elevated extinction rates separate the Cambrian and Ordovician radiations. Geology 43(9), 807-810.

Sarmiento, J.L., Gruber, N., 2006. Ocean Biogeochemical Dynamics. Princeton University Press, pp. 1-503.

Scotese, C.R., 2014. Atlas of Cambrian and Early Ordovician Paleogeographic Maps (Mollweide Projection), Maps 81-88. Early Paleozoic, PALEOMAP Atlas for ArcGIS, PALEOMAP Project, Evanston, IL 5.

Servais, T., Cascales-Miñana, B., Cleal, C.J., Gerrienne, P., Harper, D.A.T., Neumann, M., 2019. Revisiting the Great Ordovician Diversification of land plants: Recent data and perspectives. Palaeogeogr. Palaeoclimatol. Palaeoecol. 534.

Servais, T., Lehnert, O., Li, J.U.N., Mullins, G.L., Munnecke, A., NÜTzel, A., Vecoli, M., 2008. The Ordovician Biodiversification: revolution in the oceanic trophic chain. Lethaia 41(2), 99-109.

Servais, T., Owen, A.W., Harper, D.A.T., Kröger, B., Munnecke, A., 2010. The Great Ordovician Biodiversification Event (GOBE): The palaeoecological dimension. Palaeogeogr. Palaeoclimatol. Palaeoecol. 294(3-4), 99-119.

Shang, M., Tang, D., Shi, X., Zhou, L., Zhou, X., Song, H., Jiang, G., 2019. A pulse of oxygen increase in the early Mesoproterozoic ocean at ca. 1.57–1.56 Ga. Earth Planet. Sci. Lett. 527.

Song, H., Tong, J., Algeo, T.J., Song, H., Qiu, H., Zhu, Y., Tian, L., Bates, S., Lyons, T.W., Luo, G., Kump, L.R., 2014. Early Triassic seawater sulfate drawdown. Geochim. Cosmochim. Acta 128, 95-113.

Sperling, E.A., Frieder, C.A., Raman, A.V., Girguis, P.R., Levin, L.A., Knoll, A.H., 2013. Oxygen, ecology, and the Cambrian radiation of animals. Proc. Natl. Acad. Sci. U. S. A. 110(33), 13446-13451.

Stigall, A.L., Edwards, C.T., Freeman, R.L., Rasmussen, C.M.Ø., 2019. Coordinated biotic and abiotic change during the Great Ordovician Biodiversification Event: Darriwilian assembly of early Paleozoic building blocks. Palaeogeogr. Palaeoclimatol. Palaeoecol. 530, 249-270.

Stirling, C.H., Andersen, M.B., Warthmann, R., Halliday, A.N., 2015. Isotope fractionation of 238U and 235U during biologically-mediated uranium reduction. Geochim. Cosmochim. Acta 163, 200-218.

Tissot, F.L.H., Chen, C., Go, B.M., Naziemiec, M., Healy, G., Bekker, A., Swart, P.K., Dauphas, N., 2018. Controls of eustasy and diagenesis on the 238U/235U of carbonates and evolution of the seawater (234U/238U) during the last 1.4 Myr. Geochim. Cosmochim. Acta 242, 233-265.

Tissot, F.L.H., Dauphas, N., 2015. Uranium isotopic compositions of the crust and ocean: Age corrections, U budget and global extent of modern anoxia. Geochim. Cosmochim. Acta 167, 113-143.

Togo, Y.S., Takahashi, Y., Amano, Y., Matsuzaki, H., Suzuki, Y., Terada, Y., Muramatsu, Y., Ito, K., Iwatsuki, T., 2016. Age and speciation of iodine in groundwater and mudstones of the Horonobe area, Hokkaido, Japan: Implications for the origin and migration of iodine during basin evolution. Geochim. Cosmochim. Acta 191, 165-186.

Tostevin, R., Clarkson, M.O., Gangl, S., Shields, G.A., Wood, R.A., Bowyer, F., Penny, A.M., Stirling, C.H., 2019. Uranium isotope evidence for an expansion of anoxia in terminal Ediacaran oceans. Earth Planet. Sci. Lett. 506, 104-112.

Tripathy, G.R., Hannah, J.L., Stein, H.J., Yang, G., 2014. Re-Os age and depositional environment for black shales from the Cambrian-Ordovician boundary, Green Point, western Newfoundland. Geochem. Geophys. Geosyst. 15(4), 1021-1037.

Trotter, J.A., Williams, I.S., Barnes, C.R., Lécuyer, C., Nicoll, R.S., 2008. Did Cooling Oceans Trigger Ordovician Biodiversification? Evidence from Conodont Thermometry. Science 321, 550-554.

Truesdale, V.W., Bailey, G.W., 2000. Dissolved Iodate and Total Iodine During an Extreme Hypoxic Event in the Southern Benguela System. Estuar. Coast. Shelf Sci. 50(6), 751-760.

van der Velden, A.J., van Staal, C.R., Cook, F.A., 2004. Crustal structure, fossil subduction, and the tectonic evolution of the Newfoundland Appalachians: Evidence from a reprocessed seismic reflection survey. Geol. Soc. Am. Bull. 116(11-12), 1485-1498.

Waldron, J.W.F., Anderson, S.D., Cawood, P.A., Goodwin, L.B., Hall, J., Jamieson, R.A., Palmer, S.E., Stockmal, G.S., Williams, P.F., 1998. Evolution of the Appalachian Laurentian margin: Lithoprobe results in western Newfoundland. Can. J. Earth Sci. 35, 1271-1287.

Wei, G.-Y., Planavsky, N.J., He, T., Zhang, F., Stockey, R.G., Cole, D.B., Lin, Y.-B., Ling, H.-F., 2021. Global marine redox evolution from the late Neoproterozoic to the early Paleozoic constrained by the integration of Mo and U isotope records. Earth-Science Reviews 214.

Wei, G.-Y., Planavsky, N.J., Tarhan, L.G., Chen, X., Wei, W., Li, D., Ling, H.-F., 2018. Marine redox fluctuation as a potential trigger for the Cambrian explosion. Geology 46(7), 587-590.

Wei, H., Wang, X., Shi, X., Jiang, G., Tang, D., Wang, L., An, Z., 2019. Iodine content of the carbonates from the Doushantuo Formation and shallow ocean redox change on the Ediacaran Yangtze Platform, South China. Precambrian Res. 322, 160-169.

Weyer, S., Anbar, A.D., Gerdes, A., Gordon, G.W., Algeo, T.J., Boyle, E.A., 2008. Natural fractionation of 238U/235U. Geochim. Cosmochim. Acta 72(2), 345-359.

Wilde, P., Quinby-Hunt, M.S., Berry, W.B.N., Orth, C.J., 1989. Palaeo-oceanography and biogeography in the Tremadoc (Ordovician) Iapetus Ocean and the origin of the chemostratigraphy of Dictyonema flabelliforme black shales. Geol. Mag. 126(1), 19-27.

Wong, G.T.F., Brewer, P.G., 1977. The marine chemistry of iodine in anoxic basins. Geochim. Cosmochim. Acta 41, 151-159.

Zaffos, A., Finnegan, S., Peters, S.E., 2017. Plate tectonic regulation of global marine animal diversity. Proc. Natl. Acad. Sci. U. S. A. 114(22), 5653-5658.

Zhang, F., Algeo, T.J., Cui, Y., Shen, J., Song, H., Sano, H., Rowe, H.D., Anbar, A.D., 2018a. Global-ocean redox variations across the Smithian-Spathian boundary linked to concurrent climatic and biotic changes. Earth-Science Reviews 195, 147-168.

Zhang, F., Lenton, T.M., del Rey, Á., Romaniello, S.J., Chen, X., Planavsky, N.J., Clarkson, M.O., Dahl, T.W., Lau, K.V., Wang, W., Li, Z., Zhao, M., Isson, T., Algeo, T.J., Anbar, A.D., 2020. Uranium isotopes in marine carbonates as a global ocean paleoredox proxy: A critical review. Geochim. Cosmochim. Acta 287, 27-49.

Zhang, F., Romaniello, S.J., Algeo, T.J., Lau, K.V., Clapham, M.E., Richoz, S., Herrmann, A.D., Smith, H., Horacek, M., Anbar, A.D., 2018b. Multiple episodes of extensive marine anoxia linked to global warming and continental weathering following the latest Permian mass extinction. Science Advances 4, 1-9.

Zhang, S., Barnes, C.R., 2004. Late Cambrian and Early Ordovician conodont communities from platform and slope facies, western Newfoundland: a statistical approach. Geological Society, London, Special Publications 230, 47-72.

Zhao, Z., Thibault, N.R., Dahl, T.W., Schovsbo, N.H., Sorensen, A.L., Rasmussen, C.M.O., Nielsen, A.T., 2022. Synchronizing rock clocks in the late Cambrian. Nat Commun 13(1), 1990.

Zheng, Y., Anderson, R.F., Alexander, V.G., Martin, Q.F., 2002a. Preservation of particulate non-lithogenic uranium in marine sediments. Geochim. Cosmochim. Acta 60, 3085-3092.

Zheng, Y., Anderson, R.F., Alexander, V.G., Martin, Q.F., 2002b. Remobilization of authigenic uranium in marine sediments by bioturbation. Geochim. Cosmochim. Acta 66, 1759-1772.

Zhou, X., Jenkyns, H.C., Owens, J.D., Junium, C.K., Zheng, X.-Y., Sageman, B.B., Hardisty, D.S., Lyons, T.W., Ridgwell, A., Lu, Z., 2015. Upper ocean oxygenation dynamics from I/Ca ratios during the Cenomanian-Turonian OAE 2. Paleoceanography 30(5), 510-526.

Zhou, X., Thomas, E., Rickaby, R.E.M., Winguth, A.M.E., Lu, Z., 2014. I/Ca evidence for upper ocean deoxygenation during the PETM. Paleoceanography 29(10), 964-975.

Chapter 5

5. Conclusions and suggestions for future work

5.1. Conclusions

In this thesis, the isotopic and elemental signals of Mo and U, I/Ca ratios, and pyrite textures and $\delta^{34}S_{py}$ signals in shale and/or limestone from the Є-O boundary GSSP section at Green Point in western Newfoundland (Canada) were employed to investigate the depositional environments and contemporaneous marine redox states. The following section provides a summary of the key findings and general conclusions derived from this research:

1. The wide range of the shale $\delta^{98}Mo_{auth}$ values (–0.40 to +3.16‰) points to variable and less intensely reducing (~dysoxic/suboxic to anoxic) bottom water conditions during the deposition. A strong positive correlation between the $[Mo]_{auth}$ and $[U]_{auth}$ values, together with relatively low Mo concentrations compared to Phanerozoic euxinic shale, further suggests that the dissolved sulfide was mainly confined to sedimentary porewaters. Instead of being evidence for minor episodes of ocean oxygenation, two extraordinarily high shale $\delta^{98}Mo_{auth}$ values (+2.25‰ and +3.16‰) might be attributed to a combination of 1) the diffusion of ^{98}Mo-enriched shallower weak sulfidic porewaters into more intensely sulfidic deeper porewaters and 2) the subsequent (near)quantitative removal of aqueous Mo during early diagenesis.

2. The highly fluctuated $\delta^{98}Mo_{carb}$ values (–0.30 to +2.34‰) imply variable H_2S_{aq} levels in sedimentary porewaters during the deposition. Substantially low Mo concentrations in the limestone ($[Mo]_{carb} = 0.25 \pm 0.80$ μg/g, 2σ) and a lack of correlation between $[Mo]_{carb}$ and $\delta^{98}Mo_{carb}$ values point to weak sulfidic ($[H_2S]_{aq} < 11$ μM) porewater conditions during early diagenesis.

3. Several lines of evidence suggest that the investigated interval was likely deposited in a semi-restricted basin. Firstly, the shale exhibits an inverse relationship between the authigenic δ^{98}Mo and δ^{238}U values, similar to those observed in modern semi-restricted basins such as the Black Sea, the Cariaco Basin, and the Mediterranean. Secondly, the lime mudstone displays a prominent negative $\delta^{13}C_{carb}$ shift near the Є-O boundary, which contrasts with the positive $\delta^{13}C_{carb}$ excursions reported in age-equivalent stratigraphic sections on other continents. Moreover, the shale records significant negative correlations ($R^2 = 0.2$ to 0.4) between the $\delta^{34}S_{py}$ values and their [Al], [Th], and ∑REE counterparts, suggesting that regional terrestrial sulfate inputs likely regulated seawater sulfate levels along the continental margin. Furthermore, the eastern Laurentian continental margin at that time was surrounded by a series of off-margin microcontinents, which could have potentially separated the regional continental marginal seawater within the Taconic Seaway from the open ocean. The changeable connectivity between the local water mass and open ocean may have influenced the variability of authigenic Mo_{EF}/U_{EF} ratios recorded in the shale.

4. Two types of sedimentary biological pyrite are identified in the shale: (1) framboidal pyrite and (2) anhedral to euhedral pyrite. The latter is further categorized into two subtypes: type 2a anhedral to subhedral pyrite characterized by relict framboidal textures and larger sizes (~10 to 300 μm), and type 2b smaller (typically <10 μm) subhedral to euhedral pyrite. Type 1 pyrite was precipitated near the sediment-water interface (SWI), whereas type 2b pyrite was formed in sediments below the SWI with limited access to the overlying seawater sulfate. Type 2a pyrite was evolved from framboids during early and burial diagenesis.

5. The abundance of type 2b pyrite generally mimics the changes in $\delta^{34}S_{py}$, suggesting that the substantial $\delta^{34}S_{py}$ dispersion could be partially attributed to differing proportions of type

2b pyrite within the samples. Moreover, notable negative correlations exist between the $\delta^{34}S_{py}$ values and the abundances of Al, Th, ∑REE, and Fe, indicating that riverine fluxes might have influenced the $\Delta^{34}S_{seawater-pyrite}$ by modulating the regional sulfate and iron reservoir sizes.

6. The bulk sedimentary $\delta^{34}S_{py}$ fluctuation may be attributed to a combination of changes in regional terrigenous input and varying amounts of pyrite formed at different diagenetic stages within the samples. The general opposing trends between the $\delta^{34}S_{py}$ signals and the abundances of Al, Th, ∑REE, and Fe, however, imply that fluctuations in riverine influxes might exert a stronger influence on the major $\delta^{34}S_{py}$ trend. As a result, it is not recommended to use the bulk sedimentary $\delta^{34}S_{py}$ variability alone as evidence for perturbations in global sulfur cycle.

7. The substantially low lime mudstone I/Ca ratios, which fall below the background ratios of ~0.5 to 1 μmol/mol during the Proterozoic Eon, indicate the presence of a shallow marine oxic-anoxic interface along the regional continental margin. Significantly low carbonate I/Ca ratios (<0.5 μmol/mol) and dysoxic to anoxic depositional conditions have also been reported from several other age-equivalent sections deposited along the shelf and slope of ancient Iapetan and Laurentian continental margins. Therefore, seawater along the Iapetan and Laurentian continental margins at the Є-O transition might have been generally poorly oxygenated with a shallow oxycline or expanded oxygen minimum zones in the shelf and/or slope areas. This inference aligns with the greenhouse climates and suppressed ocean circulations at that time.

8. The average oceanic $\delta^{238}U$ signature during the Є-O transition, estimated from the limestone $\delta^{238}U_{carb}$ values, was approximately −0.70 ± 0.24‰ (1σ). Using this estimate, our three-sink U-isotope mass balance model predicts that this time interval experienced extensive marine anoxia, with anoxic to euxinic water covering ~ 1.0 to 21.1% of the ocean floor. This

finding is consistent with earlier viewpoints that the slowness of marine biodiversity accumulation from the middle-late Cambrian to the Early Ordovician was linked to expanded marine anoxia.

9. Large variations of the estimated oceanic $\delta^{238}U_{OC}$ (−1.22 to −0.25‰) potentially indicate marine redox oscillations during the Є-O transition. However, it is important to consider that these fluctuations could also be attributed to variable accumulations of the ^{238}U-enriched authigenic U phases in the limestone and the application of an approximate average estimate for the $\Delta^{238}U_{\text{bulk carbonate-seawater}}$.

5.2. Suggestions for future work

The $\delta^{34}S$ signals of carbonate-associated sulfate have played a significant role in studying variations in sulfur isotope records of paleo-seawater. Given that lime mudstone of the sampled interval is well preserved with near-micritic textures, analyzing the $\delta^{34}S$ signatures of carbonate-associated sulfate may provide valuable insights into the global marine sulfur cycle during the Є-O transition. Additionally, measuring coeval seawater sulfate levels can be achieved if coupled with analyzing the pyrite $\delta^{34}S$ signals in the lime mudstone. However, it is important to exercise caution in interpreting these results, as these limestones were likely deposited in a partially restricted basin.

The wide range of the $\delta^{238}U$ offset between bulk carbonates and seawater presents challenges when approximating paleo-seawater $\delta^{238}U$ signatures using bulk carbonate $\delta^{238}U$ values. Therefore, it is crucial to develop a refined and more reliable method for estimating ancient oceanic $\delta^{238}U$ signatures using bulk $\delta^{238}U_{carb}$ signals. This advancement will contribute to more accurate reconstructions of $\delta^{238}U$ variations over geological time, enhancing our understanding of past oceanic redox conditions.

Appendices

Appendix 3.1: Pyrite SEM and optical microscopic images

This file can be downloaded through the following google drive link:
https://docs.google.com/document/d/1CR5i9IjIEoykrUKBIAsg8lS6u7ujx9g4/edit?usp=sharing&ouid=110832369128749161575&rtpof=true&sd=true

Appendix 3.2: The original chromium-reducible sulfur extraction result

Sample ID	Material	Mass extracted/g	Corrected $\delta^{34}S$/‰	Purity %	Average $\delta^{34}S$/‰	SD	Yield Ag_2S/mg	S wt%	Compiled $\delta^{34}S$ CRS/‰
GPS1	CRS	0.214	-6.6	95.4	-6.8	0.3	11.344	0.7	-6.8
GPS1rpt	CRS		-6.9	102.0					
GPS3	CRS	0.529	-12.9	98.8			20.619	0.5	-12.9
GPS4	CRS	0.522	-10.7	106.7			39.62	1.0	-10.7
GPS7	CRS	0.522	-15.1	98.1			7.835	0.2	-15.1
GPS8	CRS	0.493	-9.5	112.4	-9.5	0.04	17.413	0.5	-9.5
GPS8rpt	CRS		-9.5	97.1					
GPS10	CRS	0.220	-3.9	103.8	-3.3	0.9	14.68	0.9	-3.3
GPS10rpt	CRS		-2.7	106.6					
GPS13	CRS	0.526	-13.4	96.9			46.09	1.1	-13.4
GPS14	CRS	0.491	-2.2	98.3	-2.1	0.1	20.96	0.6	-2.1
GPS14rpt	CRS		-2.0	106.5					
GPS16	CRS	0.301	-1.8	109.4			14.47	0.6	-1.8
GPS19	CRS	0.306	-10.7	89.8			19.79	0.8	-10.7
GPS26	CRS	0.315	-4.8	106.0	-4.6	0.3	14.88	0.6	-4.6
GPS26rpt	CRS		-4.4	98.1					
GPS27	CRS	0.319	-13.9	98.5			5.20	0.2	-13.9
GPS30	CRS	0.315	-14.3	85.7	-14.4	0.2	1.90	0.1	-14.4
GPS30rpt	CRS		-14.6	97.6					
GPS34	CRS	0.296	-10.7	99.5			7.43	0.3	-10.7
GPS39	CRS	0.309	-6.8	99.5	-6.4	0.5	8.64	0.4	-6.4
GPS39rpt	CRS		-6.1	107.8					
GPS41	CRS	0.261	-2.4	100.1			9.54	0.5	-2.4
GPS44	CRS	0.238	-12.0	99.8			8.68	0.5	-12.0
GPS47	CRS	0.230	-17.4	98.5			10.17	0.6	-17.4
GPS49	CRS	0.274	-17.6	100.6			10.74	0.5	-17.6
GPS53	CRS	0.229	9.3	97.6	9.6	0.4	4.16	0.2	9.6
GPS53rpt	CRS		9.8	102.7					
GPS57	CRS	0.211	11.4	104.6			9.67	0.6	11.4
GPS61	CRS	0.213	0.9	98.0	1.1	0.4	9.136	0.6	1.1
GPS61rpt	CRS		1.4	97.8					
GPS63	CRS	0.230	3.4	104.3	3.2	0.3	6.65	0.4	3.2
GPS63rpt	CRS		3.0	102.9					
GPS66	CRS	0.208	1.9	106.5			10.08	0.6	1.9
GPS68	CRS	0.246	13.9	109.2			10.94	0.6	13.9
GPS71	CRS	0.211	7.0	96.9			10.322	0.6	7.0
GPS75	CRS	0.214	13.7	95.5			9.541	0.6	13.7
GPS79	CRS	0.246	6.1	104.8			3.413	0.2	6.1
GPS82	CRS	0.201	22.4	107.2			5.02	0.3	22.4
GPS84	CRS	0.226	14.5	98.6	14.4	0.1	8.159	0.5	14.4
GPS84rpt	CRS		14.3	102.1					
GPS149	CRS	0.261	12.2	95.9	12.4	0.3	9.05	0.4	12.4
GPS149rpt	CRS		12.6	96.9					
GPS150	CRS	0.217	-1.4	107.2	-1.3	0.2	22.35	1.3	-1.3
GPS150rpt	CRS		-1.2	105.1					

Table continued

Sample ID	Material	Mass extracted/g	Corrected $\delta^{34}S$/‰	Purity %	Average $\delta^{34}S$/‰	SD	Yield Ag_2S/mg	S wt%	Compiled $\delta^{34}S$ CRS/‰
GPS151	CRS	0.210	3.9	99.8			12.23	0.8	3.9
GPS157	CRS	0.241	12.0	103.6	11.6	0.6	17.33	0.9	11.6
GPS157rpt	CRS		11.1	103.8					
GPS166	CRS	0.213	2.0	95.5			11.23	0.7	2.0

Rpt = replicate analysis.
CRS = chromium-reducible sulfur
SD = standard deviation

Appendix 3.3: Mo and U isotopic data of semi-restricted basins' sediments

Mo and U isotopic data of the Black Sea sediments (Brüske et al., 2020):

Locality	**Station**	**$\delta^{98}Mo_{bulk}$ / ‰**	**$\delta^{98}Mo_{auth}$ / ‰**	**$\delta^{238}U_{bulk}$ / ‰**	**$\delta^{238}U_{auth}$ / ‰**
Black Sea	29-11	1.98	2.00	0.03	0.09
Black Sea	30-4	1.57	1.60	-0.08	-0.02
Black Sea	31-4	1.73	1.74	0.01	0.05
Black Sea	22-1	1.72	1.76	0.02	0.15
Black Sea	32-23	1.46	1.47	0.04	0.08
Black Sea	46-8	0.23	0.00	0.05	0.28
Black Sea	47-1	-0.52	-0.55	0.19	0.39
Black Sea	49-1	1.81	1.83	0.03	0.17
Black Sea	44-1	1.70	1.72	-0.02	0.05
Black Sea	43-6	1.52	1.54	0.01	0.05
Black Sea	42-3	1.14	1.14	0.07	0.11
Black Sea	59-1	0.56	0.56	0.00	0.18
Black Sea	55-2	1.44	1.45	0.17	0.27
Black Sea	54-1	1.06	1.07	0.08	0.22
Black Sea	51-1	1.51	1.52	0.21	0.29
Black Sea	29-11	0.81	0.82	0.00	0.09
Black Sea	30-4	1.65	1.67	0.03	0.07
Black Sea	31-4	1.68	1.70	0.03	0.06
Black Sea	22-1	1.99	2.04	0.01	0.11
Black Sea	46-8	0.02	-0.51	0.24	0.43
Black Sea	47-1	-0.10	-0.12	0.26	0.43
Black Sea	45-11	0.61	0.61	-0.07	0.01
Black Sea	49-1	1.97	1.99		
Black Sea	44-1	1.74	1.76	0.03	0.08
Black Sea	43-6	1.68	1.69	0.04	0.07
Black Sea	42-3	1.55	1.56	0.08	0.11
Black Sea	59-1	0.61	0.61	0.23	0.38
Black Sea	55-2	1.40	1.41	0.17	0.25
Black Sea	54-1	1.20	1.20	0.35	0.43
Black Sea	51-1	1.46	1.47	0.23	0.30
Black Sea	32MUC24	1.69	1.71	-0.03	-0.01
Black Sea	32MUC24	1.91	1.94	0.03	0.05
Black Sea	32MUC24	1.86	1.89	-0.04	-0.03
Black Sea	32MUC24	1.94	1.97	-0.05	-0.03
Black Sea	32MUC24	2.01	2.04	-0.04	-0.03

Table continued

Locality	**Station**	**$\delta^{98}Mo_{bulk}$ / ‰**	**$\delta^{98}Mo_{auth}$ / ‰**	**$\delta^{238}U_{bulk}$ / ‰**	**$\delta^{238}U_{auth}$ / ‰**
Black Sea	32MUC24	1.97	1.99	-0.03	-0.02
Black Sea	32MUC24	2.00	2.03	-0.08	-0.07
Black Sea	32MUC24	2.01	2.03	-0.25	-0.25
Black Sea	32MUC24	2.23	2.24	-0.17	-0.17
Black Sea	32MUC24	2.38	2.4	0.04	0.05
Black Sea	32MUC24	2.18	2.27	-0.21	-0.18
Black Sea	32MUC24	1.23	1.23	0.47	0.55

Auth = authigenic

Mo and U isotopic data of the Cariaco Basin sediments (Brüske et al., 2020):

Locality	**Station**	**$\delta^{98}Mo_{bulk}$ / ‰**	**$\delta^{98}Mo_{auth}$ / ‰**	**$\delta^{238}U_{bulk}$ / ‰**	**$\delta^{238}U_{auth}$ / ‰**
Cariaco Basin	22BX	2.8	2.92	-0.05	0.23
Cariaco Basin	89BX	1.53	1.56	-0.05	0.09
Cariaco Basin	82BX	2.03	2.06	0.02	0.19
Cariaco Basin	105BX	1.16	1.19	-0.03	0.27
Cariaco Basin	67BX	1.6	1.62	0.02	0.22
Cariaco Basin	69BX	1.83	1.85	-0.01	0.13
Cariaco Basin	12GGC	1.51	1.53	-0.06	0.04
Cariaco Basin	12GGC	1.55	1.57	0.03	0.15
Cariaco Basin	12GGC	1.47	1.49	0.02	0.15
Cariaco Basin	12GGC	1.48	1.51	0.01	0.13
Cariaco Basin	12GGC	1.53	1.55	0.02	0.13
Cariaco Basin	12GGC	1.53	1.56	0.00	0.12
Cariaco Basin	12GGC	1.34	1.35	0.00	0.16
Cariaco Basin	12GGC	1.5	1.52	-0.01	0.12
Cariaco Basin	12GGC	1.47	1.49	-0.01	0.12
Cariaco Basin	12GGC	1.3	1.32	0.02	0.18
Cariaco Basin	12GGC	0.96	0.96	0.04	0.11
Cariaco Basin	12GGC	1.4	1.41	-0.11	0.01
Cariaco Basin	12GGC	1.49	1.5	-0.17	-0.12
Cariaco Basin	12GGC	1.58	1.59	-0.21	-0.18
Cariaco Basin	12GGC	1.28	1.29	-0.13	-0.04
Cariaco Basin	12GGC	1.31	1.31	-0.11	-0.01
Cariaco Basin	12GGC	1.33	1.34	-0.12	-0.05
Cariaco Basin	12GGC	1.4	1.41	-0.12	-0.02
Cariaco Basin	70GGC	1.49	1.51	-0.06	0.01
Cariaco Basin	70GGC	1.4	1.41	0.00	0.06
Cariaco Basin	70GGC	1.43	1.44	0.01	0.07
Cariaco Basin	70GGC	1.38	1.39	0.01	0.06
Cariaco Basin	70GGC	1.55	1.57	0.02	0.08
Cariaco Basin	70GGC	1.48	1.49	0.00	0.05
Cariaco Basin	70GGC	1.77	1.78	-0.03	0.04
Cariaco Basin	70GGC	1.44	1.45	-0.06	0.02
Cariaco Basin	70GGC	1.79	1.81	-0.07	0.01
Cariaco Basin	70GGC	1.03	1.04	-0.06	-0.01
Cariaco Basin	70GGC	1.56	1.58	-0.05	0.01
Cariaco Basin	70GGC	1.58	1.59	-0.01	0.04
Cariaco Basin	70GGC	1.61	1.62	-0.07	-0.02
Cariaco Basin	70GGC	1.28	1.28	0.05	0.12
Cariaco Basin	70GGC	1.76	1.78	-0.14	-0.09
Cariaco Basin	70GGC	1.1	1.1	0.20	0.25
Cariaco Basin	1002B	1.17	1.17	0.09	0.12

Table continued

Locality	Station	$\delta^{98}\mathrm{Mo}_{\mathrm{bulk}}$ / ‰	$\delta^{98}\mathrm{Mo}_{\mathrm{auth}}$ / ‰	$\delta^{238}\mathrm{U}_{\mathrm{bulk}}$ / ‰	$\delta^{238}\mathrm{U}_{\mathrm{auth}}$ / ‰
Cariaco Basin	1002B	1.08	1.08	0.06	0.10
Cariaco Basin	1002B	1.15	1.15	0.11	0.16
Cariaco Basin	1002B	0.98	0.99	0.09	0.11
Cariaco Basin	1002B	0.91	0.91	0.11	0.16
Cariaco Basin	1002B	0.9	0.9	0.13	0.18
Cariaco Basin	1002B	1.05	1.05	0.10	0.16
Cariaco Basin	1002B	1.2	1.21	0.05	0.08
Cariaco Basin	1002B	1.3	1.3	0.04	0.05
Cariaco Basin	1002B	1.18	1.19	-0.08	-0.07
Cariaco Basin	1002B	1.62	1.63	-0.11	-0.08
Cariaco Basin	1002B	1.58	1.59	-0.14	-0.12
Cariaco Basin	1002B	1.59	1.6	-0.07	-0.04
Cariaco Basin	1002B	1.72	1.73	-0.10	-0.07
Cariaco Basin	1002B	1.67	1.68	-0.09	-0.08

Auth = authigenic

Mo and U isotopic data of the Cariaco Basin sediments (Andersen et al., 2018):

Locality	Sample ID	$\delta^{98}\mathrm{Mo}_{\mathrm{auth}}$ / ‰	$\delta^{238}\mathrm{U}_{\mathrm{auth}}$ / ‰
Mediterranean Sea	70-71	1.62	-0.35
Mediterranean Sea	71-72	1.70	-0.28
Mediterranean Sea	72-73	1.90	-0.29
Mediterranean Sea	76-77	2.31	-0.14
Mediterranean Sea	78-79	2.03	-0.14
Mediterranean Sea	84-85	2.05	-0.11
Mediterranean Sea	85-86	2.05	-0.13
Mediterranean Sea	86-87	2.06	-0.07
Mediterranean Sea	87-88	2.25	-0.04
Mediterranean Sea	90-91	2.20	-0.13
Mediterranean Sea	93-94	1.99	0.08
Mediterranean Sea	94-95	1.84	0.03
Mediterranean Sea	96-97	1.54	0.12
Mediterranean Sea	97-98	1.32	0.11
Mediterranean Sea	101-102	1.29	0.11
Mediterranean Sea	106-107	2.40	-0.31
Mediterranean Sea	107-108	2.03	-0.21
Mediterranean Sea	108-109	2.10	-0.28
Mediterranean Sea	109-110	2.28	-0.33

Auth = authigenic

Mo and U isotopic data of the Green Point shale (This study, Li et al., 2022)

Locality	Sample ID	$\delta^{98}\mathrm{Mo}_{\mathrm{auth}}$ / ‰	$\delta^{238}\mathrm{U}_{\mathrm{auth}}$ / ‰
Green Point	GPS1	-0.04	-0.28
Green Point	GPS3	0.34	-0.42
Green Point	GPS4	0.08	-0.07
Green Point	GPS10	0.37	-0.26
Green Point	GPS13	0.24	-0.04
Green Point	GPS14	0.82	-0.26
Green Point	GPS19	0.54	-0.29
Green Point	GPS26	0.48	
Green Point	GPS30		

Table continued			
Locality	**Sample ID**	**$\delta^{98}Mo_{auth}$ / ‰**	**$\delta^{238}U_{auth}$ / ‰**
Green Point	GPS41	0.73	-0.37
Green Point	GPS49	3.16	
Green Point	GPS53	-0.14	0.12
Green Point	GPS57		
Green Point	GPS61	2.25	
Green Point	GPS63	1.31	-0.18
Green Point	GPS66	-0.08	0.12
Green Point	GPS68	0.47	-0.30
Green Point	GPS71	0.70	0.03
Green Point	GPS75	0.92	-0.62
Green Point	GPS79	0.07	-0.18
Green Point	GPS82	0.69	-0.42
Green Point	GPS149		
Green Point	GPS151	0.54	-0.31
Green Point	GPS157	-0.40	-0.09
Green Point	GPS166	1.51	-0.07

Auth = authigenic

Appendix 4.1: Inverse correlations between the $\delta^{98}Mo_{auth}$ and $\delta^{238}U_{auth}$ values observed from the Green Point shale and partially restricted basins' sediments

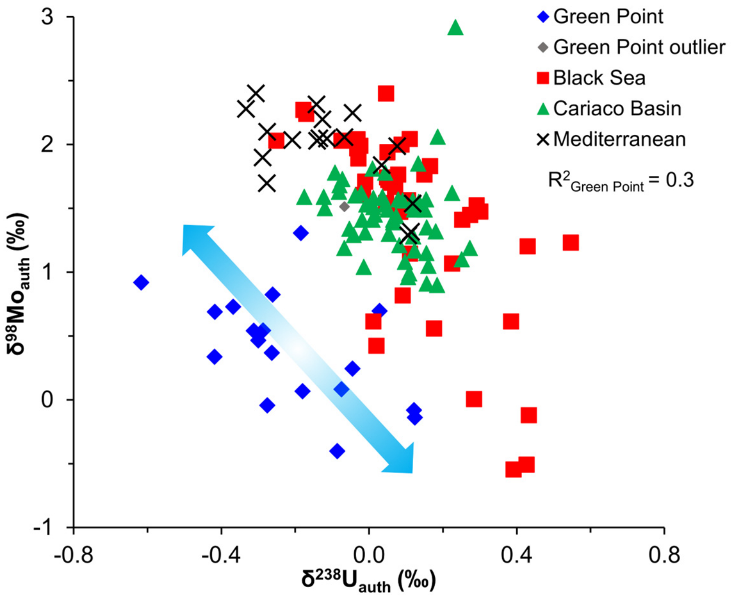

The Green Point shale displaying an inverse correlation of $\delta^{98}Mo_{auth}$ with $\delta^{238}U_{auth}$ ($R^2 = 0.3$, $p < 0.05$), which is analogous to those observed in semi-restricted basins' sediments (Li et al., 2022). The isotopic data of deposits in the Black Sea, the Cariaco Basin, and the Mediterranean Sea are collected from Andersen et al. (2018) and Brüske et al. (2020). Auth = authigenic.

Appendix 4.2: The average limestone grain size

The excel file with measured grain sizes and photomicrographs can be downloaded via the following google drive link:

https://docs.google.com/spreadsheets/d/1MgZe2GvUHGb-xwQkMy5zzHVmAdkjK3GH/edit?usp=drive_link&ouid=110832369128749161575&rtpof=true&sd=true

Appendix 4.3: Diagenetic effect on bulk carbonate δ^{238}U signatures

The δ^{238}U of modern bulk carbonates, and the current oceanic δ^{238}U signature is ~−0.39‰ (Tissot and Dauphas, 2015).

Study	**Sample location**	**Sample**	**Sample depth**	**$\delta^{238/235}$U /‰**	**2σ**	**n**
Romaniello et al., 2013	Bahamas, Core 1	Bulk carbonates	0-3 cm	-0.19	0.14	3
Romaniello et al., 2013	Bahamas, Core 1	Bulk carbonates	4-6 cm	-0.12	0.29	3
Romaniello et al., 2013	Bahamas, Core 1	Bulk carbonates	8-11 cm	-0.15	0.09	3
Romaniello et al., 2013	Bahamas, Core 1	Bulk carbonates	12-14 cm	-0.13	0.04	3
Romaniello et al., 2013	Bahamas, Core 1	Bulk carbonates	16-18 cm	-0.16	0.05	3
Romaniello et al., 2013	Bahamas, Core 1	Bulk carbonates	24-26 cm	0.03	0.17	3
Romaniello et al., 2013	Bahamas, Core 1	Bulk carbonates	32-34 cm	0.07	0.19	3
Romaniello et al., 2013	Bahamas, Core 1	Bulk carbonates	40-42 cm	0.14	0.25	3
Romaniello et al., 2013	Bahamas, Core 2	Bulk carbonates	0-3 cm	-0.16	0.04	3
Romaniello et al., 2013	Bahamas, Core 2	Bulk carbonates	6-9 cm	-0.13	0.03	3
Romaniello et al., 2013	Bahamas, Core 2	Bulk carbonates	12-15 cm	-0.21	0.11	3
Romaniello et al., 2013	Bahamas, Core 2	Bulk carbonates	18-21 cm	-0.19	0.05	3
Romaniello et al., 2013	Bahamas, Core 2	Bulk carbonates	21-24 cm	-0.12	0.16	3
Romaniello et al., 2013	Bahamas, Core 3	Bulk carbonates	1-4 cm	-0.23	0.15	3
Romaniello et al., 2013	Bahamas, Core 3	Bulk carbonates	6-9 cm	-0.24	0.14	3
Romaniello et al., 2013	Bahamas, Core 3	Bulk carbonates	10-14 cm	-0.16	0.17	3
Romaniello et al., 2013	Bahamas, Core 3	Bulk carbonates	17-21 cm	-0.18	0.09	3
Romaniello et al., 2013	Bahamas, Core 3	Bulk carbonates	19-22 cm	-0.18	0.15	3
Romaniello et al., 2013	Bahamas, Core 4	Bulk carbonates	0-4 cm	-0.22	0.10	3
Romaniello et al., 2013	Bahamas, Core 4	Bulk carbonates	4-8 cm	-0.17	0.04	3
Romaniello et al., 2013	Bahamas, Core 4	Bulk carbonates	8-12 cm	-0.03	0.13	3
Romaniello et al., 2013	Bahamas, Core 4	Bulk carbonates	12-16 cm	-0.06	0.11	3
Tissot et al., 2018	Bahamas, Core 166	Bulk carbonates	0.32 m	0.01	0.03	7
Tissot et al., 2018	Bahamas, Core 166	Bulk carbonates		0.01	0.03	4
Tissot et al., 2018	Bahamas, Core 166	Bulk carbonates	5.12 m	0.10	0.02	5
Tissot et al., 2018	Bahamas, Core 166	Bulk carbonates		0.11	0.03	5
Tissot et al., 2018	Bahamas, Core 166	Bulk carbonates	9.62 m	0.09	0.03	7
Tissot et al., 2018	Bahamas, Core 166	Bulk carbonates		0.09	0.01	6
Tissot et al., 2018	Bahamas, Core 166	Bulk carbonates	14.62 m	-0.10	0.03	8
Tissot et al., 2018	Bahamas, Core 166	Bulk carbonates	19.12 m	-0.31	0.02	9
Tissot et al., 2018	Bahamas, Core 166	Bulk carbonates	35.12 m	-0.14	0.03	8
Tissot et al., 2018	Bahamas, Core 166	Bulk carbonates	53.62 m	-0.11	0.03	8
Tissot et al., 2018	Bahamas, Core 166	Bulk carbonates	58.12 m	-0.03	0.02	9
Tissot et al., 2018	Bahamas, Core 166	Bulk carbonates		-0.08	0.02	8
Tissot et al., 2018	Bahamas, Core 166	Bulk carbonates	61.62 m	-0.12	0.04	9
Tissot et al., 2018	Bahamas, Core 166	Bulk carbonates	64.62 m	-0.23	0.03	7
Tissot et al., 2018	Bahamas, Core 166	Bulk carbonates	69.12 m	-0.11	0.02	8
Tissot et al., 2018	Bahamas, Core 166	Bulk carbonates	74.12 m	0.15	0.03	7
Tissot et al., 2018	Bahamas, Core 166	Bulk carbonates		0.13	0.03	4
Tissot et al., 2018	Bahamas, Core 166	Bulk carbonates	78.62 m	-0.23	0.03	8
Tissot et al., 2018	Bahamas, Core 166	Bulk carbonates	89.62 m	-0.18	0.02	9
Tissot et al., 2018	Bahamas, Core 166	Bulk carbonates	94.12 m	-0.16	0.03	8
Tissot et al., 2018	Bahamas, Core 166	Bulk carbonates	108.62 m	-0.02	0.02	9
Tissot et al., 2018	Bahamas, Core 166	Bulk carbonates		0.01	0.03	7
Tissot et al., 2018	Bahamas, Core 166	Bulk carbonates	113.59 m	-0.32	0.02	9
Tissot et al., 2018	Bahamas, Core 166	Bulk carbonates		-0.32	0.03	7
Tissot et al., 2018	Bahamas, Core 166	Bulk carbonates	115.62 m	-0.17	0.04	9

Table continued

Study	Sample location	Sample	Sample depth	$\delta^{238/235}$U /‰	2σ	n
Tissot et al., 2018	Bahamas, Core 166	Bulk carbonates		-0.18	0.02	4
Tissot et al., 2018	Bahamas, Core 166	Bulk carbonates	120.12 m	-0.10	0.03	12
Tissot et al., 2018	Bahamas, Core 166	Bulk carbonates		-0.11	0.03	7
Tissot et al., 2018	Bahamas, Core 166	Bulk carbonates	125.32 m	-0.37	0.03	9
Tissot et al., 2018	Bahamas, Core 166	Bulk carbonates		-0.33	0.03	5
Tissot et al., 2018	Bahamas, Core 166	Bulk carbonates			0.03	9
Tissot et al., 2018	Bahamas, Core 166	Bulk carbonates	142.82 m	-0.12	0.03	12
Tissot et al., 2018	Bahamas, Core 166	Bulk carbonates	145.81 m	-0.16	0.03	7
Tissot et al., 2018	Bahamas, Core 166	Bulk carbonates		-0.18	0.03	4
Tissot et al., 2018	Bahamas, Core 166	Bulk carbonates	161.82 m	0.02	0.02	8
Tissot et al., 2018	Bahamas, Core 166	Bulk carbonates		0.04	0.04	4
Tissot et al., 2018	Bahamas, Core 166	Bulk carbonates	166.32 m	-0.15	0.03	12
Tissot et al., 2018	Bahamas, Core 166	Bulk carbonates		-0.19	0.02	4
Tissot et al., 2018	Bahamas, Core 166	Bulk carbonates	172.62 m	0.02	0.03	7
Tissot et al., 2018	Bahamas, Core 166	Bulk carbonates		0.01	0.01	6
Tissot et al., 2018	Bahamas, Core 166	Bulk carbonates	177.12 m	-0.28	0.02	9
Tissot et al., 2018	Bahamas, Core 166	Bulk carbonates		-0.26	0.04	4
Tissot et al., 2018	Bahamas, Core 166	Bulk carbonates	181.92 m	-0.15	0.02	5
Tissot et al., 2018	Bahamas, Core 166	Bulk carbonates		-0.15	0.04	4
Tissot et al., 2018	Bahamas, Core 166	Bulk carbonates	191.22 m	-0.08	0.04	9
Tissot et al., 2018	Bahamas, Core 166	Bulk carbonates	197.22 m	-0.13	0.02	9
Tissot et al., 2018	Bahamas, Core 166	Bulk carbonates	201.82 m	-0.07	0.02	9
Tissot et al., 2018	Bahamas, Core 166	Bulk carbonates	207.92 m	-0.10	0.03	7
Tissot et al., 2018	Bahamas, Core 166	Bulk carbonates	212.42 m	-0.06	0.02	9
Tissot et al., 2018	Bahamas, Core 166	Bulk carbonates	216.92 m	-0.12	0.03	8
Tissot et al., 2018	Bahamas, Core 166	Bulk carbonates	219.26 m	-0.26	0.03	6
Tissot et al., 2018	Bahamas, Core 166	Bulk carbonates		-0.24	0.03	4
Tissot et al., 2018	Bahamas, Core 166	Bulk carbonates	222.26 m	0.00	0.02	9
Bura-nakić et al., 2020	Adriatic Sea, Core C3	Bulk carbonates	1 cm	-0.06	0.02	n/a
Bura-nakić et al., 2020	Adriatic Sea, Core C3	Bulk carbonates	5 cm	-0.10	0.03	n/a
Bura-nakić et al., 2020	Adriatic Sea, Core C3	Bulk carbonates	9 cm	-0.10	0.03	n/a
Bura-nakić et al., 2020	Adriatic Sea, Core C3	Bulk carbonates	13 cm	-0.09	0.03	n/a
Bura-nakić et al., 2020	Adriatic Sea, Core C3	Bulk carbonates	15 cm	-0.10	0.03	n/a
Bura-nakić et al., 2020	Adriatic Sea, Core C3	Bulk carbonates	17 cm	-0.08	0.05	n/a
Bura-nakić et al., 2020	Adriatic Sea, Core C3	Bulk carbonates	19 cm	-0.10	0.05	n/a
Bura-nakić et al., 2020	Adriatic Sea, Core C3	Bulk carbonates	21 cm	-0.12	0.04	n/a
Bura-nakić et al., 2020	Adriatic Sea, Core C3	Bulk carbonates	23 cm	-0.06	0.03	n/a
Bura-nakić et al., 2020	Adriatic Sea, Core C3	Bulk carbonates	25 cm	-0.11	0.05	n/a
Bura-nakić et al., 2020	Adriatic Sea, Core C3	Bulk carbonates	27 cm	-0.13	0.05	n/a
Bura-nakić et al., 2020	Adriatic Sea, Core C3	Bulk carbonates	29 cm	-0.05	0.05	n/a
Bura-nakić et al., 2020	Adriatic Sea, Core C3	Bulk carbonates	31 cm	-0.07	0.05	n/a
Bura-nakić et al., 2020	Adriatic Sea, Core C3	Bulk carbonates	33 cm	-0.15	0.05	n/a
Bura-nakić et al., 2020	Adriatic Sea, Core C3	Bulk carbonates	35 cm	-0.12	0.05	n/a
Bura-nakić et al., 2020	Adriatic Sea, Core C3	Bulk carbonates	37 cm	-0.15	0.04	n/a
Bura-nakić et al., 2020	Adriatic Sea, Core C3	Bulk carbonates	39 cm	-0.08	0.05	n/a

Appendix 4.4: The δ^{238}U of semi-restricted basins and open oceans

The δ^{238}U of semi-restricted basins:

Study	Standard	Station	Sample location	Water depth/m	Sample	δ^{238}U /‰	2σ
Tissot and Dauphas, 2015	CRM-112a	n/a	SW Mediterranean Sea	n/a	Water	-0.40	0.04
Tissot and Dauphas, 2015	CRM-112a	n/a	SW Mediterranean Sea	n/a	Water	-0.39	0.05
Tissot and Dauphas, 2015	CRM-112a	n/a	SW Mediterranean Sea	n/a	Water	-0.36	0.06
Tissot and Dauphas, 2015	CRM-112a	n/a	SW Mediterranean Sea	n/a	Water	-0.39	0.04
Noordmann et al. 2015	CRM-112a	n/a	Kyllaren fjord, Norway	2	Water	-0.35	0.01
Noordmann et al. 2015	CRM-112a	n/a	Kyllaren fjord, Norway	3	Water	-0.37	0.02
Noordmann et al. 2015	CRM-112a	n/a	Kyllaren fjord, Norway	3.5 (Chemocline)	Water	-0.41	0.02
Noordmann et al. 2015	CRM-112a	n/a	Kyllaren fjord, Norway	4	Water	-0.44	0.08
Noordmann et al. 2015	CRM-112a	n/a	Kyllaren fjord, Norway	4.6	Water	-0.49	0.08
Noordmann et al. 2015	CRM-112a	n/a	Kyllaren fjord, Norway	7	Water	-0.60	0.03
Noordmann et al. 2015	CRM-112a	n/a	Kyllaren fjord, Norway	15	Water	-0.73	0.01
Noordmann et al. 2015	CRM-112a	n/a	Kyllaren fjord, Norway	20	Water	-0.70	0.04
Noordmann et al., 2015	CRM-112a	342390	Landsort Deep, Baltic Sea	45	Water	-0.33	0.03
Noordmann et al., 2015	CRM-112a	342390	Landsort Deep, Baltic Sea	73	Water	-0.39	0.08
Noordmann et al., 2015	CRM-112a	342390	Landsort Deep, Baltic Sea	76	Water	-0.43	0.11
Noordmann et al., 2015	CRM-112a	342390	Landsort Deep, Baltic Sea	85 (Chemocline)	Water	-0.36	0.01
Noordmann et al., 2015	CRM-112a	342390	Landsort Deep, Baltic Sea	112	Water	-0.39	0.04
Noordmann et al., 2015	CRM-112a	342390	Landsort Deep, Baltic Sea	436	Water	-0.41	0.02
Noordmann et al., 2015	CRM-112a	342370	Gotland Deep, Baltic Sea	110	Water	-0.36	0.07
Noordmann et al., 2015	CRM-112a	342370	Gotland Deep, Baltic Sea	130 (Chemocline)	Water	-0.40	0.01
Noordmann et al., 2015	CRM-112a	342370	Gotland Deep, Baltic Sea	134	Water	-0.43	0.08
Noordmann et al., 2015	CRM-112a	342370	Gotland Deep, Baltic Sea	140	Water	-0.44	0.04
Noordmann et al., 2015	CRM-112a	342370	Gotland Deep, Baltic Sea	150	Water	-0.50	0.07
Rolison et al., 2017	CRM-145	2.1.24	Black Sea	9	Water	−0.35	0.06
Rolison et al., 2017	CRM-145	2.1.22	Black Sea	39	Water	−0.52	0.06
Rolison et al., 2017	CRM-145	2.1.18	Black Sea	99 (Chemocline)	Water	−0.44	0.06
Rolison et al., 2017	CRM-145	2.1.16	Black Sea	129	Water	−0.45	0.06
Rolison et al., 2017	CRM-145	2.1.12	Black Sea	204	Water	−0.48	0.05
Rolison et al., 2017	CRM-145	2.1.10	Black Sea	300	Water	−0.55	0.07
Rolison et al., 2017	CRM-145	2.1.8	Black Sea	498	Water	−0.55	0.06
Rolison et al., 2017	CRM-145	2.1.6	Black Sea	999	Water	−0.69	0.06
Rolison et al., 2017	CRM-145	2.1.4	Black Sea	1499	Water	−0.86	0.07
Rolison et al., 2017	CRM-145	2.1.3	Black Sea	1749	Water	−0.77	0.06
Rolison et al., 2017	CRM-145	2.1.2	Black Sea	2070	Water	−0.68	0.06
Rolison et al., 2017	CRM-145	2.1.1	Black Sea	2120	Water	−0.63	0.06
Rolison et al., 2017	CRM-145	5.1.24	Black Sea	10	Water	−0.39	0.06
Rolison et al., 2017	CRM-145	5.1.22	Black Sea	40	Water	−0.49	0.07
Rolison et al., 2017	CRM-145	5.1.18	Black Sea	100 (Chemocline)	Water	−0.43	0.06
Rolison et al., 2017	CRM-145	5.1.16	Black Sea	130	Water	−0.45	0.06
Rolison et al., 2017	CRM-145	5.1.12	Black Sea	205	Water	−0.41	0.06
Rolison et al., 2017	CRM-145	5.1.10	Black Sea	300	Water	−0.52	0.07
Rolison et al., 2017	CRM-145	5.1.8	Black Sea	500	Water	−0.55	0.06
Rolison et al., 2017	CRM-145	5.1.6	Black Sea	1000	Water	−0.74	0.07
Rolison et al., 2017	CRM-145	5.1.4	Black Sea	1500	Water	−0.75	0.07
Rolison et al., 2017	CRM-145	5.1.3	Black Sea	1751	Water	−0.84	0.05
Rolison et al., 2017	CRM-145	5.1.2	Black Sea	1989	Water	−0.66	0.06
Rolison et al., 2017	CRM-145	5.1.1	Black Sea	2040	Water	−0.73	0.08
Rolison et al., 2017	CRM-145	9.1.24	Black Sea	10	Water	-0.33	0.09
Rolison et al., 2017	CRM-145	9.1.23	Black Sea	25	Water	-0.41	0.08
Rolison et al., 2017	CRM-145	9.1.22	Black Sea	46	Water	-0.37	0.09
Rolison et al., 2017	CRM-145	9.1.21	Black Sea	55	Water	-0.41	0.08
Rolison et al., 2017	CRM-145	9.1.20	Black Sea	70	Water	-0.37	0.09
Rolison et al., 2017	CRM-145	9.1.19	Black Sea	85	Water	-0.43	0.08
Rolison et al., 2017	CRM-145	9.1.18	Black Sea	100 (Chemocline)	Water	-0.43	0.06
Rolison et al., 2017	CRM-145	9.1.17	Black Sea	115	Water	-0.40	0.08
Rolison et al., 2017	CRM-145	9.1.16	Black Sea	130	Water	-0.43	0.09
Rolison et al., 2017	CRM-145	9.1.15	Black Sea	150	Water	-0.46	0.09
Rolison et al., 2017	CRM-145	9.1.14	Black Sea	175	Water	−0.50	0.09
Rolison et al., 2017	CRM-145	9.1.13	Black Sea	200	Water	−0.55	0.10

Table continued							
Study	**Standard**	**Station**	**Sample location**	**Water depth/m**	**Sample**	**δ^{238}U /‰**	**2σ**
Rolison et al., 2017	CRM-145	9.1.12	Black Sea	300	Water	−0.54	0.09
Rolison et al., 2017	CRM-145	9.1.11	Black Sea	400	Water	−0.52	0.10
Rolison et al., 2017	CRM-145	9.1.10	Black Sea	501	Water	−0.54	0.09
Rolison et al., 2017	CRM-145	9.1.9	Black Sea	750	Water	−0.56	0.09
Rolison et al., 2017	CRM-145	9.1.8	Black Sea	1000	Water	−0.71	0.10
Rolison et al., 2017	CRM-145	9.1.7	Black Sea	1250	Water	−0.67	0.10
Rolison et al., 2017	CRM-145	9.1.6	Black Sea	1500	Water	−0.75	0.09
Rolison et al., 2017	CRM-145	9.1.5	Black Sea	1750	Water	−0.72	0.11
Rolison et al., 2017	CRM-145	9.1.4	Black Sea	2000	Water	−0.66	0.09
Rolison et al., 2017	CRM-145	9.1.3	Black Sea	2050	Water	−0.60	0.11
Rolison et al., 2017	CRM-145	9.1.2	Black Sea	2101	Water	−0.69	0.07
Rolison et al., 2017	CRM-145	9.1.1	Black Sea	2157	Water	−0.74	0.09

The δ^{238}U of open oceans.

Study	Standard	Location	Sample	δ^{238}U	2σ
Tissot and Dauphas, 2015	CRM-145	Makarov Basin weighted mean	Seawater	-0.44	0.06
Tissot and Dauphas, 2015	CRM-145	North Sea weighted mean	Seawater	-0.53	0.06
Tissot and Dauphas, 2015	SRM-950a	Bermuda	Seawater	-0.40	0.06
Tissot and Dauphas, 2015	SRM-950a	Bermuda	Seawater	-0.41	0.03
Tissot and Dauphas, 2015	SRM-950a	Bermuda	Seawater	-0.38	0.05
Tissot and Dauphas, 2015	CRM-112a	Arguin, France, SW Atlantic Ocean	Seawater	-0.39	0.04
Tissot and Dauphas, 2015	CRM-112a	Miami, FL, SW Atlantic Ocean	Seawater	-0.35	0.06
Tissot and Dauphas, 2015	CRM-112a	Gravelines, France, SW English Channel	Seawater	-0.35	0.05
Tissot and Dauphas, 2015	CRM-112a	Guaymas, Mexico, SW Gulf of California	Seawater	-0.38	0.06
Tissot and Dauphas, 2015	CRM-112a	SW Gulf of Mexico	Seawater	-0.36	0.03
Tissot and Dauphas, 2015	CRM-112a	SW Gulf of Mexico	Seawater	-0.37	0.05
Tissot and Dauphas, 2015	CRM-145	Oeno Pacific	Seawater	-0.41	0.04
Tissot and Dauphas, 2015	CRM-145	Henderson Pacific	Seawater	-0.50	0.07
Tissot and Dauphas, 2015	SRM-950a	Hawaii Pacific	Seawater	-0.41	0.02
Tissot and Dauphas, 2015	SRM-950a	Hawaii Pacific	Seawater	-0.41	0.02
Tissot and Dauphas, 2015	SRM-950a	Hawaii Pacific	Seawater	-0.42	0.10
Tissot and Dauphas, 2015	CRM-145	SW Pacific/Atlantic	Seawater	-0.39	0.02
Tissot and Dauphas, 2015	CRM-145	SW Pacific/Atlantic	Seawater	-0.39	0.01
Tissot and Dauphas, 2015	CRM-112a	SW Pacific Ocean	Seawater	-0.39	0.03
Tissot and Dauphas, 2015	CRM-112a	SW Pacific Ocean	Seawater	-0.41	0.05
Tissot and Dauphas, 2015	CRM-112a	SW Pacific Ocean	Seawater	-0.41	0.03
Rolison et al., 2017	CRM-145	Pacific SW	Seawater	-0.40	0.08
Rolison et al., 2017	CRM-145	Pacific SW	Seawater	-0.38	0.09
Rolison et al., 2017	CRM-145	Pacific SW	Seawater	-0.39	0.08
Rolison et al., 2017	CRM-145	Pacific SW	Seawater	-0.36	0.08
Rolison et al., 2017	CRM-145	Pacific SW	Seawater	-0.39	0.07

Appendix 4.5: The relationship between planktic I/Ca ratios and the nearby seawater oxygen availability

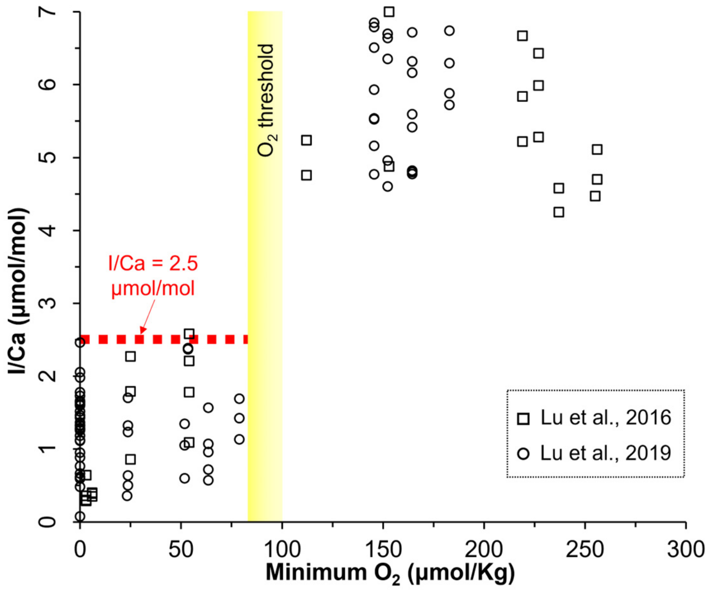

The modern and Holocene core-top planktic I/Ca ratios vs. minimum O_2 concentrations in nearby subsurface seawater with depth >50m, data from Lu et al. (2016) and Lu et al. (2019). The carbonate I/Ca <2.6 µmol/mol marks the boundary of poorly oxygenated subsurface seawater (depth >50m) with $[O_2]_{aq}$ <~70–100 µmol/kg (Lu et al., 2016; Lu et al., 2019).

Appendix 4.6: The three-sink U isotope mass balance model MATLAB codes

The code can be downloaded via the following google drive link:

https://drive.google.com/drive/folders/1oUcljUlfamIJiIz8BpeEPTfI82aOpzid?usp=share_link

Appendix 4.6.1: MATLAB codes for the three-sink U mass balance model

%parameters and values

```
ko=1.45*10^-21;% The rate constant for U removal under oxic condition.

kop=4.63*10^-20;% The rate constant for U removal under oxygen-poor condition.

ka=4.44*10^-19;% The rate constants for U removal under anoxic/euxinic condition.

do=0.02;% The U isotopic fractionation between seawater and the oxic sink.

dop=0.1;% The U isotopic fractionation between seawater and the oxygen-poor sink.
```

da=0.6;% The U isotopic fractionation between seawater and the anoxic/euxinic sink.

Ur=-0.24;% The δ^{238}U of discharged river waters.

%The following is the calculation of the max and min values of f_{anox} of by using equations 16 and 17 in the manuscript, which is based on restrictions that f_{anox} is a member of set [0,1] and f_{ox} + f_{oxp}<=1

x=linspace(-0.84,0)% The range of the oceanic δ^{238}U, this model produces negative values when δ^{238}U<-0.84‰.

y1=linspace(0,1);% y1=-b1/k1, the y or x intercept, is the maximum value of f_{anox} for a given δ^{238}U value.

y2=linspace(0,1);% y2=-b2/k2, the y or x intercept, is the minimum value of f_{anox} for a given δ^{238}U value.

k1=[(ka-kop)*(Ur-x)+kop*dop-ka*da]./[ko*do-kop*dop-(Ur-x)*(ko-kop)];% k1 and b1 are calculated using equation 16.

b1=[kop*(Ur-x-dop)]./[ko*do-kop*dop-(Ur-x)*(ko-kop)];

y1=-b1./k1;

k2=[(ka-ko)*(Ur-x)+ko*do-ka*da]./[kop*dop-ko*do-(Ur-x)*(kop-ko)];% k2 and b2 are calculated using equation 17.

b2=[ko*(Ur-x-do)]./[kop*dop-ko*do-(Ur-x)*(kop-ko)];

y2=-b2./k2;

% The following is the calculation of the max and min value of f_{oxp} using equations 18 and 19 in Section 4.3.3, which is based on restrictions that f_{oxp} is a member of set [0,1] and f_{ox} + f_{anox} <= 1

```
x1=linspace(-0.84,-0.34);% The range of the oceanic δ238U is (-0.84,0), there is an incontinuity at -0.34, therefore we divided δ238U into two sets: (-0.84,-0.34) and (-0.34,0).
x2=linspace(-0.34,0);
y3=linspace(0,1);% y3=-b3/k3, the y or x intercept, denotes the max estimate of foxp when δ238U is a member of set (-0.84,-0.34).
y4=linspace(0,1);% y4=-b4/k4, the y or x intercept, denotes the max estimate of foxp when δ238U is a member of set (-0.34,0).
k3=[(kop-ka)*(Ur-x1)+ka*da-kop*dop]./[ko*do-ka*da-(Ur-x1)*(ko-ka)];% k3 and b3 are calculated using equation 18.
b3=[ka*(Ur-x1-da)]./[ko*do-ka*da-(Ur-x1)*(ko-ka)];
y3=-b3./k3;
k4=[(kop-ko)*(Ur-x2)+ko*do-kop*dop]./[ka*da-ko*do-(Ur-x2)*(ka-ko)];% k4 and b4 are calculated using equation 19.
b4=[ko*(Ur-x2-do)]./[ka*da-ko*do-(Ur-x2)*(ka-ko)];
y4=-b4./k4;
% The estimated minimum values of foxp are negative, so the min of foxp should be 0 because foxp is a member of set [0,1]
%graphing code
yyaxis left
plot(x,y1,'b-',x,y2,'b-'); axis([-0.9 0 0 1]);
ylabel('f_{anox}(%)');
xlabel('δ^{238}U_{oc}(‰)');
set(gca,'yticklabel',{'0','10', '20', '30', '40' ,'50','60', '70', '80', '90' ,'100'});
```

```
yyaxis right
plot(x1,y3,'r-',x2,y4,'r-'); axis([-0.9 0 0 1]);
set(gca,'yticklabel',{'0','10', '20', '30', '40' ,'50','60', '70', '80', '90' ,'100'});
ylabel('f_{oxp}(%)');
ax=gca;
exportgraphics(ax,'fred_anox_Max and Min.jpg','Resolution',600)
```

Appendix 4.6.2: MATLAB codes for analysis of model sensitivity to the δ^{238}U of river water

```
% The max and min values of fanox are calculated by using equations 16 and 17 in Section 4.3.3,
        which is based on restrictions that fanox is a member of set [0,1] and fox + foxp<=1
%parameters and values
ko=1.45*10^-21;% The rate constant for U removal under oxic condition.
kop=4.63*10^-20;% The rate constant for U removal under oxygen-poor condition.
ka=4.44*10^-19;% The rate constant for U removal under anoxic/euxinic condition.
do=0.02;% The U isotopic fractionation between seawater and the oxic sink.
dop=0.1;% The U isotopic fractionation between seawater and the oxygen-poor sink.
da=0.6;% The U isotopic fractionation between seawater and the anoxic/euxinic sink.
% The calculation of the max and min values of fanox under different δ238Uriv scenarios.
Ur1=-0.24;% The δ238U of river = -0.24‰
x=linspace(-0.84,0);% The range of the oceanic δ238U, this model produces negative values when
        δ238U<-0.84.
y1=linspace(0,1);% y1=-b1/k1, the y or x intercept, is the maximum value of fanox for a given
        δ238U value.
```

```
y2=linspace(0,1);% y2=-b2/k2, the y or x intercept, is the minimum value of fanox for a given δ238U value.
k1=[(ka-kop)*(Ur1-x)+kop*dop-ka*da]./[ko*do-kop*dop-(Ur1-x)*(ko-kop)];% k1 and b1 are calculated using equation 16.
b1=[kop*(Ur1-x-dop)]./[ko*do-kop*dop-(Ur1-x)*(ko-kop)];
y1=-b1./k1;
k2=[(ka-ko)*(Ur1-x)+ko*do-ka*da]./[kop*dop-ko*do-(Ur1-x)*(kop-ko)];% k2 and b2 are calculated using equation 17
b2=[ko*(Ur1-x-do)]./[kop*dop-ko*do-(Ur1-x)*(kop-ko)];
y2=-b2./k2;
Ur2=-0.3;% The δ238U of river = -0.3‰
x1=linspace(-0.9,0);% The range of the oceanic δ238U, this model produces negative values when δ238U<-0.9.
y3=linspace(0,1);%y3=-b3/k3, the y or x intercept, is the maximum value of fanox for a given δ238U value.
y4=linspace(0,1);% y4=-b4/k4, the y or x intercept, is the minimum value of fanox for a given δ238U value.
k3=[(ka-kop)*(Ur2-x1)+kop*dop-ka*da]./[ko*do-kop*dop-(Ur2-x1)*(ko-kop)];% k3 and b3 are calculated using equation 16.
b3=[kop*(Ur2-x1-dop)]./[ko*do-kop*dop-(Ur2-x1)*(ko-kop)];
y3=-b3./k3;
k4=[(ka-ko)*(Ur2-x1)+ko*do-ka*da]./[kop*dop-ko*do-(Ur2-x1)*(kop-ko)];% k4 and b4 are calculated using equation 17.
```

```
b4=[ko*(Ur2-x1-do)]./[kop*dop-ko*do-(Ur2-x1)*(kop-ko)];
y4=-b4./k4;

Ur3=-0.34;% The δ238U of river = -0.34‰
x2=linspace(-0.94,0);% The range of the oceanic δ238U, this model produces negative values
        when δ238U<-0.94.
y5=linspace(0,1);% y5=-b5/k5, the y or x intercept, is the maximum value of fanox for a given
        δ238U value.
y6=linspace(0,1);% y6=-b6/k6, the y or x intercept, is the minimum value of fanox for a given
        δ238U value.
k5=[(ka-kop)*(Ur3-x2)+kop*dop-ka*da]./[ko*do-kop*dop-(Ur3-x2)*(ko-kop)];% k5 and b5 are
        calculated using equation 16.
b5=[kop*(Ur3-x2-dop)]./[ko*do-kop*dop-(Ur3-x2)*(ko-kop)];
y5=-b5./k5;
k6=[(ka-ko)*(Ur3-x2)+ko*do-ka*da]./[kop*dop-ko*do-(Ur3-x2)*(kop-ko)];% k6 and b6 are
        calculated using equation 17.
b6=[ko*(Ur3-x2-do)]./[kop*dop-ko*do-(Ur3-x2)*(kop-ko)];
y6=-b6./k6;

%graphing code
plot(x,y1,'b-',x,y2,'b-',x1,y3,'g-',x1,y4,'g-',x2,y5,'k-',x2,y6,'k-'); axis([-1 0 0 1]);
ylabel('f_{anox}(%)');
xlabel('δ^{238}U_{oc}(‰)');
set(gca,'yticklabel',{'0','10', '20', '30', '40' ,'50','60', '70', '80', '90' ,'100'});
set(gca,'XTick',-1.0:0.1:0);
```

```
ax=gca;
exportgraphics(ax,'fred_anox_Max and Min1.jpg','Resolution',600)
```

Appendix 4.6.3: MATLAB codes for analysis of model sensitivity to the U isotopic fractionation between seawater and the anoxic/euxinic sink

```
% The max and min values of fanox are calculated by using equations 16 and 17 in Section 4.3.3, which is based on restrictions that fanox is a member of set [0,1] and fox + foxp<=1.
%parameters and values
ko=1.45*10^-21;% The rate constant for U removal under oxic condition.
kop=4.63*10^-20;% The rate constant for U removal under oxygen-poor condition.
ka=4.44*10^-19;% The rate constant for U removal under anoxic/euxinic condition.
do=0.02;% The U isotopic fractionation between seawater and the oxic sink.
dop=0.1;% The U isotopic fractionation between seawater and the oxygen-poor sink.
Ur1=-0.24;% The δ238U of riverine= -0.24‰.
%the calculation of the max and min values of fanox under different Δa scenarios
da=0.6;% The U isotopic fractionation between seawater and the anoxic/euxinic sink, danox=0.6‰
x=linspace(-0.84,0);% The range of the oceanic δ238U, this model produces negative values when δ238U<-0.84‰.
y1=linspace(0,1);% y1=-b1/k1, the y or x intercept, is the maximum value of fanox for a given δ238U value.
y2=linspace(0,1);% y2=-b2/k2, the y or x intercept, is the minimum value of fanox for a given δ238U value.
k1=[(ka-kop)*(Ur1-x)+kop*dop-ka*da]./[ko*do-kop*dop-(Ur1-x)*(ko-kop)];% k1 and b1 are calculated using equation 16.
```

```
b1=[kop*(Ur1-x-dop)]./[ko*do-kop*dop-(Ur1-x)*(ko-kop)];
y1=-b1./k1;
k2=[(ka-ko)*(Ur1-x)+ko*do-ka*da]./[kop*dop-ko*do-(Ur1-x)*(kop-ko)];% k2 and b2 are
        calculated using equation 17
b2=[ko*(Ur1-x-do)]./[kop*dop-ko*do-(Ur1-x)*(kop-ko)];
y2=-b2./k2;
da2=0.4;% The U isotopic fractionation between seawater and the anoxic/euxinic sink,
        danox=0.4‰.
x1=linspace(-0.64,0);% The range of the oceanic δ238U, this model produces negative values
        when δ238U<-0.64‰.
y3=linspace(0,1);% y3=-b3/k3, the y or x intercept, is the maximum value of fanox for a given
        δ238U value.
y4=linspace(0,1);% y4=-b4/k4, the y or x intercept, is the minimum value of fanox for a given
        δ238U value.
k3=[(ka-kop)*(Ur1-x1)+kop*dop-ka*da2]./[ko*do-kop*dop-(Ur1-x1)*(ko-kop)];% k3 and b3
        are calculated using equation 16.
b3=[kop*(Ur1-x1-dop)]./[ko*do-kop*dop-(Ur1-x1)*(ko-kop)];
y3=-b3./k3;
k4=[(ka-ko)*(Ur1-x1)+ko*do-ka*da2]./[kop*dop-ko*do-(Ur1-x1)*(kop-ko)];% k4 and b4 are
        calculated using equation 17.
b4=[ko*(Ur1-x1-do)]./[kop*dop-ko*do-(Ur1-x1)*(kop-ko)];
y4=-b4./k4;
```

```
da3=0.8;% The U isotopic fractionation between seawater and the anoxic/euxinic sink,
        danox=0.8‰.
x2=linspace(-1.04,0);% The range of the oceanic δ238U, this model produces negative values
        when δ238U<-1.04‰.
y5=linspace(0,1);% y5=-b5/k5, the y or x intercept, is the maximum value of fanox for a given
        δ238U value.
y6=linspace(0,1);% y6=-b6/k6, the y or x intercept, is the minimum value of fanox for a given
        δ238U value.
k5=[(ka-kop)*(Ur1-x2)+kop*dop-ka*da3]./[ko*do-kop*dop-(Ur1-x2)*(ko-kop)];% k5 and b5
        are calculated using equation 16.
b5=[kop*(Ur1-x2-dop)]./[ko*do-kop*dop-(Ur1-x2)*(ko-kop)];
y5=-b5./k5;
k6=[(ka-ko)*(Ur1-x2)+ko*do-ka*da3]./[kop*dop-ko*do-(Ur1-x2)*(kop-ko)];%k6 and b6 are
        calculated using equation 17.
b6=[ko*(Ur1-x2-do)]./[kop*dop-ko*do-(Ur1-x2)*(kop-ko)];
y6=-b6./k6;
%graphing code
plot(x,y1,'b-',x,y2,'b-',x1,y3,'r-',x1,y4,'r-',x2,y5,'k-',x2,y6,'k-'); axis([-1.1 -0.1 0 1]);
ylabel('f_{anox}(%)');
xlabel('δ^{238}U_{oc}(‰)');
set(gca,'yticklabel',{'0','10', '20', '30', '40' ,'50','60', '70', '80', '90' ,'100'});
set(gca,'XTick',-1.3:0.1:-0.1);
ax=gca;
```

```
exportgraphics(ax,'fred_anox_Max and Min_anoxic fractionation_0.8.jpg','Resolution',600)
```

Appendix 4.6.4: MATLAB codes for analysis of model sensitivity to an extreme scenario when the δ^{238}U of river water = −0.34‰ and Δ_a = 0.8‰

```
% The max and min values of fanox are calculated by using equations 16 and 17 in Section 4.3.3, which is based on restrictions that fanox is a member of set [0,1] and fox + foxp<=1.
%parameters and values
ko=1.45*10^-21;% The rate constant for U removal under oxic condition.
kop=4.63*10^-20;% The rate constant for U removal under oxygen-poor condition.
ka=4.44*10^-19;% The rate constant for U removal under anoxic/euxinic condition.
do=0.02;% The U isotopic fractionation between seawater and the oxic sink.
dop=0.1;% The U isotopic fractionation between seawater and the oxygen-poor sink.
da=0.8;% The U isotopic fractionation between seawater and the anoxic/euxinic sink.
Ur1=-0.34;% The δ238U of river = -0.34‰.

%the calculation of the max and min values of fanox
x=linspace(-1.14,0);% The range of the oceanic δ238U, this model produces negative values when oceanic δ238U<-1.14.
y1=linspace(0,1);% y1=-b1/k1, the y or x intercept, is the maximum value of fanox for a given oceanic δ238U value.
y2=linspace(0,1);% y2=-b2/k2, the y or x intercept, is the minimum value of fanox for a given oceanic δ238U value.
k1=[(ka-kop)*(Ur1-x)+kop*dop-ka*da]./[ko*do-kop*dop-(Ur1-x)*(ko-kop)];% k1 and b1 are calculated using equation 16.
b1=[kop*(Ur1-x-dop)]./[ko*do-kop*dop-(Ur1-x)*(ko-kop)];
```

```
y1=-b1./k1;

k2=[(ka-ko)*(Ur1-x)+ko*do-ka*da]./[kop*dop-ko*do-(Ur1-x)*(kop-ko)];%k2 and b2 are calculated using equation 17.

b2=[ko*(Ur1-x-do)]./[kop*dop-ko*do-(Ur1-x)*(kop-ko)];

y2=-b2./k2;

%graphing code

plot(x,y1,'k-',x,y2,'k-'); axis([-1.2 -0.2 0 1]);

ylabel('f_{anox}(%)');

xlabel('δ^{238}U_{oc}(‰)');

set(gca,'yticklabel',{'0','10', '20', '30', '40' ,'50','60', '70', '80', '90' ,'100'});

set(gca,'XTick',-1.2:0.1:-0.2);

ax=gca;

exportgraphics(ax,'fred_anox_Max and Min_anoxic fractionation_0.34_0.8.jpg','Resolution',600)
```

Appendix 4.7: The $\delta^{238}U_{carb}$ values and U contents of the Green Point Formation limestone and the modern Bahamas primary aragonite precipitates

The $\delta^{238}U_{carb}$ values and U contents of the Green Point Formation limestone (this study).

Sample ID	**Mg/Ca**	**U μg/g**	**$\delta^{238}U^{d}$ ‰**	**±2σ**	***n***
GP 2	0.009	1.56	-0.27	0.04	4
GP 7	0.009	2.44	-0.46	0.05	3
GP 14	0.009	2.53	-0.18	0.08	4
GP 18	0.009	1.62	-0.23		1
GP 22	0.009	3.10	-0.19	0.01	3
GP 25	0.011	0.78	-0.37		1
GP 28	0.014	1.83	-0.41	0.09	3
GP 29	0.010	0.46	-0.49	0.10	4
GP 30	0.010	0.24	-0.70	0.04	3
GP 33	0.015	1.19	-0.21		1
GP 34	0.011	0.60	-0.69	0.12	4
GP 35	0.012	2.08	0.00	0.05	3
GP 38	0.011	0.35	-0.63	0.09	4
GP 40	0.011	0.30	-0.97	0.15	4

Table continued

Sample ID	Mg/Ca	U µg/g	$\delta^{238}U^{d}$ ‰	±2σ	*n*
GP 41A	0.020	0.30	-0.41	0.02	3
GP 45	0.011	0.24	-0.82	0.02	3
GP 46	0.009	0.20	-0.41		1
GP 47	0.009	0.41	-0.53	0.06	3
GP 48	0.014	0.77	-0.44	0.09	2
GP 53	0.012	0.11	-0.66	0.11	4
GP 59	0.021	1.25	-0.33	0.13	4

The modern primary aragonite precipitates in the Great Bahamas (Romaniello et al., 2013).

Location	Depth cm	Mg/Ca	U µg/g	$\delta^{238}U^{d}$ ‰	±2σ	*n*
Core 1	0-3	0.041	2.99	-0.19	0.14	3
T. testudium Flat	4-6	0.043	3.35	-0.12	0.29	3
	8-11	0.043	3.61	-0.15	0.09	3
	12-4	0.042	4.15	-0.13	0.04	3
	16-18	0.041	4.69	-0.16	0.05	3
	24-26	0.038	5.00	0.03	0.17	3
	32-34	0.041	4.73	0.07	0.19	3
	40-42	0.043	5.44	0.14	0.25	3
Core 2	0-3	0.018	3.78	-0.16	0.04	3
Tidal Flat	6-9	0.018	3.91	-0.13	0.03	3
	12-15	0.020	3.98	-0.21	0.11	3
	18-21	0.020	3.97	-0.19	0.05	3
	21-24	0.020	3.96	-0.12	0.16	3
Core3	1-4	0.057	3.12	-0.23	0.15	3
T. testudium Flat	6-9	0.052	3.44	-0.24	0.14	3
	10-14	0.055	3.43	-0.16	0.17	3
	17-21	0.056	3.52	-0.18	0.09	3
	19-22	0.053	3.92	-0.18	0.15	3

References

Andersen, M.B. et al., 2018. A 10-fold decline in the deep Eastern Mediterranean thermohaline overturning circulation during the last interglacial period. Earth Planet. Sci. Lett. 503, 58-67.

Brüske, A., et al., 2020. Correlated molybdenum and uranium isotope signatures in modern anoxic sediments: Implications for their use as paleo-redox proxy. Geochim. Cosmochim. Acta 270, 449-474.

Bura-Nakić, E., Sondi, I., Mikac, N., Andersen, M.B., 2020. Investigating the molybdenum and uranium redox proxies in a modern shallow anoxic carbonate rich marine sediment setting of the Malo Jezero (Mljet Lakes, Adriatic Sea). Chem. Geol. 533.

Li, J., Azmy, K., Kendall, B., 2022. The Mo- and U-isotope signatures in alternating shales and carbonate beds of rhythmites: A comparison and implications for redox conditions across the Cambrian-Ordovician boundary. Chem. Geol. 602, p.120882.

Lu, W., Dickson, A.J., Thomas, E., Rickaby, R.E.M., Chapman, P., Lu, Z., 2019. Refining the planktic foraminiferal I/Ca proxy: Results from the Southeast Atlantic Ocean. Geochim. Cosmochim. Acta 287, 318-327.

Lu, Z., Hoogakker, B.A.A., Hillenbrand, C.-D., Zhou, X., Thomas, E., Gutchess, K.M., Lu, W., Jones, L., Rickaby, R.E.M., 2016. Oxygen depletion recorded in upper waters of the glacial Southern Ocean. Nature communications 7, 1-8.

Noordmann, J., et al., 2015. Uranium and molybdenum isotope systematics in modern euxinic basins: Case studies from the central Baltic Sea and the Kyllaren fjord (Norway). Chem. Geol. 396: 182-195.

Rolison, J.M., Stirling, C.H., Middag, R., Rijkenberg, M.J.A., 2017. Uranium stable isotope fractionation in the Black Sea: Modern calibration of the 238U/235U paleo-redox proxy. Geochim. Cosmochim. Acta 203, 69-88.

Romaniello, S.J., Herrmann, A.D., Anbar, A.D., 2013. Uranium concentrations and 238U/235U isotope ratios in modern carbonates from the Bahamas: Assessing a novel paleoredox proxy. Chem. Geol. 362, 305-316.

Tissot, F.L.H., et al., 2018. Controls of eustasy and diagenesis on the 238U/235U of carbonates and evolution of the seawater (234U/238U) during the last 1.4 Myr. Geochim. Cosmochim. Acta 242, 233-265.

Tissot, F.L.H., Dauphas, N., 2015. Uranium isotopic compositions of the crust and ocean: Age corrections, U budget and global extent of modern anoxia. Geochim. Cosmochim. Acta 167, 113-143.